Tailoring the Electronic Properties of TMDs through Atomic Scale Interfaces, Defects, and Dopants

Edmonds, Matthew

Award date:
2020

Awarding institution:
University of Bath

Tailoring the Electronic Properties of TMDs through Atomic Scale Interfaces, Defects, and Dopants

Matthew Peter Edmonds

A thesis submitted for the degree of Doctor of Philosophy

University of Bath

Department of Physics

October 2019

Acknowledgements

I would like first and foremost to express my gratitude to Dr Adelina Ilie for her guidance and support over the last 4 years. She has been an excellent supervisor and her assistance has been invaluable in all aspects of this research. I would also like to thank Dr Simon Crampin, for providing his theoretical expertise, and acknowledge him for the calculations he provided that are presented in this thesis.

I would like to thank Dr Mattia Cattelan for assistance with the NanoESCA measurements and the helpful discussions, and Dr Alexei Barinov for the Nano-ARPES measurements.

I am very grateful for the funding provided by the Department of Physics at the University of Bath, that allowed me to complete this work.

I would like to thank Paul Reddish for his technical help over the years, and for fabricating the double-sided flange mount for use on the ion source line. I am also grateful to Paul Frith for designing and making the supports for the ion source. I would also like to thank Wendy Lambson for her help with various chemicals and lab equipment, Harry Bone for his assistance with the gas and water lines, and Dr Kei Takashina for help with filling the cryostats with LHe.

Thank you to all the members of the research group, Dr Zichen Liu, Luca Lipani, Anamaria Trandafir, and Maha Alqarni for your help with various things, many useful discussions, and providing a pleasant environment in which to work.

These years would not have been the same without all of those at the University of Bath Jiujitsu club, Bath Town club, and the wider West Country region. Thank you all for sharing the mat with me.

Ling, your support and patience has helped me so much. Thank you for being a source of comfort and happiness over the years.

My sister Katharine for your words of encouragement and belief in me, thank you, it means more than you know. And Oscar, thanks for all the headbutts.

Finally, my Mum and Dad, for their constant support and encouragement, for always pushing me forward and motivating me to continue, and for being there when I need them. I am forever grateful.

Abstract

Quasi-particle interference (QPI) from defects combined with Fourier-transform scanning tunnelling spectroscopy (FT-STS) proved to be a powerful probe of the electronic structure, most notably in a complex 1H-WSe_2/Au(111) heterostructure system. Combined with angle-resolved photoemission spectroscopy (ARPES) and theory, the electronic states could be mapped; revealing that the R25° 1H-WSe_2/Au(111) could be described as a weakly interacting Umklapp system. QPI patterns showed the signature band-folding induced by the moiré super-lattice, and were used to experimentally determine the location of the shifted Au(111) Shockley state. Both FT-STS and ARPES identified a non-dispersive intragap state, which was explained by simulations as a hybridised continuum of states between the W and Se gap edge states and Au bulk bands; now indicating that the system was of metallic nature. To our knowledge this the most extensive analysis involving QPI over such a wide range of energies in a complex system. In addition, FT-STS was used to investigate defects in the transition metal dichalcogenide (TMD) WSe_2; where the presence of spin-flip scattering processes determined a magnetic defect. One such defect with a structure corresponding to a column defect of which is predicted to be magnetic, induced these spin-flip channels, whereas other defects only displayed spin-conserving processes. The structures of other intrinsic defects were also explored with scanning tunnelling microscopy (STM), and two types were identified; the Se monovacancy and the Se, or O interstitial defect. A separate study was done on the decoration of Pd atoms on the WSe_2 crystal surface. Pd dopants were found to locally and globally influence the material; introducing edge states into the electronic structure and a resulting p-type doping of the material. High-temperature annealing then resulted in a large-scale reconstruction of the surface, mediated by the Pd adatoms. Regions were observed with a 1T'-WSe_2 structural phase indicating a phase transition.

Contents

1. **Motivation and aims**..... 1

2. **Physics of TMDs: Structural and electronic properties of WSe_2**

   2.1. Crystal structure..... 7

   2.2. Structural phases..... 9

   2.3. Electronic band-structure of the 2H phase..... 14

   2.4. Spin-orbit coupling and spin-splitting..... 18

   2.5. Spin-valley coupling..... 23

3. **Scanning tunnelling microscopy and spectroscopy (STM/STS) and angle-resolved photoemission spectroscopy (ARPES)**

   3.1. Basic theory of STM..... 26

   3.2. Measurement techniques..... 32

      3.2.1. Topography..... 32

      3.2.2. Scanning tunnelling spectroscopy (STS)..... 35

      3.2.3. Variable-z spectroscopy..... 36

      3.2.4. Fourier transform-STS (FT-STS)..... 38

   3.3. STM instruments..... 49

   3.4. Moiré super-lattice in STM..... 50

   3.5. Angle-resolved photoemission spectroscopy (ARPES)..... 55

      3.5.1. Fundamental theory of photoemission spectroscopy..... 56

4. **Techniques for sample preparation**

   4.1. Tip preparation and assessment..... 63

   4.2. 1H-WSe_2/Au(111) heterostructure preparation..... 67

   4.3. Pd decoration of WSe_2 crystal..... 69

   4.4. Low-energy Ion source for induced defects and substitutional dopants..... 70

5. Defects in a WSe_2 crystal

5.1. The clean WSe_2 surface..... 75
5.2. Defects: atomic scale characterisation..... 77
5.3. Quasi-particle interference (QPI) from defects..... 84
5.4. Conclusions..... 91

6. 1H-WSe_2/Au(111) heterostructure

6.1. Moiré super-lattice..... 95
6.2. Spectroscopy: Electronic band-structure..... 98
6.3. ARPES: Optical band-structure..... 103
6.4. Using atomic scale defects as probes of the electronic structure of the WSe_2/Au(111) heterostructure..... 111
6.4.1. Heterostructure characterisation via STM and $\mathrm{d}I/\mathrm{d}V$ mapping..... 111
6.5. Discussion: R25° 1H-WSe_2/Au(111) is an Umklapp, hybridised system..... 115
6.5.1. Important features revealed by ARPES and comparisons with electronic structure theory..... 115
6.5.2. Important features of electronic structure and quasi-particle scattering as revealed by FT-STS..... 125
6.6. Conclusions..... 136

7. Phase transitions and doping of TMDs

7.1. Conditions and mechanism for phase transition..... 138
7.2. Absence of phase transition in 1H-WSe_2/Au(111) heterostructure..... 142
7.3. Electronic doping via Pd atomic decoration..... 145
7.4. Phase transition via Pd intercalation/alloying..... 149
7.5. Conclusions..... 153

8. Conclusions and future work..... 156

Appendix 1..... 159
Appendix 2..... 160

List of publications and conferences

1) *Defects in WSe_2 investigated by Quasi-Particle Interference mapping and STM/STS*
   M. Edmonds, A. Ilie
   Conference on Physics of Defects in Solids: Quantum Mechanics Meet Topology, ICTP, July 2018

2) *WSe_2/Au heterostructure investigated using scanning tunnelling microscopy/spectroscopy, quasi-particle interference, and ARPES*
   M. Edmonds, M. Cattelan, A. Barinov, A. Ilie
   Atomic structure of nanosystems from first-principles simulations and microscopy experiments, Physics Boat Conference, May 2019

3) *1H-WSe_2/Au(111) as a hybridised Umklapp system*
   M. Edmonds, S. Crampin, M. Cattelan, A. Barinov, A. Ilie
   Paper in preparation

Chapter 1

Motivation and aims

The family of transition metal dichalcogenides (TMDs) extends across multiple different combinations of metal and chalcogenides. The variety of properties this results in has led to great interest in their fabrication, engineering and applications. For example, some naturally exist in a metallic state such as VS_2 and NbS_2, some as semimetals like $MoTe_2$ and $TiSe_2$, while $TaSe_2$ and $PdTe_2$ exhibit low-temperature superconducting properties [1]. The vast majority, however, are semiconducting, with examples including the well know MoS_2 and WSe_2, as well as PtS_2 and TiS_2. The ability to further vary their properties has produced even more varied and tuneable materials. It has been shown that VS_2 can be synthesised as nanoflowers that exhibit low temperature ferromagnetism [2], and it is predicted that this ferromagnetism can be tuned by forming S vacancies [3]. The combination of Se and S chalcogens with Mo has resulted in a material with a tuneable bandgap depending on the ratio [4]. However, for the work presented here, we focus on the semiconducting WSe_2.

The basic 'sandwich' layer of TMDs consists of a layer of metal atoms between two layers of chalcogen atoms to form a monolayer. The covalent bonding in these monolayers is strong, however the layers are held together by a weak van der Waals force meaning that these materials can be easily thinned down to the monolayer [5]. An important consequence for WSe_2 is the spin-splitting of the bands due to a combination of large spin-orbit coupling and the breaking of inversion symmetry in the 1H phase [6]. The spin is coupled to the valleys so adjacent valleys have opposite spin. Control of the spin and valleys therefore would open up a variety of uses in spintronics and valleytronics such as spin valves and for information transfer using the valley index [7].

In addition to the individual materials, monolayer slices of TMDs can be considered building blocks in the construction of heterostructures; including other 2D materials such as graphene, and hexagonal boron nitride (h-BN) [8], as well as metal substrates. Interaction between the layers can modify or induce new properties in the structural and electronic properties of the heterostructure. For example, in a graphene/h-BN heterostructure the potential of the moiré super-lattice formed due to the lattice mismatch induced new Dirac cones either side of the original cone; potentially allowing the control of the transport properties by inducing anisotropic velocities for the charge carriers [9]. The moiré super-lattice can also tune the bandgap of MoS_2, with a strong dependence on the twist angle between the layers. The angle changes the orbital overlap between layers, shifting the out-of-plane Γ states accordingly [10].

A feature of these materials that has proved both a challenge and an opportunity is that of defects. Intrinsically prevalent in most synthesised and exfoliated TMD layers, they have been found to reduce the carrier mobility in monolayers [11, 12]. Therefore, oxygenation methods have been developed to passivate the defects and negate their effect [13]. On the other hand, the potential to tune the material using defects has been realised, with the bandgap of being tuned through grain-boundaries [14] and the n-doping of MoS_2 by S vacancies [15]. The effect of dopants has also been investigated in the scope of modifying the properties, with Mn dopants inducing ferromagnetism in MoS_2 [16], and hydrogenation predicted to induce magnetic moments in the Pt dichalcogenides and MoS_2 [17, 18].

Defects on and under the surface act as scattering centres for quasi-particles, which results in the formation of standing wave patterns in the local density of state (LDOS) due to the interference between incident and reflected electron wavefunctions; called quasi-particle interaction (QPI). This can be exploited to gain an insight into the nature of the defect and the electronic structure of the material. Scanning tunnelling microscopy (STM) is the ideal tool to examine these features as it can directly probe the surface LDOS; by performing a Fourier transform (FT) on the resultant maps, the scattering processes can be identified [19, 20]. The scattering in multivalley system like WSe_2 gives rise to a complex scattering picture, including both intravalley and intervalley scattering channels. The spin-valley coupling and time-reversal symmetry however limits the allowed processes for non-magnetic defects i.e. spin-conserving processes. It is predicted that magnetic defects can lift the valley degeneracy hence allowing for spin-flip processes; indeed, by identifying whether the defect induces spin-flip processes allows us to determine that it has a magnetic moment.

The first focus of this thesis will be structural defects in a WSe_2 crystal; which have been investigated before but there is no unanimous agreement in the appearance of the many different types. Probing the QPI provides another route to achieve this characterisation. One of the big questions regarding magnetic defects is the ability to locally detect and characterise them; using STM we show the first step towards this by distinguishing between the spin-flip and spin-conserving processes for two different defects. The defect inducing spin-flip matched very well structurally with one predicted to carry a magnetic moment. As far as we're aware this is the first observation of this type. Being able to locally determine magnetic moments shows potential to examine the coupling between two moments directly on the surface of materials, further leading to inducing tuneable ferromagnetism.

The second area of focus involved a 1H-WSe_2/Au(111) heterostructure which through preliminary scanning tunnelling spectroscopy (STS) measurements revealed a unique electronic structure. Heterostructures involving metals have previously been shown to modify the band-structure through hybridisation of states [21], however this explanation alone is not sufficient to describe the features observed here. A combination of techniques was used to analyse the origin of the features; angle-resolved photoemission spectroscopy

(ARPES) imaged the valence band states directly indicating a more complex electronic structure than first thought. The moiré super-lattice induced by the lattice mis-match, meant a robust theoretical model for our system could be determined with support from the observed ARPES bands. Further evidence came from an in-depth study of the sub-surface defects which proved the QPI phenomenon as a good probe of the evolving electronic structure across the range of energies investigated. We were able to identify the non-dispersive intra-gap states seen in ARPES, which theoretical simulations showed to be in good agreement with a hybridised continuum of states; intervalley scattering revealing they retain a strong WSe_2 nature. In addition, by selecting certain energy ranges, the QPI determined $\vec{q}$ scattering vectors could map the bands folded by the moiré vectors. This comprehensive study of this heterostructure reveals the interlayer interactions can occur in multiple ways; understanding how this particular twist angle and the annealing conditions led to this is the next step. Seeing how the interest in heterostructure devices is growing rapidly, it is important to understand the potential interlayer interactions that could skew the desired properties.

The final focus dealt with potential phase transitions, both in terms of a substrate-induced transition and the formation through intercalation. The interest for this stems from the previous heterostructure; the modified electronic structure could have indicated a shift from the 1H phase, as seen in a similar case [22]. Analysis through comparison of the surface structures as observed by STM, and the electronic band-structures showed that it remained in the base 1H phase; however, the reason for this is presently not determined, and the future plans for the 1H-WSe_2/Au(111) combine with the previous focus point to explore this. In contrast, Pd decoration of the surface of a WS_2 crystal not only showed its ability to modulate the local and global electronic structure, but through annealing treatment led to regions with observed structural phase transition resembling the 1T' phase in STM images. This phase is not a pure 1T'-WSe_2 though, as it exhibits a slightly different electronic structure. The overall reconstruction of the surface is unusual and hints at different reasons for the phase transition; identification of the mechanism behind it could lead to a new method via which the phase transition could be tuned.

Thesis outline

The thesis is organised into the following chapters:

Chapter 2 introduces the fundamental physics of WSe_2 and similar TMDs covering the basic chemistry and phases with different structures. The electronic band-structures of the different phases are then discussed and their differences noted. Finally, the concepts of spin-orbit coupling leading into the spin-splitting of bands and spin-valley coupling is introduced.

Chapter 3 describes the techniques of scanning tunnelling microscopy/spectroscopy (STM/STS) and angle-resolved photoemission spectroscopy (ARPES) and the basic theory behind them. The modes of STM and STS are introduced, and the concept of Fourier-transform STS (FT-STS) is discussed as well as the various possible scattering processes and selection rules. An overview of moiré super-lattices in heterostructures is given and discussed in the context of STM.

Chapter 4 describes the method of STM tip preparation and characterisation, and the sample preparation techniques. Additionally, a description of a low-energy ion source mounted on the system is given.

Chapter 5 presents a study of intrinsic defects on a WSe_2 crystal using STM/S and FT-STS, identifying their structure and position where possible. The scattering features of two different defects are examined; showing the difference between spin-conserving and spin-flipping processes.

Chapter 6 present an experimental and theoretical study of the origin of the unique electronic structure in a 1H-WSe_2/Au(111) heterostructure. Combined ARPES, FT-STS, and STM observations are backed by calculations to describe the hybridisation of states due to interlayer interaction, and the band-folding by the moiré super-lattice.

Chapter 7 explores the possibility of substrate-induced phase transition in heterostructures. Furthermore, the effect of Pd decoration on a WSe_2 crystal is explored, as well as a potential route of phase transition via Pd intercalation/alloying.

Chapter 8 summarises the results and presents the future direction of work.

References

[1] Chhowalla M, Shin H S, Eda G, Li L J, Loh K P and Zhang H (2013) The chemistry of two-dimensional layered transition metal dichalcogenide nanosheets. *Nature Chemistry.* **5** 263-75

[2] Zhong M, Li Y, Xia Q, Meng X, Wu F and Li J (2014) Ferromagnetism in VS2 nanostructures: Nanoflowers versus ultrathin nanosheets. *Materials Letters.* **124** 282-5

[3] Liu B, Wu L J, Zhao Y Q, Wang L Z and Cai M Q (2016) A first-principles study of magnetic variation via doping vacancy in monolayer VS2. *Journal of Magnetism and Magnetic Materials.* **420** 218-24

[4] Gong Y J, Liu Z, Lupini A R, Shi G, Lin J H, Najmaei S, Lin Z, Elias A L, Berkdemir A, You G, Terrones H, Terrones M, Vajtai R, Pantelides S T, Pennycook S J, Lou J, Zhou W and Ajayan P M (2014) Band gap engineering and layer-by-layer mapping of selenium-doped molybdenum disulfide. *Nano Letters.* **14** 442-9

[5] Mak K F, Lee C, Hone J, Shan J and Heinz T F (2010) Atomically thin MoS2: a new direct-gap semiconductor. *Physical Review Letters.* **105** 4

[6] Xiao D, Liu G B, Feng W X, Xu X D and Yao W (2012) Coupled spin and valley physics in monolayers of MoS2 and other group-VI dichalcogenides. *Physical Review Letters.* **108** 5

[7] Xu X D, Yao W, Xiao D and Heinz T F (2014) Spin and pseudospins in layered transition metal dichalcogenides. *Nature Physics.* **10** 343-50

[8] Geim A K and Grigorieva I V (2013) Van der Waals heterostructures. *Nature.* **499** 419-25

[9] Yankowitz M, Xue J M, Cormode D, Sanchez-Yamagishi J D, Watanabe K, Taniguchi T, Jarillo-Herrero P, Jacquod P and LeRoy B J (2012) Emergence of superlattice Dirac points in graphene on hexagonal boron nitride. *Nature Physics.* **8** 382-6

[10] Trainer D J, Putilov A V, Wang B K, Lane C, Saari T, Chang T R, Jeng H T, Lin H, Xi X X, Nieminen J, Bansil A and Iavarone M (2019) Moire superlattices and 2D electronic properties of graphite/MoS2 heterostructures. *Journal of Physics and Chemistry of Solids.* **128** 325-30

[11] Fang H, Chuang S, Chang T C, Takei K, Takahashi T and Javey A (2012) High-performance single layered WSe2 p-FETs with chemically doped contacts. *Nano Letters.* **12** 3788-92

[12] Ma N and Jena D (2014) Charge scattering and mobility in atomically thin semiconductors. *Physical Review X.* **4** 9

[13] Shearer M J, Li W J, Foster J G, Stolt M J, Hamers R J and Jin S (2019) Removing defects in WSe2 via surface oxidation and etching to improve solar conversion performance. *ACS Energy Letters.* **4** 102-9

[14] Huang Y L, Chen Y F, Zhang W J, Quek S Y, Chen C H, Li L J, Hsu W T, Chang W H, Zheng Y J, Chen W and Wee A T S (2015) Bandgap tunability at single-layer molybdenum disulphide grain boundaries. *Nature Communications.* **6** 8

[15] Lu C P, Li G, Mao J, Wang L M and Andrei E Y (2014) Bandgap, mid-gap states, and gating effects in MoS2. *Nano Letters.* **14** 4628-33

[16] Wang J Q, Sun F, Yang S, Li Y T, Zhao C, Xu M W, Zhang Y and Zeng H (2016) Robust ferromagnetism in Mn-doped MoS2 nanostructures. *Applied Physics Letters.* **109** 5

[17] Manchanda P, Enders A, Sellmyer D J and Skomski R (2016) Hydrogen-induced ferromagnetism in two-dimensional Pt dichalcogenides. *Physical Review B.* **94** 5

[18] Yang S, He J, Zhou P and Sun L Z (2017) Magnetic control of single transition metal doped MoS2 through H/F chemical decoration. *Journal of Magnetism and Magnetic Materials.* **422** 243-8

[19] Liu H J, Chen J L, Yu H Y, Yang F, Jiao L, Liu G B, Ho W K, Gao C L, Jia J F, Yao W and Xie M H (2015) Observation of intervalley quantum interference in epitaxial monolayer tungsten diselenide. *Nature Communications.* **6** 6

[20] Yankowitz M, McKenzie D and LeRoy B J (2015) Local spectroscopic characterization of spin and layer polarization in WSe2. *Physical Review Letters.* **115** 5

[21] Dendzik M, Bruix A, Michiardi M, Ngankeu A S, Bianchi M, Miwa J A, Hammer B, Hofmann P and Sanders C E (2017) Substrate-induced semiconductor-to-metal transition in monolayer WS2. *Physical Review B.* **96** 6

[22] Yin X M, Tang C S, Wu D, Kong W L, Li C J, Wang Q X, Cao L, Yang M, Chang Y H, Qi D Y, Ouyang F, Pennycook S J, Feng Y P, Breese M B H, Wang S J, Zhang W J, Rusydi A and Wee A T S (2019) Unraveling high-yield phase-transition dynamics in transition metal dichalcogenides on metallic substrates. *Advanced Science.* **6** 14

Chapter 2

Physics of TMDs: Structural and electronic properties of WSe_2

TMDs have displayed a remarkable host of properties, lending them well to applications in variety of fields. The following chapter explains their properties starting from the basic chemistry of TMDs. This has direct consequences on the phases they can exhibit; all of which show different properties in themselves. These phases are characterised by their structure and electronic band-structures which is discussed in detail. Finally, the spin and valley properties of these materials is introduced, which plays a major part in the interest generated for these materials.

2.1 Crystal structure

The transition metal dichalcogenide (TMD), tungsten diselenide (WSe_2) is a compound with the general form MX_2, where M commonly represents the transition metals W or Mo which are 6-fold coordinated, and X represents the chalcogens S, Se, or Te which are 3-fold coordinated. This results in a single layer of W atoms arranged in a hexagonal format, sandwiched between two hexagonal layers of Se atoms, as shown in figure 2-1. The bonding geometry of the metal can either be trigonal prismatic where the chalcogen atomic planes lie coincident to each other, or octahedral where they are staggered [1]. The preferred phase adopted by a particular TMD depends primarily on the number of d-electrons the transition metal has, and since W is a group 6 metal it normally forms the trigonal prismatic structure. Each of these slices forms a single layer of the structure, with covalent bonding between individual layers. The bonding states are filled by 4 electrons donated from the metal atoms,

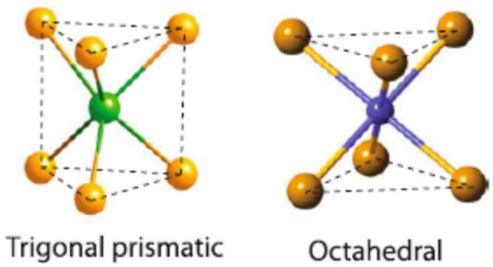

Figure 2-1. Schematic showing the two bonding geometries of the metal atom and the chalcogen atoms. [1]

which is different from most transition metal complexes. This means the metal atoms and chalcogen atoms have a charge (or oxidation state) of +4 and -2 respectively [2].

In the electronic structure of chalcogens, the highest valence shell contains 6 electrons in the configuration of ns^2p^4 or $ns^2p_x^1p_y^1p_z^2$. This means there are two unpaired electrons and one electron pair, commonly known as lone-pair (LP) electrons. The *s*- and *p*-orbitals can also become hybridised which is believed to happen in these TMDs, where the chalcogen atoms have sp^3-hybridised orbitals including the LP electrons. In the transition metals, the partially filled d-band is the main contributing factor to their structure and properties. The different shapes of the p-, and d-orbitals are shown in figure 2-2, and sets of s-, p-, and d-orbitals hybridise to maximise the orbital overlap. Using two valence d-orbitals and the ns and np orbitals, where n is the quantum number, they can hybridise to form 6 sp^3d^2 orbitals. Whether the orbitals are out of plane or not is very important when the spin properties of the bands are considered.

Initially the d orbitals have a degenerate energy level, but when forming TMDs this degeneracy is broken. The non-bonding d-bands are located in the gap between the bonding σ and anti-bonding σ* bands of the metal-chalcogen bonds, shown by figure 2-3. For the trigonal prismatic phase, the d-orbitals split into three degenerate bands consisting of d_{Z^2} in the a_1 band, $d_{x^2-y^2}$ and d_{xy} in the e band, and d_{xz} and d_{yz} in the e' band. On the other hand, the octahedral phase form just two bands with d_{z^2} and $d_{x^2-y^2}$ in the e_g band, and d_{xy}, d_{xz}, and d_{yz} in the t_{2g} band. As mentioned above, this is determined by the metal d-electron count and has a significant effect on the properties of the TMD. The semiconducting character of WSe_2 is given by the band gap between the fully occupied d_{z^2} band and the

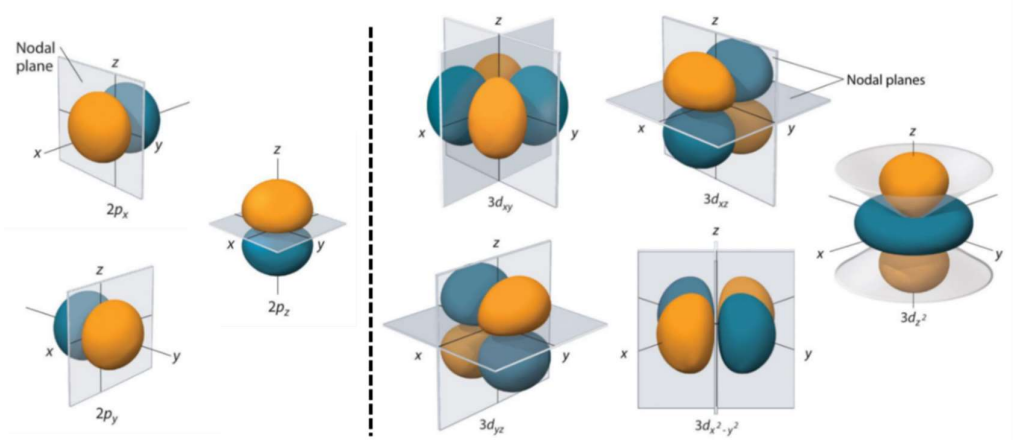

Figure 2-2. Diagram showing the different shapes of the different atomic p and d orbitals of the chalcogen and transition metal atoms. [3]

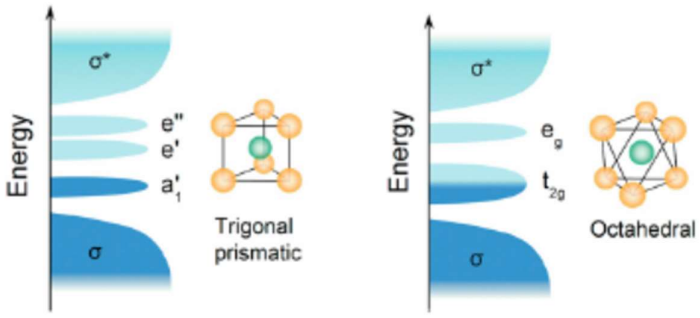

Figure 2-3. Schematic showing the DOS for TMDs from different groups where σ and σ represent the bonding and anti-bonding states respectively. WSe_2 and WS_2 are from group 6. The lifting of d-orbital energy degeneracy is shown, with a difference between the trigonal prismatic and octahedral coordination. [2]*

empty $d_{x^2-y^2}$, d_{xy} bands. In the case of $NbSe_2$ which now has only a partially filled d_{z^2} the overall nature of the material is now metallic [4].

Bonding between layers is due to van der Waals' interaction, which can be described as a combination of the attractive and repulsive forces between similar species. Typically, these are dipole-dipole, dipole-induced dipole and London (induced dipole-induced dipole) interactions. This interaction is much weaker than the in-plane covalent-like bonds and therefore it is easy to cleave the material by layer, in a similar manner to graphene. The surface energy of WS_2 which is very similar to WSe_2, has been shown to be comparable to that of graphene [5]. The LP electrons from the chalcogen which do not contribute to the intra-layer bonding, are perpendicular to the surface which results in no dangling bonds. Due to this these materials are very stable and generally unreactive, although with a reactivity higher than graphene, there is still potential for their functionalisation.

2.2 Structural phases

One of the unique features of TMDs is the wide range of structure phases they exhibit, especially in the monolayer which lends to the great variety of electronic properties they can possess. In the bulk the phase is mainly determined by the different stacking of layers with the 3 most common types being the 1T, 2H, and 3R polymorphs, shown in figure 2-1. The unit cell for each is determined by the number of layers and the symmetry, namely T-trigonal, H-hexagonal, and R-rhombohedral [2]. WSe_2 commonly stacks in the 2H configuration, as this is the lowest energy configuration, of which there are 3 different modifications. The WSe_2 layers stack in the $2H_c$ polymorph which is characterised by AcA CaC stacking sequence where the metal atom lies on top of the two chalcogen atoms in the subsequent layer, as

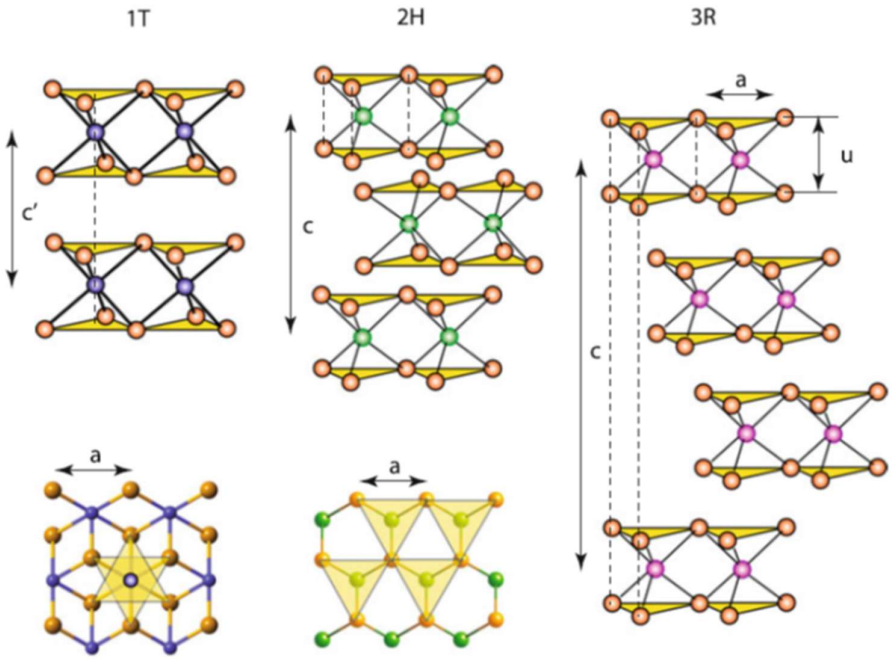

Figure 2-4. Diagram of the 1T, 2H, and 3R polymorphs commonly formed by TMDs. The orange spheres represent the chalcogen atoms, and the purple, green, and pink spheres represent the metal atoms in the different polymorphs. The 1T polymorph has an octahedral phase as shown by the non-aligned top and bottom chalcogen atoms, whilst the 2H and 3R have the chalcogen aligned trigonal prismatic phase. The top down views of the octahedral and trigonal prismatic phases are underneath their corresponding 1T and 2H polymorph, with the yellow triangles showing chalcogen atoms in plane. [1]

shown for 2H in figure 2-4. The unit cell of the 2H phase contains 6 atoms, 3 each from the two subsequent layers. In the 1T phase the bonding configuration of the metal is now octahedral, and only has one stacking configuration of AbC AbC as seen. Each unit cell now contains just one monolayer of the material.

While the 2H phase is most commonly occurring, the other phases are also frequently observed although they usually require different growth conditions or external influences to form. For the 3R phase of MoS_2 and $MoSe_2$ this can be achieved using high pressure and temperature [6]. However, in most cases these phases are unstable and will relax back into the 2H, or other more stable configuration [7, 8].

In the monolayer the layer stacking is no longer viable, so the available phases are either trigonal prismatic or octahedral, which are now called 1H and 1T respectively. Another phase, known as the distorted 1T structure or 1T' is also possible. The 1T' structure can be loosely said to be octahedral like 1T, but with the metal atoms sliding along the x direction resulting in a doubling of the periodicity. The pairs of dislocated metal atoms now form zigzag chains along the y direction and the deformation makes the chalcogen atoms above the zigzag chains rise higher than those adjacent to it, as indicated in figure 2-5(c). This now means the

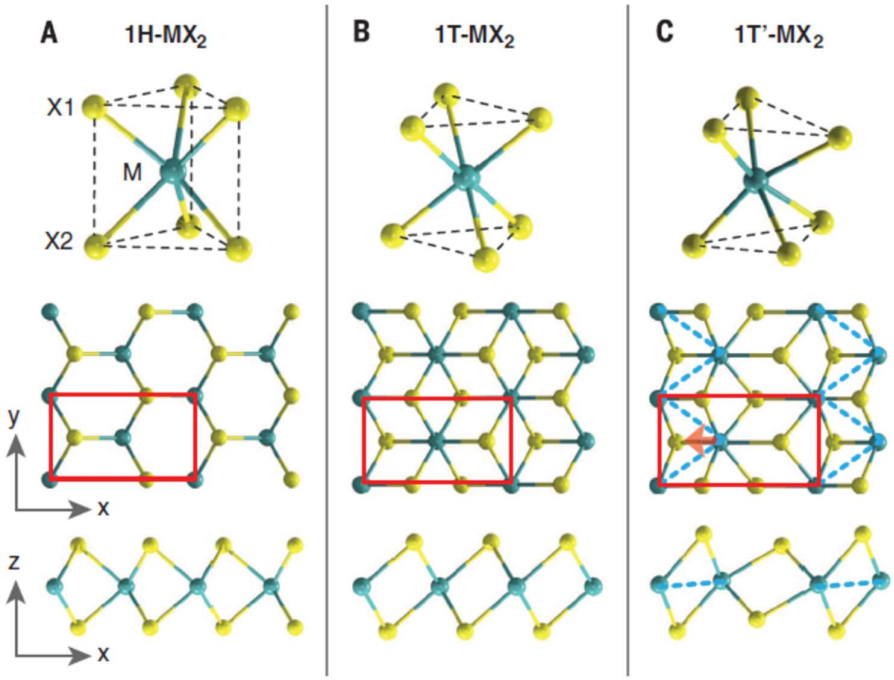

Figure 2-5. Structures of the monolayer phases of TMDs showing the 1H, 1T, and 1T' varieties. The 1H phase has trigonal prismatic structure, the 1T has octahedral, and the 1T' has a distorted octahedral, with the metal zigzag chain shown by the blue dotted line. The red rectangles show potential unit cells. [8]

1T' structure has a rectangular unit cell rather than a hexagonal one. The 1T' phase is stable in WSe_2, but it will usually grow as a mixture of phases as only in WTe_2 is it the most energetically favourable phase [9].

Appearance of the structural phases

Different techniques have been used to image the surface structure of the different phases, with scanning tunnelling microscopy (STM) and scanning transmission electron microscopy (STEM) providing some of the clearest evidence. Figure 2-6 shows STM scans of 2H-WSe_2 in (a) and 1T-MoS_2 in (b). The structural difference between the two TMDs is only a slight difference in the lattice spacing with the WSe_2 Se-Se spacing being 0.328 nm and the MoS_2 S-S spacing being 0.34 nm in the 2H phase. The 2H phase appears a pattern of bright spots arranged in a hexagonal pattern, with the bright intensity corresponding to the Se (or S) atoms in the top layer. The surface height is uniform with no distortions. In the case of the 1T phase, it maintains the hexagonal structure of the top layer but STM studies have shown this is the form of a ($\sqrt{3}a \times \sqrt{3}a$) superstructure [10]. This could be due to the method of formation by intercalation of K, with the superstructure created due to distortions from

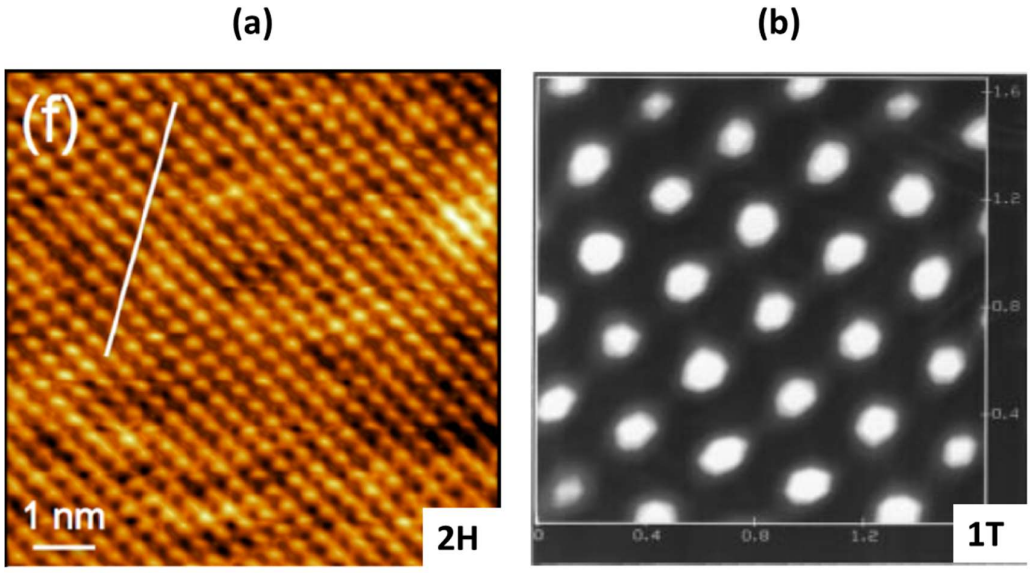

Figure 2-6. (a) STM image of 2H-WSe_2 showing a hexagonal pattern of top layer Se atoms (bright spots). (b) STM image of 1T-MoS_2 showing a (√3a × √3a) *superstructure, with bright spots assigned to S atoms in the superstructure. [12, 13]*

the interstitials. This can also lead to different superstructures such as (2a × 2a) , or (2a × a) for Li intercalates [10, 11].

Experimental observations with scanning transmission electron microscope (STEM) also show that the lattice spacing of the metal and chalcogen atoms don't significantly shift between the 2H and ideal 1T phases [7]. This is seen in figure 2-7, showing an area of the 2H phase (a) and the 1T phase (b). The difference between the phases can be seen in the increased intensity of the stacked chalcogen atoms in the 2H phase, leading to 3 different sites of contrast. The staggered arrangement of the 1T chalcogens means only the metal atoms are seen.

On the other hand, the 1T' phase displays a different structure consisting of rows along one direction, as displayed in the STM image in figure 2-8(a). These rows are along the zigzag metal chains created from the distortion, with an overlay of the atomic positions shown in the inset of the figure. The bright points along the rows are the Se atoms pushed higher due to the chain, and the less intense points in the darker adjacent row are the lower Se atoms. The unit cell is shown by the blue rectangle and the lattice parameters are a=0.58 nm (direction perpendicular to the rows) and b=0.33nm (spacing between Se atoms along the rows) [14]. These chains are also clearly seen in the STEM image in figure 2-7(c), indicating that they are due to a structural distortion. This pattern makes this phase very easy to identify in STM and STEM images. An STM spectroscopy measurement is shown in figure 2-8(b), taken from areas of 2H-WSe_2 and 1T'-WSe_2. The green curve shows the $\mathrm{d}I/\mathrm{d}V$ spectroscopy from the 2H phase and shows a clear quasi-particle bandgap of about 1.8 eV,

indicating the semiconducting character. The orange curve from the 1T' phase reveals only a very short bandgap of -130 meV, as well as having a very different LDOS [13]. This contrast between the phases also makes them easy to distinguish.

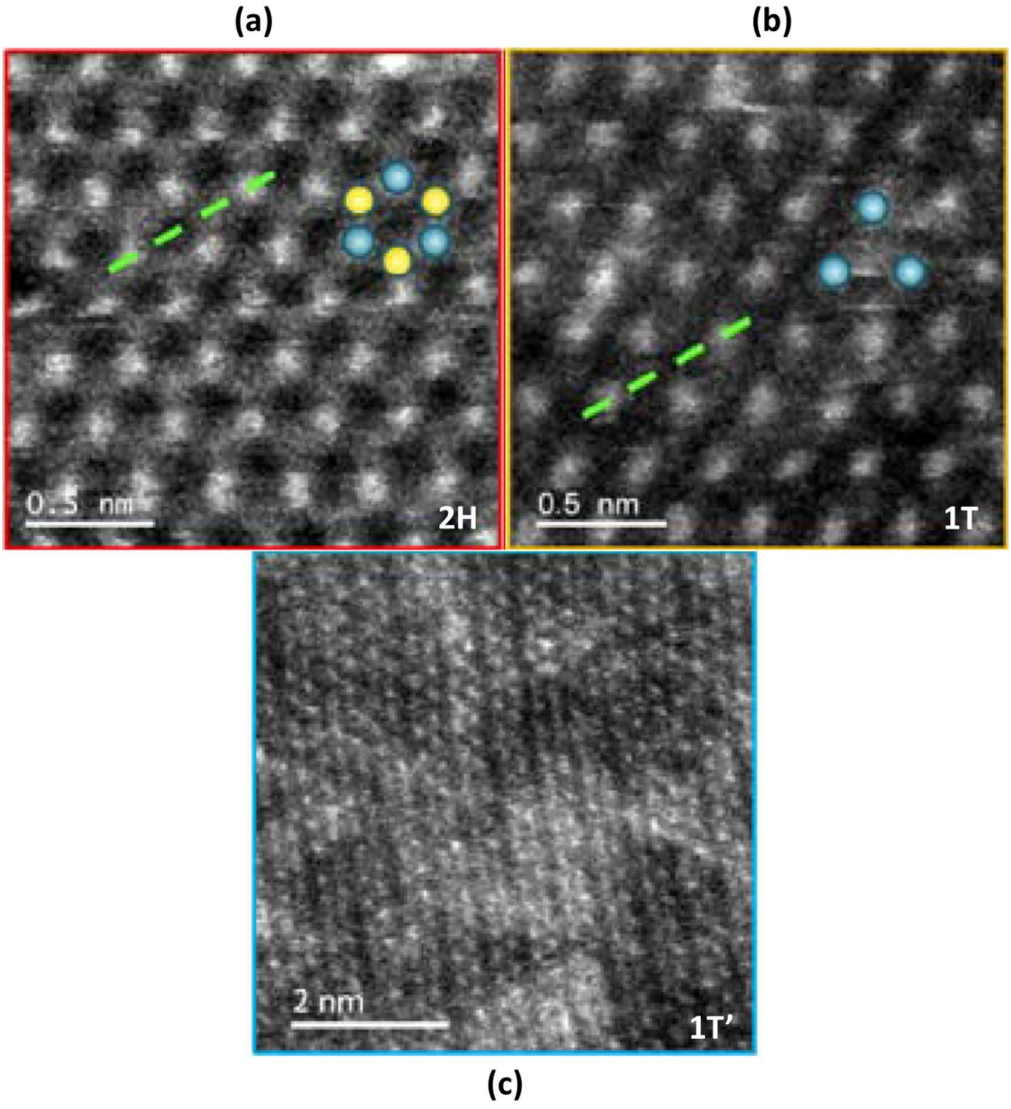

Figure 2-7. STEM images of the 2H (a), 1T (b), and 1T' (c) phases of MoS_2.The blue dots indicate the Mo atom positions and the yellow dots the S positions. [7]

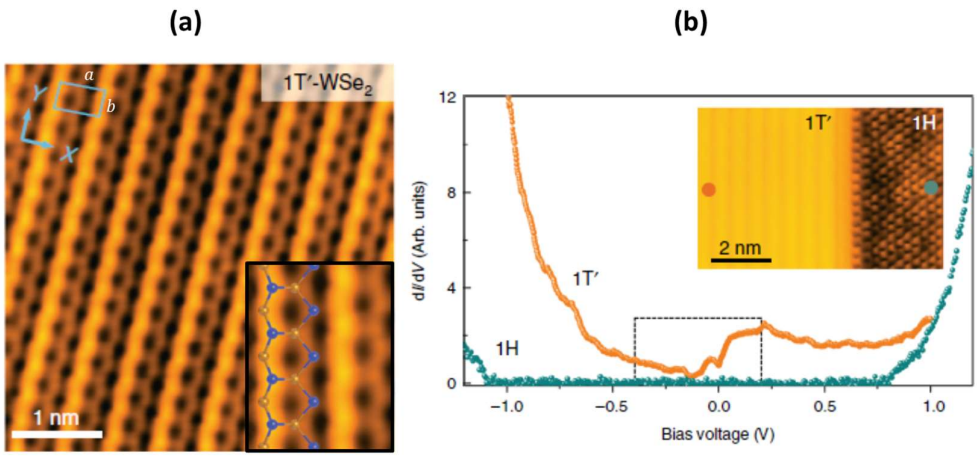

Figure 2-8. (a) STM image of 1T′-WSe_2. The surface structure is arranged in rows along the direction of the W zigzag chains, with the bright spots assigned to the higher Se atomic array, and the adjacent less intense spots to the lower array. The unit cell is displayed as the blue rectangle. The atomic overlay is shown in the inset, with Se and W as blue and orange dots respectively. (b) dI/dV measurements from the 2H (green) and 1T′ (orange) regions. [15]

2.3 Electronic band-structure of the 2H phase

To understand the band structure of a material, the concept of the Brillouin zone (BZ) first must be introduced. This idea arises from the concept of reciprocal space (also known as momentum space or k-space) which is the Fourier transform of the real space periodic lattice. The crystal lattice for a 2H phase TMD is shown in figure 2-9(a), and the lattice vectors are given by,

$$\vec{a} = a\left(\frac{\sqrt{3}}{2}\hat{x} + \frac{1}{2}\hat{y}\right), \qquad \vec{b} = a\left(-\frac{\sqrt{3}}{2}\hat{x} + \frac{1}{2}\hat{y}\right), \qquad \vec{c} = c.\hat{z}, \tag{2-1}$$

where a is the atomic lattice spacing and c is the height of the unit cell in the z-direction. The resulting reciprocal space lattice vectors are then,

$$\vec{a}^* = \frac{4\pi}{\sqrt{3}a}\left(\frac{1}{2}\hat{x} + \frac{\sqrt{3}}{2}\hat{y}\right), \qquad \vec{b}^* = \frac{4\pi}{\sqrt{3}a}\left(-\frac{1}{2}\hat{x} + \frac{\sqrt{3}}{2}\hat{y}\right), \qquad \vec{c}^* = \frac{2\pi}{c}.\hat{z}, \tag{2-2}$$

This give a BZ that can be visualised by the Wigner-Seitz primitive cell shown in figure 2-9(b), which is a construction of line bisectors from the reciprocal lattice vectors between the reciprocal lattice points. The encompassed area is known as the first BZ and contains the high symmetry points of the structure, which for the 2D case are the Γ point situated at the centre, the K points located at the corners of the hexagon, and M points at the halfway point

between neighbouring K points. These are shown in figure 2-9(c), along with the quasi-symmetry Q point located between the Γ and K points. The energy bands of a material are mapped along the lines between these high symmetry points to create what is known as the band structure. The non-equivalence of the W and Se sublattices result in a non-equivalence at the K and Q points, where they alternate between K(Q) and −K(Q) valleys instead, shown in figure 2-9(d). This has a direct impact on the spin and valley physics in these materials.

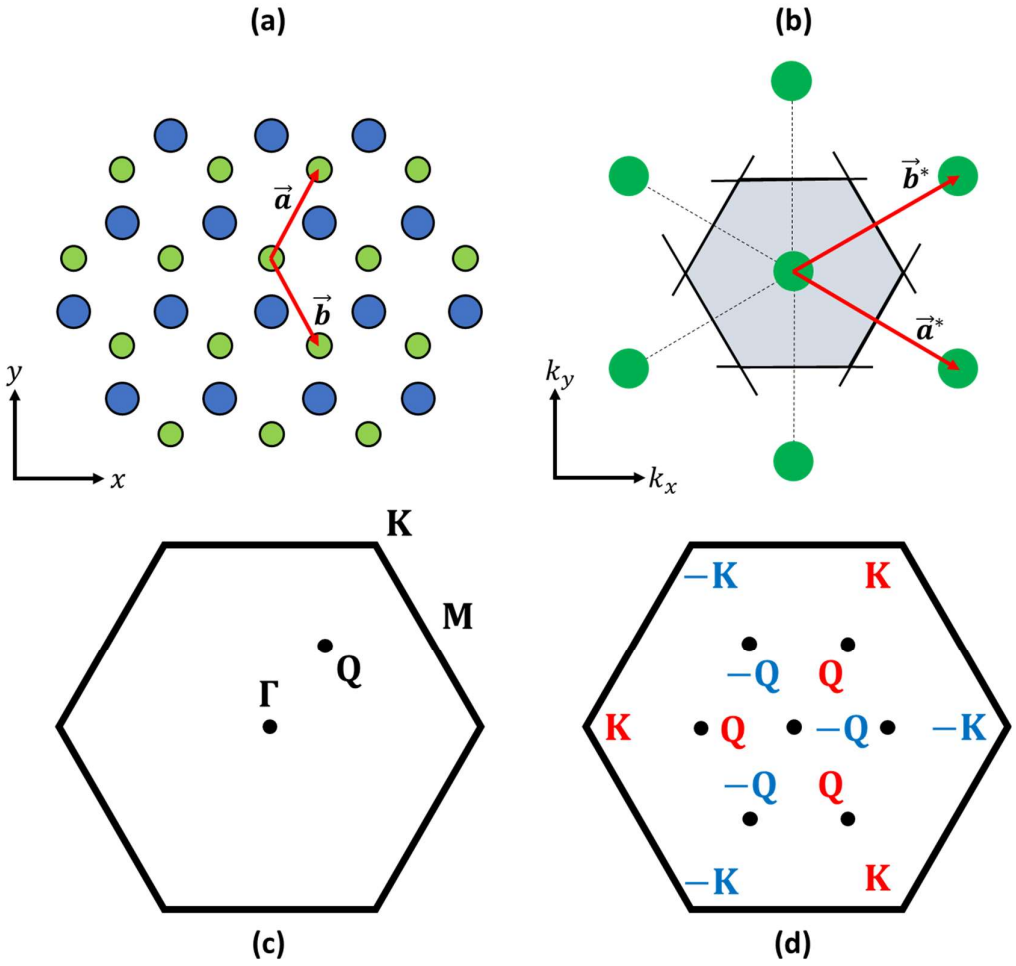

Figure 2-9. (a) Schematic showing the top down structure of 2H phase with the blue dots representing the metal atoms and the green dots the chalcogen atoms. The vectors $\vec{a}$ and $\vec{b}$ are the lattice vectors. (b) A representation of reciprocal space, with the reciprocal space vectors $\vec{a}^*$ and $\vec{b}^*$ indicated and the green dots as the reciprocal lattice points. The line bisectors of the reciprocal lattice vectors enclose an area known at the first Brillouin zone (BZ). (c) Diagram of the BZ with the high symmetry points, or critical points labelled. (d) BZ with the non-equivalent K and $-K$ valleys shown in red and blue, which is a consequence of the non-equivalent W and Se sublattices.

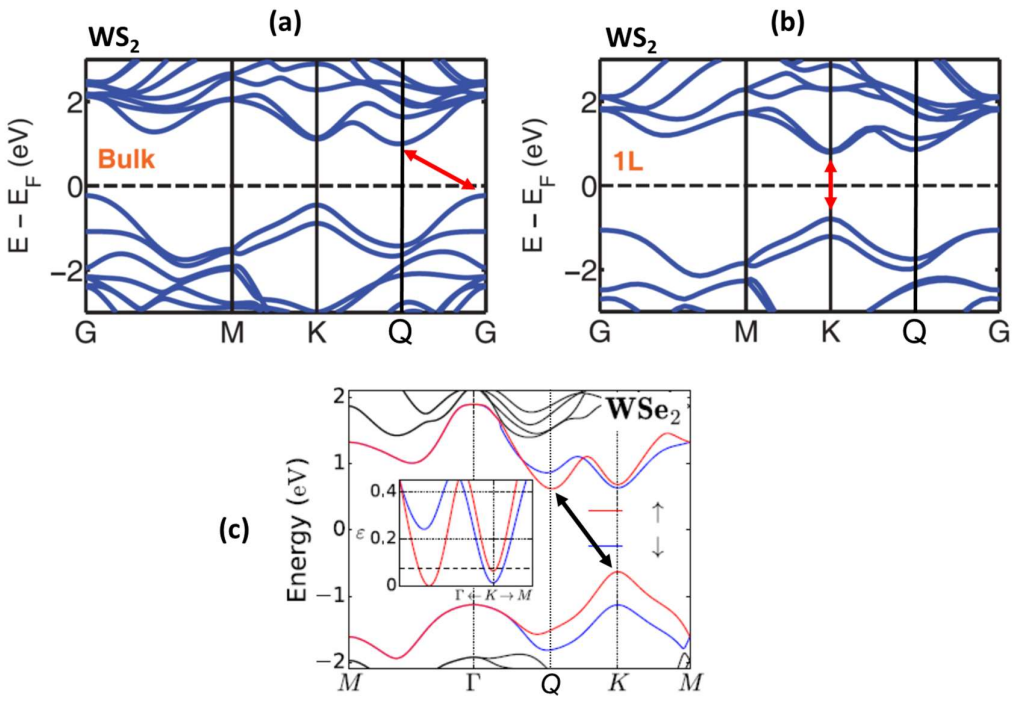

Figure 2-10. DFT calculated band structures for the bulk WS_2 (a) and monolayer WS_2 (b), showing the transition from the indirect bandgap between $\Gamma(G)$ and Q, to the direct one between K points. (c) Calculated band-structure including spin-split valleys for monolayer WSe_2, showing instead an indirect gap between the K and Q points. [16, 20]

The band-structure of the common bulk TMDs including WSe_2 have been calculated to have an indirect band gap, located between the valence band edge (VBE) at the Γ point, and the conduction band edge (CBE) at the Q point. A DFT calculated band-structure of WS_2 is presented in figure 2-10(a), indicating the indirect gap with the red arrow. The states at these points are mainly comprised of orbitals with strong out-of-plane or z-dependence, which is along the c-axis of the crystal in figure 2-4. This means they have stronger interlayer coupling and explains why the bandgap is indirect when there is more than one layer. The dispersion of the orbitals will be discussed in more detail below.

The properties of the monolayer are distinctly different from the bulk and for this reason thinning down these crystals is of great interest. As the number of layers decreases the states with z-dependence are shifted due to the change in the interlayer coupling. The calculated band-structure for the WS_2 monolayer is displayed in figure 2-10(b). The states with a more in-plane nature are largely unaffected by this, resulting in the VBE and CBE shifting to the K point for most semiconducting TMDs, making them direct gap semiconductors in the monolayer. However, recent calculations [16] and experiments of both quasi-particle and optical nature [17, 18] have shown that in WSe_2 at the CBM the Q band is slightly lower than the K band with as shown by figure 2-10(c). This means it retains an indirect bandgap as marked by the black arrow, although since they are almost degenerate in energy the direct

bandgap between the K points is expected to only be slightly larger in energy. This was also the earlier prediction for strained monolayer systems, which is a potential effect for any monolayer placed or grown on a substrate [19].

Modified band-structures for the 1T and 1T' phases

The structural differences of the 1T phase compared to the 2H phase mean it has a very different electronic band-structure. A calculated band-structure is presented in figure 2-11 along with a corresponding partial density of states (PDOS). The fact that bands cross the Fermi level at the K and Γ points indicate that the 1T phase has a metallic character and does not possess a bandgap, in contrast to the semiconducting 2H phase. This means it has a much great conductivity, and studies have shown that 1T phase TMDs can be used as an efficient carrier injection layer for 2H TMD field-effect transistors forming p-type contacts at the interface [21, 22]. Due to almost no structural mis-match and low contact resistance, these interfaces are not constrained as typical metal contacts are [23].

The distorted structure of the 1T' phase results in a change of the BZ to a rectangular shape as shown in figure 2-12(a). The critical points are now different and change the electronic band-structure completely which can be seen in figure 2-12(b). A characteristic feature of this phase is the inverted band-structure around the Γ point, the origin of this arising from

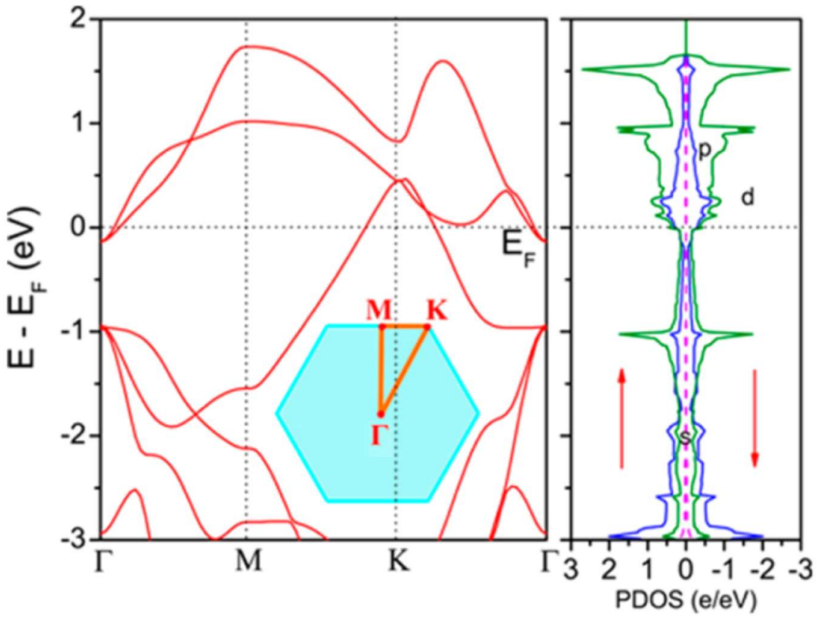

Figure 2-11. Calculated band-structure for the 1T phase. The bands at K and Γ cross the Fermi level (dotted line at 0 eV) resulting in the metallic character. The BZ is shown as an inset. (b) PDOS lined up with the band-structure showing the presence of d-, and p-orbitals at 0 eV and no opening of a bandgap.

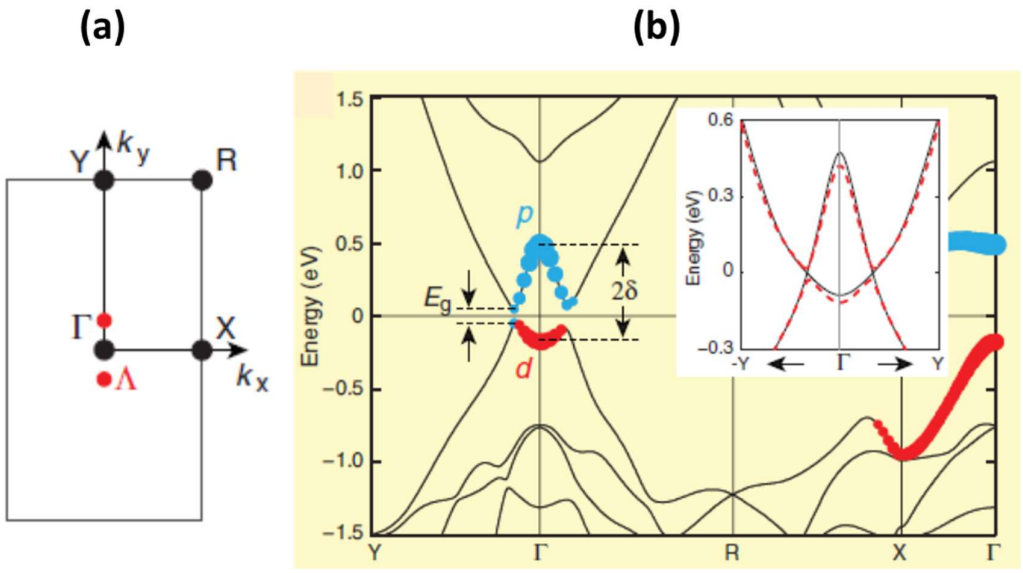

Figure 2-12. (a) Rectangular BZ for the 1T' phase with Γ *at the centre and other critical points* Y, R, *and* X *are labelled. The red dots labelled* Λ *are the positions of the fundamental gap. (b) Calculated band-structure of 1T' showing the inverted bands at* Γ *and their orbital nature of* p *(blue) and* d *(red). The fundamental gap (*E_g*) and inverted gap (*2δ*) are shown. The inset compares the inverted structure with spin-orbit coupling (SOC) (red dashed line) and without (black line). [8]*

the orbital nature of the bands. The VB mainly consists of the metal d-orbitals and the CB of the chalcogen p-orbitals, and due to the period doubling of the metal zigzag chain in the structure the metal d-orbitals are shifted below the chalcogen p-orbitals at this point. For WSe_2 the calculated band inversion gap is between 0.7-0.85 eV depending on the calculation method [8]. Without spin-orbit coupling, the calculations show two Dirac cones along the Y-Γ-Y direction but including it leads to the opening of a fundamental gap at these two cones, as shown in the inset of figure 2-12(b). This means that the 1T' phase can be considered a quantum spin Hall (QSH) insulator, which are insulators in the bulk but have topologically protected conducting edge states. The fundamental gap for the 1T'-WSe_2 is considered relatively large at around 0.1 eV.

2.4 Spin-orbit coupling and spin-splitting

Electrons possess an internal degree of freedom known as their spin. As fermions this can take a half-integer value, so for electrons this is $+1/2$ (spin-up) or $-1/2$ (spin-down). Spin-orbit coupling (SOC) or interaction is a phenomenon involving the interaction of an electrons spin and orbital angular momentum. In its simplest terms, the motion of the electron within the atom generates a magnetic field which interacts with its spin magnetic moment. Due to

this there is a breaking of the spin degeneracy, resulting in separate spin-up and spin-down energy levels.

In WSe_2 the SOC originates from the metal d-orbitals and is very large due to the heavy nature of the W atom, with WSe_2 having the largest and therefore the greatest spin-splitting of the most common TMDs. The layered structure of these materials means that the unit cell of the bulk 2H phase crystal contains 2 monolayers arranged in an AcA CbC stacking pattern, shown in figure 2-13(a). Because of this the bulk is inversion symmetric,

$$[E(\vec{k},\uparrow) = E(-\vec{k},\uparrow)], \tag{2-3}$$

which combined with time reversal symmetry,

$$[E(\vec{k},\uparrow) = E(-\vec{k},\downarrow)], \tag{2-4}$$

results in Kramer's degeneracy [24, 25].

$$[E(\vec{k},\uparrow) = E(\vec{k},\downarrow)], \tag{2-5}$$

This states that every energy level is at least doubly degenerate if it has half-integer spin, or in other words, the energy cannot depend on the electron spin, and so there is no spin-splitting observed in the bulk crystal. This can be explained by looking at the unit cell of the bulk. In each layer the bands have a spin polarisation, but in the stacking of the bulk, adjacent layers are rotated 180° from each other, with means the sign of the spin polarisation is opposite between layers. This leads a spin degeneracy in the bulk, and therefore spin-layer

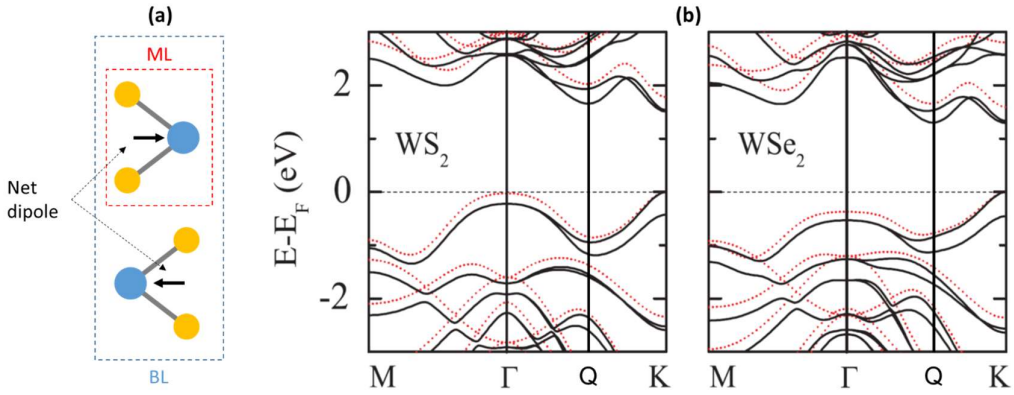

Figure 2-13. (a) Schematic of the unit cells for bi-layer (BL) highlighted in blue and monolayer (ML) highlighted in red. The bulk unit cell is the same as the BL one. In the monolayer unit cell there is no inversion symmetry. The net dipole for each layer is highlighted and is opposite for adjacent layers. (b) DFT calculated band-structures for WS_s and WSe_2 shown for the cases with the inclusion of spin-orbit interaction (solid black line) and without (dotted red line). The spin-splitting can clearly be seen at the K point of the VBE and the K and Q points of the CBM. The spin-splitting is larger in the WSe_2 owing to its greater SOC. [24]

locking. It has been reported that spin-resolved ARPES can observe spin-polarisation in an individual layer of the bulk, with a spin-orbit splitting of 500meV seen. This is seemingly at odds with the nature of the bulk, however this was put down to local inversion symmetry breaking due to the surface sensitivity of the photoemission measurement, so it effectively probes only the top monolayer [25]. The bulk displays no spin-splitting, which demonstrates the layer dependent spin-splitting via an experimental manner and therefore the strong spin-layer coupling.

The SOC can induce spin-splitting if there is breaking of the inversion symmetry, as this will break the Kramer's degeneracy and lift the spin degeneracy of the energy levels. Since the 2H-WSe_2 monolayer unit cell has a lack of inversion symmetry, shown by figure 2-13(a), the degeneracy of both the valence and conduction bands is lifted. This is prevalent along the high symmetry line Γ-K, as seen in figure 2-13(b) where the calculated band structures for the monolayer show the spin-splitting in the case with spin-orbit interaction included. In the valence band the greatest energy splitting occurs at the K point, and it commonly found to be in the range of 450-550meV from both experiment [26, 27], and theory [24, 26]. Along the line Γ-M, there is no observed spin-degeneracy which is due to time reversal symmetry combined with translational symmetry, and at the Γ point it is due to time-reversal symmetry alone [24]. Due to the purely 2D in-plane motion of the electrons, and the mirror reflection symmetry about the metal atom plane resulting in a net in-plane dipole across the unit cell, the full spin polarisation of the bands is directed in the out of plane direction. This can be seen when considering the origin of the SOC Hamiltonian. The induced dipole leads to an induced magnetic field of a Zeeman interaction type given by,

$$\vec{B} = \frac{1}{c}\vec{E} \times \vec{v} = \frac{1}{mc}\vec{E} \times \vec{p}, \tag{2-6}$$

where $\vec{v}$ is the carrier velocity and $\vec{p}$ is its momentum. By considering relativistic effects the Hamiltonian can be written as,

$$\hat{H} \propto \vec{\sigma} \cdot \vec{B} = \vec{\sigma} \cdot (\vec{E} \times \vec{p}), \tag{2-7}$$

where $\vec{\sigma}$ is the Pauli matrix vector describing the gradient of potential felt by the carriers. The SOC Hamiltonian can then be given as,

$$\hat{H}_{SO} = \alpha(\vec{\nabla}V \times \vec{p}) \cdot \vec{\sigma}, \tag{2-8}$$

where α is the Rashba coupling constant and $\vec{\nabla}V$ is the electric field across the unit cell. The electron carriers' momentum is in-plane due to their motion, so if the dipole across the unit cell affecting the carrier is also in-plane, then the spins are orientated in the out-of-plane direction for a Rashba type spin-splitting. Equation 2-8 also clearly highlights the role of an electric field in establishing the spin-dependent Hamiltonian.

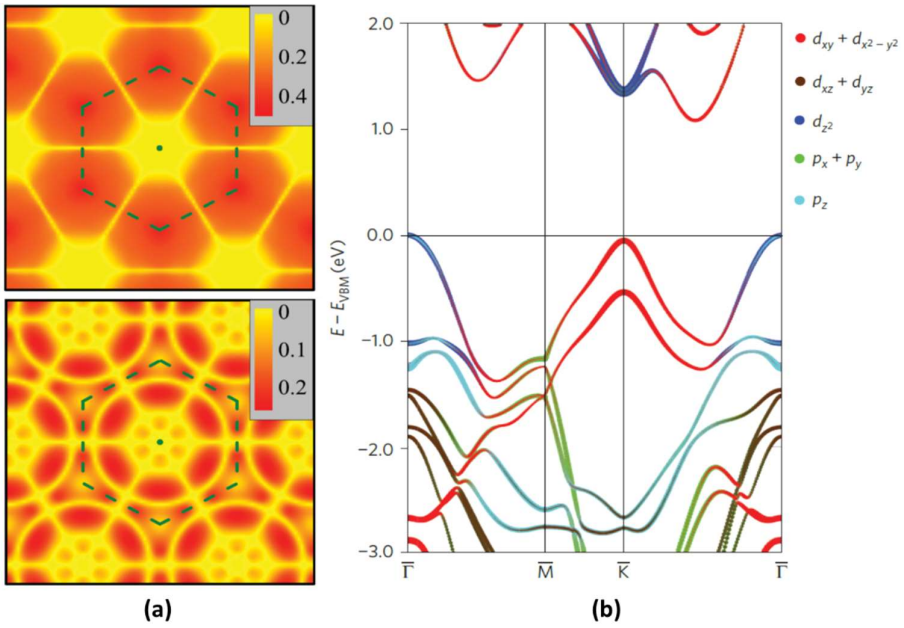

Figure 2-14. (a) Plots showing the calculated magnitude of the spin-splitting as it varies with $\vec{k}$, in the valence band (top) and conduction band (bottom). [24] (b) Orbital projected band-structure calculation for bulk WSe_2 showing the contribution of the orbitals at different points. The dominance of in-plane orbitals and their significant overlaps leads to the strong out-of-plane spin polarisation. [25]

As can be seen in figure 2-13(b) the spin-splitting along Γ-K display different behaviour in the valence band (VB) and conduction band (CB). The splitting in the VB first turns negative before rising steadily to its maximum at the Γ point, while in the CB it switches sign several times with a minimum at about the midpoint. This splitting dependence on $\vec{k}$ is also confirmed by spin-splitting magnitude plots shown for the valence band and conduction band in figure 2-14(a). An explanation for this dependence is given through analysis of the orbital contributions to the VBE and CBE, and a band-structure depicting the orbital dependence with $\vec{k}$ is shown in figure 2-14(b). As figure 2-2 shows, the Se p_z and W d_{z^2} have an out of plane orientation which means they have no contribution to spin-splitting. This can be seen using the Rashba SOC Hamiltonian for an orbital dipole that is perpendicular to the surface, which will suppress the net in-plane dipole of the layer. At the Γ point in the VBE these orbitals dominate hence the lack of spin-splitting but moving towards the K point they are slowly replaced by the other orbitals with in-plane orientation. Therefore, at the K point, the VBE is primarily composed of the $m = \pm 2$ d-orbitals, d_{xy} and $d_{x^2-y^2}$ of the W atoms, their in-plane orientation shown by figure 2-2. At the CBE this is also the case, although slightly more complicated [24]. The largest spin-splitting in the CB is at the Q point, and here the orbital contribution comes from the in-plane W $d_{x^2-y^2}$ and d_{xy} and chalcogen p_x and p_y orbitals. This suggests a strong hybridisation of the metal and chalcogen atoms [19].

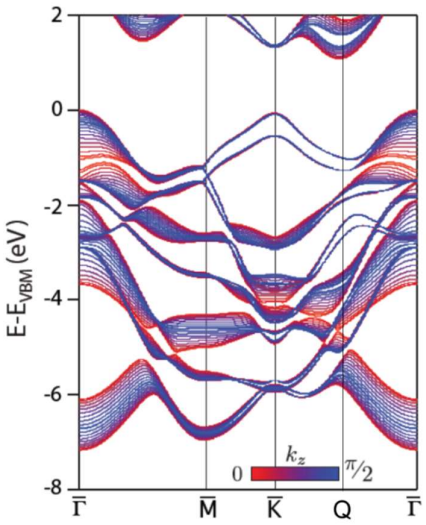

Figure 2-15. DFT calculation of the dispersion of the bands with k_z for bulk WSe_2. The different coloured lines represent different values of k_z. The bands at the G point have strong 3D character shown by the large distribution of the lines for different k_z, whilst those at the K and Q points display a 2D nature. [25]

The dispersion of the bands with k_z also varies at the different points. The Γ points have a large dispersion with k_z due to their contributing orbitals, as seen in figure 2-15. This means the states have a strong 3D character. At the K point however, there is no k_z dispersion displaying the purely 2D nature of the states with confines them to the layer and means there is a 100% spin separation between layers. At the Q points there is a bit of spatial mixing between the spins from different layers, but overall, they are separate and have a 2D nature [25]. This strong layer confinement of states with spin-polarisation further explains the spin-layer locking at these points.

The importance of this spin-layer locking in bulk is that it shows that the spin orientation between adjacent layers is opposite, and only through stacking them does the spin become degenerate for the overall material. These layers still individually have a spin-polarisation, which means techniques with high surface sensitively like the STM can treat the top layer as if it was a monolayer for detecting the type of spin.

Due to the single layer nature of the unit cells in the 1T phase and their octahedral configuration, odd and even layer stackings are the same meaning that the single layer is inversion symmetric. This however means that there is no breaking of the inversion symmetry in either bulk or monolayer [28, 29], and therefore no spin-splitting of the bands. A spin-polarised calculation has also revealed that the 1T phase remains nonmagnetic [30]. The inversion symmetry can be broken by an applied electric field though, leading the way for spin-split states in the 1T and 1T' phases [8].

2.5 Spin-valley coupling

The valley degree of freedom, often referred to as the valley pseudospin is another degree of freedom or index possessed by the electron carriers, which is associated with their momentum. The valleys are the energy extrema in momentum space which can be described as local maximums/minimums in the valence/conduction bands. In TMDs, due to the hexagonal lattice structure, these valleys are expected at the corners of the 2D hexagonal Brillouin zone, at the K and $-\mathrm{K}$ points, shown in figure 2-9(d). A consequence of this is that the carriers can be valley polarised, in which they prefer to occupy valleys with the same polarisation. In a similar manner to spintronics, the field of valleytronics aims to use this valley index of carriers as a means of information processing. However, unlike the electron spin which can be controlled and measured relatively easily, the valley pseudospin lacks any intrinsic properties which can be used to identify the valley polarisation.

Broken inversion symmetry and SOC lead to spin and valley coupling in monolayers of WSe_2 which means that the spin polarisation of a carrier is also locked to the valley polarisation at the band edges. This suppresses spin and valley relaxation, as a flip of each index alone is forbidden in the absence of a process enabling spin-flip, such as a magnetic defect. Time reversal symmetry requires that the spin-splitting must be opposite in different valleys [31], as shown in figure 2-16.

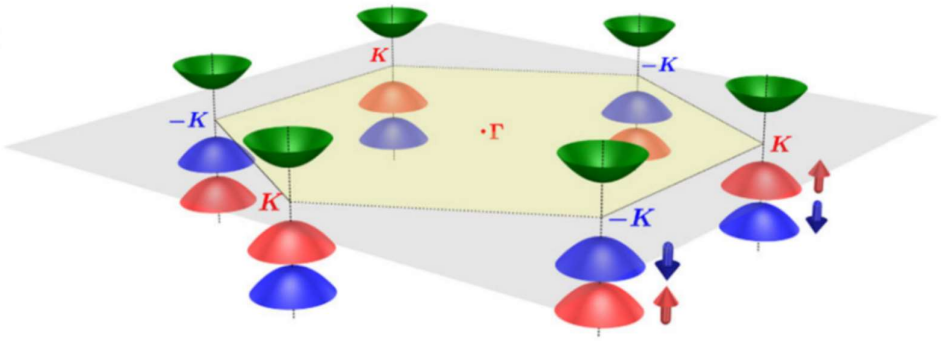

Figure 2-16. Diagram showing the first Brillouin zone with the 6 valleys located at the K and $-K$ symmetry points. At each valley the spin-orbit splitting of the valence band is represented by the red (spin-up) and blue (spin-down) cones. The splitting is opposite in the K and $-K$ valleys due to time reversal symmetry. The green cones show the bottom of the CBM, which has a very small splitting effect. [31]

References

[1] Kolobov A V and Tominaga J (2016) *Two-Dimensional Transition-Metal Dichalcogenides.*

[2] Chhowalla M, Shin H S, Eda G, Li L J, Loh K P and Zhang H (2013) The chemistry of two-dimensional layered transition metal dichalcogenide nanosheets. *Nature Chemistry.* **5** 263-75

[3] Averill B and Eldredge P (2011) *General Chemistry: Principles, Patterns, and Applications.*

[4] Mattheis.Lf (1973) Band structures of transition-metal-dichalcogenide layer compounds. *Physical Review B.* **8** 3719-40

[5] Cunningham G, Lotya M, Cucinotta C S, Sanvito S, Bergin S D, Menzel R, Shaffer M S P and Coleman J N (2012) Solvent exfoliation of transition metal dichalcogenides: dispersibility of exfoliated nanosheets varies only weakly between compounds. *ACS Nano.* **6** 3468-80

[6] Towle L C, Oberbeck V, Brown B E and Stajdoha.Re (1966) Molybdenum diselenide - rhombohedral high pressure - high temperature polymorph. *Science.* **154** 895

[7] Eda G, Fujita T, Yamaguchi H, Voiry D, Chen M W and Chhowalla M (2012) Coherent atomic and electronic heterostructures of single-layer MoS2. *ACS Nano.* **6** 7311-7

[8] Qian X F, Liu J W, Fu L and Li J (2014) Quantum spin Hall effect in two-dimensional transition metal dichalcogenides. *Science.* **346** 1344-7

[9] Tang S J, Zhang C F, Wong D, Pedramrazi Z, Tsai H Z, Jia C J, Moritz B, Claassen M, Ryu H, Kahn S, Jiang J, Yan H, Hashimoto M, Lu D H, Moore R G, Hwang C C, Hwang C, Hussain Z, Chen Y L, Ugeda M M, Liu Z, Xie X M, Devereaux T P, Crommie M F, Mo S K and Shen Z X (2017) Quantum spin Hall state in monolayer 1T'-WTe2. *Nature Physics.* **13** 683

[10] Wypych F, Weber T and Prins R (1998) Scanning tunneling microscopic investigation of 1T-MoS2. *Chemistry of Materials.* **10** 723-7

[11] Heising J and Kanatzidis M G (1999) Structure of restacked MoS2 and WS2 elucidated by electron crystallography. *Journal of the American Chemical Society.* **121** 638-43

[12] Addou R and Wallace R M (2016) Surface analysis of WSe2 crystals: spatial and electronic variability. *ACS Applied Materials & Interfaces.* **8** 26400-6

[13] Ugeda M M, Pulkin A, Tang S J, Ryu H, Wu Q S, Zhang Y, Wong D, Pedramrazi Z, Martin-Recio A, Chen Y, Wang F, Shen Z X, Mo S K, Yazyev O V and Crommie M F (2018) Observation of topologically protected states at crystalline phase boundaries in single-layer WSe2. *Nature Communications.* **9** 7

[14] Chen W, Xie X D, Zong J Y, Chen T, Lin D J, Yu F, Jin S E, Zhou L J, Zou J Y, Sun J, Xi X X and Zhang Y (2019) Growth and thermo-driven crystalline phase transition of metastable monolayer 1T'-WSe2 thin films. *Scientific Reports.* **9** 6

[15] Bradley A J, Ugeda M M, da Jornada F H, Qiu D Y, Ruan W, Zhang Y, Wickenburg S, Riss A, Lu J, Mo S K, Hussain Z, Shen Z X, Louie S G and Crommie M F (2015) Probing the role of interlayer coupling and coulomb interactions on electronic structure in few-layer MoSe2 nanostructures. *Nano Letters.* **15** 2594-9

[16] Kaasbjerg K, Martiny J H J, Low T and Jauho A P (2017) Symmetry-forbidden intervalley scattering by atomic defects in monolayer transition-metal dichalcogenides. *Physical Review B.* **96** 6

[17] Zhang C D, Chen Y X, Johnson A, Li M Y, Li L J, Mende P C, Feenstra R M and Shih C K (2015) Probing critical point energies of transition metal dichalcogenides: surprising indirect gap of single layer WSe2. *Nano Letters.* **15** 6494-500

[18] Hsu W T, Lu L S, Wang D, Huang J K, Li M Y, Chang T R, Chou Y C, Juang Z Y, Jeng H T, Li L J and Chang W H (2017) Evidence of indirect gap in monolayer WSe2. *Nature Communications.* **8** 7

[19] Roldan R, Lopez-Sancho M P, Guinea F, Cappelluti E, Silva-Guillen J A and Ordejon P (2014) Momentum dependence of spin-orbit interaction effects in single-layer and multi-layer transition metal dichalcogenides. *2D Materials.* **1** 21

[20] Wickramaratne D, Zahid F and Lake R K (2014) Electronic and thermoelectric properties of few-layer transition metal dichalcogenides. *Journal of Chemical Physics.* **140** 13

[21] Hu X H, Wang Y F, Shen X D, Krasheninnikov A V, Sun L T and Chen Z F (2018) 1T phase as an efficient hole injection layer to TMDs transistors: a universal approach to achieve p-type contacts. *2D Materials.* **5** 10

[22] Kappera R, Voiry D, Yalcin S E, Branch B, Gupta G, Mohite A D and Chhowalla M (2014) Phase-engineered low-resistance contacts for ultrathin MoS2 transistors. *Nature Materials.* **13** 1128-34

[23] Ma Y G, Liu B L, Zhang A Y, Chen L, Fathi M, Shen C F, Abbas A N, Ge M Y, Mecklenburg M and Zhou C W (2015) Reversible semiconducting-to-metallic phase transition in chemical vapor deposition grown mono layer WSe2 and applications for devices. *ACS Nano.* **9** 7383-91

[24] Zhu Z Y, Cheng Y C and Schwingenschlogl U (2011) Giant spin-orbit-induced spin splitting in two-dimensional transition-metal dichalcogenide semiconductors. *Physical Review B.* **84** 5

[25] Riley J M, Mazzola F, Dendzik M, Michiardi M, Takayama T, Bawden L, Granerod C, Leandersson M, Balasubramanian T, Hoesch M, Kim T K, Takagi H, Meevasana W, Hofmann P, Bahramy M S, Wells J W and King P D C (2014) Direct observation of spin-polarized bulk bands in an inversion-symmetric semiconductor. *Nature Physics.* **10** 835-9

[26] Le D, Barinov A, Preciado E, Isarraraz M, Tanabe I, Komesu T, Troha C, Bartels L, Rahman T S and Dowben P A (2015) Spin-orbit coupling in the band structure of monolayer WSe2. *Journal of Physics-Condensed Matter.* **27** 5

[27] Zeng H L, Liu G B, Dai J F, Yan Y J, Zhu B R, He R C, Xie L, Xu S J, Chen X H, Yao W and Cui X D (2013) Optical signature of symmetry variations and spin-valley coupling in atomically thin tungsten dichalcogenides. *Scientific Reports.* **3** 5

[28] Ribeiro-Soares J, Almeida R M, Barros E B, Araujo P T, Dresselhaus M S, Cancado L G and Jorio A (2014) Group theory analysis of phonons in two-dimensional transition metal dichalcogenides. *Physical Review B.* **90** 10

[29] Shirodkar S N and Waghmare U V (2014) Emergence of ferroelectricity at a metal-semiconductor transition in a 1T monolayer of MoS2. *Physical Review Letters.* **112** 5

[30] Kan M, Wang J Y, Li X W, Zhang S H, Li Y W, Kawazoe Y, Sun Q and Jena P (2014) Structures and phase transition of a MoS2 monolayer. *Journal of Physical Chemistry C.* **118** 1515-22

[31] Xiao D, Liu G B, Feng W X, Xu X D and Yao W (2012) Coupled spin and valley physics in monolayers of MoS2 and other group-VI dichalcogenides. *Physical Review Letters.* **108** 5

Chapter 3

Scanning tunnelling microscopy and spectroscopy (STM/STS) and angle-resolved photoemission spectroscopy (ARPES)

Since the invention of the scanning tunnelling microscope in 1982 by Binnig and Rohrer it has proved a powerful instrument to explore the structural and electronic properties of surfaces. The ability to probe with sub-angstrom spatial resolution and meV energy resolution has led to a great many advances in surface and material science. The probe is simply a metal wire with an atomically sharp tip, that is scanned across a surface using piezoelectric actuators. The very short distance between the tip and sample surface of a few angstroms allows for quantum tunnelling of electrons across the gap due to the overlap of their wavefunctions. Applying a bias voltage between the tip and sample results in a tunnelling current. A feedback loop then controls the height of the tip to maintain constant current. As well as the standard topographic mode, the STM can also probe the local density of states (LDOS) of the sample through its spectroscopic mode. This involves ramping the bias voltage over an energy range to measure the LDOS as a function of energy, or scanning at a certain energy while applying a modulating voltage to acquire a spatially resolved slice in the LDOS. Exploiting the quasi-particle interference (QPI) patterns formed from defects and steps in the LDOS allows for a more in-depth insight into the electronic structure of the sample. Another technique used in the study of materials is angle-resolved photoemission spectroscopy (ARPES). Using this, the electronic band-structure of materials can be directly measured, and advances in this technique now allow for 2D imaging of k-space. This chapter will aim to introduce the theory and methods of these techniques, and their applications in the context of this thesis.

3.1 Basic theory of STM

In 1961 Bardeen developed his theory describing the tunnelling current flowing between two electrodes separated by a potential barrier [1]. This was later expanded upon by Tersoff and Hamann, whose model has since become the most widely used to describe the results of STM, and which accounts for tunnelling into the 2D Bloch states of a periodic surface [2]. Here the formalism as described by Chen is used to show these key results [3].

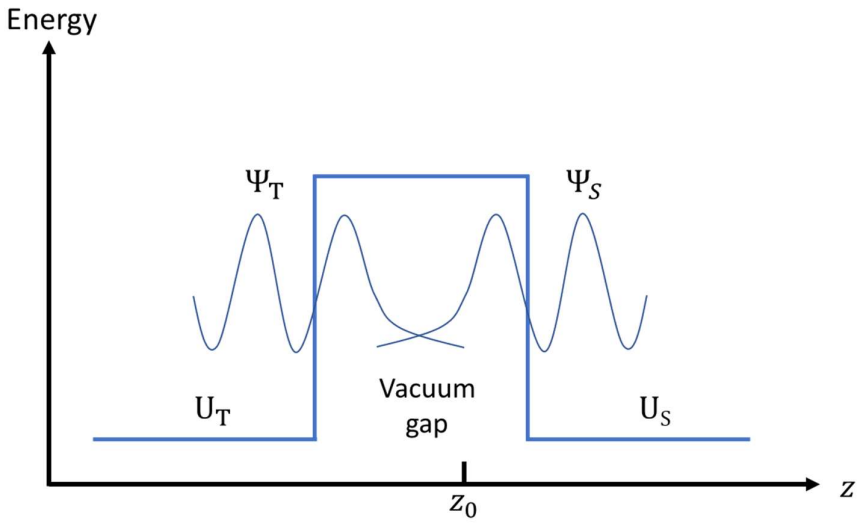

Figure 3-1. Simple tunnelling junction with a potential barrier (vacuum) between the tip and sample electrodes. The wavefunctions of the tip and sample exponentially decay as they propagate into the vacuum. Bringing the tip and sample close together, results in the wavefunctions overlapping.

Bardeen's approach

A typical tunnelling junction can be represented by two electrodes separated by a vacuum barrier, as shown in figure 3-1. The left and right electrodes represent the tip and the sample respectively, with the wavefunction of the tip electrode satisfying the Schrödinger's equation as,

$$i\hbar\frac{\partial\Psi}{\partial t} = \left[-\frac{\hbar^2}{2m}\frac{\partial^2}{\partial z^2} + U_T\right]\Psi\,, \tag{3-1}$$

where U_T is the potential function of the tip. The stationary states are,

$$\Psi = \psi_T e^{-iE_T\frac{t}{\hbar}}\,, \tag{3-2}$$

which satisfies,

$$\left[-\frac{\hbar^2}{2m}\frac{\partial^2}{\partial z^2} + U_T\right]\psi_T = E_T\psi_T\,, \tag{3-3}$$

This is the same for the other electrode, in this case the sample. When the tip and sample are far apart, their wavefunctions decay into the vacuum. However, once they are brought closer together and their wavefunctions overlap, the Schrödinger equation for the combined system becomes,

$$i\hbar\frac{\partial\Psi}{\partial t} = \left[-\frac{\hbar^2}{2m}\frac{\partial^2}{\partial z^2} + U_T + U_S\right]\Psi\,, \tag{3-4}$$

The wavefunctions ψ_T and ψ_S are not solutions to this combined Schrödinger equation, as they originate from different Hamiltonians. The first assumption of Bardeen's tunnelling theory is that the two sets of wavefunctions are approximately orthogonal to each other,

$$\int \psi_T^* \psi_S d^3\vec{r} \cong 0\,, \tag{3-5}$$

In the presence of the combined potential, there is some probability that a charge carrier will jump from a state in the tip to a state in the sample. Assuming an initial eigenstate of the tip electrode ψ_T, and a final state of the sample ψ_S, then the time evolution of the carrier wavefunction goes as,

$$\Psi = \psi_T e^{-iE_T\frac{t}{\hbar}} + \sum_{S=1}^{\infty} c_S(t)\psi_S e^{-E_S\frac{t}{\hbar}}\,, \tag{3-6}$$

where $c_s(0) = 0$ for all T. Substituting eq. 3-6 into eq. 3-4 gives,

$$i\hbar\frac{dc_S(t)}{dt}\psi_S e^{-iE_S\frac{t}{\hbar}} = U_S\psi_T e^{-iE_T\frac{t}{\hbar}} + U_T\sum_{S'=1}^{\infty} c_{S'}(t)\psi_{S'} e^{-iE_{S'}\frac{t}{\hbar}}\,, \tag{3-7}$$

Since $c_{S'}$ and $U_T\psi_S$, are both very small the second term on the right side of eq. 3-7 can be neglected, and further projecting on the state $|\psi_S\rangle$ results in,

$$i\hbar\frac{dc_S(t)}{dt} = \int_{z>z_0} \psi_T U_S \psi_S^* d^3\vec{r} e^{-i(E_T-E_S)\frac{t}{\hbar}}\,, \tag{3-8}$$

If the tunnelling matrix element, which is a surface integral of the wavefunctions from the tip and sample on a separation surface, is defined as,

$$M_{TS} = \int_{z>z_0} \psi_T U_S \psi_S^* d^3\vec{r}\,, \tag{3-9}$$

and then by integrating over time, the probability of a carrier tunnelling from the T-th state of the tip to the S-th state of the sample, is found to be,

$$p_{TS}(t) \equiv |c_S(t)|^2 = |M_{TS}|^2\frac{4\sin^2[(E_T-E_S)t/2\hbar]}{(E_T-E_S)^2}\,, \tag{3-10}$$

The second assumption of the Bardeen theory is that the tunnelling is elastic, and so energy of the carrier is the same after hopping to the sample as it was previously on the tip, $E_S = E_T$. So far only tunnelling from a single tip state to a single sample state have been considered, and therefore by summing over all possible sample states with energy E_S, the total probability of tunnelling from the tip to the sample in time t is given,

$$p_{TS}(t) = \frac{2\pi}{\hbar}|M_{TS}|^2 \rho_S(E_S)t\,, \tag{3-11}$$

where $\rho_S(E_S)$ is the density of states of the sample at energy E_S. To get the total tunnelling rate at a particular energy, ε, the rate of tunnelling from a particular tip state to a sample state of the same energy, as shown in eq. 3-11, needs to be multiplied by the DOS of the tip at that energy, $\rho_T(E_T)$, to give the total elastic tunnelling rate at that energy,

$$p_\varepsilon(t) = \frac{2\pi}{\hbar}|M_{TS}|^2 \rho_S(\varepsilon)\rho_T(\varepsilon)t\,, \tag{3-12}$$

For tunnelling to occur is it required that the tip state be occupied and the sample state unoccupied. When the temperature is 0 K this only happens if a bias voltage is applied between tip and sample, so that their individual Fermi levels are no longer aligned. This is shown in figure 3-2, now showing the range of energies ε_T to $\varepsilon_T - eV_B$ which states from the tip can elastically tunnel into unoccupied sample states [4]. Integrating over all these possible states multiplied by their respective tunnelling rate, the total tunnelling current for a given V_B is obtained,

$$I_t = \frac{4\pi e}{\hbar}\int_0^{eV_b} \rho_T(E_F - eV_b + \varepsilon)\rho_S(E_F + \varepsilon)|M_\varepsilon|^2 d\varepsilon\,, \tag{3-13}$$

This describes the tunnelling current as a convolution of the sample and tip DOS, assuming the matrix element does not vary significantly with energy. The issue here is that a

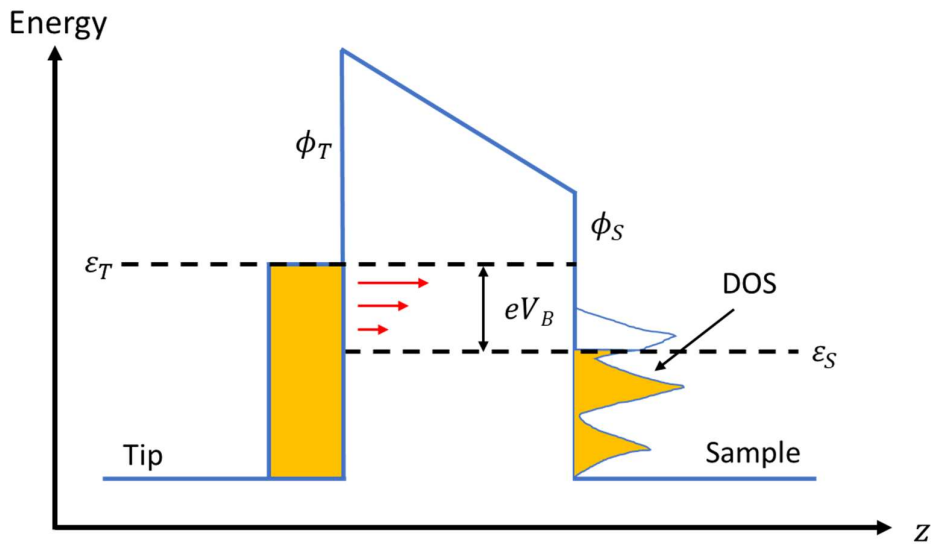

Figure 3-2. Diagram showing the tunnelling junction of the tip and sample with a bias voltage V_B applied. The DOS of the tip is assumed to be flat so that the DOS of the sample can be probed. The red arrows indicate the possible tunnelling route from the tip to the sample. The workfunctions of the tip and sample are shown by ϕ_T and ϕ_S respectively.

contribution from the tip is included, when this method is employed primarily to investigate the sample surface. A model introduced by Tersoff and Hamann provides an answer to this and is described in the next section.

The tunnelling matrix elements

First, by taking the matrix element in eq. 3-9 and substituting for eq. 3-3, applying the elastic tunnelling condition, $E_S = E_T$, and noting that $U_T = 0$ for $z > z_0$, the two-dimensional integral of the tunnelling matrix is,

$$M_{TS} = -\frac{\hbar^2}{2m} \int\limits_{z=z_0} \left(\psi_T \frac{\partial \psi_S^*}{\partial z} - \psi_S^* \frac{\partial \psi_T}{\partial z} \right) dxdy \,, \tag{3-14}$$

This is Bardeen's tunnelling matrix element in one-dimensional form. To extend this to the three-dimensional case, a similar argument can be used to give,

$$M_{TS} = -\frac{\hbar^2}{2m} \int\limits_{\Sigma} (\psi_T \nabla \psi_S^* - \psi_S^* \nabla \psi_T) \cdot d\vec{S} \,, \tag{3-15}$$

where Σ is an integration surface between the volumes defining the tip and sample.

Ideally the STM tip should have a spherical apex with a single atom on the end. Tersoff and Hamann modelled this as a locally spherical potential well centred at $\vec{r}_0$ with a radius of $\vec{r}$, and assumed that the tip wavefunction can be approximated as an s-wave solution. The s-wave tip has the property of the Green's function for the Schrödinger equation in vacuum, which is,

$$(\nabla^2 - \kappa^2)\psi_T = -\delta(\vec{r} - \vec{r}_0) \,, \tag{3-16}$$

where $\kappa = \sqrt{2m\phi}/\hbar$ is the decay constant, and ϕ is the workfunction. The tip wavefunction is then,

$$\psi_T(\vec{r} - \vec{r}_0) \sim \frac{e^{-\kappa|\vec{r} - \vec{r}_0|}}{4\pi|\vec{r} - \vec{r}_0|} \,, \tag{3-17}$$

Substituting this into eq. 3-15, and using the divergence theorem gives,

$$M_{TS} = \frac{\hbar^2}{2m} \int\limits_{\Omega_T} (\psi_T \nabla^2 \psi_S^* - \psi_S^* \nabla^2 \psi_T) \cdot d\vec{\tau} \,, \tag{3-18}$$

where τ is the volume. This is now a volume integral on the tip side, to account for its non-planar shape. Using eq. 3.16 and assuming the tip and sample wavefunctions decay at the same rate, eq. 3-18 can be simplified to,

$$M_{TS} \sim \psi_S(\vec{r}_0)\,, \tag{3-19}$$

This shows that the tunnelling matrix element is proportional to the value of the wavefunction as seen by the apex atom of the tip, and so states on the surface that decay further into the vacuum will have a higher contribution to the tunnelling current.

The Tersoff-Hamann model also assumes a low bias voltage, so eV_B is small, and that the tip DOS is flat. Taking the previous result and these assumptions, in the low temperature limit, the tunnelling current can be expressed as,

$$I_t \propto \sum_{E_F - eV_B}^{E_F} |\psi_S(\vec{r}_0)|^2 = eV_B \rho_S(\overrightarrow{r_0}, E_F)\,, \tag{3-20}$$

This shows that at low bias, the tunnelling current is proportional to the LDOS of the sample at the Fermi level energy measured by the centre, $\vec{r}_0$, of the spherical tip.

One drawback of this model is that it fails to explain the observed atomic resolution images in STM. This is due to it modelling the tip as a macroscopic continuum. In reality the W and Pt-Ir tips are d-band metals, meaning they have localised metallic d_{z^2} states at the tip apex. For these d-wave tips, the tunnelling matrix element is proportional to the second derivative of the surface wavefunction of the surface. This means the tip now follows a charge density contour depending on this derivative which has much stronger corrugation than the Fermi level LDOS. Figure 3-3 shows a diagram displaying the reciprocity principle, which states that

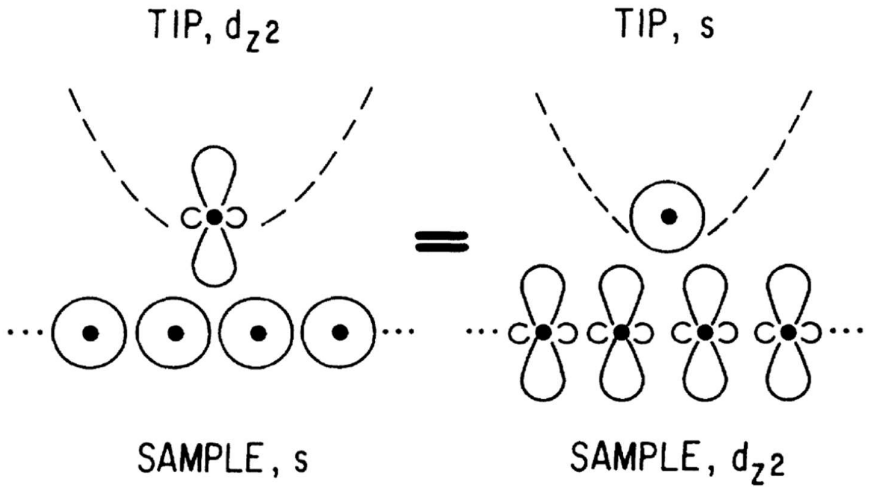

Figure 3-3. Demonstration of the reciprocity effect showing that a d_{z^2} tip scanning an s terminated sample, is the sample as scanning a d_{z^2} terminated surface with an s tip. [5]

interchanging the tip and sample states should result in the same image. The non-spherical orbitals of the d_{z^2} tip lead to this enhancement in corrugation [5].

2D Bloch States

The general 3D form of a Bloch wave in a crystal is,

$$\psi(\vec{r}) = e^{i\vec{k}\cdot\vec{r}} \cdot u(\vec{r}) \,, \tag{3-21}$$

where $u(\vec{r}) = u(\vec{r} + \vec{R})$, and $\vec{R}$ is a periodic vector of the 3D lattice. This can be adapted for the 2D case and written as,

$$\psi_{\vec{k}_\parallel} = f(z) \cdot e^{i(\vec{k}_\parallel \cdot \vec{r}_\parallel)} \cdot u(\vec{r}_\parallel) \,, \tag{3-22}$$

where $\vec{k}_\parallel$ is the in-plane surface wavevector, $f(z)$ is a function describing the decay of states into the vacuum, and $u(\vec{r}_\parallel) = u(\vec{r}_\parallel + \vec{R})$, where $\vec{R}$ is now periodic to the 2D lattice. To account for this momentum dependent correction in the 2D surface Tersoff and Hamann expanded this in the form,

$$\psi_{\vec{k}_\parallel} = \sum_G e^{-(\kappa^2 + |\vec{k}_\parallel + \vec{G}|^2)^{-\frac{1}{2}} z} \cdot e^{i(\vec{k}_\parallel + \vec{G})\cdot\vec{r}_\parallel} \,, \tag{3-23}$$

where G is the surface reciprocal lattice vector. This shows that the wavefunction and therefore the tunnelling current depends on the surface wavevector $\vec{k}_\parallel$, and reciprocal lattice vector $\vec{G}$. States with a larger parallel momentum will decay faster into the vacuum than those with zero $\vec{k}_\parallel$, even if they have the same energy, meaning they contribute less to the tunnelling current. This factor become especially important when considering spectroscopy of TMDs and their critical point states.

3.2. Measurement techniques

3.2.1. Topography

The STM has the ability to image the surface topography of a sample, which makes it a very powerful tool. There are two modes of operation, constant-current and constant-height. A diagram showing the basic setup of the STM is shown in figure 3-4.

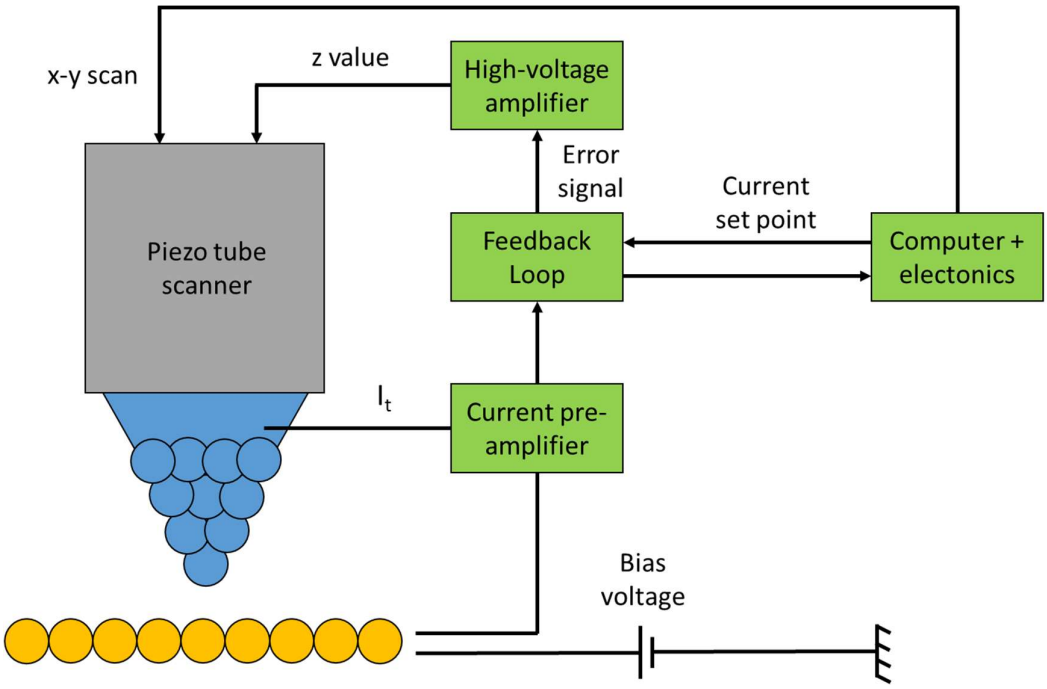

Figure 3-4. Diagram showing a very simplified representation of how the STM works. In this set-up, the bias voltage is applied to the tip, but in the software it is set as though it's applied to the sample to avoid having to invert the bias for probing the CB and VB.

The imaging mode is commonly carried out in constant-current mode, which means that as the tip is raster-scanned across the surface, the tunnelling current is maintained at a current setpoint specified by the user. This mode is also called the topographic mode and captures both structural and electronic information about the surface. The tunnelling current is typically in the range of pA to nA and so is measured by a preamplifier, which converts this into a voltage signal. The z-position of the tip is controlled by the feedback loop which compares the input tunnelling current signal to the setpoint, and produces an output signal, which is amplified and fed into the z-piezo control. This moves the tip closer to, or further away from the surface to compensate for this difference, which is called the error signal. The sensitivity of the feedback reaction is controlled by the percentage gain (both proportional and integral) which is applied to this error signal. The gain is important, as setting it too high or low can result in feedback oscillations or loss of details respectively.

The tip is mounted into a scanner that consists of two sets of piezo actuators. These are made from piezoelectric material which change their shape in an electric field due to their anisotropic crystal structure. By attaching electrodes to the sides of a bar and applying a voltage, the length of the bar can be altered, which is called the transverse piezoelectric effect. The first set of actuators control the coarse motion of the tip and allow for the x-y position on the surface to be chosen and the coarse approach of the tip to the surface [6]. The second actuator is called the tube scanner and controls the fine motion of the tip,

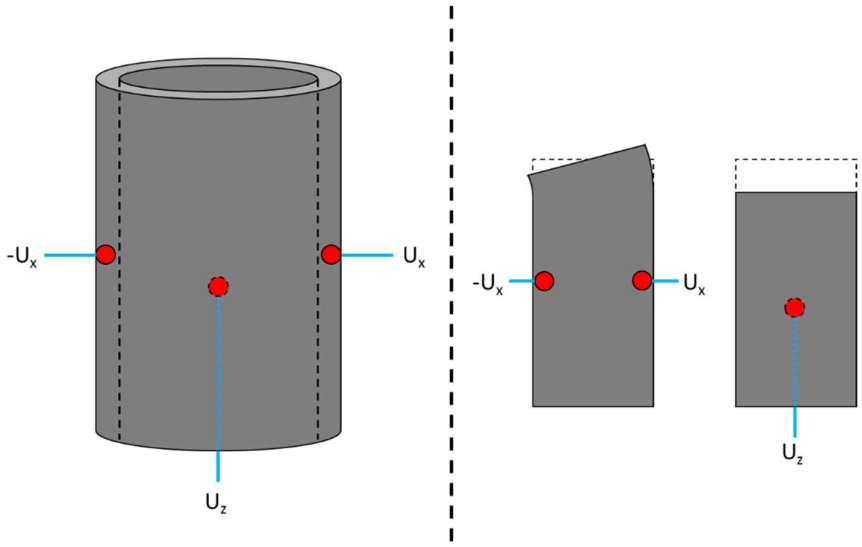

Figure 3-5. Diagram of the tube scanner showing the x and z electrodes. The x electrodes are attached to the outside and applying a voltage results in the tube extending and contracting on opposite sides as shown. The z electrode is attached inside the tube, and voltage applied causes a shortening or lengthening of the tube. The effects shown are greatly exaggerated for clarity.

including the fine approach and is responsible for the raster-scanning of the tip. Figure 3-5 shows how this tube scanner works with different applied voltages.

The tip is first approached towards the surface using the coarse motion and observed using a telescope mounted with a CCD camera. The lighting of the chamber is arranged so that both the tip and its shadow on the sample surface can be seen. Once they are close, with only a small gap between them, the tip is auto-approached under the Matrix software control. Conditions here must be carefully chosen so as not to crash the tip.

Once the tip has landed, another variable to consider is the raster scan speed, which is changed by altering time to raster one line and the size of the area scanned. Scanning too slow results in the drift of the sample and can result in the tip picking up atoms, whereas scanning too fast results in a loss of features if not correctly compensated by the gain. On Au where the atoms have high mobility, the tip can be scanned very fast, and needs to be for atomic resolution. For most scanning speeds and a good tip, a gain of 2% is used to scan with no issues. However, at faster scanning speeds this must be increased so that the feedback is fast enough to correctly adjust the z position. On the WSe_2, the raster time is much lower so a gain of 2% or just below is used. When scanning over molecules or dopants on the surface, the gain is adjusted to be much higher at $\geq$5% so that the feedback can react to the larger height difference between the surface and molecule compared to the normal surface corrugation and prevent the tip from crashing.

One issue that needs to be taken into account is the thermal drift of the sample. This results in it shifting whilst scanning, so that the image obtained does not represent the actual

surface and can appear stretched or with features smeared. Lowering the temperature of the system can help to mitigate this effect, but a more effective method is to apply a drift correction. By measuring how far a feature of the surface drifts between scans, a correction can be applied to the scanner. This means the scanner moves to account for this drift and keeps the tip over the same area. Often this needs to be repeated several times over successive scans to obtain a good correction. This becomes especially important when performing STS.

3.2.2. Scanning tunnelling spectroscopy (STS)

To perform spectroscopy and extract information about the DOS of the sample, the derivative of the tunnelling current is taken. The tunnelling matrix element from eq. 3-10 can be assumed as energy independent over small energy ranges ($\sim 10\%$ variation over 200 meV) and therefore can be taken out of the integral. The DOS of the tip can also be assumed to be flat over the energy range of interest and removed from the integral too. Setting $E_F = 0$ and taking the derivative of eq. 3-13 with respect to V_B now gives,

$$\frac{dI_t}{dV_B} = \frac{4\pi e}{\hbar}\rho_t \rho_s(V_B)|M_0|^2 \,, \tag{3-24}$$

These $\mathrm{dI/dV}$ or differential conductance measurements are experimentally obtained by taking an $\mathrm{I/V}$ measurement and differentiating. This is achieved by positioning the tip over a point on the surface and switching off the feedback loop. The voltage is then ramped over the selected range, taking a measurement of the current at every step designated [7]. However, this method requires a large number of I/V curves taken from the same point to average over [8].

Another method to obtain dI/dV curves with a better resolution is with the use of a lock-in amplifier. This works by applying a small modulating AC voltage to the existing DC bias voltage and measuring the resulting AC current using the lock-in amplifier [9]. This technique relies on phase sensitive detection, meaning that signals that are outside of the range of the reference frequency and phase are filtered out. This means it has a high signal-to-noise ratio, and even signals of a few nanovolts can be detected. To perform this technique, the voltage ramp is slowed down such that there is enough time at every voltage step to integrate over the measured signal. The delay time is dependent on the time constant of the lock-in amplifier, and typically set to 10 times 1/frequency of the voltage modulation. The longer the time constant, the greater the signal-to-noise ratio. The raster time of the spectroscopic measurement should be long enough to include all the time steps, from switching off the feedback, adjusting to the specified starting bias, then ramping slowly over all the voltage

steps, and finally returning to the original bias and switching back on the feedback loop. The frequency of the modulating voltage should not be set to a multiple of 50Hz to avoid including signal from any mains power supply.

dI/dV mapping

The spectroscopy mode can be extended to acquire energy and spatially resolved maps of the LDOS. This is especially useful when similar topographic features have different electronic structure. It is also very important for the detection of quasi-particle interference (QPI) patterns which are oscillations in the LDOS. There are two different ways to obtain $\mathrm{dI/dV}$ maps [10].

The first involves taking a $\mathrm{dI/dV}$ measurement at every point of the scan, and simultaneously recording the tip-sample distance. This is achieved by moving the tip according to the set bias voltage, acquiring the tip-sample distance from the feedback loop, and finally holding the tip in position while taking $\mathrm{I/V}$ and $\mathrm{dI/dV}$ curves. This means a complete picture of the topographic and electronic structure can be built up over a range of energies. The downside of this method is that they take a very long time to complete due to having to hold over every pixel of the image for a short delay.

The other method is much faster by comparison but only allows for a single energy to be mapped at a time. In this method, a normal topographic image is taken with a modulating voltage applied constantly by the lock-in amplifier. This allows the simultaneous acquisition of the $\mathrm{dI/dV}$ signal at each point for the energy selected. There is no voltage ramp and the tip-sample distance is varied by the feedback loop. This results in a slice of the LDOS, which can be built up by performing more scans at different energies. These maps still take a relatively long time to acquire, due to the requirements of the lock-in amplifiers time constant. The raster time should allow enough time at each point to sufficiently integrate the signal as set by the time constant. Since the time constant for this method is longer than the previous method, the noise level is lower. Typically, these maps took 2-4 hours, although for energies with low signal they could take up to 6 hours.

3.2.3. Variable-z spectroscopy

In the case of semiconductors with larger bandgaps, the normal spectroscopy measurements are not always reflective of the actual electronic structure around the edges of the gap. Gap states and band-bending are the usual causes of this, but most importantly in the case of

WSe_2 is the fact seen previously that the STM tunnelling current is sensitive to the parallel momentum of the different states. This means that around the edges of the band gap, the tunnelling conductivities can range over many orders of magnitude. For normal spectroscopy measurements, the feedback loop is turned off so that the tip-sample distance is kept constant, and the sudden drop in conductivity at the edge leads to some edge states not being observed. To correct for this, a technique called variable-z spectroscopy can be utilised. As the name suggests, in this method the tip height is varied with the bias voltage ramp to enhance the level of measured current at each bias. In practice this is typically done as a normal $\mathrm{dI/dV}$ measurement with the addition of a z step with each bias step. This tip-sample separation normalisation of the spectroscopy can be described using a lowest order multiplicative correction of the form $\exp(2\kappa\Delta s)$, where $\kappa = \kappa(s, V)$ is the inverse decay constant, and Δs are known values of the relative tip-sample separation [11]. Since the dependencies on the decay constant are usually small, it can be expressed as $\kappa = \kappa_0 = (2m\phi)^{1/2}/\hbar$. If the tunnelling current is then measured and a modulation voltage is used to determine the conductivity at a fixed tip-sample separation, it can be written,

$$\sigma[s(V), V] = \left(\frac{\partial I}{\partial V}\right)_s, \tag{3-25}$$

A requirement of this technique is choosing a suitable tip-sample separation contour, or the z position of the tip. An expression of the relationship between the voltage ramp and z position contour is given by,

$$z = z_{Start} + z_0 + \begin{cases} \alpha_1 \cdot |V|, V > 0 \\ \alpha_2 \cdot |V|, V < 0 \end{cases}, \tag{3-26}$$

This is a typical linear ramp of z where α determines the step size. The tip reaches its minimum z position when $V = 0$ and increases either side with the same of different steps. The issue with this method of varying the z position in this manner is that there is a risk of crashing the tip into the sample if the step size is incorrectly chosen. As with normal STM scanning, the feedback loop can be used to minimise this risk and skip having to manually choose the z position of the tip. If, instead of turning off the feedback loop when the spectroscopy is taken, it is left on, the feedback will maintain constant current throughout the measurement, varying the z position with the bias ramp. Since the frequency of the modulation can be set to be faster than the feedback time constant, each derivative of the tunnelling current at every bias value, is evaluated at a constant z value, just as in a normal $\mathrm{dI/dV}$. This gives a differential conductance at constant current, $(\partial I/\partial V)_I$, meaning regions of the curve which previously were hard to observe can now be seen.

In the above, the decay constant κ was assumed to have no variation with the parallel momentum of states $k_{\parallel}$, however this is not quite the case. Following the Tersoff-Hamann

theory, the effective tunnelling decay constant can be written to include the parallel momentum term [12], as,

$$\kappa = \left(\frac{2m\phi + k_{\parallel}^2}{\hbar^2}\right)^{\frac{1}{2}}, \tag{3-27}$$

where ϕ is the energy barrier for tunnelling. The failure to detect certain critical points becomes clear when considering this, as those states with larger $k_{\parallel}$ such as the K critical point states have a much larger value in the decay constant than the Γ states with $k_{\parallel} = 0$, meaning their wavefunction decays faster and extends much less into vacuum. By moving the tip closer to the surface, the tail end of these wavefunctions can now be detected.

3.2.4. Fourier transform-STS (FT-STS)

Defects, impurities, or edges in materials act as scattering centres and cause electrons to be elastically scattered from wave vector $\vec{k}_a$ to $\vec{k}_b$. The quantum interference between the incident and scattered electron wavefunctions results in standing wave patterns in the LDOS. These are known as Friedel patterns and they can be imaged by the STM. The principle of this arises from the screening of electrons around the defect in order to reduce its induced electric field, and the system response can be described by the dielectric constant, for a given momentum $\vec{q}$,

$$\varepsilon(\vec{q}) = 1 - \left(\frac{4\pi\chi(\vec{q})}{\varepsilon_0|\vec{q}|^2}\right), \tag{3-28}$$

where the susceptibility $\chi(\vec{q})$ is dependent on $\vec{q}$ in reciprocal space. If it is assumed that all the eigenstates are mixed in the scattering process then the Lindhard theory can be applied, and the susceptibility calculated from first order perturbation theory is,

$$\chi(\vec{q}) = \sum_{\vec{k}} \frac{f(k) - f(|\vec{k} + \vec{q}|)}{E_{\vec{k}} - E_{\vec{k}+\vec{q}}}, \tag{3-29}$$

where $f(k)$ is the Fermi-Dirac distribution function, which ensures all the states described by the $\vec{k}$ vectors are occupied. This shows that the main contribution to the variation in the charge density is due to q wave vectors that connect two points of a state on the constant energy contour (CEC).

For larger values of q, the explicit value of the susceptibility for a two-dimensional gas is given by,

$$\chi^{2D}(\vec{q}) = n^{2D}(E_F)\left[\left(1-\left(\frac{q}{2k_F}\right)^2\right)^{\frac{1}{2}}\theta(q-2k_F)\right], \tag{3-30}$$

where $n^{2D}(E_F)$ is the DOS at the Fermi level. In the case of a nearly free electron gas, $E_k = \frac{\hbar^2 k^2}{2m}$, all the $\vec{q}$ vectors connecting two points have length [13],

$$|\vec{q}| = 2\left|\vec{k}_F\right|, \tag{3-31}$$

This is the basis for intravalley scattering of electrons or back-scattering, which see them scatter from one side of an energy band to the other. The LDOS oscillations are therefore dependent on the band-structure, as the $\vec{k}$ vector of the valley varies with energy, and the oscillation wavelength and scattering momentum $\vec{q}$ are inversely proportional.

The first observations by STM of the confined Shockley states of Au(111) by Hasegawa and Avouris [14], and Cu(111) by Crommie *et al* [15], who found that the change of the LDOS by a point defect can be described by,

$$\Delta LDOS = (E', r) \propto \frac{1}{k_0 r}\left[\cos^2\left(k_0 r - \frac{\pi}{4} + \varphi\right) - \cos^2\left(kr - \frac{\pi}{4}\right)\right], \tag{3-32}$$

where $k_0 = (2m^* E/h)^{\frac{1}{2}}$, and φ is the phase shift. Here E' is the energy of the electron with respect to the surface state band edge. The amplitude of oscillation decays with distance from the scattering centre as $1/r^{\alpha}$, where the decay factor α is determined by the scattering centre and the dimensionally of the electron gas. For a point defect and an ideal 2D electron gas, $\alpha = 1$). By taking a Fourier transform of such an STM image around the Fermi level showing these quasi-particle interference (QPI) patterns, the Fermi surface contour can be observed, as first seen by Sprunger on the Be(0001) surface [16]. However, if the image is instead a dI/dV image the energy is no longer limited to the Fermi level, and the resulting Fourier transform describes a constant energy contour (CEC) at a given energy. This is known as FT-STS.

The features observed in the FT-STS maps can be explained using a joint density of states (JDOS) approach. As mentioned, in the presence of defects, quasi-particles scatter from wave vector $\vec{k}_a$ to $\vec{k}_b$ with a scattering vector of $\vec{q}$. Since this is a periodic 2D surface, this can be considered scattering between two Bloch states $\vec{k}_a$ to $\vec{k}_b$, and from perturbation theory, new eigenstates can be constructed as a linear combination of the degenerate unperturbed $\vec{k}_a$ states on a CEC $E(k) = \omega$. Considering this combination, the charge density and

therefore energy-resolved DOS can be described, from which the leading Fourier component of the LDOS for wave vectors $\vec{q} = \vec{k}_a - \vec{k}_b + \vec{G}$ is given by,

$$g(\omega, \vec{q}) = \frac{1}{4\pi^2} \iint_{E(k_a)=E(k_b)=\omega} f(\vec{k}_a, \vec{k}_b, \vec{G}) \delta(\vec{q} - \vec{k}_a + \vec{k}_b \pm \vec{G}) d^2\vec{k}_a d^2\vec{k}_b \,, \qquad (3\text{-}33)$$

where $f(\vec{k}_a, \vec{k}_b, \vec{G})$ is a weight factor that depends on the scattering matrix elements and therefore the overall nature and distributions of defects [13, 17]. This function describes a JDOS with a main contribution from the $\vec{G} = 0$ components and replicas shifted by $\vec{G}$.

The JDOS calculation consists of counting the number of $\vec{q}$ vectors and adding those with the same length and direction, to build up the scattering picture. The more equivalent $\vec{q}$ vectors there are, the more intense that particular scattering process will be in the JDOS, and therefore what is expected to be seen in the FT-STS. This is a simple phenomenological approach of the generalisation of the Lindhard susceptibility to the surface Bloch wave states [13]. Figure 3-6(a) shows a simple example of a CEC with bands at Γ and K points, and some of the possible $\vec{q}$ wave vectors that contribute to the scattering picture. Here the $\vec{q}_1$ process describes an intravalley back-scattering process between either side of the central Γ band,

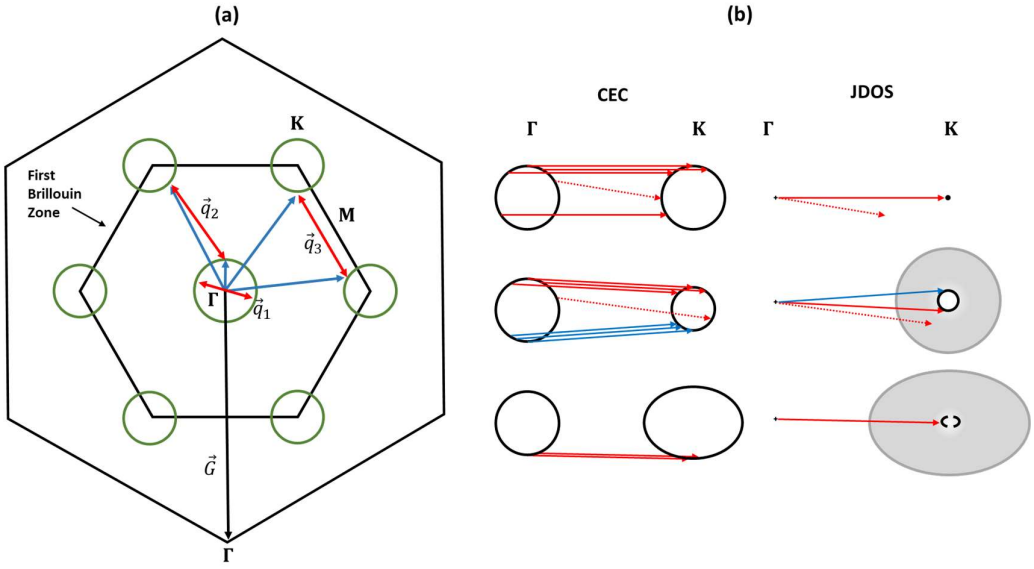

Figure 3-6. (a) CEC contour with states around the Γ and K points. The first Brillouin zone is highlighted, and the $\vec{G}$ vectors point to the reciprocal lattice. The red vectors are scattering processes described by $\vec{q} = \vec{k}_a - \vec{k}_b + \vec{G}$, where $\vec{k}_a$ and $\vec{k}_b$ are the initial and resultant vectors respectively and are generically shown with the blue arrows. (a) Schematic drawing of scattering between 3 different valleys. The left CECs show example vectors with the same length and direction between points on the two valleys, and the right side shows a representation of the JDOS from the addition of these vectors. The dashed vectors describe scattering vectors that have few similar vectors and so contribute little to the JDOS picture. (adapted from [17])

and $\vec{q}_2$ and $\vec{q}_3$ represent intervalley scattering between the Γ and K, and K and K valleys respectively. Because the JDOS is constructed from the addition of similar vectors, the patterns arising from scattering from different valleys with dissimilar radius, or shape are quite varied and can be used to help identify the origin of the scattering process. Figure 3-6(b) shows a diagram with a few possible JDOS representations from the mixing of different CECs. The main contributing $\vec{q}$ vectors build up the primary features, with the other less common $\vec{q}$ scattering vectors making up the surrounding cloud.

Intra-valley scattering

The shape of the CECs is important to consider for intravalley scattering too, as can be seen in the geometric constructions in figure 3-7. The scattering wave vector $\vec{q}$ is shown for different directions, with the contour thickness determined by the lock-in bias modulation, and the wavevector gradient due to the energy range of the mixed unperturbed eigenstates [17]. For a circular CEC, an isotropic JDOS pattern is expected as the intersection area in all directions is the same. For a hexagonal CEC, the intersection area varies depending on which direction the scattering process is in, so the JDOS will show as more intense in those directions with a larger intersection. To relate back to the JDOS approach, the number of $\vec{q}$ wave vectors allowed for the larger intersection areas is greater than that of the smaller area.

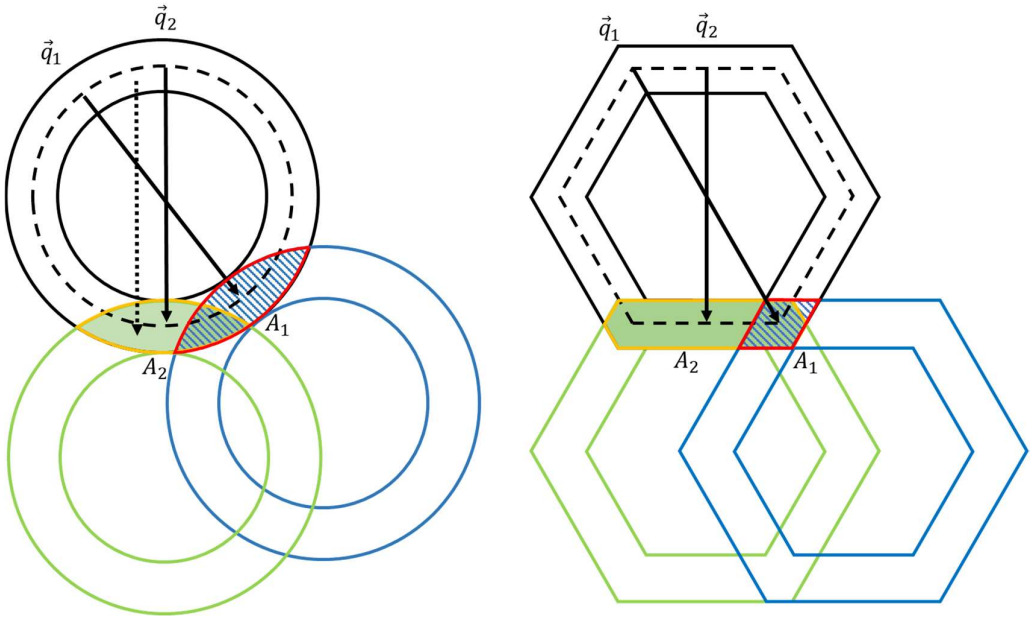

Figure 3-7. Geometric construction of circular and hexagonal CECs, showing the difference in intersection area A_{1-2} for two scattering vectors $\vec{q}_{1-2}$ along different directions of the contour. The dashed vector is another example of a possible $\vec{q}_2$ vector for the circular CEC, to highlight the larger addition potential of larger intersection areas. (adapted from [17])

Localised surface states

The Au(111) surface exhibits an sp-derived Shockley type surface state which is located in the gap of the projected bulk bands as shown in figure 3-8(a) [18]. This results in localised electron states trapped between the surface and bulk states, and can be considered as a free-electron like 2D electron gas [19]. The screening of defects from these surface state electrons is expected to follow the Friedel approach as discussed in the earlier part of this section [20]. This can be observed in $\mathrm{d}I/\mathrm{d}V$ maps as shown in figure 3-8(b), with the corresponding FT-STS shown in (c). In any system with a ring-like CEC such as the Au Shockley

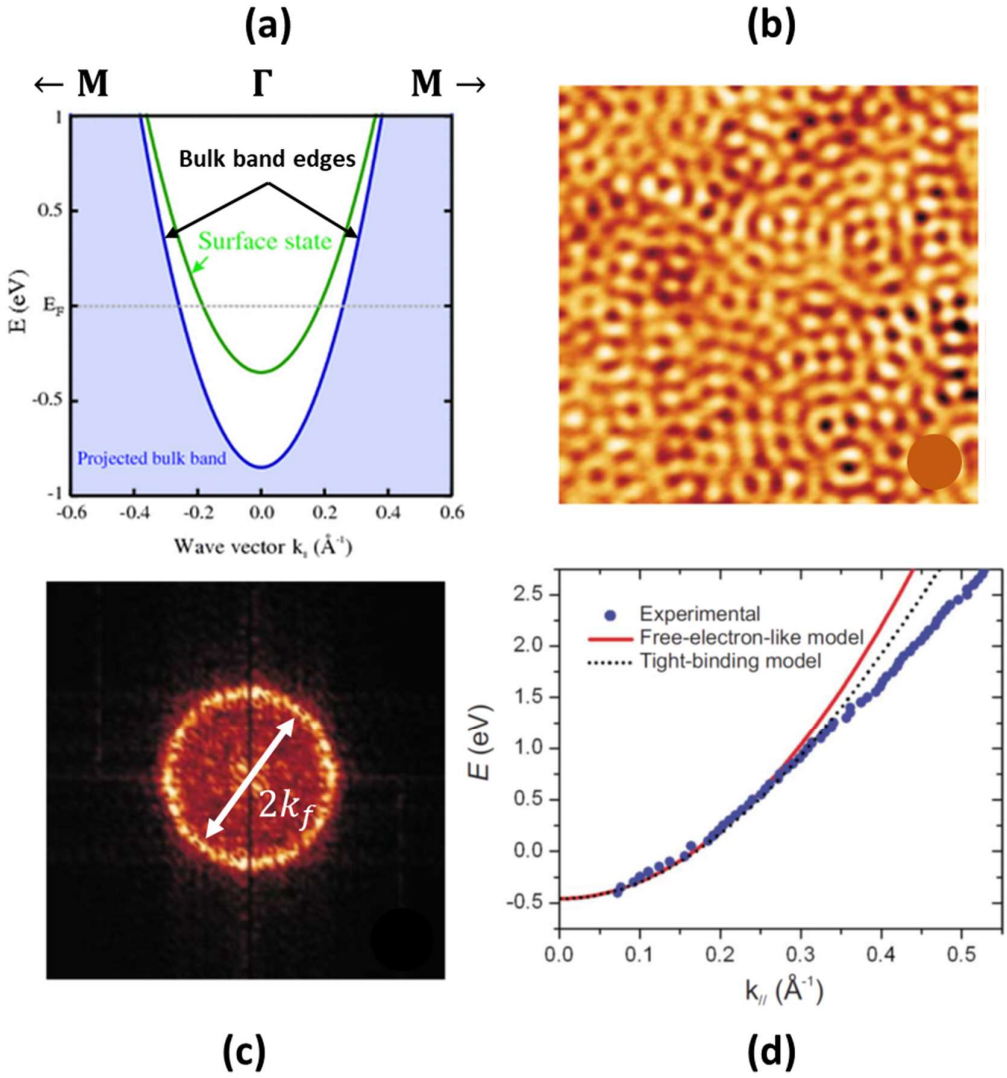

Figure 3-8. (a) Band diagram of Au(111) showing the surface state in green and the bulk band continuum shaded in light blue. The bulk band edge is marked by the dark blue line. (b) dI/dV map at -30 meV of the Au(111) surface; showing Friedel like oscillations around defect sites. (c) FT-STS map of the image in (b). Intravalley backscattering results in a ring of radius $2k_f$. (d) Dispersion of the Shockley surface state with energy. [22, 23]

surface state, the scattering wave vector q connecting opposite momentum at stationary points of the CEC is associated with the long wavelength interference patterns. This backscattering process from $k \leftrightarrow -k$ is the most efficient for the ring-like CEC due to enhanced phase space [21], and will result in a ring of $q = 2k_F$ in the FT-STS map. By scanning through a range of energies, the dispersion of the surface state can be mapped as shown in figure 3-8(d). This shows the bottom of the surface state lies at around -470 meV, and after this cut-off there are no states present aside from the bulk continuum of states. If the pseudo-spin texture of the valley means that states with opposite momentum have opposite pseudo-spin, then this backscattering is strongly suppressed [24].

Scattering from bulk states

As well as the surface state, some FT-STS measurements on Au(111) have detected contributions to the screening waves from electrons in bulk states [20, 23]. The reason for this lies in the fact that the surface and bulk state wavefunctions have to be matched at the surface, and then decay into the vacuum. This means that the STM can pick up contributions to the tunnelling current from both at the tip apex, and consequently see the screening waves they create. The wavefunctions can be written,

$$\psi = \phi_{\vec{k}_\parallel}(\vec{r}_\parallel) e^{-\left(\kappa^2 + \vec{q}^2\right)^{-\frac{1}{2}} z}, \tag{3-34}$$

where $\phi_{\vec{k}_\parallel}$ is the in-plane part of the wavefunction, $\kappa = \sqrt{2m\phi}/\hbar$ is the decay constant, and ϕ is the workfunction. For a bulk state, the dispersion is given by,

$$E(k) = \frac{\hbar^2\left(\vec{q}^2 + \vec{k}_\perp^2\right)}{2m}, \tag{3-35}$$

where $\vec{k}_\perp$ is the component of the wavevector perpendicular to the surface. This means $|\vec{q}|$ now lies in the range from 0 to $q_E = (2mE/\hbar^2)^{1/2}$. To then find the bulk contribution to the LDOS a sum over all the $\vec{q}$ vectors at the energy E is required such that,

$$LDOS(E, \vec{r}) \propto \int_0^{2\pi} \int_{q_0}^{q_E} \left|\phi_{\vec{k}_\parallel}\right|^2 e^{-2\left(\kappa^2 + \vec{q}^2\right)^{-\frac{1}{2}} z} \vec{q}\, d\vec{q}\, d\theta, \tag{3-36}$$

The bulk Fermi surface can be modelled as a sphere with a hole in the top and bottom which represent the “neck” or sp-related bulk bandgap of the Au(111) plane, the radius of which corresponds to q_0 [20]. When a defect is screened, the LDOS will now oscillate with wave vectors $\vec{q} = 2\vec{k}_B$, where $\vec{k}_B$ is the magnitude of wavevectors available in the bulk continuum of states around the “neck” region. Figure 3-9 shows a diagram of the Au 3D brillioun zone modelled for this case showing an FT-STS of Au(111) and the two rings corresponding to the

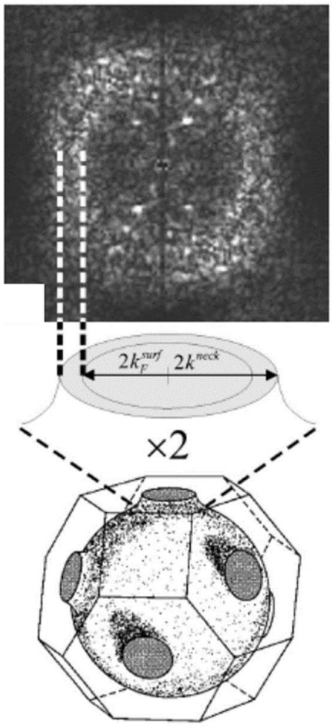

Figure 3-9.FFT of the QPI from the Au(111) surface showing the presence of two rings of different radius. The corresponding model shows the origin of these rings as backscattering of electron in the localised surface state and the "neck" of the projected bulk bands. [20]

surface state and bulk state contributions. The factor of 2 in the scattering wavevector indicates that this is a backscattering process. The shape of the bulk Fermi surface means that there will be more wavevectors with the magnitude $\vec{k}_B$ which explains the appearance of the bulk ring as broad or blurred.

Anisotropic scattering from non-circular CEC

For the case of silicene on an Ag(111) substrate an interesting feature in the QPI patterns is observed [25]. The patterns surrounding H defects on the surface have a hexagonal pattern rather than a circular one as seen in the $\mathrm{dI/dV}$ maps in figure 3-10(a). This results in a hexagon at the centre of the BZ in the FT-STS derived QPI pattern presented in figure 3-10(b). This is unusual as silicene, like graphene, has 6 Dirac cones at the K and $-\mathrm{K}$ points of the BZ which are circular at low energies, and can evolve to become trigonally warped at higher energies, however they are not expected to become hexagonal. The explanation arises from the (√3 × √3) R30° superstructure induced in the silicene by the Ag(111) substrate. Whilst other superstructure have been observed in this system, this is the only one to produce these QPI patterns, ruling out the Ag(111) surface as the source. By looking at the electronic band-

structure it can be seen that because of the (√3 × √3) R30° superstructure, the K and $-\mathrm{K}$ points of the (1×1) phase BZ are folded onto the Γ point of the (√3 × √3) R30° superstructure BZ. This is shown in the schematic diagram in figure 3-10(c). The orientation of the warping at the K and $-\mathrm{K}$ points is opposite, meaning that the 6 Dirac cones with opposite orientations of warping are folded onto the new Γ point, resulting in a single hexagonally

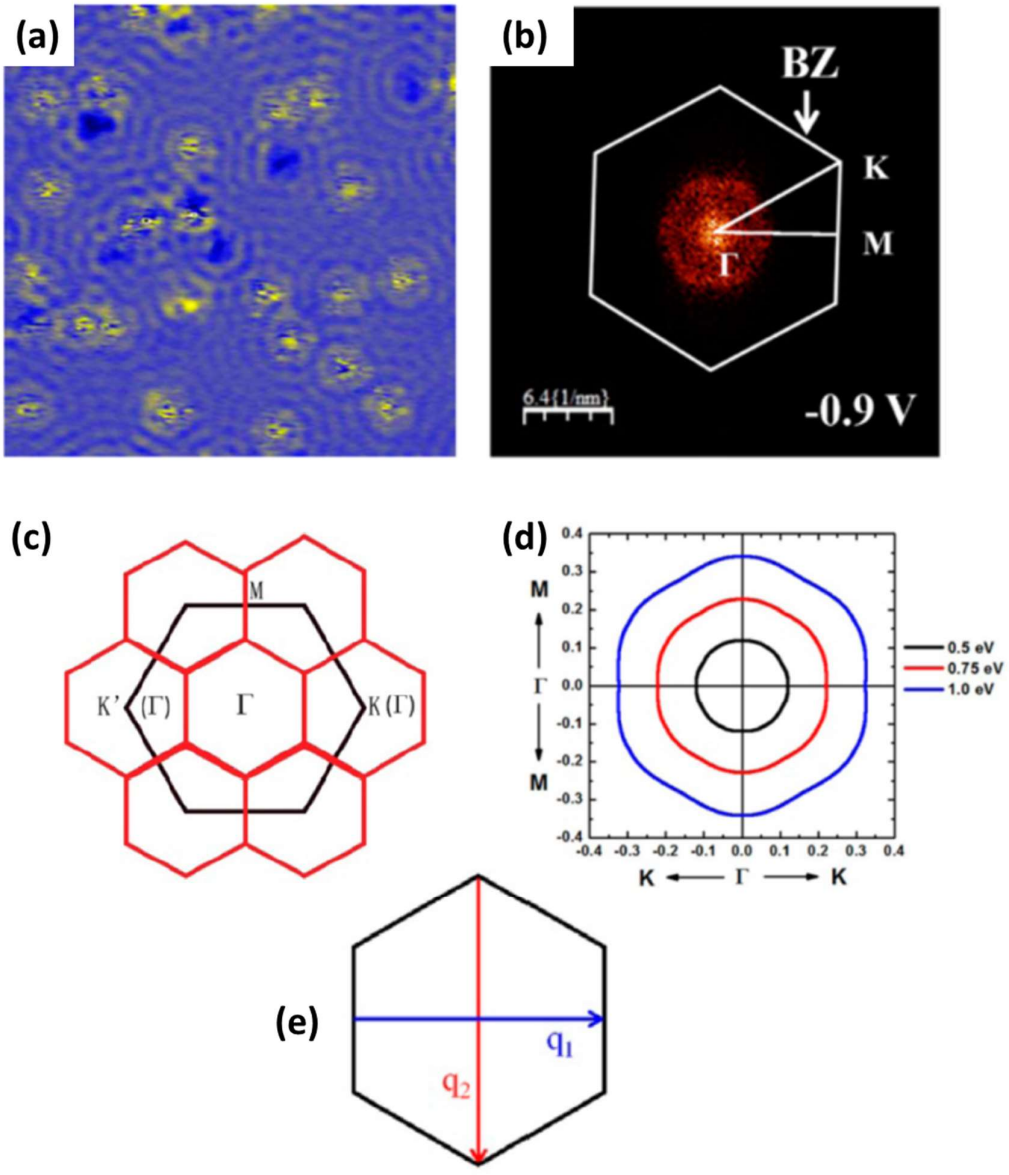

Figure 3-10. (a) $\mathrm{dI/dV}$ *image at -2 V of the hydrogenated silicene surface showing hexagonal standing wave pattern from scattering of the hydrogen dopants. (b) FT-STS plot of the image in (a) revealing the hexagonal shape of the scattering vectors in* k*-space. (c) Diagram showing the BZ of the* (1×1) *(black line) and* (√3 × √3) R30° *(red line) silicene. Note the position of the new* Γ *point at the* K *point of the* (1×1) *BZ. (d) Evolution of the silicene Dirac cone with energy, showing a circular contour that warps into a hexagonal contour. (e) Diagram showing the scattering vectors in the hexagonally warped CEC of the Dirac cone. [25]*

warped Dirac cone. This can be seen in the CECs for different energies in figure 3-10(d), where at lower energies the Dirac cone is circular and backscattering results in a circle of radius $2k_F$, but as the energy rises above 0.75 eV the Dirac cone is hexagonally warped.

The primary scattering process still occurs as backscattering between opposite edges of the hexagon and is displayed in figure 3-10(e) as q_1. This scattering vector was clarified by looking at the decay of the QPI patterns along different scattering directions from the step edge. The decay behaviour can be fitted using an exponential decaying equation,

$$\delta p(x) \propto \cos\left(2\vec{k}x + \varphi\right) x^{\alpha}, \tag{3-37}$$

where $\vec{k}$ is the standing wave wavevector, and φ is the phase shift of the scattering potential. It was found that along the armchair edge of the step corresponding to the Γ-K direction of (1×1) BZ, the decay factor $\alpha = -1.5$. Along the zigzag edge corresponding to the Γ-M direction of the (1×1) BZ, $\alpha = -1$. This displays the anisotropic decay behaviour of the QPI patterns which must be explained by the backscattering vector q_1 along opposite edges.

Inter-valley scattering

When considering TMDs, the scattering picture becomes more complicated due the multi-valley bands they possess which can lead to a variety of different QPI patterns. This is even further complicated due the large spin-splitting occurring in some of these bands, with adjacent valleys of the spin-split bands having opposing spin as required by time-reversal symmetry. For non-magnetic defects, the scattering process which involves spin-flip is inefficient and therefore these scattering channels are restricted. This has been observed in Bi(110) which due to SOC has spin-split surface bands, but the QPI analysis revealed a reduced number of scattering processes which corresponded to only spin-conserving channels [26]. This is because the time-reversal symmetry prohibits scattering between valleys of opposing spin [27]. Further evidence for the forbidden spin-flipping process comes from investigating the topological surface states of the topological insulator Bi_2Te_3 which are protected by time-reversal symmetry. Here STM [28] and theoretical [29] studies found that backscattering between states of opposite spin $\vec{k}$ and $-\vec{k}$ was quantum mechanically forbidden, which again was caused by the time-reversal invariance.

Figure 3-11(a) shows a schematic drawing of a typical TMD CEC near to the edge of the conduction band, with both spin orientation valleys of the K points and one at the Q point. The green arrows represent possible spin-conserving intervalley scattering processes between the K and Q valleys. A schematic drawing of the respective JDOS map for the CEC in figure 3-5(a), showing the points corresponding to the sum of all the $\vec{q}$ vectors is shown by figure 3-5(b). The labelled green arrows here correspond to the same $\vec{q}$ vectors in the CEC,

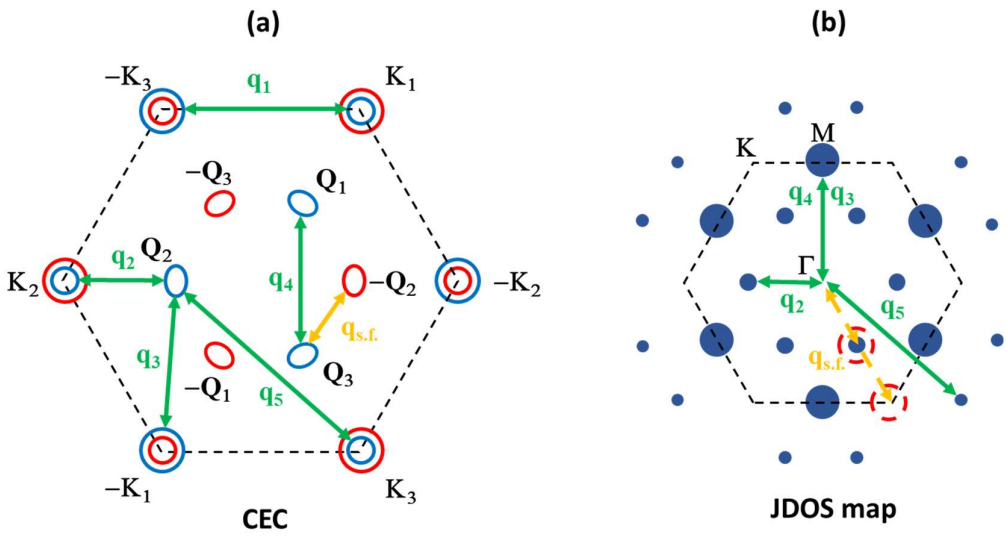

Figure 3-11. (a) Schematic CEC from near the conduction band edge of a typical TMD, showing the split spin-up (blue) and spin-down (red) bands at the K and Q points. Possible spin-conserving intervalley scattering processes are represented by the green arrows, while a potential spin-flip scattering process between Q valleys of opposite spin is highlighted by the yellow arrow. (b) Schematic of a JDOS map obtained from a construction of the vectors in (a), with the blue points representing the spin conserving channels. The dashed red circled indicate points that would also appear if spin-flip processes were allowed. (adapted from [27])

and as seen some of the vectors can be harder to distinguish such as $\vec{q}_3$ and $\vec{q}_4$ due to their similar length and direction. A consequence of the STMs insensitivity to the K points as well as the suppressed spin-flip scattering channels means that scattering between K valleys such as $\vec{q}_1$ are not observed experimentally. In the VB near to the edge where the large spin-splitting at the K point means QPI between K and $-\mathrm{K}$ valleys is prohibited, and in the CB whilst possible through spin-conserving scattering due to the much smaller spin-split energy levels, the insensitivity means the intensity of such spots are very small [27, 30].

QPI selection rules: spin-flip processes

In the case of a magnetic defect, it is predicted that the spin-flip scattering process becomes available [31], which is represented by the yellow arrows in figures 3-11(a-b). An important consequence of this is the ability to determine whether a defect is magnetic or not simply from STS. The basis for this lies in the ability of the magnetic impurity to break the time-reversal symmetry. This has been predicted for topological insulators with time-reversal symmetry protected surface states, and in this case the effective Hamiltonian of the edge states is given by,

$$\widehat{H}_0 = v_F \int dx(\psi^*_{R+} i\delta_x \psi_{R+} - \psi^*_{L-} i\delta_x \psi_{L-}) = v_F \int dx \Psi^* i\sigma^3 \delta_x \Psi\,, \qquad (3\text{-}38)$$

where $\pm$ indicates the Kramer's doublet, L/R indicates left of right movers, v_F is the Fermi velocity, and $\Psi = (\psi_{R+}, \psi_{L-})^T$ [32]. The coupling between a magnetic impurity and the Hamiltonian is therefore,

$$\widehat{H}_M = \int dx \Psi^* \sum_{a=1,2,3} m_a(x,t)\sigma_a \Psi = \int d_x \Psi^* \sum_{a,i} t_{ai} B_i(x,t)\sigma_a \Psi\,, \qquad (3\text{-}39)$$

where B_i is the three-dimensional magnetic field, and t_{ai} is the model-dependent coefficient matrix which is determined by the coupling between the magnetic field and the edge states. The presence of a mass term, which is proportional to the Pauli matrices, shows the ability of the magnetic impurity to couple and break the time-reversal symmetry, which is predicted to induce previously forbidden scattering between states $|\vec{k}\uparrow\rangle$ and $-|\vec{k}\downarrow\rangle$ [28, 33-35]. While this is not the same system as WSe_2 the surface states here have SOC leading to spin-splitting of the states and have Kramer's degeneracy [34, 36]. The ability to break the time-reversal effect in WSe_2 have also been shown experimentally [37-39], indicating that a magnetic perturbation such as a dopant or defect will lift the degeneracy of the valleys and allow for spin-flip scattering processes to occur.

QPI selection rules: defect type

In addition to the selection of processes based on the spin-valley coupling, the position and symmetry type of defects is also predicted to give rise to selection rules for intervalley scattering. Simulations of intervalley coupling in quantum dots confined on TMDs showed that it could be several orders of magnitude smaller for QDs with a circular shape, or triangular and hexagonal shapes with sides along the zigzag crystalline axis, than for confinement potentials with the threefold rotational symmetry (C_3) [40]. This means intervalley scattering is most likely to be observed in defects with C_3 symmetry, which is the same symmetry of the lattice. However, there are additional selection rules for these defects depending on their location in the lattice [41]. A calculated band-structure for WSe_2 is shown in figure 3-12(a) and a CEC schematic at the energy of 75 meV marked by the dashed line in (a) is shown in figure 3-12(b). As described earlier the available intervalley scattering channels are marked by q_{1-5}. Simulated FT-STS maps of QPI at this energy are shown in figures 3-12(c) and (d) for metal and chalcogen vacancies respectively; the difference between the patterns arises from the $\mathrm{K} \leftrightarrow -\mathrm{K}$ intervalley matrix element, which is strongly supressed in all cases except for metal-centred defects in the conduction band. For the metal vacancy case in figure 3-12(c), scattering features at the K and M points are predicted indicating the presence of the intervalley scattering processes q_{1-4}. In the case of the

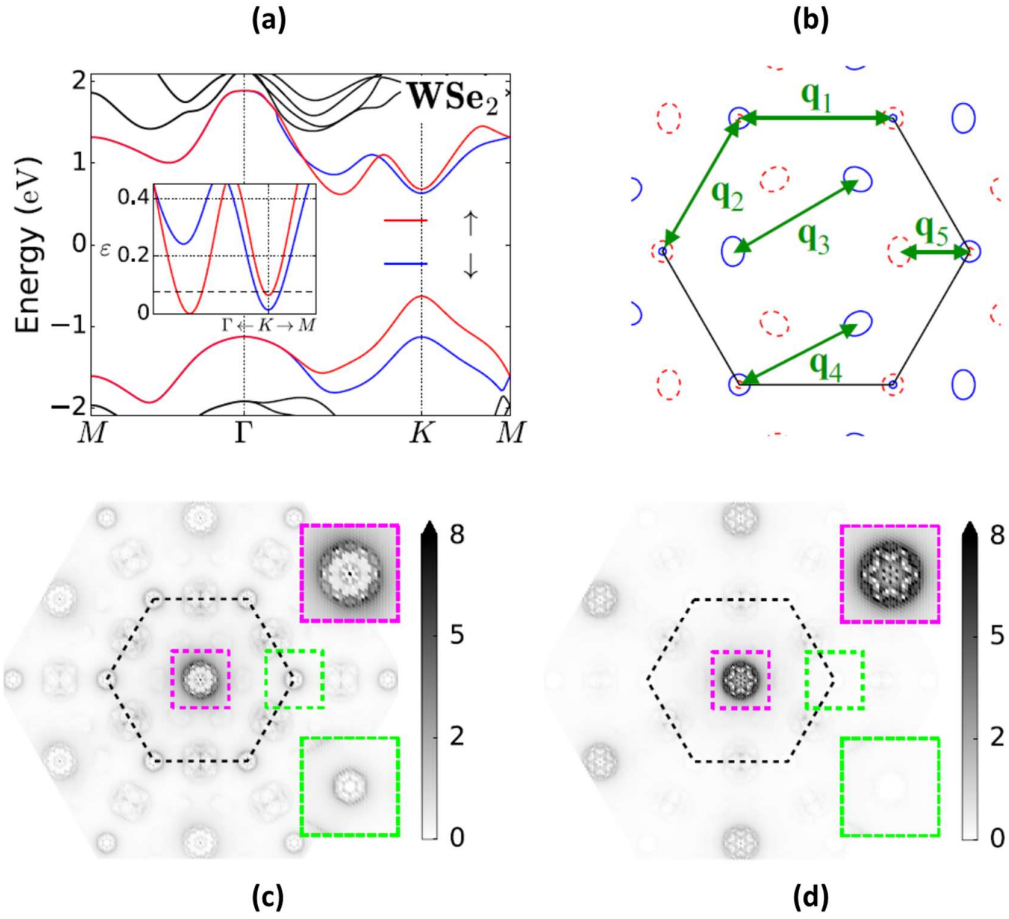

Figure 3-12. (a) Calculated band-structure of WSe_2 showing the large spin split bands. (b) CEC at 75 meV (dotted line in (a)) showing both spin split bands at K and one at Q, and the intervalley spin-conserving scattering processes marked by green arrows. Simulated FT-STS spectra for a metal vacancy (c) and a chalcogen vacancy (d).

chalcogen vacancy FT-STS in figure 3-12(d), the features at K indicating a spin-conserving $\mathrm{K} \leftrightarrow -\mathrm{K}$ process are supressed, which demonstrates it as a symmetry forbidden process. While the $\mathrm{Q} \leftrightarrow -\mathrm{Q}$ and $\mathrm{Q} \leftrightarrow \mathrm{K}$ processes are still permitted they are much weaker due to the overall smaller intervalley matrix element. These results are predicted to hold for all metal- and chalcogen-centred defects not just the vacancies [41].

3.3. STM instruments

The measurements were taken using two different systems; an Omicron low temperature STM (LT-STM) and an Omicron LT-STM/AFM with a preparation chamber attached, pictured in figure 3-13. Both were operated under ultra-high vacuum (UHV) conditions, achieved via

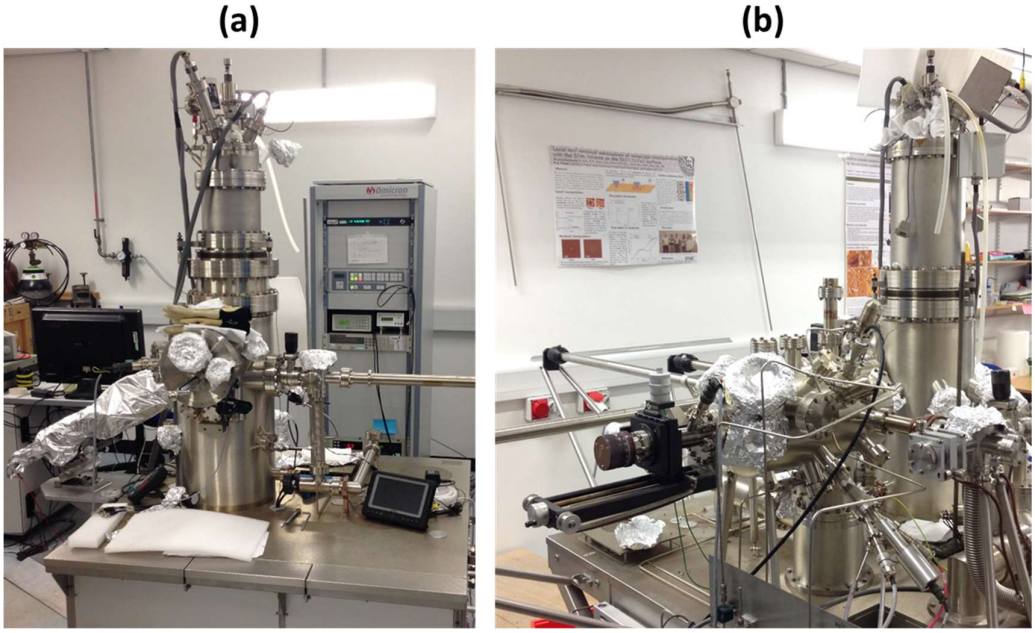

Figure 3-13. (a) LT-STM and (b) LT-STM/AFM with attached preparation chamber.

a combination of turbo molecular pumps (TMP) and ion pumps, where $< 5 \times 10^{-11}$ mbar is considered good vacuum. The TMPs were switched off during scanning to reduce vibrational noise. All measurements shown in this thesis were taken at LN_2 (77K) or LHe (5K) temperatures. The preparation chamber consists of a high temperature heater (up to 1400 °C), an Ar ion sputter gun, and an e-beam evaporator.

3.4. Moiré super-lattice in STM

When a periodic pattern is placed on top of another periodic pattern which have a difference in lattice constant, twist angle between the layers, or a different symmetry, the appearance of a moiré pattern is often observed. In standard cases these are large scale interference patterns due to the beat of two waves with slightly different frequencies. This explanation using the simple superposition of atomic structure of overlayer and substrate fits well in the case of moiré patterns in TEM images; however, it cannot be applied to STM as the STM images are acquired using the tunnelling phenomena. In the case of TEM the electrons are transmitted through both layers of the system, but for this picture to apply to STM the electrons now have to tunnel directly from the substrate and overlayer, where the tunnelling from inner layers is not well understood.

Systems with a lattice mismatch between layers result in a strain at these interface layers which can lead to shifting of atomic positions and buckling in the overlayer. This was

originally used to explain the moiré patterns in STM, however since no moiré patterns have been observed by AFM this cannot be the case. This highlights the importance of electronic effects in the moiré super-lattice. Another factor in these systems is the modulation of the overlayer electronic structure due to the interfacial interaction with the substrate. Whilst this is important for the moiré, it is not enough to explain it completely as moiré patterns have been observed in systems where the interaction between substrate and overlayer is very weak, such as in the case of graphite, graphene, and TMDs.

An explanation of the origin of the moiré super-lattice in STM was given by Kobayashi [42]. The main component of the wavefunctions near the surface is the wave with parallel momentum $2\pi/a$, which corresponds to the atomic lattice. A component with smaller amplitude, which is produced by multiple scattering of the electrons due to the mismatched layers a and b, has parallel momentum $2\pi/l = |2\pi/a - 2\pi/b|$, where l is the period of the super-lattice. Since waves in the vacuum region decay as,

$$e^{-\lambda z}, \qquad \lambda = \sqrt{2|E| + q^2} \tag{3-39}$$

where $|E|$ is the work function, the waves with a larger parallel momentum q are seen to decay faster. This means the atomic lattice component will decay faster than the super-lattice component, and even with its small amplitude the large super-lattice can be observed in STM with a larger tip-sample distance. Both the atomic lattice and the super-lattice can be observed simultaneously with certain tip-sample distances, which corresponds to the moiré pattern seen by the STM.

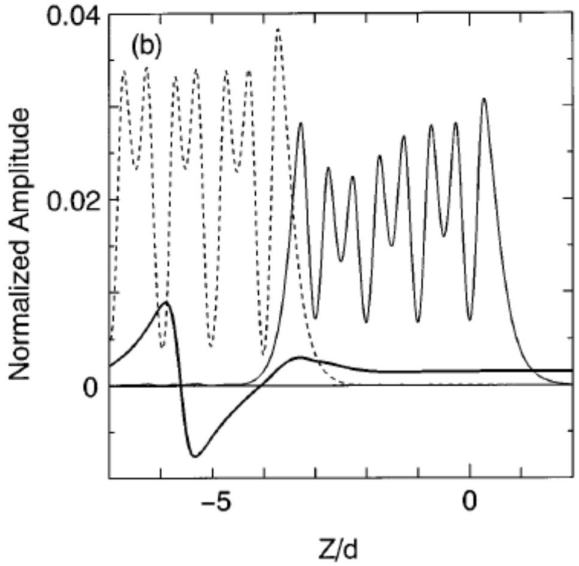

Figure 3-14. Amplitude variation of the LDOS showing the super-lattice (thick solid line), the atomic structure of the overlayer (solid line), and the substrate (dotted line). [42]

For a typical work function of 5 eV, the difference in decay behaviour between the atomic-scale waves and the nanoscale waves can be seen using eq. 3-39. Due to the difference in the parallel momentum, the decay of the atomic-scale waves is governed by the lattice spacing whilst for nanoscale waves the work function governs it. This means that these nanoscale waves can propagate through many layers of the material without decay, as the lateral kinetic energy of the nanoscale structure is smaller than the Fermi energy of the crystal; which is of the order of the typical work function. This behaviour allows for nanoscale structures such as the moiré super-lattice, and therefore information about the interface, to be observed many layers under the surface by STM. Figure 3-14 shows this decay in terms of the variation of wave amplitude along the z-axis. Kobayashi calculated the amplitude from the LDOS of the surface, using the Tersoff and Haman model. The waves corresponding to the atom lattices of the substrate and overlayer decay rapidly at the edge of their respective interfaces, whilst the nanoscale wave of the moiré super-lattice produced at the interface propagates through the 4 overlayers without decay.

Effect of moiré super-lattices in heterostructures

A moiré super-lattice in the case of heterostructures can have a large influence on the system produced. A slight mismatch in the atomic lattice parameters or rotation between layers at an interface results in a large scale quasi-periodic moiré super-lattice, with an associated long wavelength periodic potential. Both the geometric strain on the layers (resulting in distortion) and the moiré potential can affect the electronic structure of the system at the interface and lead to effects otherwise not observed.

The modification of the electronic structure has been observed experimentally in many different cases, but the focus here will be on 2-dimensional materials and those with a hexagonal structure. The Dirac cone of graphene makes for a simple system to observe changes, as extra states or shifts are clearly seen. The graphene/Rh(111) system has been investigated using STM and exhibits a clear moiré pattern of different intensities [43]. STS measurements showed additional states either side of the Fermi energy, with differences depending on which part of the moiré super-lattice they were taken from, as shown in figure 3-15(a). The sites showing spectra almost the same as pristine graphene were found to have buckled from the substrate surface, and therefore having a larger interlayer distance. As the other sites are closer to the substrate, the state formation was explained as a hybridisation of the graphene and Rh states. A similar system of graphene/h-BN agrees with the observation of new states, however the cause here is put down to the periodic moiré potential which induces $k \rightarrow -k$ processes for values $2k = G_\alpha$, where G_α is a superlattice reciprocal vector. [44]. In this case the twist angle between the two layers is also investigated, and the emergence energy of these new 'Dirac points' is correlated with the degree of

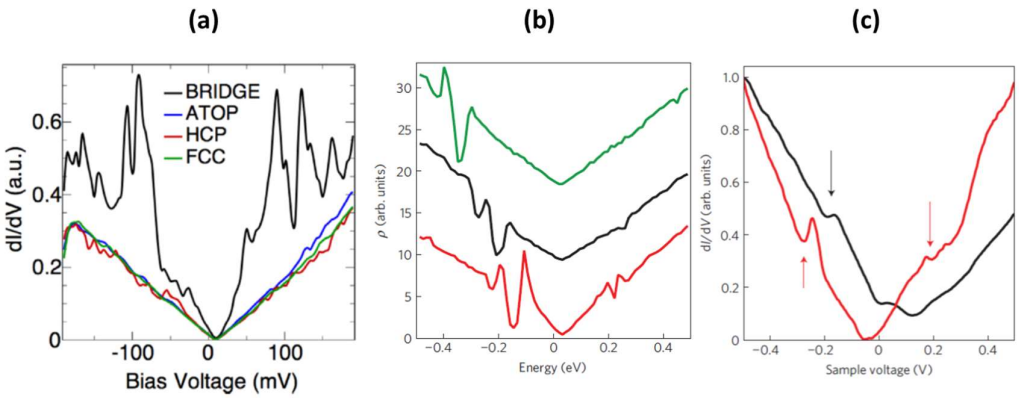

Figure 3-15. (a) STS taken from different symmetry points of the moiré pattern of graphene/Rh(111), showing the site dependent presence of additional states. The ATOP side corresponds to a C ring with a Rh atom in the centre, the BRIDGE site to a Rh atom between 2 C atoms, and the HCP and FCC sites to local stacking of that type [43]. Theoretical (b) and experimental (c) STS spectra showing the variation of new 'Dirac' points with twist angle in graphene/h-BN. The red line is $\phi = 0.5°$, the black is $\phi = 1°$, and green is $\phi = 2°$. [44]

rotation. The theoretical and experimental results for this are shown in figure 3-15(b)-(c). The larger the moiré wavelength, the further away from the original Dirac point the new points are. However, another study on a graphene/h-BN system showed no significant differences in the spectra taken from different twist angle moiré patterns [45], while a study of rotated layers in a cleaved HOPG crystal showed increased conductance from some moiré patterns but no difference from others [46].

In the case of TMDs similar observations have been made, for example with observations of new interface induced state seen in a MoS_2/Au(111) system [47]. It was noticed that the two different hollow site locations of the moiré super-lattice alternated in intensity with AFM and STM measurements in the band gap, showing that the site which was closer to the surface and therefore lower in AFM, gave a larger tunnelling current. Again, this showed a higher level of hybridisation at these points, and the importance that small deviations in the interlayer distance have on the electronic structure. A change in the electronic structure was also observed, not just with the appearance of a new state above the CBE but a significant modification of the states around the VBE. The Γ states at the VBE were not seen at all in STS measurements with only a state at Q observed, which is explained by the hybridisation of MoS_2 states with the d-band continuum of Au(111), supported by theory and ARPES in [48]. The influence of the moiré super-lattice is seen from STS measures taken on different regions, with the bands shifting differently between the top site and two hollow sites, as shown in figure 3-16(a). The main states shift between top and hollow sites, but the interface induced state shows differences between hollow sites. What this shows is that the atomic registry of the two layers is important in the interfacial interaction, as in the case of TMDs this interaction can affect the M-X bond length and therefore the band structure [49].

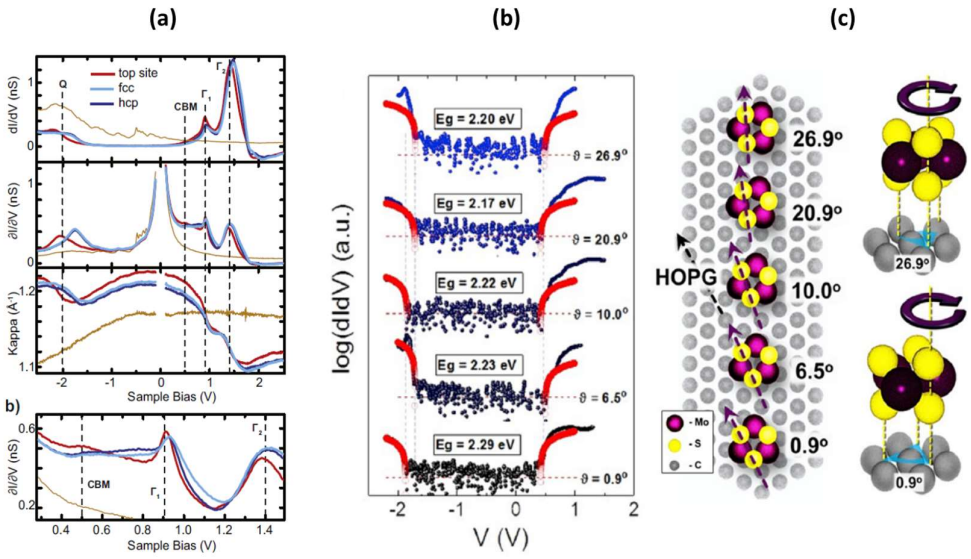

Figure 3-16. (a) dI/dV, $(\partial I/\partial V)_I$, and κ measurements from MoS_2/Au(111). Labelling the Mo atom lattice site A, the interfacial S atom B, and the top Au atom C, the top site has ABB stacking, the fcc site ABC stacking and the hcp site ABA stacking. The lower panel shows a zoomed in area around the CBE of the $(\partial I/\partial V)_I$ spectra [47]. (b) STS showing the bandgap size variation with increasing twist angle between layers in a MoS_2/HOPG heterostructure. (c) Diagram showing the arrangement of the atoms for different twist angles. [50]

Considering the moiré super-lattice, the twist angle results in different levels of coincident atoms, with a higher number enhancing the coupling between layers. In a MoS_2/HOPG heterostructure this reasoning is used to explain the decrease of the bandgap with an increase of the twist angle [50]. Figure 3-16(b)-(c) shows the experimental bandgaps measured, along with the relative layer rotation and position of the atoms. Theoretical calculations to unravel the moiré mechanism showed that the Γ states are shifted upwards, which can be explained by the nature of the orbitals that contribute to them. The S p_z-orbitals overlap with the top layer graphene p-orbitals, mediated by the Mo d_{z2}-orbitals which have out-of-plane z extension. At the K points, the dominant orbitals are Mo d_{x2-y2} and d_{xy} which have very little overlap with the S p_z-orbitals and are therefore insensitive to the S-graphene orbital overlap. The influence of the atomic registry and orbital character has been explored in MoS_2/WSe_2 heterostructures as well. For rotationally aligned (0° or 180°) layers there are 4 sites observed in the moiré super-lattice that correspond to difference arrangements of the atoms. STS has shown the bandgap size to be site dependent, a consequence of the varied interlayer coupling, and again due to a shift in the Γ states due to the orbital contribution to them [51]. This means that the moiré super-lattice results in a laterally periodic modulation of the bandgap. A similar study of this system at lower temperature, revealed the presence of spatially confined states within the moiré unit cell as well as the band edge shifts [52]. The potential of the moiré super-lattice perturbing the parabolic bands of the MoS_2 and WSe_2 is what leads to this confinement.

As discussed, previous investigations have explained modifications to the electronic structure in systems which exhibit a moiré super-lattice, by interlayer coupling resulting in hybridised states or due to the moiré potential associated with the super-lattice wavelength. One explanation that has not been mentioned so far but will also be considered is that of band-folding due to the moiré super-lattice, which can also induce significant changes the band structure.

3.5. Angle-resolved photoemission spectroscopy (ARPES)

The principle of photoemission spectroscopy comes from the photoelectric effect. Electrons in the sample are excited by photons originating from a light source such as a discharge lamp or a synchrotron beamline. The energy of the photon can be absorbed by the electron and converted to kinetic energy. If this is sufficiently large enough to overcome the binding energy of the crystal and the work function of the sample, it results in the electron escaping the surface into the vacuum. This now free electron has a specific kinetic energy and initial angle.

For spatially localised ARPES a particular region of the sample surface can be isolated to collect photoelectrons from. Measurements were performed in two different systems, one being at the NanoESCA facilty at Bristol University and the other a Nano-ARPES at the Spectromicroscopy beamline in the Elettra synchrotron. These two machines excite and collect the photoelectrons using different methods.

The NanoESCA instrument is called a photoemission electron microscope (PEEM) and the one at Bristol uses a monochromatized He discharge lamp, with the monochromator improving the energy resolution over a standard lamp. The photon energy used was 21.2 eV. The PEEM must be equipped with an energy filter to allow it to scan the photoelectron kinetic energy spectrum, and this combination is referred to as momentum microscopy. The aperture can be used to select a micron sized region from which the measurement is taken, using the real-space imaging mode. The excited photoelectrons are accelerated towards an electron optical column using an extractor electrode, as displayed by the diagram in figure 3-17(a). This contains the various electrostatic or magnetic lenses, corrector elements such as deflectors, and apertures for the contrast and image plane.

In the Nano-ARPES system at the Elettra synchrotron, the bright light from the beamline is focused using a dedicated Schwarzschild objective which can focus it down into a few nanometers sized spot. The region is first imaged by using the Schwarzschild objective as an optical microscope under the illumination of a lamp to determine where to position the spot.

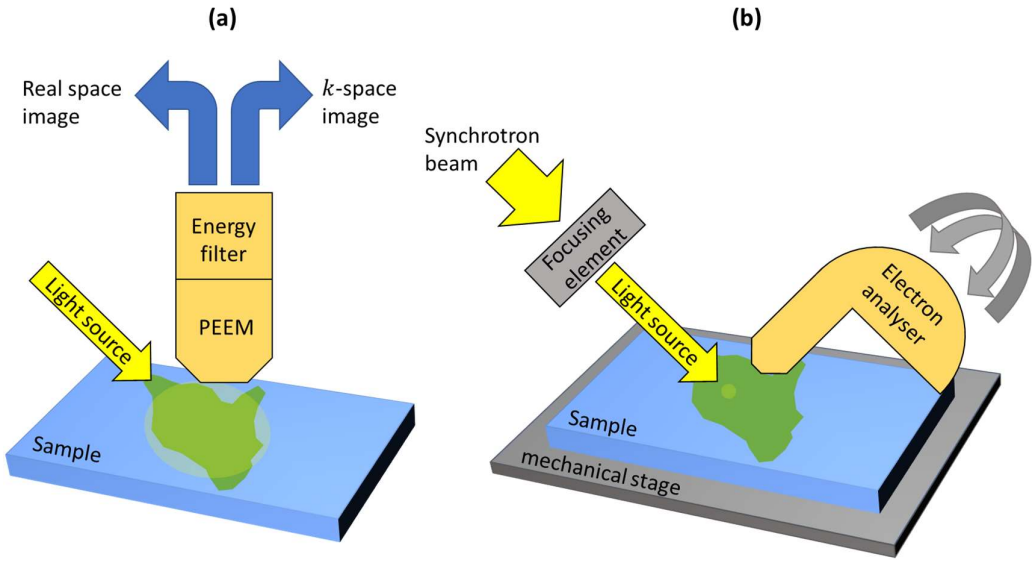

Figure 3-17. Schematic diagrams of the (a) Bristol NanoESCA and (b) Elettra Nano-ARPES set-ups.

The sample is moved by a mechanical stage and the lateral resolution of the image directly related to the beam spot size. The photoelectrons are then collected in by an electron analyser which moves in UHV over a range of different emission angles. A photon energy of 27 eV was used and the energy resolution is 14 meV. A diagram of this method is shown in figure 3-17(b).

After passing through the lenses and energy filter the photoelectron distribution as a function of the lateral momentum k_x and k_y is projected onto a two-dimensional screen and can be acquired as an image. By acquiring these isoenergetic images for all energies below the Fermi level allows for a 3D stack to be formed, which can be cut along various symmetry directions to obtain typical kinetic energy vs electron momentum plots. The NanoESCA allows for the mapping of a complete BZ in one isoenergetic slice, due to the ability of its double hemispherical energy filter to collect the full wavevector landscape [53].

3.5.1. Fundamental theory of photoemission spectroscopy

The photoelectric effect was discovered by Hertz in 1887 and this result led Einstein to propose that electromagnetic radiation is carried in quantised energy packets to explain these observations. According to his theory, photons are quantised with energy $h\nu$, where h is Planck's constant and ν is the frequency of the photon. Therefore, the relation between the kinetic energy of the photoelectrons and the frequency of the photons required to excite them out of the crystal is,

$$E_{kin} = \frac{1}{2} m_e v^2 = eV = h\nu - E_{bin} - \Phi, \tag{3-40}$$

where m_e is the electron mass, v is the electron velocity, and e the electron charge. Electrons which are excited from the core levels of the band structure need to overcome the binding energy E_{bin} as well as the workfunction Φ. Electrons in states at the Fermi level must only overcome the workfunction to become free electrons.

The three-step model is typically used to describe the photoemission process. The first step is the photo-excitation of the electron, the second is the transport of the electrons to the surface, and the final step is the transmission of the electron through the surface [54].

The wavefuntion of an electron in the periodic lattice of a crystal can be described with Bloch functions, which are written as,

$$\left|\Psi_{n,l,s}(\vec{k})\right\rangle = \left|n, l, \vec{k}, s\right\rangle, \tag{3-41}$$

where n is the band index, l is the orbital momentum quantum number, $\vec{k}$ is the electron wave vector, and s the spin quantum number. These functions have eigenstates $E_{n,l,s}(\vec{k})$. The electron is transferred from an initial state $\left|i, \vec{k}_i\right\rangle$ in the occupied band structure to a final unoccupied state $\left|f, \vec{k}_f\right\rangle$ during the photo-excitation process via optical transition. This is a momentum conserving transition with the conservation law for the electron's momentum $\hbar\vec{k}$ given by,

$$\vec{k}_f = \vec{k}_i + \vec{q} \pm \vec{G}, \tag{3-42}$$

where $\vec{q}$ is the photons momentum and $\vec{G}$ is the reciprocal lattice vector. The probability of transition between these two states is given by Fermi's Golden rule,

$$P_{i\to f} = \frac{2\pi}{\hbar} \left|\langle f, \vec{k}_f | H_{int} | i, \vec{k}_i \rangle\right|^2 \delta\left(E_f - E_i - h\nu\right), \tag{3-43}$$

$$H_{int} = -\frac{e}{mc} \vec{A}(\vec{r}) \cdot \vec{p}, \tag{3-44}$$

where E_i and E_f are the binding energies, $\vec{A}$ is the vector potential of the electric field, and $\vec{p}$ is the momentum operator. If the wavelength of the electromagnetic field is large compared to the inter-atomic lattice spacing, the matrix element $M_{fi} = \langle f, \vec{k}_f | H_{int} | i, \vec{k}_i \rangle$ can be simplified to,

$$M_{fi} = \frac{ie}{\hbar c} A_0 (E_f - E_i) \langle f, \vec{k}_f | \vec{e} \cdot \vec{r} | i, \vec{k}_i \rangle, \tag{3-45}$$

where A_0 is the amplitude of the vector potential and $\vec{e}$ is its polarisation. Eq. 3-43 describes a single particle approximation, and therefore the total photo-current from the photo-

excitation process is proportional to the sum of $P_{i\to f}$ over all allowed transitions. However, to fully describe the photoemission process the electronic correlations between the electrons in the many-body theory should also be considered.

The photoelectrons path to the surface can result in various elastic and inelastic scattering processes such as electron-electron scattering or scattering from defects in the crystal. These processes can cause a change in the photoelectron's momentum $\vec{k}$. For inelastic scattering it also leads to a loss of kinetic energy, which means it now only contributes to the featureless background in the spectrum. The photoemission intensity of elastically- or non-scattered electrons depends on the way they travel to the surface and can be described,

$$I(t, E_{kin}, \alpha) = I_0 \exp\left(-\frac{t}{\lambda(E_{kin})\, cos(\alpha)}\right), \tag{3-46}$$

where t is the layer thickness in which the photoexcitation took place, α is the emission angle with respect to the surface normal, λ is the inelastic mean free path which depends on E_{kin}.

The final step of the process is to overcome the surface potential barrier, which matches the periodic potential of the crystal to the vacuum. After the photoexcitation, photoelectrons travel in a potential of depth $V_{iP} = E_{vac} - E_0$, where E_{vac} is the vacuum level and E_0 is the bottom of the valence band. The final state energy after the photoexcitation process can be described by a free electron parabola starting at E_0 as $E_f = ((\hbar k_f)^2/2m^*)$, where m^* is the effective electron mass. The energy is the same after leaving the crystal potential so the magnitude of the electron momentum $|\vec{K}|$ is determined by the intersection with a free electron parabola, $E_f = ((\hbar K)^2/2m^*)$ now starting at E_{vac}. To overcome the potential barrier, $k_\perp$must meet the condition,

$$E_{kin,\perp} = \frac{(\hbar k_\perp)^2}{2m_e} \geq E_{vac} - E_0, \tag{3-47}$$

During the refraction at the surface potential, the parallel momentum $k_{f,\parallel}$ of the photoelectron's momentum is conserved. Therefore, in the vacuum the parallel momentum becomes,

$$K_\parallel = k_{f,\parallel} + G_{f,\parallel}, \tag{3-48}$$

where $G_{f,\parallel}$ is the surface parallel component of the surface reciprocal lattice. By applying a field between the sample and extractor, only the perpendicular component of the photoelectron's momentum $K_\perp$ is increased, while the parallel momentum is conserved. This means that the distribution of $K_\parallel$ detected corresponds to the final state momentum of the crystal.

Angular and momentum resolved photoemission

In the energy filtered momentum microscope, the kinetic energy of the photoelectron along with its parallel momentum $K_{\parallel}$ are directly measured. They are related by,

$$E_{kin} = \frac{\hbar}{2m_e}\left(K_{\parallel}^2 + K_{\perp}^2\right) = E_f\left(\vec{k}\right) - E_{vac}, \tag{3-49}$$

The final state component $k_{f,\perp}^2$ can be calculated if the inner potential V_0 is known as,

$$k_{f,\perp}^2 = \frac{2\mathrm{m_e}}{\hbar}(E_{kin} + V_{iP}) - K_{\parallel}^2, \tag{3-50}$$

As all effects are repeated periodically like $\vec{k}_1 = \vec{k}_2 + \vec{G}$, the description of all momentum dependent effects in a periodic crystal can be done within a reduced zone scheme only considering the first BZ.

References

[1] Bardeen J (1961) Tunnelling from a many-particle point of view. *Physical Review Letters.* **6** 57

[2] Tersoff J and Hamann D R (1983) Theory and application for the scanning tunneling microscope. *Physical Review Letters.* **50** 1998-2001

[3] Chen C J (2008) *Introduction to scanning tunneling microscopy.* (Oxford:Oxford University Press)

[4] Brar V W (2010) Scanning tunneling spectroscopy of graphene and magnetic nanostructures. *PhD Thesis.* (UC Berkeley)

[5] Chen C J (1990) Origin of atomic resolution on metal-surfaces in scanning tunneling microscopy. *Physical Review Letters.* **65** 448-51

[6] Binnig G and Smith D P E (1986) Single-tube 3-dimensional scanner for scanning tunneling microscopy. *Review of Scientific Instruments.* **57** 1688-9

[7] Stroscio J A, Feenstra R M and Fein A P (1986) Electronic-structure of the Si(111)2X1 surface by scanning-tunneling microscopy. *Physical Review Letters.* **57** 2579-82

[8] Feenstra R M and Stroscio J A (1987) Tunneling spectroscopy of the GaAs(110) surface. *Journal of Vacuum Science & Technology B.* **5** 923-9

[9] Binnig G and Rohrer H (1986) Scanning tunneling microscopy. *IBM Journal of Research and Development.* **30** 355-69

[10] Tromp R M (1989) Spectroscopy with the scanning tunneling microscope: A critical review. *Journal of Physics: Condensed Matter.* **1** 10211-28

[11] Stroscio J A and Kaiser W J (1993) *Scanning tunneling microscopy* (Boston: Academic Press)

[12] Zhang C D, Chen Y X, Johnson A, Li M Y, Li L J, Mende P C, Feenstra R M and Shih C K (2015) probing critical point energies of transition metal dichalcogenides: surprising indirect gap of single layer WSe2. *Nano Letters.* **15** 6494-500

[13] Simon L, Bena C, Vonau F, Cranney M and Aubel D (2011) Fourier-transform scanning tunnelling spectroscopy: the possibility to obtain constant-energy maps and band dispersion using a local measurement. *Journal of Physics D: Applied Physics.* **44** 19

[14] Hasegawa Y and Avouris P (1993) Direct observation of standing-wave formation at surface steps using scanning tunneling spectroscopy. *Physical Review Letters.* **71** 1071-4

[15] Crommie M F, Lutz C P and Eigler D M (1993) Imaging standing waves in a 2-dimensional electron-gas. *Nature.* **363** 524-7

[16] Sprunger P T, Petersen L, Plummer E W, Laegsgaard E and Besenbacher F (1997) Giant Friedel oscillations on the beryllium(0001) surface. *Science.* **275** 1764-7

[17] Simon L, Vonau F and Aubel D (2007) A phenomenological approach of joint density of states for the determination of band structure in the case of a semi-metal studied by FT-STS. *Journal of Physics: Condensed Matter.* **19** 14

[18] Reinert F, Nicolay G, Schmidt S, Ehm D and Hufner S (2001) Direct measurements of the L-gap surface states on the (111) face of noble metals by photoelectron spectroscopy. *Physical Review B.* **63** 6

[19] Kevan S D and Gaylord R H (1987) High-resolution photoemission-study of the electronic-structure of the noble-metal (111) surfaces. *Physical Review B.* **36** 5809-18

[20] Petersen L, Laitenberger P, Laegsgaard E and Besenbacher F (1998) Screening waves from steps and defects on Cu(111) and Au(111) imaged with STM: Contribution from bulk electrons. *Physical Review B.* **58** 7361-6

[21] Brihuega I, Mallet P, Bena C, Bose S, Michaelis C, Vitali L, Varchon F, Magaud L, Kern K and Veuillen J Y (2008) Quasiparticle chirality in epitaxial graphene probed at the nanometer scale. *Physical Review Letters.* **101** 4

[22] Voigtländer B (2015) *Scanning Probe Microscopy: Atomic Force Microscopy and Scanning Tunneling Microscopy.* (Berlin, Heidelberg: Springer)

[23] Schouteden K, Lievens P and Van Haesendonck C (2009) Fourier-transform scanning tunneling microscopy investigation of the energy versus wave vector dispersion of electrons at the Au(111) surface. *Physical Review B.* **79** 7

[24] Mallet P, Brihuega I, Cherkez V, Gomez-Rodriguez J M and Veuillen J Y (2016) Friedel oscillations in graphene-based systems probed by scanning tunneling microscopy. *Comptes Rendus Physique.* **17** 294-301

[25] Feng B J, Li H, Liu C C, Shao T N, Cheng P, Yao Y G, Meng S, Chen L and Wu K H (2013) Observation of dirac cone warping and chirality effects in silicene. *ACS Nano.* **7** 9049-54

[26] Pascual J I, Bihlmayer G, Koroteev Y M, Rust H P, Ceballos G, Hansmann M, Horn K, Chulkov E V, Blugel S, Echenique P M and Hofmann P (2004) Role of spin in quasiparticle interference. *Physical Review Letters.* **93** 4

[27] Liu H J, Chen J L, Yu H Y, Yang F, Jiao L, Liu G B, Ho W K, Gao C L, Jia J F, Yao W and Xie M H (2015) Observation of intervalley quantum interference in epitaxial monolayer tungsten diselenide. *Nature Communications.* **6** 6

[28] Zhang T, Cheng P, Chen X, Jia J F, Ma X C, He K, Wang L L, Zhang H J, Dai X, Fang Z, Xie X C and Xue Q K (2009) Experimental demonstration of topological surface states protected by time-reversal symmetry. *Physical Review Letters.* **103** 4

[29] Lee W C, Wu C J, Arovas D P and Zhang S C (2009) Quasiparticle interference on the surface of the topological insulator Bi2Te3. *Physical Review B.* **80** 5

[30] Yankowitz M, McKenzie D and LeRoy B J (2015) Local spectroscopic characterization of spin and layer polarization in WSe2. *Physical Review Letters.* **115** 5

[31] Xiao D, Liu G B, Feng W X, Xu X D and Yao W (2012) Coupled spin and valley physics in monolayers of MoS2 and other group-VI dichalcogenides. *Physical Review Letters.* **108** 5

[32] Wu C J, Bernevig B A and Zhang S C (2006) Helical liquid and the edge of quantum spin Hall systems. *Physical Review Letters.* **96** 4

[33] Liu Q, Liu C X, Xu C K, Qi X L and Zhang S C (2009) Magnetic impurities on the surface of a topological insulator. *Physical Review Letters.* **102** 4

[34] Qi X L, Hughes T L and Zhang S C (2008) Fractional charge and quantized current in the quantum spin Hall state. *Nature Physics.* **4** 273-6

[35] Qi X L, Hughes T L and Zhang S C (2008) Topological field theory of time-reversal invariant insulators. *Physical Review B.* **78** 43

[36] Roushan P, Seo J, Parker C V, Hor Y S, Hsieh D, Qian D, Richardella A, Hasan M Z, Cava R J and Yazdani A (2009) Topological surface states protected from backscattering by chiral spin texture. *Nature.* **460** 1106-U64

[37] Norden T, Zhao C, Zhang P, Sabirianov R, Petrou A and Zeng H (2019) Giant valley splitting in monolayer WS2 by magnetic proximity effect. *Nature Communications.* **10** 4163

[38] Zhao C, Norden T, Zhang P Y, Zhao P Q, Cheng Y C, Sun F, Parry J P, Taheri P, Wang J Q, Yang Y H, Scrace T, Kang K F, Yang S, Miao G X, Sabirianov R, Kioseoglou G, Huang W, Petrou A and Zeng H (2017) Enhanced valley splitting in monolayer WSe2 due to magnetic exchange field. *Nature Nanotechnology.* **12** 757

[39] Tang Y H, Mak K F and Shan J (2019) Long valley lifetime of dark excitons in single-layer WSe2. *Nature Communications.* **10** 7

[40] Liu G B, Pang H L, Yao Y G and Yao W (2014) Intervalley coupling by quantum dot confinement potentials in monolayer transition metal dichalcogenides. *New Journal of Physics.* **16** 23

[41] Kaasbjerg K, Martiny J H J, Low T and Jauho A P (2017) Symmetry-forbidden intervalley scattering by atomic defects in monolayer transition-metal dichalcogenides. *Physical Review B.* **96** 6

[42] Kobayashi K (1996) Moire pattern in scanning tunneling microscopy: Mechanism in observation of subsurface nanostructures. *Physical Review B.* **53** 11091-9

[43] Holtsch A, Euwens T, Uder B, Grandthyll S, Muller F and Hartmann U (2018) Analysis of atomic moire patterns on graphene/Rh(111). *Surface Science.* **668** 107-11

[44] Yankowitz M, Xue J M, Cormode D, Sanchez-Yamagishi J D, Watanabe K, Taniguchi T, Jarillo-Herrero P, Jacquod P and LeRoy B J (2012) Emergence of superlattice Dirac points in graphene on hexagonal boron nitride. *Nature Physics.* **8** 382-6

[45] Decker R, Wang Y, Brar V W, Regan W, Tsai H Z, Wu Q, Gannett W, Zettl A and Crommie M F (2011) Local electronic properties of graphene on a BN substrate via scanning tunneling microscopy. *Nano Letters.* **11** 2291-5

[46] Patil S, Kolekar S and Deshpande A (2017) Revisiting HOPG superlattices: Structure and conductance properties. *Surface Science.* **658** 55-60

[47] Krane N, Lotze C and Franke K J (2018) Moire structure of MoS2 on Au(111): Local structural and electronic properties. *Surface Science.* **678** 136-42

[48] Bruix A, Miwa J A, Hauptmann N, Wegner D, Ulstrup S, Gronborg S S, Sanders C E, Dendzik M, Cabo A G, Bianchi M, Lauritsen J V, Khajetoorians A A, Hammer B and Hofmann P (2016) Single-layer MoS2 on Au(111): Band gap renormalization and substrate interaction. *Physical Review B.* **93** 10

[49] Ebnonnasir A, Narayanan B, Kodambaka S and Ciobanu C V (2014) Tunable MoS2 bandgap in MoS2-graphene heterostructures. *Applied Physics Letters.* **105** 5

[50] Trainer D J, Putilov A V, Wang B K, Lane C, Saari T, Chang T R, Jeng H T, Lin H, Xi X X, Nieminen J, Bansil A and Iavarone M (2019) Moire superlattices and 2D electronic properties of graphite/MoS2 heterostructures. *Journal of Physics and Chemistry of Solids.* **128** 325-30

[51] Zhang C D, Chuu C P, Ren X B, Li M Y, Li L J, Jin C H, Chou M Y and Shih C K (2017) Interlayer couplings, moire patterns, and 2D electronic superlattices in MoS2/WSe2 hetero-bilayers. *Science Advances.* **3** 7

[52] Pan Y, Folsch S, Nie Y F, Waters D, Lin Y C, Jariwala B, Zhang K H, Cho K, Robinson J A and Feenstra R M (2018) Quantum-confined electronic states arising from the moire pattern of MoS2-WSe2 heterobilayers. *Nano Letters.* **18** 1849-55

[53] Cattelan M and Fox N A (2018) A perspective on the application of spatially resolved ARPES for 2D materials. *Nanomaterials.* **8** 26

[54] Patt M C and Forschungszentrum Jülich GmbH Verlag Z (2016) *Bulk and surface sensitive energy-filtered photoemission microscopy using synchrotron radiation for the study of resistive switching memories*. (Forschungszentrum Jülich GmbH, Zentralbibliothek)

Chapter 4

Techniques for sample preparation

The most important part of the STM system is the tip. Therefore, the preparation and assessment of the tip must be undertaken with great care. A description of the process is described in this chapter, from the initial etching of the tips to the final checks of quality by STM. Alongside this the methods of sample preparation are outlined; the priority being to produce an atomically clean surface allowing for high quality STM measurements. The process of decoration of the WSe_2 crystal achieved through evaporation is explained. Another method of dopant incorporation into a sample is via an ion source. In particular, a low-energy ion source allowing for substitution of atoms in the surface layer is described. This equipment was installed onto the system; however, it did not see use due to reasons discussed below.

4.1. Tip preparation and assessment

As the probe part of the STM system, care must be taken with the creation and conditioning of the tip. These tips were mounted securely into an Omicron tip holder before being placed into the system and annealed at 150°C to remove water. The tip holder was then mounted at the top of the scanner. The tips used were made from 0.25 mm diameter wire of either tungsten (W) (99.95% purity) or platinum iridium (Pt-Ir) (90%-10%). The Pt-Ir tips were pre-etched and came from Omicron.

Tip etching procedure

The W tips are electrochemically etched using 1M sodium hydroxide solution (NaOH) as the electrolyte. Figure 4-1 shows a diagram of the etching apparatus. A length of W wire is cut and cleaned using ethanol and DI water, before being threaded through the small 3 mm diameter hole in the centre of the metal plate. It is clamped in place at the top by another plate fixed with a screw. This leaves the wire suspended in a plastic tube below that acts as a collection block. Drops of solution are then pipetted onto the hole to form a meniscus across it surrounding the W wire. A DC voltage of 2-3 V is applied between the tip and the metal clamp, with the current limited to 50 mA. The etching process usually takes about 2-3 minutes, and once finished the bottom part of the wire drops down into the plastic collection tube. It is then washed with ethanol and DI water again to remove any residual solution.

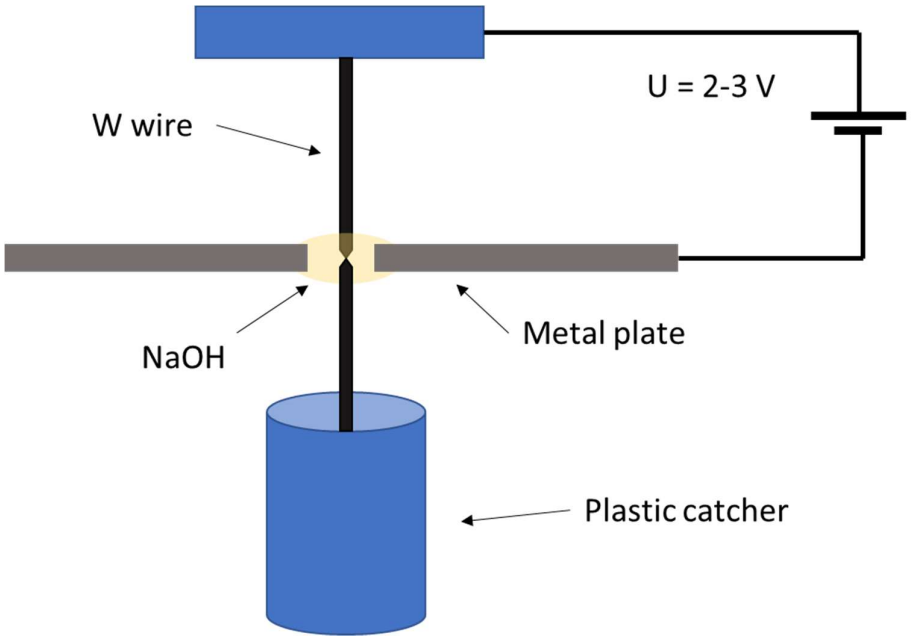

Figure 4-1. Schematic of the W tip etching apparatus. (adapted from [1])

The advantage of this method is that it is self-limiting, so there is no risk of over-etching the tip. The tips' weight determines the point at which it tears off from the upper portion of wire, with an optimal length of about 1 cm for sharp tips. This also means that it doesn't require a system to automatically shut off the voltage when the detected current goes below a threshold as in other methods. To protect the tip once it falls, the plastic tube was not as high as the tip length so that the end of the tip would not touch the sides. This procedure was from [1].

Tips were first characterised by an optical microscope to select the sharpest and disregard any that appeared damaged or bent. A selection of tips under the optical microscope is shown in figure 4-2. The tip in figure 4-2(a) has a 'vanishing' end meaning that the end of the tip cannot be seen. Tips like this were considered good and generally gave good performance with a small amount of assessment and conditioning. The tip in figure 4-2(b) is blunt as the end is clearly seen, so these tips were disregarded. Tips (c) and (d) show examples of different etching patterns depending on the shape of the solution and other factors. The tip in figure 4-2(c) has a neck higher up, which resulted from vibrations while etching. After observing this the tip making was moving onto the vibration isolated base of the STM system. Figure 4-2 shows a tip with a short neck. While these tips could be good, the shorter neck meant it was hard to position them on the samples as they would obscure part of it.

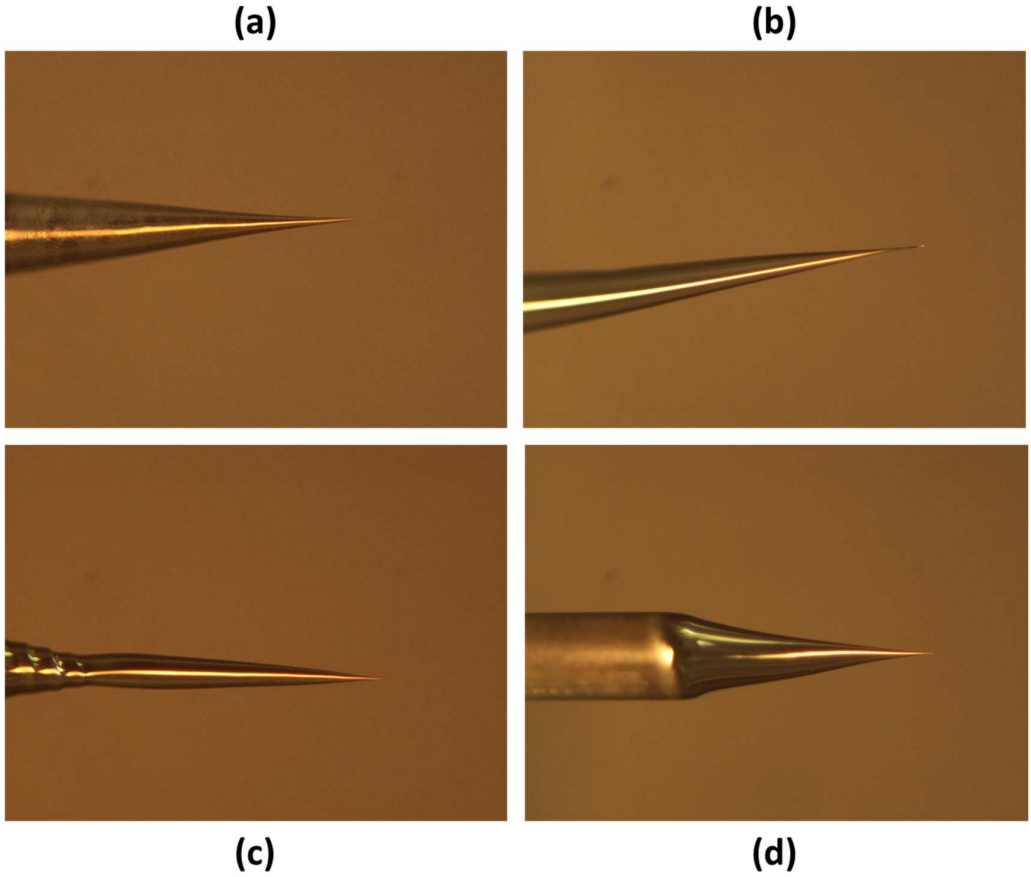

Figure 4-2. Etched W tips under the optical microscope showing (a) a 'vanishing' tip, (b) a blunt tip, (c) a tip with a neck due to vibrations during etching, and (d) a short etch length tip.

Methods of tip conditioning

While sharp tips may be fabricated by this method, the final test they must pass is that by STM and STS. The performance of the tip in STM therefore determines its quality [2]. From the previous chapter, eq. 3-13 shows that the electronic structure of the tip can contribute to the tunnelling current in addition to the samples electronic structure. It is therefore necessary to ensure that a flat tip DOS is achieved for the range of energies to be examined. The metals W, Pt, and Ir used for tips have a constant DOS near the Fermi energy, and any deviations from this can usually be removed through the tip conditioning procedure. Before scanning on the WSe_2 samples, the tip was characterised on the Au(111) surface, which is a typical standard to calibrate an STM system [2]. The Au(111) surface has a threefold rotational symmetry with a lattice separation of 0.288nm; exhibiting a clear surface ($22 \times \sqrt{3}$) reconstruction known as the Herringbone pattern. Figure 4-3(a) shows an STM images of the Au(111) surface. The Shockley surface state gives a peak at around -470 mV in STS

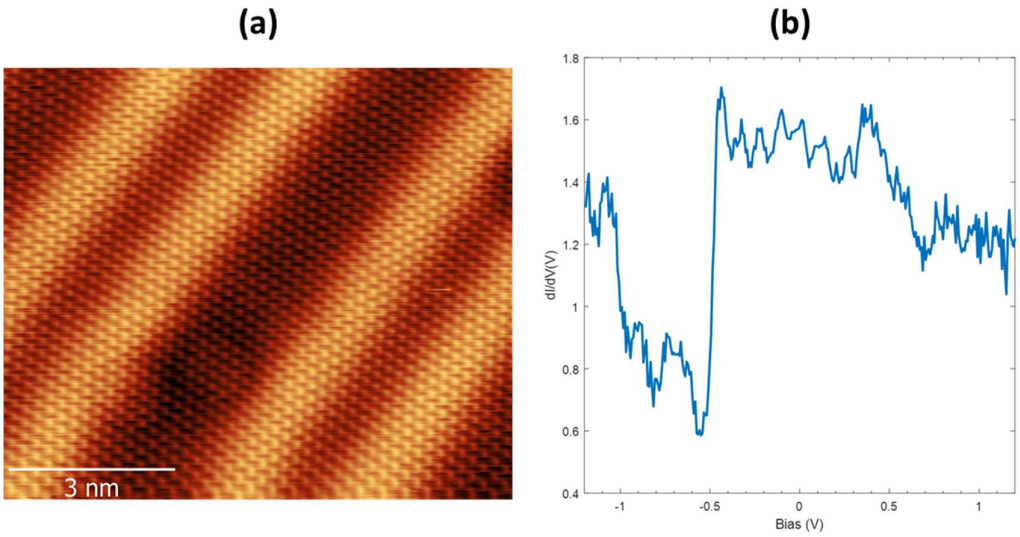

Figure 4-3. (a) STM image at -1.2 V, 0.17 nA showing the Au(111) surface with atomic resolution. (b) dI/dV measurement from the Au(111) showing the sharp Shockley surface state at ~-470 mV.

measurements as shown in figure 4-3(b) [3]. The presence of this state is a test of the quality of the tip, as it indirectly demonstrates that the tip states are not contributing to the tunnelling current. The reconstructed Au(111) surface is prepared in UHV by Ar ion sputtering an Au/mica or an Au single crystal and then annealing at 470°C for 15 minutes with a ramp up/down time of 45 minutes. This cycle can be repeated if the sample has not been cleaned for a long time.

If the tip requires reshaping there are many ways to do this. The primary method is to use voltage pulses to alter the apex of the tip. This begins by finding a clean area to work on without molecules or other impurities. The pulse magnitude is typically started at 0.5 V and slowly increased up to 4 V. Multiple pulses are done at each voltage due to the statistical probability of change with each pulse. The tip is checked between pulses to identify any change. Scanning the tip fast can also induce a change in the tip if it is unstable at the end, and this can also help stabilise the tip once it is good. Toggling the bias voltage between +ve and -ve can be used as a method too and also ensures that the tip can scan on both bias, as scanning on only one bias indicates that the tip has states. For more extreme cases, the tip can be pulsed up to 10 V. This causes a large reformation at the end of the tip and usually results in a lot of material being dropped onto the surface. The tip must be moved to a new clean area after this procedure to continue scanning.

While usually the tip apex consists of W or Pt-Ir atoms, it can also be prepared with a Au terminated tip. This is achieved by carefully dipping the tip into the Au surface using I/z spectroscopy to pick up a chain of atoms. Due to the change in tip type to an s-terminated tip, it will no longer be able to atomically resolve the s-terminated surface of the Au. Therefore, another test is required to determine the quality of the tip. This involves scanning

over a single atom and checking for its spherical nature and that the FWHM of the point is 0.7 nm or less.

4.2. 1H-WSe_2/Au(111) heterostructure preparation

To further understand the effect of defects and the interaction at the interface of WSe_2, a heterostructure of WSe_2 on Au(111) was created. A WSe_2 single crystal was mechanically exfoliated using scotch tape, peeling off with a small angle between the crystal and tape to pick up larger flakes and avoid damage to them. The peeled flakes were then repeatedly peeled with more tape to thin the flakes down. The final tape was cut to match the shape of the flake to reduce the substrate contact with glue. The tape was then placed down onto an Au(111) single crystal that had been heated to 60°C on a heating plate, and pressed lightly on the back to ensure contact between the flakes and Au. It was then peeled off slowly, maintaining a small angle as before. The sample was then imaged by optical microscope to confirm the presence of the flakes, before being placed into ultra-high vacuum via the load lock. Figure 4-4 shows optical microscope (a) and STM (b) images of an area with mono-, few-layer, and bulk flakes.

The flake was also imaged with PEEM when in the NanoESCA system. This is displayed in figure 4-6(a) and shows a much higher contrast of the monolayer flake. This shows that the multilayer flake sits on top of the monolayer. There is an impurity lying on top of the flake,

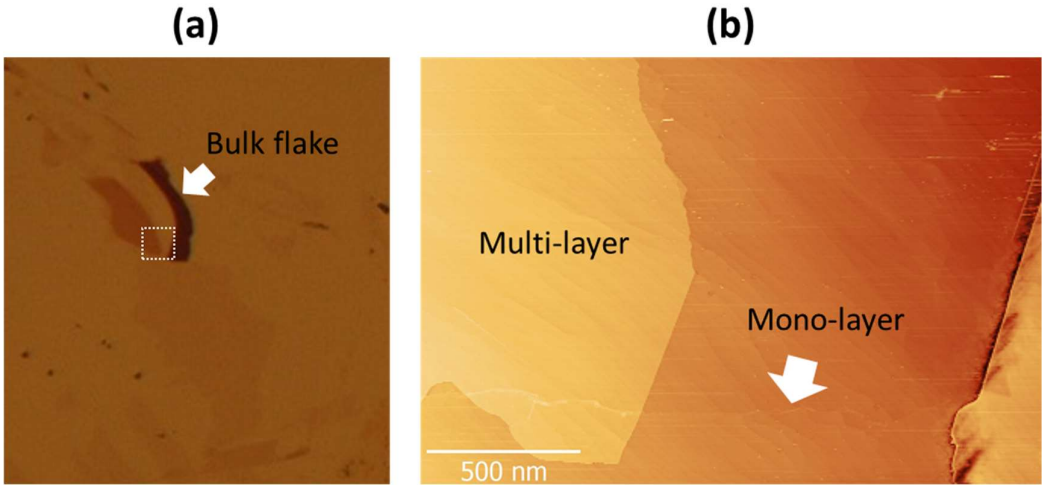

Figure 4-4. (a) Optical image of area on the Au crystal covered WSe_2 exfoliated flakes, showing mono-, few-layer, and bulk flakes. (b) STM image from the white dashed box in (a). The few-layer flake is 4 layers as measured by the STM across an edge. The faint ripple structures are due to terraces on the underlying Au(111) substrate.

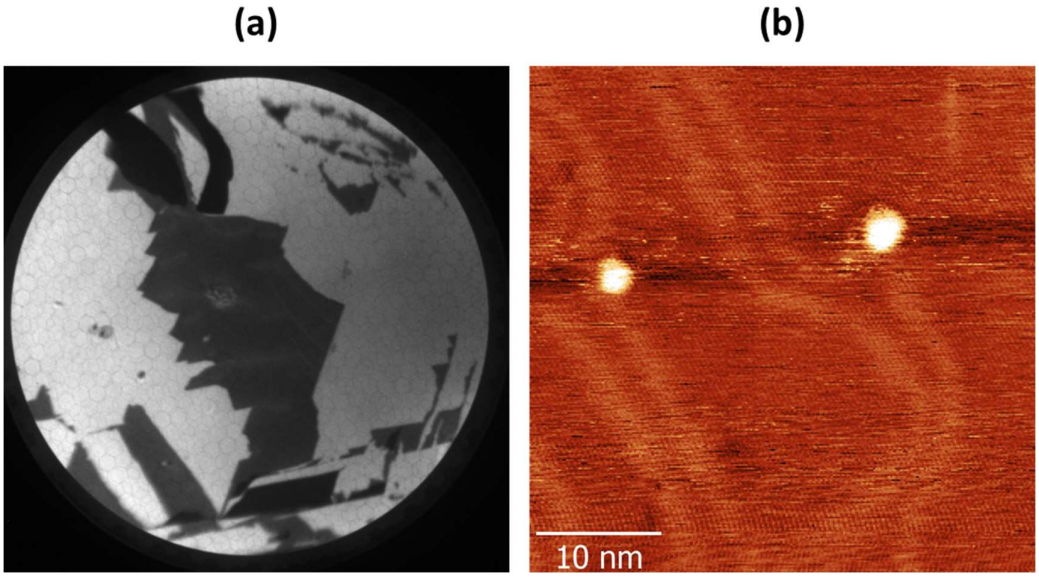

Figure 4-5. (a) PEEM image of the WSe_1 flakes on Au. The large flake at the centre and extending vertically is the monolayer as seen in the optical and STM images. The darker flakes above it are the multilayer on the left and the bulk on the right. The monolayer is seen to extend underneath the multilayer flake. (b) STM image at -0.87 V, 1.31 nA showing the Herringbone pattern underneath the WSe_2 surface. The bright spots are impurity atoms on the surface.

which likely occurred during the transfer to the NanoESCA as it was not observed in large area STM scans.

The sample was scanned with STM before being annealed to check the surface. One feature that was observed was the Herringbone pattern of Au underneath the WSe_2 monolayer (shown in figure 4-5(b)). After annealing this feature disappeared, showing that the annealing process improved the contact between the two layers.

Transfer for ARPES measurements

The sample was transferred to the facilities for ARPES measurements in vacuum conditions. First it was moved into LT2, as this system allowed for vacuum containers to be attached. For the NanoESCA a vacuum suitcase was used, which had a built-in mini ion pump. This was mounted onto the system as in figure 4-6(a) The load-lock was pumped prior to opening the connecting gate valve so as not to introduce impurities. Once at the NanoESCA laboratory, the sample was annealed at 400°C to clean it and remove any surface impurities it may have picked up. For transfer to the Nano-ARPES at the Elettra beamline facility, the sample was mounted in a small vacuum container as shown in figure 4-6(b). This container was then

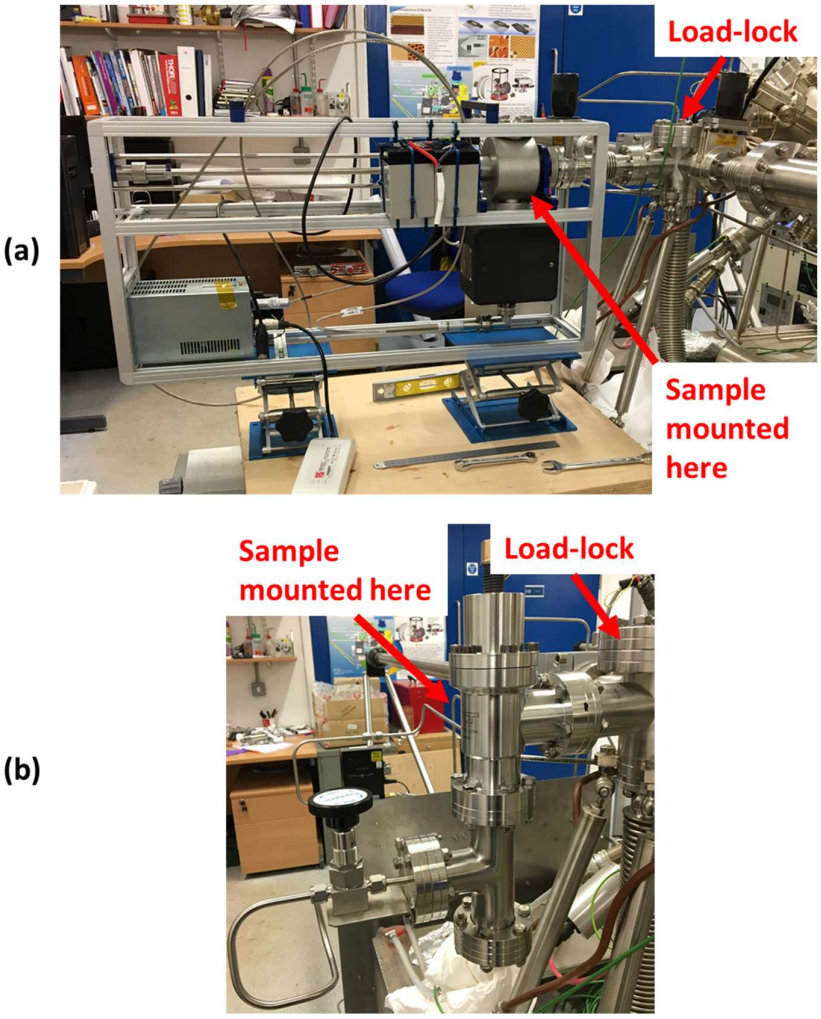

Figure 4-6 (a) Vacuum suitcase mounted to LT2 system. The suitcase had its own manipulator for moving samples in and out, and a mini ion pump. (b) Small vacuum container with a gate valve for sealing and venting valve for breaking vacuum. The sample was pre-mounted in the container, which was then pumped down by the TMP connected to one of the load-locks.

pumped down overnight to obtain a good vacuum before transfer. It was then annealed at 400°C before measurements were taken.

4.3. Pd decoration of WSe_2 crystal

A Mantis evaporator was used to deposit Pd atoms in UHV onto the surface of a bulk WSe_2 crystal. This was done with a flux of 2-2.5 nA for 10 seconds to achieve a low deposition rate of the atoms. Investigating the density of Pd deposited on graphite helped to decide the

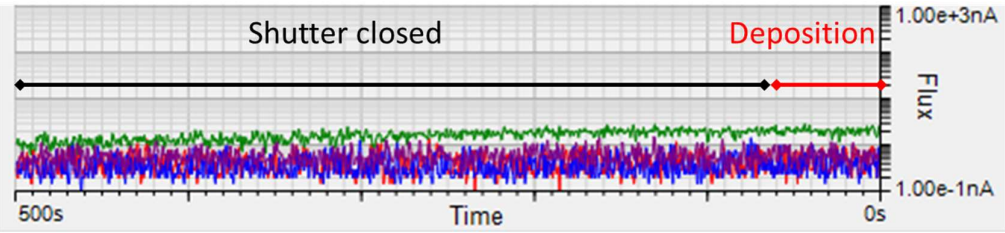

Figure 4-7. Deposition profile for Pd atoms on graphite for a deposition time of 60 seconds, indicated in green. The flux is gradually increased up to the desired value whilst the shutter is closed to prevent unwanted deposition. Once the desired value is reached and the flux is stable, the shutter is opened for the duration of the deposition time and then closed. The flux remains at a value of 2-2.5 nA.

deposition time to be used. First the deposition was carried out for 60 seconds and resulted in a large density of Pd atoms on the graphite surface, but not monolayer coverage. This sample was then cleaned via exfoliation and Pd atoms deposited for 15 seconds with the same conditions, which resulted in individual and clusters of Pd atoms distributed on the surface; however, it had large areas of the surface uncovered. Since the interest was on the individual atoms and clusters, the deposition time was reduced further for the WSe_2 to ensure that these would be possible to find and image. The flux against time profile for the first deposition on graphite is shown in figure 4-7. This shows the flux is increased to just above the threshold for deposition and then maintained, so the only factor affecting the deposition rate is the time. After deposition the sample was scanning using the STM. To then investigate the diffusion of the Pd on the surface, the sample was annealed in UHV first at 600°C and then checked with the STM. After this it was annealed a second time at 900°C.

4.4. Low-energy Ion source for induced defects and substitutional dopants

An ion source was connected to the system to provide a method to induce defects into sample surfaces. This is of interest for many reasons; primarily to allow for the characterisation of controllable defects, which could be used to tune a sample [4, 5]. Further application would have been to introduce H decoration or substitutional atoms into the lattice, as they have been predicted to exhibit a magnetic moment and induce ferromagnetism in TMDs [6-8]. The low-energy of the ions mean this will be a very surface targeted process of introducing dopants [9]; ideal for STM studies, however care must be taken to not destroy the surface in the process of irradiation.

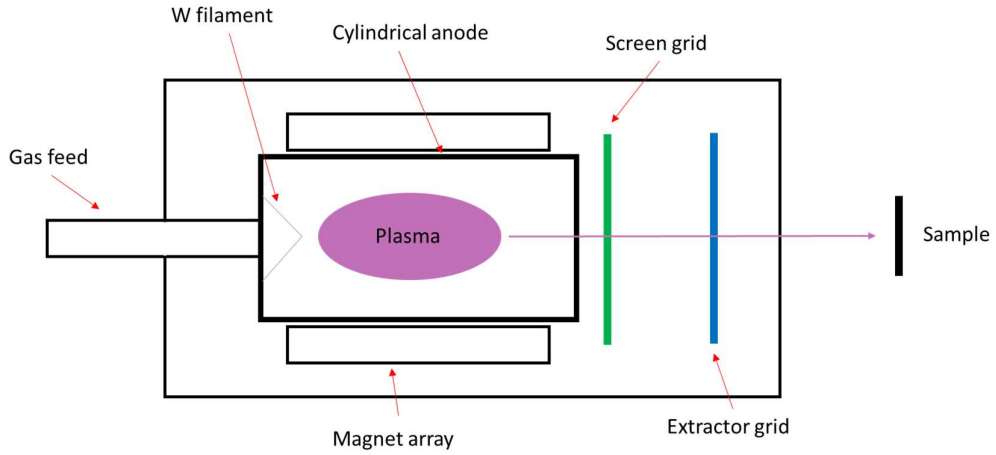

Figure 4-8. Simple diagram of the ion source showing the component and acceleration route of the ions from the plasma to the sample.

Unfortunately, the conductance of the vacuum pipes to the pump was not sufficient to reach the required flow rate before the pressure had increased too high. Calculations by the ion source manufacturers indicated that the line on which it was mounted was at the flow and pressure limit for its usage. Future work is planned to move it to another section which has enough flow conductance to reach the required flow rate.

Principle of operation

A schematic of the ion source is shown in figure 4-8. This low-energy ion source works by a filament driven electrical discharge method. The W filament (cathode) is suspended within a cylindrical anode, which makes up the discharge zone. A water-cooled magnet array surrounds this discharge zone. Applying a high voltage between the cathode and anode, whilst introducing the target gas through a gas feed at the rear, generates the plasma in the discharge zone. The magnets act to confine the plasma and increase its density. On the other side of the zone there are two grids, the screen (anode) and extractor (cathode). Applying a voltage between them generates an electric field, which extracts ions from the plasma and accelerates them down towards a ground potential and the sample plate. The energy of the ions can be determined by the voltage applied to the screen grid, with a range of ion energies between 10-200 eV available.

Implementation of a dedicated ultrahigh-vacuum line

The ion source was mounted onto the LT2 system and has its own vacuum line that can be isolated from the rest of the system via a gate valve. The line consists of the ion source

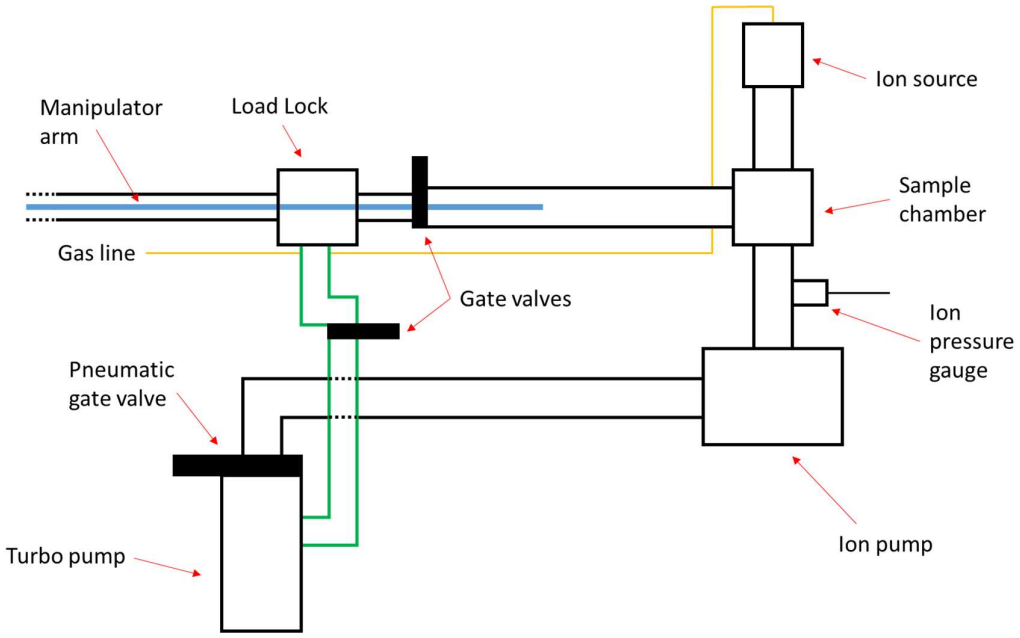

Figure 4-9. Schematic of the assembled ion source line. The manipulator arm (blue) allows samples to be moved between the load lock and sample chamber. The line highlighted in green is a bypass that allows the load lock to be pumped down to UHV. The gas line (yellow) is connected to a leak valve attached to the top of the ion source, and a mass flow meter at the other end.

chamber and a load lock separated by a gate valve. An ion pump is used to maintain vacuum in the line. A TMP is also connected to pump the load lock, and for when the ion source is in operation. Figure 4-9 shows a schematic of the ion source line, and figure 4-10 shows its position within the system. The manipulator arms allow for samples to be transferred between all sections of the system without having to be removed to atmospheric pressure. This means in-situ measurements can be performed on samples before and after irradiation without the risk of outside contaminants.

Application

Before starting the ion source, the water-cooling valve is opened to provide a minimum flow rate 0.5 L/min. The sample is inserted into the load lock, which is then sealed with a Cu gasket between the knife edges of the two flanges. The lower gate valve is then opened, and the TMP switched on. Once pumped for at least one hour (ideally longer) this gate valve is closed and the second, upper gate valve is opened, allowing the sample to be moved into the sample chamber via the manipulator arm. The large pneumatic gate valve is opened, and the ion pump switched off so that the TMP is pumping the whole system. This is to protect the ion pump from the species introduced by the ion source, which can damage it if still powered on. The target gas is then introduced to the ion source by opening the leak valve and

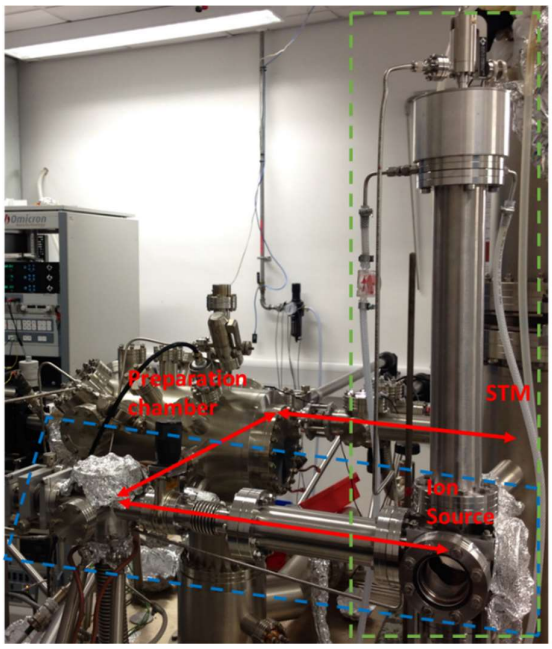

Figure 4-10. Photo of the low-energy ion source (green box) and its dedicated UHV line (blue box). The possible movement of samples in the system between the different instruments, is represented by the red arrows. Each section can be isolated with gate valves. This shows that is possible to perform in-situ STM measurements before and after bombarding a sample with ions.

using the flow meter to set a flow rate between 3-10 sccm. The ion source conditions are programmed, and it is switched on, igniting the plasma and beginning irradiation of the sample. Once finished, the leak valve is closed, and the pressure is allowed to recover. Once the pressure reaches below 5×10^{-1} mbar the large gate valve is closed, and the ion source turned back on. The sample is then moved back to the load lock, closing the upper gate valve behind it, from where it can be moved to another part of the system, or removed.

References

[1] Muller A D, Muller F, Hietschold M, Demming F, Jersch J and Dickmann K (1999) Characterization of electrochemically etched tungsten tips for scanning tunneling microscopy. *Review of Scientific Instruments.* **70** 3970-2

[2] Ernst S, Wirth S, Rams M, Dolocan V and Steglich F (2007) Tip preparation for usage in an ultra-low temperature UHV scanning tunneling microscope. *Science and Technology of Advanced Materials.* **8** 347-51

[3] Kaiser W J and Jaklevic R C (1986) Spectroscopy of electronic states of metals with a scanning tunneling microscope. *IBM Journal of Research and Development.* **30** 411-6

[4] Stanford M G, Pudasaini P R, Belianinov A, Cross N, Noh J H, Koehler M R, Mandrus D G, Duscher G, Rondinone A J, Ivanov I N, Ward T Z and Rack P D (2016) Focused helium-ion beam irradiation effects on electrical transport properties of few-layer WSe2: enabling nanoscale direct write homo-junctions. *Scientific Reports.* **6** 10

[5] Inoue A, Komori T and Shudo K-i (2013) Atomic-scale structures and electronic states of defects on Ar+-ion irradiated MoS2. *Journal of Electron Spectroscopy and Related Phenomena.* **189** 11-8

[6] Manchanda P, Enders A, Sellmyer D J and Skomski R (2016) Hydrogen-induced ferromagnetism in two-dimensional Pt dichalcogenides. *Physical Review B.* **94** 5

[7] Yang S, He J, Zhou P and Sun L Z (2017) Magnetic control of single transition metal doped MoS2 through H/F chemical decoration. *Journal of Magnetism and Magnetic Materials.* **422** 243-8

[8] He J G, Wu K C, Sa R J, Li Q H and Wei Y Q (2010) Magnetic properties of nonmetal atoms absorbed MoS2 monolayers. *Applied Physics Letters.* **96** 3

[9] Willke P, Amani J A, Sinterhauf A, Thakur S, Kotzott T, Druga T, Weikert S, Maiti K, Hofsass H and Wenderoth M (2015) Doping of graphene by low-energy ion beam implantation: structural, electronic, and transport properties. *Nano Letters.* **15** 5110-5

Chapter 5

Defects in a WSe_2 crystal

In crystals of WSe_2 and other TMDs, intrinsic defects are present from their formation which have been shown to influence their structural, electronic and optical properties. Whilst there has been progress in reducing or negating the effects of these defects [1, 2], another possibility is tailoring the material through defect engineering, to enhance or induce a property in the base material. For example, defects have been found to enhance the hydrogen evolution reaction [3, 4], provide a method for tuning the bandgap [5], and tune the optical response towards the visible region [6]. They can also tune the magnetic properties of the layer [7-9]

For control of these modifications to be realised, the defects must be characterised to understand the effect they will have. There are many predictions about the appearance of defects in STM images and they often contradict, making identification a nontrivial task [10-12]. In this section a variety of defects in a WSe_2 crystal are studied and an attempt is made to identify them. The local electronic modification of the LDOS due to the defects are also observed. The defects can also act as scattering centres for quasi-particles resulting in patterns in the LDOS. By exploiting this, we can probe the nature of the defect. This can reveal whether the defect carries a magnetic moment through the presence of spin-flipping scattering processes.

5.1. The clean WSe_2 surface

The first step taken was to understand how the clean WSe_2 surface appeared in STM. Measurements were taken on a crystal obtained from HQ Graphene at both room temperature and low-temperature using LN2. While less conductive than the Au standard, the surface could be scanned in the range ±3 V and with currents of up to 3 nA. However, most of the measurements were taken in the range of ±1.8 V due to the features of interest being closer to the bandgap edges.

The structure of the WSe_2 layer means that the atoms closest to the tip will be the Se atoms, with the W atoms in the layer below. Since the STM current decays exponentially with the tip-sample distance it is expected that the Se atoms contribute most to the tunnelling current and will appear brightest in the image. This is seen in figure 5-1(a) where the STM z-image shows a hexagonal pattern of bright spots corresponding to the top layer Se atoms. This

result is supported by a calculation by Altibelli for STM images on MoS_2 with the chalcogen atoms appearing with the greatest intensity for most tip-sample distances [13], and experimental observations of WSe_2 and $MoSe_2$ [14, 15]. Combining STM and non-contact atomic force microscopy (NC-AFM) has also shown that the bright spots in AFM which have been identified as the top layer Se atoms, correspond to the bright spots in the STM images [16]. On the other hand, the W atom orbitals contribute more to the DOS than the Se atoms, so as the tip-sample distance decreases the W atoms contribution to the tunnelling current also increases. This leads to a situation as in figure 5-1(b) where the W atoms DOS compensates for the height difference and they appear much brighter, leading to a ring of alternating intensity much closer in intensity than before. However, in the calculations the tunnelling current superposition of the channels from the Se atom and the 3 surrounding W atoms experiences destructive interference resulting in the Se atoms appearing dark for much closer tip-sample distances. This prediction was confirmed for both the conduction and valence bands, but also revealed another pattern like that in figure 5-1(b), showing that the STM image is not always clear and many variables affect the appearance [17]. This pattern has also been observed on a $MoSe_2$/BLG heterostructure where the assignment of atoms is the same at figure 5-1(b), yet the discussion mentions that at small tip-sample distances the contrast is governed by the metal and hollow sites [18]. Typically, very small tip-sample distances occur in constant current scans near to the CB and VB edges as the number of states decreases, and a change of contrast different to those in figures 5-1(a) and (b) was

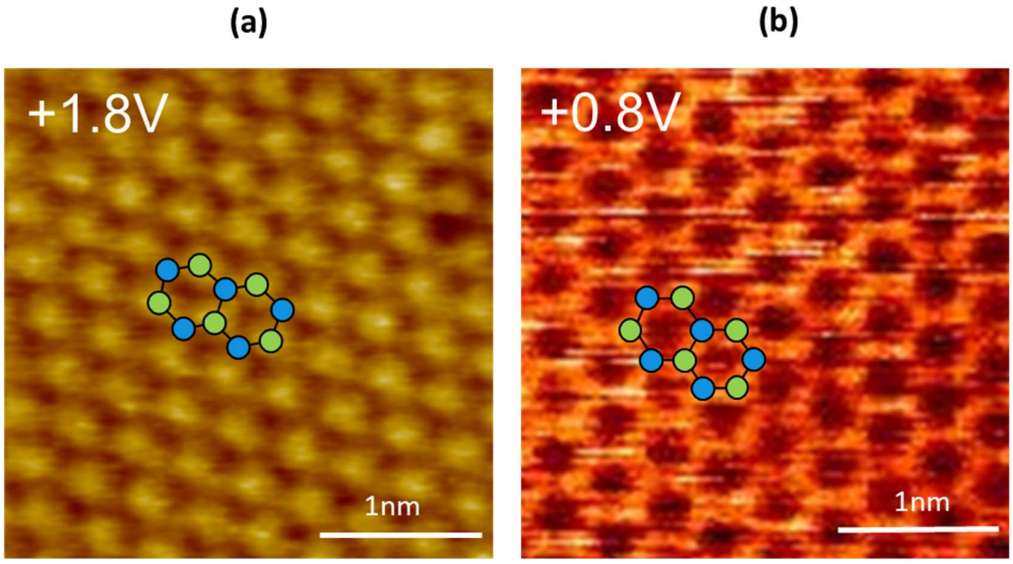

Figure 5-1. (a) STM image at +1.8 V of a clean area on the WSe_2 crystal surface showing a hexagonal pattern of bright spots. The expected positions of the W (blue) and Se (green) atoms are shown in the overlaid diagram. (b) STM image at +0.8 V, 0.28 nA where the tip is closer to the surface and the DOS compensates for the height difference and displays bright rings surrounding hollow sites. The expected structure is overlaid.

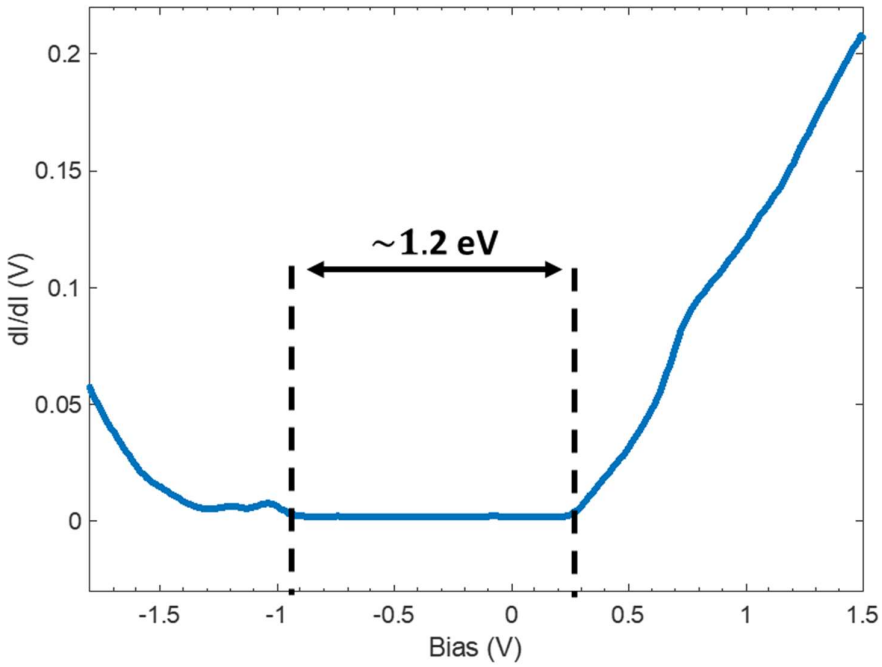

Figure 5-2. dI/dV spectroscopy of the bulk WSe_2 crystal taken from an area clear of defects.

observed. As it is very easy to crash the tip in such energy regions they were avoided in order to protect the tip.

A spectroscopy measurement of the crystal is displayed in figure 5-2. The bandgap is about 1.2 eV which agrees with the expected value of 1.2-1.3 eV. As discussed in section 2.3, the VBE in bulk is at the Γ point which can be seen as the rise in number of states below -0.95 eV. The CBE is located at the Q point at about 0.25 eV. The position of the Fermi level close to the CBE indicates that the crystal is naturally n-doped, which is probably caused during its growth through the incorporation of dopants and defects.

5.2. Defects: atomic scale characterisation

Across the surface of the WSe_2 a wide variation of intrinsic defects were observed in the STM images. They consisted of point defects occupying a single atomic site, or an extended defect, which affected a collection of adjacent sites. The distribution of defects appeared to be random with some scanned areas containing multiple defects of different types whilst others contained a single defect as shown in figure 5-3, which shows a selection of different defects across 3 different areas. The different intensity of the defects compared to the base surface reflects the effect they have on the structure and therefore the LDOS at the defect site and

the surrounding sites. The height of the defect with respect to the surrounding lattice can also affect its appearance, as a dip in the surface will appear as a dark hole barring any additional contributions from the LDOS. These two factors mean that defects will appear quite different depending on their type. However, the structure of the defect is not always obvious from the experimental images.

While most of the defects are located on the surface, some of them are sub-surface, which can put strain on the layers and affect the local electronic behaviour around the defect site. This results in areas of local depression or protrusion as seen from the area marked D in figure 5-3. These areas can be seen across the sample and the region they cover can vary in size. The depth of the defect under the surface can affect the intensity and spread of the

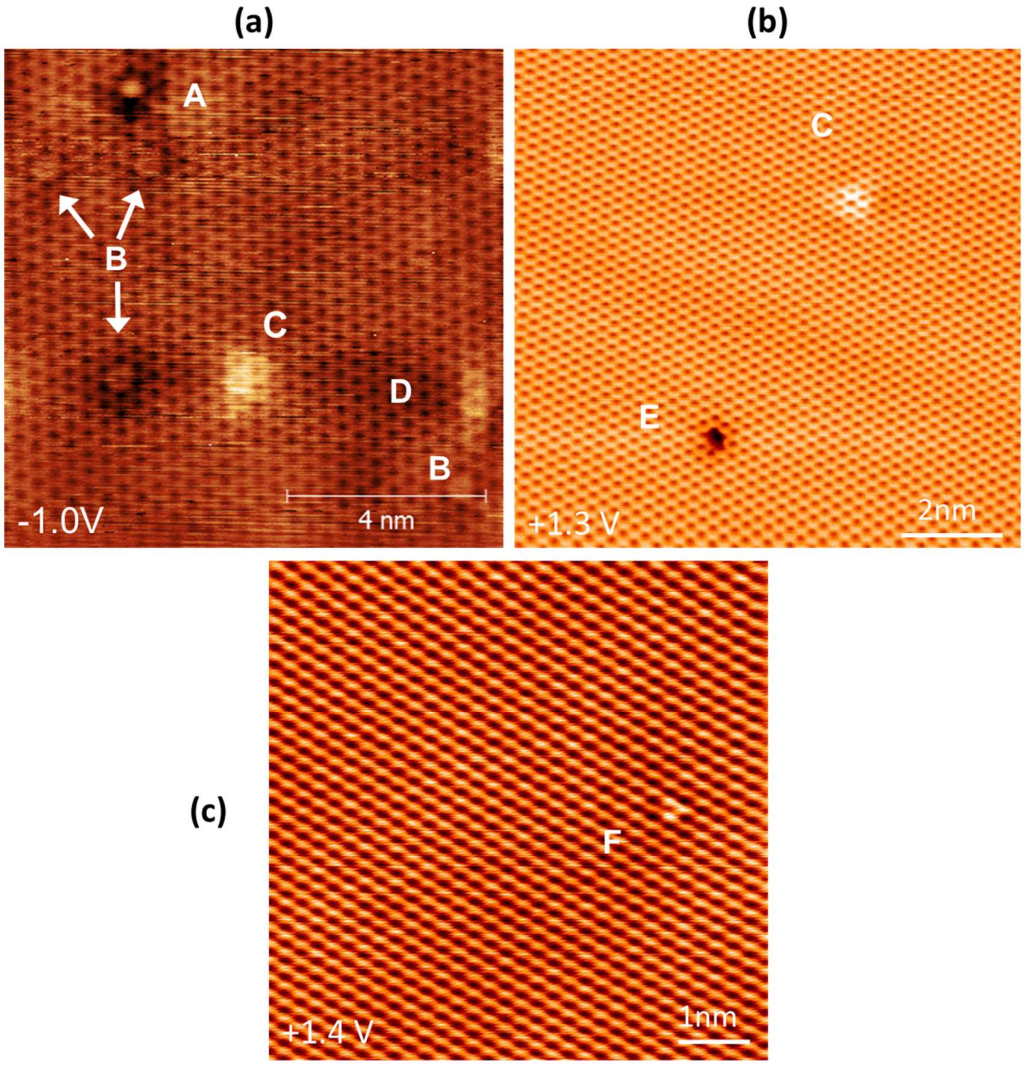

Figure 5-3. STM images taken from different regions at bias voltages (a) -1.0 V, 0.89 nA (b) +1.3 V, 0.76 nA, and (c) +1.4 V, 0.44 nA, showing a collection of defect types. The images were taken using different tips, both W and Pt-Ir.

LDOS modification, as seen for S vacancies buried in MoS_2 [19], however this defect type was not explored in sufficient detail for a conclusive description. Another observed defect, which is not strictly intrinsic to the material, is marked F in figure 5-3 and consists of a triangle of bright points located on Se atomic sites. This trimer defect has been previously seen on the surface of WSe_2 and was explained as a local breaking of bonds due to pulsing the tip above the surface [20]. The pulses to create such a defect must be small and just above the threshold of defect creation, otherwise much larger extended defects are usually formed [20, 21]. This is consistent with the experiment here as the tip was often gently cleaned with small pulses prior to scanning, which explains why these defects are observed on the surface.

The features marked B in figure 5-3 appear as a slightly brighter ring surrounding a hollow site, which implies that they cover 3 Se atom sites and 3 W atomic sites. The pattern does not appear to favour either the Se or W sites, spreading almost equally over both and is very local to these sites, without spilling out into the surrounding region. An interesting property of this defect is its bias dependence, which can be seen in figure 5-4. The STM images show the same region scanned at ±0.8 V, with the defect clearly seen as before at +0.8 V and then almost completely vanishing in the image at -0.8 V. The image from figure 5-3 was taken at -1.0 V where it is visible, showing that DOS of the defect change quite significantly over 0.2 eV energy range. A possible explanation for this is that the states induced by the defect are present at certain energies and not others. This could mean there are defect states located at -1.0 V and +0.8 V resulting in the bright ring, but not -0.8 V where it is not present. This means however that this defect does not appear to have made any clear surface structural change, which would be visible at energies without defect states. Another

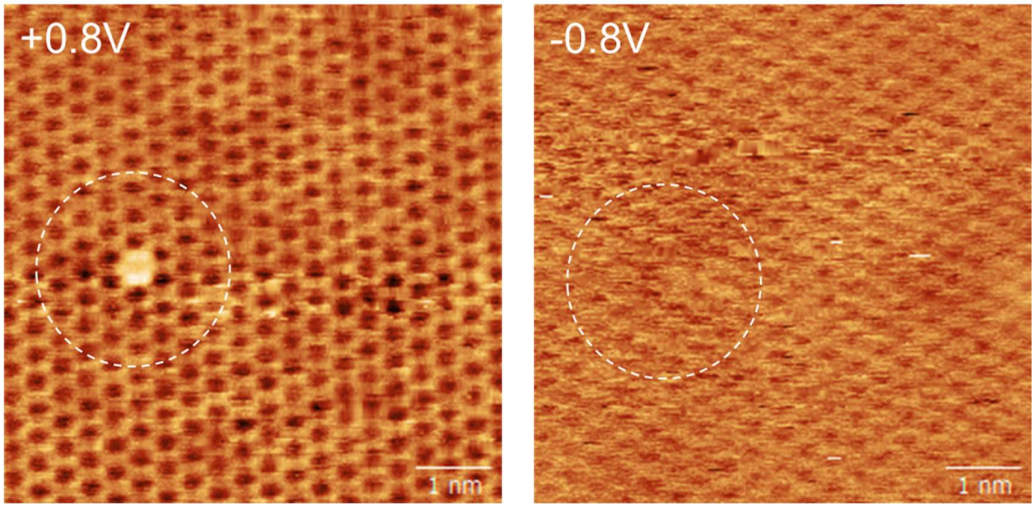

Figure 5-4. Images of the same defect taken at ±0.8 V showing as a localised bright spot in the conduction band, and almost vanishing in the valence band. Currents are 0.3 nA and 0.17 nA on the left and right respectively.

possibility is that the defect state acts to deplete the region instead, negating the topography of the defect and rendering the area featureless at energies of the state. This is perhaps a better conclusion as from the very local nature of the defect it is likely to be situated in the surface layer or just below, in which case the structure of the defect will contribute to the tunnelling current. As for the type of the defect it is difficult to tell from the STM images alone, as the structure is unclear.

Since the LDOS is a function of the energy and the $\mathrm{d}I/\mathrm{d}V$ is a function of bias voltage, spectroscopy can be used to investigate the electronic structure of the material. Single point spectroscopy was used to try and determine the states induced by defects as a tool to help determine their nature. Several simulations have predicted the existence of these states in the conduction and valence bands, as well as the bandgap, which could help to identify the defect based on their signature electronic modification. In figure 5-5(a) an STM image of a defect from the surface is shown which displays a depression or depletion covering 3 Se atomic sites. Across this defect a series of point spectroscopies were taken in the direction shown by the black arrow, and the resulting spectra are displayed in figure 5-5(b). The bottom 2 curves and the top curve show no variation from the base WSe_2 spectroscopy, but the other 4 show a clear modification to the states just within the valence band edge. The central purple curve was taken from the centre of the defect and displays a new state at

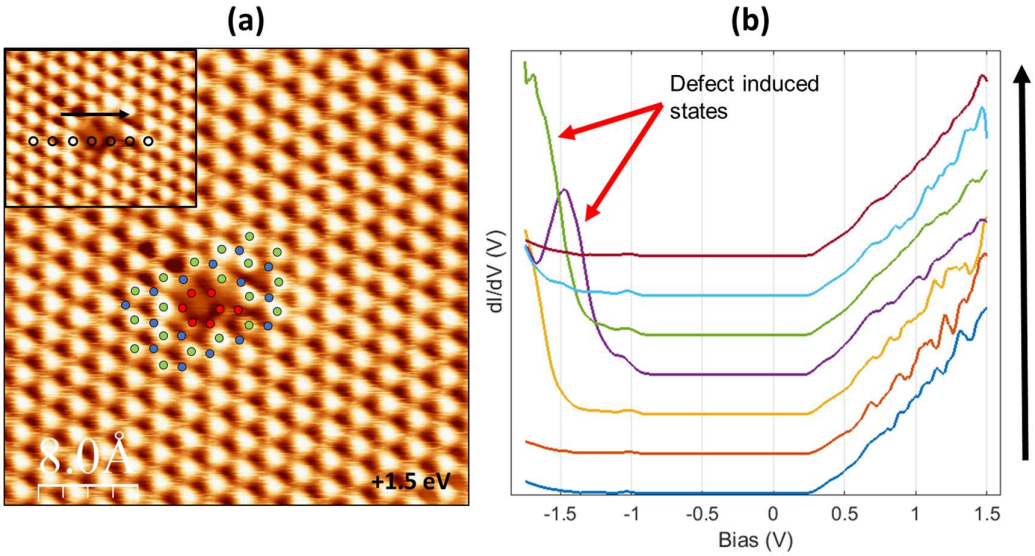

Figure 5-5. (a) STM image at +1.5 V, 2 nA of an extended defect displayed as a dark depression covering three Se sites and 4 metal sites, with the proposed sites affected marked in red. The W and Se sites are blue and green respectively. (b) A series of point spectroscopy measurements were taken from the points marked in the inset of (a) and the resulting curves are displayed. States in the valence band induced by the defect are shown for measurements at the edge and centre of the defect, with measurements taken just next to it not showing any perturbation, indicating the very local nature of the defect.

-1.5 V and what appears to be the beginning of another state further into the band. The green and yellow curves were taken at the edges of the defect and both reveal a strong state appearing, with its peak a little deeper into the valence band. These edge states are likely due to dangling bonds created from the removal or change of atoms at the defect [10]. For this defect the bandgap edges are unaffected and there are no states in the bandgap as many are predicted to have, making it difficult again to assign it a type. From the structure it looks like the removal of the 3 top-layer Se atoms; since the spectroscopy reveals little variation in the LDOS across the defect at +1.5 V, which is the bias of the STM image, purely electronic effects can be ruled out.

One of the most common defects observed on this sample is displayed in the STM images of figure 5-6(a)-(c). This type of defect shows as a triangular shaped dark depression centred on a Se atomic site, which is observable at all bias. The centre site is not completely dark as shown in figure 5-6(a) where it is still relatively bright, which is likely due to some tunnelling signal from the Se atom in the bottom layer as they are coincident. Those in figures 5-6(b)-(c) are more typically observed, and often show a faint surrounding star shaped arrangement of dark points. This pattern is due to LDOS changes from the defect rather than a structural effect. The position of the defect and its very local nature suggest it is a Se monovacancy with the proposed defect structure shown in figure 5-6(d). The position of the defect in the top layer rather than the bottom layer is because there is a high chance of it recombining with the removed Se atom or another interstitial atom if it was in the bottom layer. In contrast, surface Se atoms can more easily migrate away from the vacancy site or can be moved by the STM tip. The clear local nature of the defect is another indicator, with subsurface defects tending to extend over a larger area as mentioned previously.

This defect has been observed in several other cases of STM experiments on WSe_2 and similar TMDs, with the majority concluding that it is a Se (or S) vacancy, and noting its high occurrence [11, 22-24]. Given the low formation energy of the Se monovacancy the frequency of this defect is not surprising [7], and it is likely these defects were introduced into the crystal sample as it was mechanically exfoliated immediately prior to being placed into UHV. Simulations of this defect also generally agree with the experimental results, with most describing the defect as a depression of a single site with a slight contrast in the centre, which is exactly as observed here [11, 25, 26]. An STM study on $PtSe_2$ imaged the S monovacancy as a dark depression like others, while their calculations indicated a brighter hexagonal halo on neighbouring sites [27]. This indicates the electron trap states formed inside the bandgap.

The dark star shape pattern surrounding the defect in figure 5-6(c) has been seen by other groups which they assigned instead as a Se or S vacancy filled with an O substitution atom [12, 28, 29]. In these cases, annealing at 600°C was used to create chalcogen vacancies which were observed alongside the O substitutional defects, and identified as a dark depression

with 3 bright lobes surrounding. The O impurities are usually introduced during the growth processes due to the reactants, but they could also be introduced during the exfoliation and transfer procedure and migrate to the vacancy sites during annealing [29]. Two of the groups also used NC-AFM to compare defects and their position in the top or bottom layers, revealing slightly different STM appearances between them. The defects in this sample from figures 5-6(b) and 5-6(c) are closer in appearance to those observed in the top layer. STS measurements were taken too and while the chalcogen vacancies show in-gap defect states consistent with their calculations, the O substitutional defects showed no gap states at all, which matches with spectroscopy taken from the defects on our sample.

Since the defect is originally a Se vacancy, it is possible that the LDOS they observed in the surrounding dark star pattern has little contribution from the O substitutional atom and

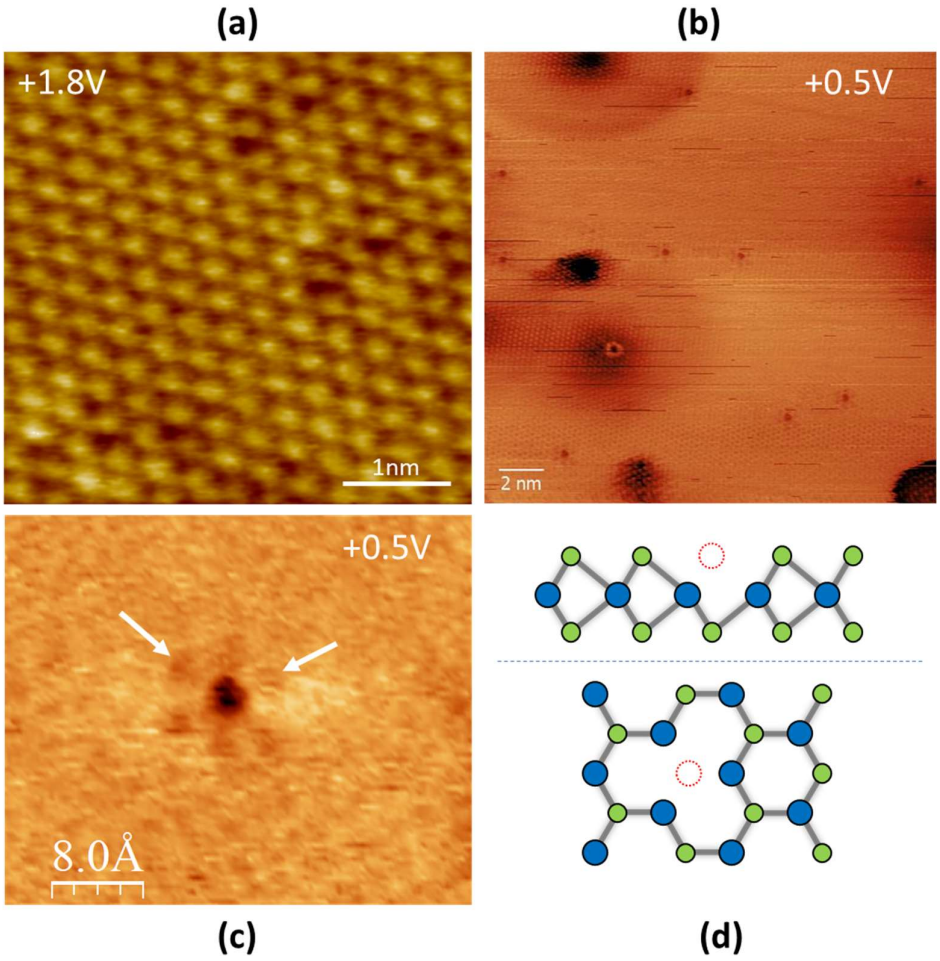

Figure 5-6. (a) STM image at +1.8 V showing a collection of point defects centred on Se atomic sites. The defect appears as a dark depression with some contrast remaining in the centre. (b) STM image at +0.5 V, 0.26 nA showing the same defect type. (c) Zoomed image of (b) with the atomic lattice filtered out. The defect now appears darker in the centre with a surrounding pattern of 6 dark spots arranged in a star pattern, examples marked by white arrows. (d) Proposed structure for this defect type as a Se monovacancy.

reflects mostly the vacancy; hence why this pattern is also observed in both cases, however, a full range of bias measurements would be needed to confirm this. Overall the evidence points towards this as an O substitutional atom in a Se monovacancy site, however as always with STM images it is difficult to identify simply from its appearance and there are many inconsistencies in the literature of this defect contrast. The local STS does support it, however the overall n-doping of the crystal is consistent with chalcogen vacancies [19].

Another defect observed was the bright triangular defect displayed in figure 5-7(a)-(b). These two images were taken at 2 different bias voltages above and below the bandgap, and both show a bright triangle of 3 Se atomic sites with the intensity extending onto the neighbouring Se sites. The dark streaks at the top right of the defect in figure 5-7(a) are a tip effect and unrelated to the defect features. The inset in 5-7(a) shows another area of the sample with multiple defects of this type, indicating that this is another defect with a high density observed on this crystal sample. Many defects have been observed to have a triangular shape, due to the symmetry of the lattice so clarifying the type is not simple.

On MoS_2 this defect has been found consistent with either the S divacancy or S interstitial models [24]. The divacancy defect was considered due to a simulation that predicted these defects appear as a bright triangular protrusion in STM images [10]. However, a V_{S2} would be centred on the Se atomic site whereas here the centre of the defect must be either above a W atomic site or a hollow site due to the 3 surrounding bright points in figure 5-7(a) clearly being situated on Se sites. Therefore, it is unlikely this is due to a Se divacancy. The other defect considered is the interstitial atom, which has been assigned to a S atom as in the above reference, or a metal atom as in the case observed in $TiSe_2$ [30]. For the $TiSe_2$ the defect was very bias dependent and almost completely vanished at positive bias, showing its electron donor character, and was only expected to occur in metal self-doped samples where there is an excess of metal atoms during growth. The metal atom interstitial in other TMDs is also expected to have a high formation energy and have an extremely low concentration at thermodynamic equilibrium which means the metal interstitial is unlikely to be the cause of this defect [31]. Other interstitial atoms such as chalcogen atoms and impurities such as O have lower formation energy and are predicted to have a higher concentration. A similar triangular defect has been assigned to the O interstitial in WSe_2, for the case where the monolayer was CVD grown. The position of this interstitial in the monolayer is usually put on top of a Se site, however since this is a bulk crystal its configuration is expected to be different as it now lies in the Van der Waals interlayer gap [31]. It could now be placed in the hollow site or below a W atom, but calculations have shown for MoS_2 that the hollow site has a higher formation energy for S interstitials [7]. This leaves the W atomic site as the most viable position as the proposed structure shows in figure 5-7(c). Another possible defect this could be from its position is a substitution of a W atom by one or two Se atoms, however calculations of these have shown they are expected to have contrast changes with bias [10].

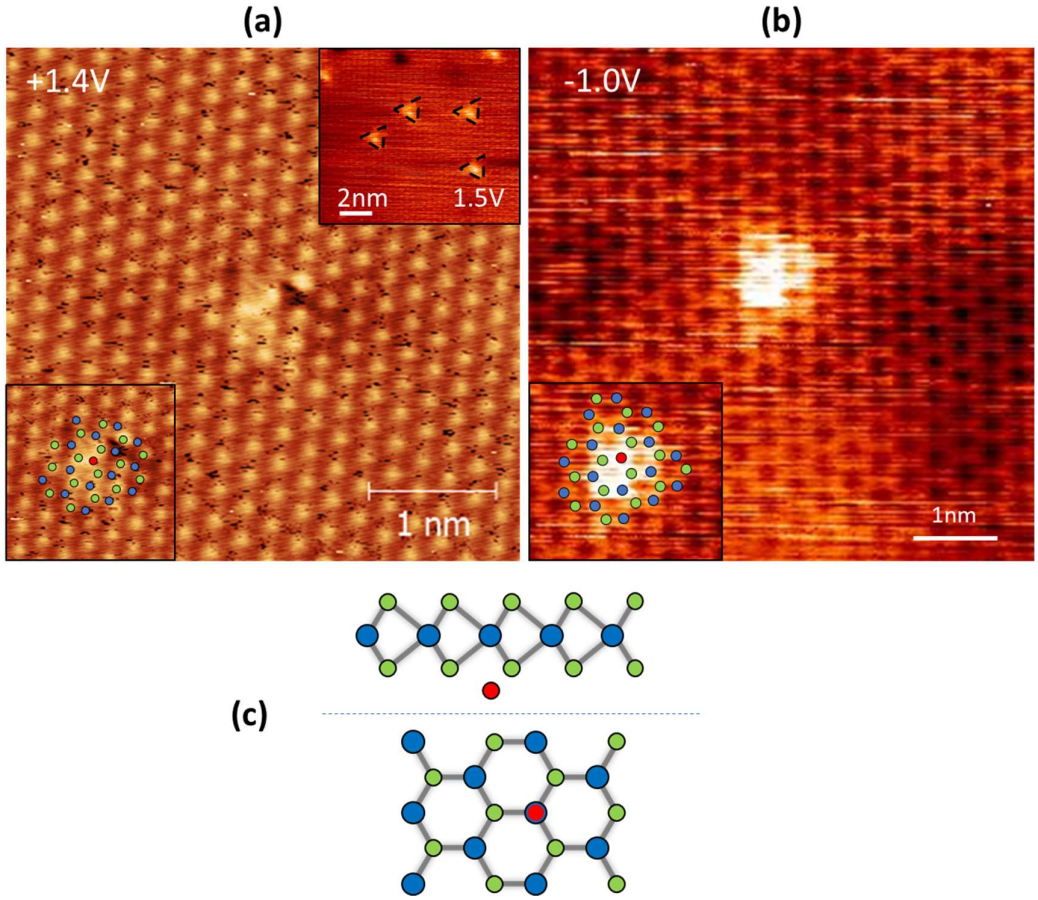

Figure 5-7. (a) STM image at +1.1 V, 0.21 nA showing triangular shaped defect with bright spots across three Se atoms and the centre. Top right inset showing another area with multiple of this defect type. Bottom left inset showing the expected atomic positions of W (blue) and Se (green), and a Se or O interstitial atom (red). (b) STM image at a different bias of -1.0 V, 0.89 nA showing this defect appearing as a bright triangle extending over a slightly larger area. The proposed atomic positions are shown in the inset. (c) Proposed structure of the defect as a Se or O interstitial atom.

5.3. Quasi-partial interference (QPI) from defects

The patterns observed from these defects, especially in $\mathrm{d}I/\mathrm{d}V$ images can be used to investigate the scattering properties of the defect. As mentioned in section 3.2.4 FT-STS can be used to identify the processes by which the electrons or holes scatter by, thus revealing information about the local electronic properties. In the case of individual defects, this information can potentially be used to identify whether spin-flip processes occur, through which the quasi-particles scatter between two valleys with opposite spin. This is predicted to only be possible for defects which hold a magnetic moment [32, 33].

Most point defects such as the Se vacancy are not expected to have a magnetic moment and so their QPI patterns should reflect this [34, 35]. Other types of point defect can be seen marked A and F in figures 5-8(a) and (b) which due to their similar pattern and location are expected to be a vacancy or substitution atom in lower layer. The position of the defect marked F appears to be centred on a W site. Around the defects the local electronic perturbation is already seen in the z image, and this pattern can be seen clearly in the $\mathrm{d}I/\mathrm{d}V$ image in figure 5-8(c) which represents the LDOS without the topography. This pattern appears like a star and extends over the neighbouring sites whilst remaining very local. The energy at which the $\mathrm{d}I/\mathrm{d}V$ image was taken is near to the conduction band edge, so the $\mathrm{Q}$and K valleys are the only bands expected to contribute to the scattering.

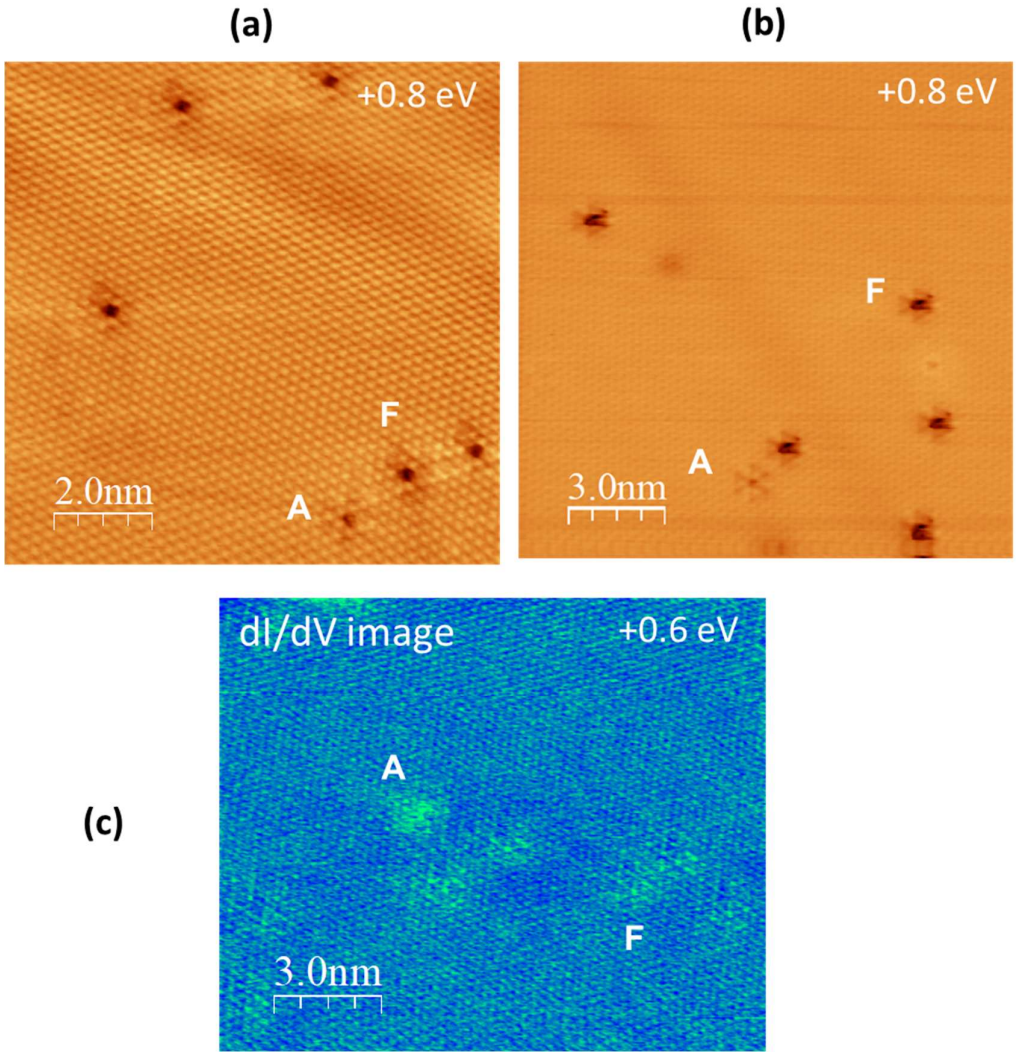

Figure 5-8. (a) STM image at +0.8 V, 0.01 nA showing Se monovacancies marked A and another type of point defect marked F, which is centred on a W site. (b) STM image at +0.8V, 0.41 nA showing the same defects imaged with different current conditions. (c) dI/dV map at +0.6 V, 0.41 nA showing the two defects A and F from (a) in a different region. The star shaped pattern around defect F is visible.

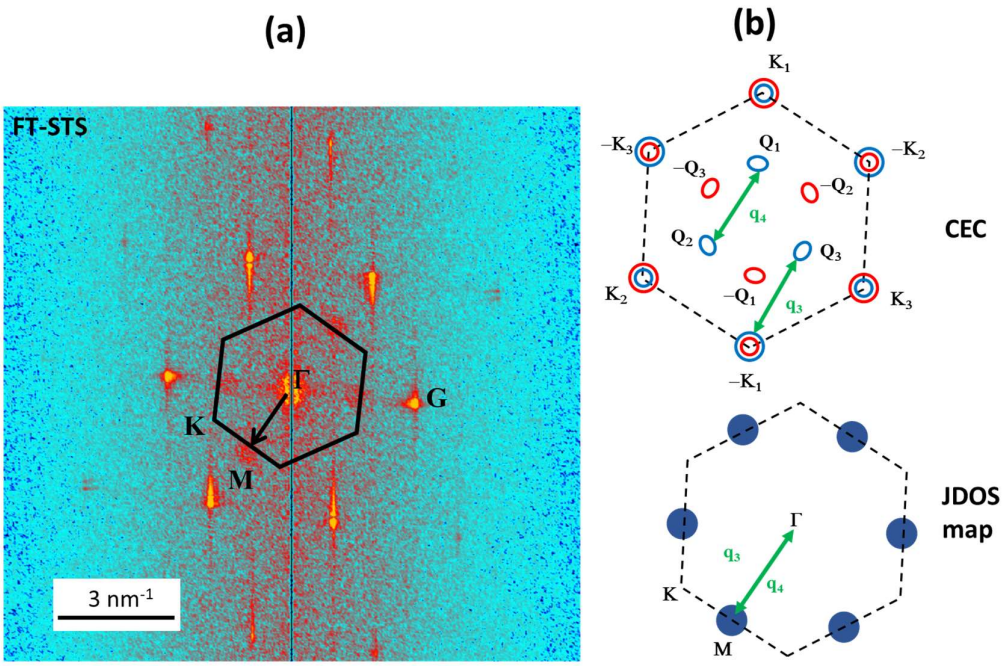

Figure 5-9. (a) FT-STS from the dI/dV in figure 5-8(c). The 6 bright outer points are the reciprocal lattice points, and the points at the M point of the Brillouin zone are due to scattering at the defect. (b) Schematic drawings of the CEC and JDOS maps just above the conduction band edge. The CEC shows potential spin-conserving scattering processes labelled q_3 and q_4, which are then marked on the JDOS map by the same green arrow. These scattering vectors result in a feature at the M point.

Taking a FT of the dI/dV image in figure 5-8(c) results in the FT map shown in figure 5-9(a). The 6 bright points arranged in a hexagon and marked G are the reciprocal lattice vectors due to the Se-Se lattice spacing of 3.28 Å of the surface. Points further out that these that are seen in this map are second order vectors. The Brillouin zone (BZ) is marked by the black hexagon, with the critical points marked. At the edges of the BZ at the M points another set of points are seen, which are the result of scattering processes and are not seen from defect free regions. By taking the vector length and direction and comparing to the CEC expected at this energy level, shown by the CEC schematic in figure 5-9(b), the possible scattering channels can be identified using the JDOS method described in 3.2.4. The resulting q scattering vector for two processes either between two Q valleys of the same spin labelled q_4 , or a Q valley and a K Valley with the same spin labelled q_3, give points in the JDOS map along the Γ - M direction. Whilst both processes are possible, it is more likely to be predominately the q_4 process, as the reduced sensitivity to the K valleys means a reduced tunnelling probability of processes involving them, and at the same energy tunnelling from the Q bands will dominate [33, 36]. This is also likely a factor in why other scattering processes involving the same spin valleys are not observed, as well as the fact that most of these channels will have a larger q and therefore are dominated by smaller q processes. This pattern is typical of most of the point defects observed across this sample.

Spin-flip scattering process in magnetic defects

One type of defect exhibited different properties in its QPI pattern compared to the defect seen previously. An STM image of the defect is displayed in figure 5-10(a), showing a bright triangular shaped protrusion centred on a dark depression. This image has been drift corrected post-scan and overlaid with a transparent image of the atomic lattice, which was obtained by taking the FT of the image and filtering out everything but the reciprocal lattice vectors. This allows for greater clarity in identifying atomic positions, and the location of the W atoms in the second layer are seen as the middle contrast site and the Se as the bright protrusions as before. Using this, the dark centre of the defect can be assigned to a W site and the surrounding three Se sites as marked by the red sites, with the bright triangle pattern located on next nearest Se atoms. There is also a local depression surrounding the defect.

The proposed site of this defect suggests it could be a W vacancy, which have a high formation energy and are not expected to have a very high concentration [31]. This would fit with the low number of these defects observed, however, they are also expected have a low stability due to the tendency of the surrounding chalcogen atoms to subsequently form vacancies around metal vacancies and form a defect complex of V_{WSe3} [5]. The W vacancy has also been proposed to be the most common type of defect in WSe_2 rather than the Se

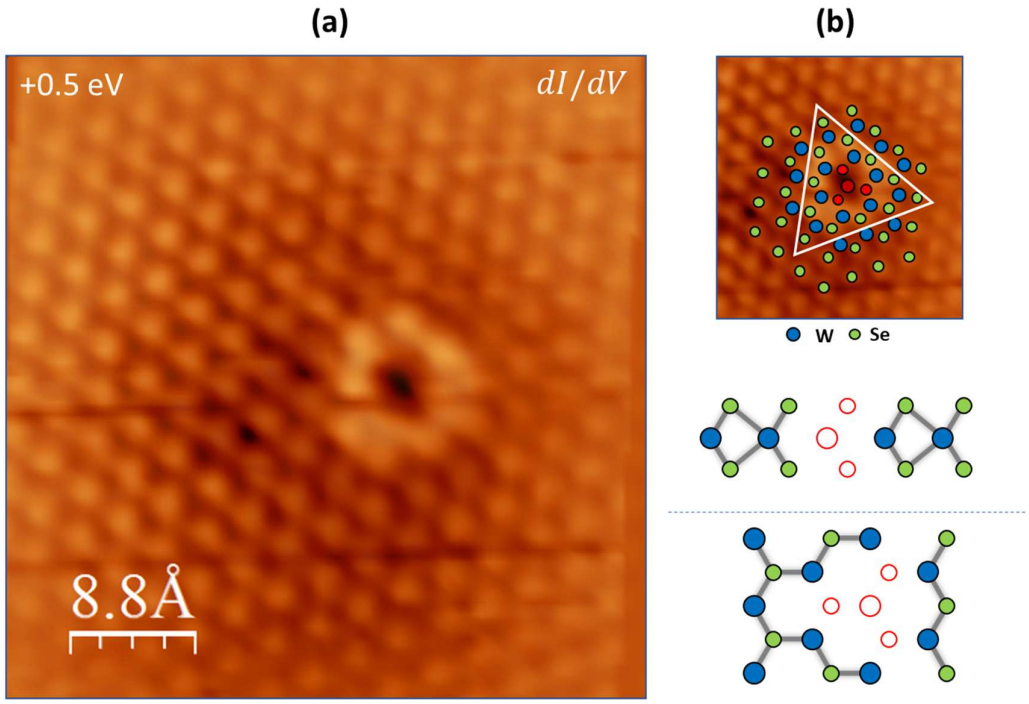

Figure 5-10. (a) STM image at +0.5 V, 0.26 nA of a defect centred on the W atomic site. (b) Proposed structure of the defect as a full column vacancy of 6 Se atoms and the W atom. The atomic positions of W (blue) and Se (green) are marked, and the red circles represent W and Se vacancies. The white triangle marks the bright triangular feature observed surrounding the centre.

monovacancy, appearing simply as a dark depression with the surrounding Se atoms appearing lower and a trigonal spatial distribution in the LDOS, whilst at other bias voltages having a surrounding bright triangle pattern [14]. Whilst the high concentration they observed does not match with this sample, the defect appearance is very similar.

Other possibilities are the defect complexes of a W vacancy and the top 3 Se atoms V_{WSe3}, or a W vacancy and all 6 of the bonded Se atoms in both layers V_{WSe6}, as represented in figure 5-11(a). Again, both have very high formation energies, but it would have been possible to form them from the mechanical exfoliation of the surface or during the annealing before scanning. Being such large vacancies, the structure of the surface is certainly affected meaning that the dark depression is almost certainly a topographic effect in figure 5-10(a) assuming this defect type. The surrounding bright ring could be due to a combination of

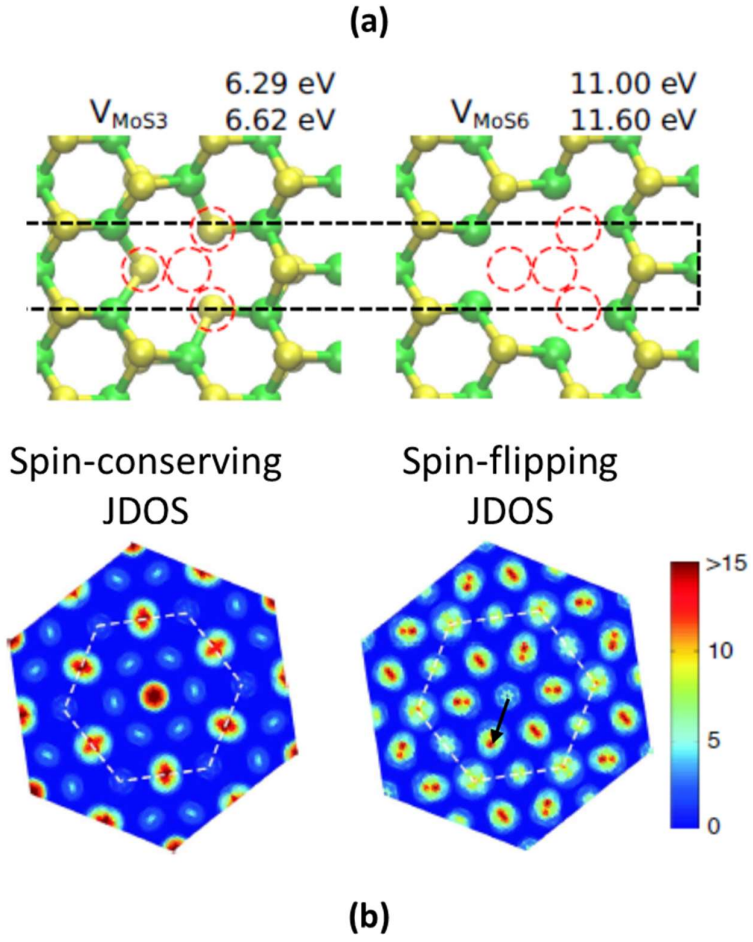

Figure 5-11. (a) Optimised geometric structures of the defect complexes V_{MoS3} and V_{MoS6}, indicating their formation energies for the monolayer (top) and bulk (bottom) in the neutral state (b) JDOS maps calculated at the bottom of the CB for both spin-conserving and spin-flipping scattering processes. The proposed spin-flip process is marked by the arrow. [7, 33]

dangling bonds or a renormalisation of the bonding and structure that could lift the edges around the defect. The different appearance of these two complexes in STM is unknown as they have not been reported so far, however considering the appearance of the Se vacancies it is very likely the bottom layer Se atoms in the V_{WSe3} complex will contribute to the tunnelling current giving this a less pit like appearance. This leans the type towards the V_{WSe6} with the proposed structure for it displayed in figure 5-10(b). However, again it is difficult to identify it purely from the STM image appearance.

A $\mathrm{d}I/\mathrm{d}V$ image of the defect shown in figure 5-10(a) is displayed in 5-12(a), with the defect appearing as a larger depression with a bright centre and a surrounding star pattern. Around this type of defect, a bright ring was observed covering a large area with a radius of about 2.6 nm under these tunnelling conditions. This could be trapped charge or another phenomenon, but so far, no further investigation of this feature has been done. The FT-STS

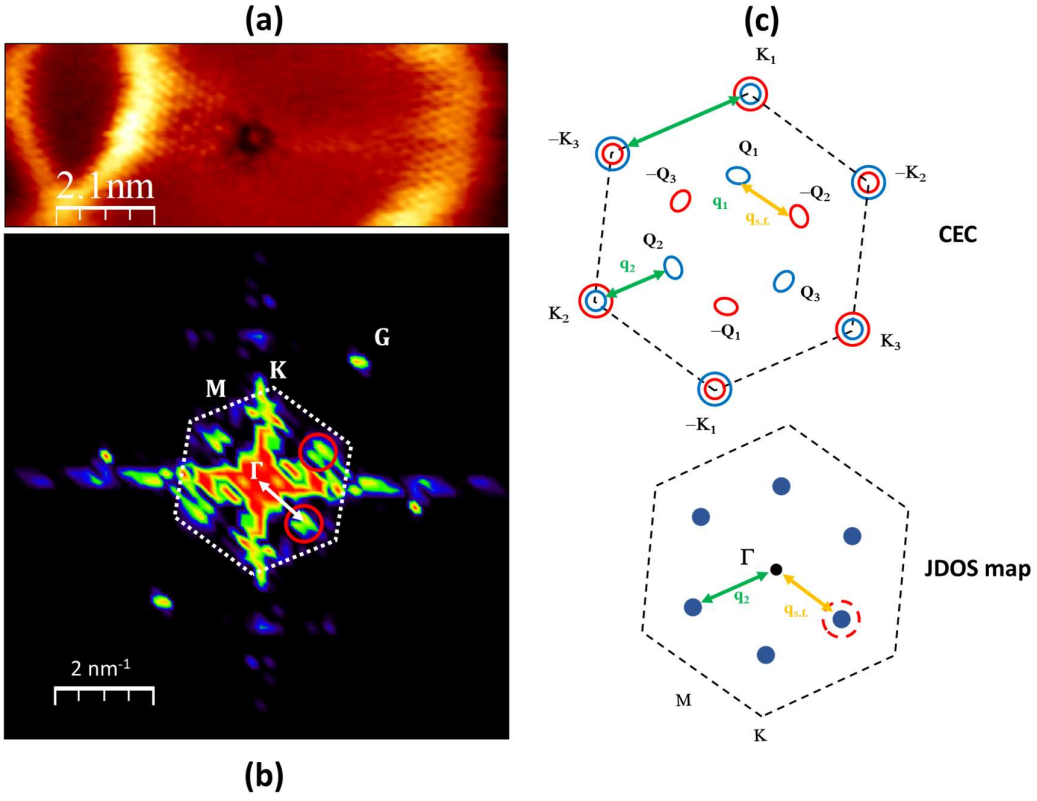

Figure 5-12 (a) dI/dV image at +0.5 V, 0.26 nA of the defect shown in figure 5-9(a). The defect appears as a dark depression with a bright centre spot and is surrounded by a bright ring with radius of about 2.6 nm at this energy. (b) FT-STS of the defect in (a). The reciprocal lattice points are marked G. 6 features are observed along the Γ-K directions just inside the K points, as marked by the example red circles. (c) CEC and JDOS maps showing the spin-conserving processes q_1 and q_2 in green and a possible spin-flip process $q_{s.f.}$ in yellow. The q_2 and $q_{s.f.}$ scattering processes give a feature between Γ and K, as indicated by the white arrow in (b).

derived QPI is shown in figure 5-12(b) revealing a different pattern to that of the point defect shown in figure 5-9(a). There are 6 points located along the Γ-K direction, about 3/5 of the way to the K point. Figure 5-11(b) shows the JDOS maps calculated for both spin-conserving and spin-flipping scattering processes for defects in WSe_2, for a similar experiment [33]. In their case only defects with the spin-conserving routes were observed. The JDOS maps match well with our results, showing that the most intense features starting at the Q point and spreading towards K along the Γ-K direction correspond to *processes involving spin-flip*. These features are marked by the arrow. Previously points were seen just beyond the M points however they are not observed here, even though some intensity is predicted. The large intensity spot at the centre is caused by noise in the dI/dV map, therefore, limiting the ability to observe any intravalley scattering contours in this case. The vertical and horizonal lines are due to systematic noise in the image and are observed from all areas independent of the defect.

This image was taken at +0.5 V which puts it about 0.2 eV above the CBE. This means that the CEC will include one Q valley and two K valleys, as the spin-splitting of the Q bands in the CB is just above 200 meV [32]. A schematic of the CEC is seen in figure 5-12(c) showing 3 possible scattering processes based on the direction of the features observed. The direction of these points is important as it means the scattering processes can now include the spin-flip scattering process marked as $q_{s.f.}$ and the yellow arrow in figure 5-12(c). Other scattering processes with similar length and direction could be between the Q and K valleys with same spin marked q_2 in figure 5-12(c) or even with opposite spin, however this would face the same problem with the measurements being more sensitive to picking up Q ↔ Q processes than those involving K valleys [33]. The process marked q_1 between two K valleys is another along this direction, but with a longer vector, which will be located at the K point itself. This type of process has only been observed for some energies from non-magnetic defects and is very weak when it does appear [33]. However, the QPI pattern reveals no features at the K points meaning this process can be disregarded. Comparing the features here with the two JDOS maps in figure 5-11(b), point towards this *process existing on the spin-flipping map* due to its position. There is a weak intensity on the spin-conserving map however the complete lack of feature at the M point which should be far more intense, shows this spin-conserving process is not occurring. For a metal centred defect that is not magnetic, this would be very unusual due to the selection rules in section 3.2.4.; therefore, this absence is likely due to the smaller q scattering vector of the spin-flip process between two adjacent Q valleys (or Q ↔ K) dominating the QPI pattern.

The evidence from the FT-STS derived QPI pattern points towards this being a *defect with a magnetic moment* which enables the spin-flip processes to occur as described in section 3.2.4. From the types of defects that match the topographic appearance, only the V_{WSe6} defect is predicted to be magnetic with a moment of 6 μ_B [7, 34], making it very likely that it is this type of defect.

5.4. Conclusions

The WSe_2 crystal surface revealed a host of different intrinsic defects of varying type and size. From these two of the most common point defects were examined and identified. These were the top layer Se monovacancy and the interstitial atoms situated below the metal atom site. The interstitial species could be either Se or O, with further work involving alternate methods required to narrow this down.

The QPI patterns due to electron screening around the defects allowed us to probe their nature. From a common metal site centred defect, FT-STS derived QPI patterns indicated characteristic features associated with spin-conserving scattering processes, which is expected for non-magnetic defects. A larger defect complex was also observed with the structural appearance suggesting a local column defect involving all three layers of the WSe_2 sandwich; this defect type has been predicted to exhibit a magnetic moment. This was confirmed by the scattering processes present in the FT-STS, which now strongly suggest a spin-flip channel is allowed.

References

[1] Shu H B, Li Y H, Niu X H and Wang J L (2016) Greatly enhanced optical absorption of a defective MoS2 monolayer through oxygen passivation. *ACS Applied Materials & Interfaces.* **8** 13150-6

[2] Shearer M J, Li W J, Foster J G, Stolt M J, Hamers R J and Jin S (2019) Removing defects in WSe2 via surface oxidation and etching to improve solar conversion performance. *ACS Energy Letters.* **4** 102-9

[3] Chen Y, Huang S X, Ji X, Adepalli K, Yin K D, Ling X, Wang X W, Xue J M, Dresselhaus M, Kong J and Yildiz B (2018) Tuning electronic structure of single layer MoS2 through defect and interface engineering. *ACS Nano* **12** 2569-79

[4] Tao L, Duan X, Wang C, Duan X and Wang S (2015) Plasma-engineered MoS2 thin-film as an efficient electrocatalyst for hydrogen evolution reaction. *Chemical Communications.* **51** 7470-3

[5] Zhou W, Zou X L, Najmaei S, Liu Z, Shi Y M, Kong J, Lou J, Ajayan P M, Yakobson B I and Idrobo J C (2013) Intrinsic structural defects in monolayer molybdenum disulfide. *Nano Letters.* **13** 2615-22

[6] Iberi V, Liang L B, Ievlev A V, Stanford M G, Lin M W, Li X F, Mahjouri-Samani M, Jesse S, Sumpter B G, Kalinin S V, Joy D C, Xiao K, Belianinov A and Ovchinnikova O S (2016) Nanoforging single layer MoSe2 through defect engineering with focused helium ion beams. *Scientific Reports.* **6** 9

[7] Komsa H P and Krasheninnikov A V (2015) Native defects in bulk and monolayer MoS2 from first principles. *Physical Review B.* **91** 17

[8] Han S W, Hwang Y H, Kim S H, Yun W S, Lee J D, Park M G, Ryu S, Park J S, Yoo D H, Yoon S P, Hong S C, Kim K S and Park Y S (2013) Controlling ferromagnetic easy axis in a layered MoS2 single crystal. *Physical Review Letters.* **110** 5

[9] Mao X Z, Xu Y, Xue Q X, Wang W X and Gao D Q (2013) Ferromagnetism in exfoliated tungsten disulfide nanosheets. *Nanoscale Research Letters.* **8**

[10] Gonzalez C, Biel B and Dappe Y J (2016) Theoretical characterisation of point defects on a MoS2 monolayer by scanning tunnelling microscopy. *Nanotechnology.* **27** 12

[11] K C S, Longo R C, Addou R, Wallace R M and Cho K (2014) Impact of intrinsic atomic defects on the electronic structure of MoS2 monolayers. *Nanotechnology.* **25** 375703

[12] Zheng Y J, Chen Y F, Huang Y L, Gogoi P K, Li M Y, Li L J, Trevisanutto P E, Wang Q X, Pennycook S J, Wee A T S and Quek S Y (2019) Point defects and localized excitons in 2D WSe2. *ACS Nano.* **13** 6050-9

[13] Altibelli A, Joachim C and Sautet P (1996) Interpretation of STM images: The MoS2 surface. *Surface Science.* **367** 209-20

[14] Zhang S, Wang C G, Li M Y, Huang D, Li L J, Ji W and Wu S W (2017) Defect structure of localized excitons in a WSe2 monolayer. *Physical Review Letters.* **119** 6

[15] Wang Y, Zhang S, Huang D, Cheng J X, Li Y G and Wu S W (2017) Screening effect of graphite and bilayer graphene on excitons in MoSe2 monolayer. *2D Materials.* **4** 6

[16] Barja S, Wickenburg S, Liu Z F, Zhang Y, Ryu H J, Ugeda M M, Hussain Z, Shen Z X, Mo S K, Wong E, Salmeron M B, Wang F, Crommie M F, Ogletree D F, Neaton J B and Weber-Bargioni A (2016) Charge density wave order in 1D mirror twin boundaries of single-layer MoSe2. *Nature Physics.* **12** 751-6

[17] Perrot E, Humbert A, Piednoir A, Chapon C and Henry C R (2000) STM and TEM studies of a model catalyst: Pd/MoS2(0001). *Surface Science.* **445** 407-19

[18] Ugeda M M, Bradley A J, Shi S F, da Jornada F H, Zhang Y, Qiu D Y, Ruan W, Mo S K, Hussain Z, Shen Z X, Wang F, Louie S G and Crommie M F (2014) Giant bandgap

renormalization and excitonic effects in a monolayer transition metal dichalcogenide semiconductor. *Nature Materials.* **13** 1091-5

[19] Lu C P, Li G, Mao J, Wang L M and Andrei E Y (2014) Bandgap, mid-gap states, and gating effects in MoS2. *Nano Letters.* **14** 4628-33

[20] Fuchs H, Schimmel T, Luxsteiner M and Bucher E (1992) Investigating atomic-scale structures generated with the STM. *Ultramicroscopy.* **42** 1295-302

[21] Park J B, Jaeckel B and Parkinson B A (2006) Fabrication and investigation of nanostructures on transition metal dichalcogenide surfaces using a scanning tunneling microscope. *Langmuir.* **22** 5334-40

[22] Whangbo M H, Ren J, Magonov S N, Bengel H, Parkinson B A and Suna A (1995) On the correlation between the scanning-tunneling-microscopy image imperfections and point-defects of layered chalcogenides 2H-MX(2) (M=MO, W X=S, SE). *Surface Science.* **326** 311-26

[23] Addou R and Wallace R M (2016) Surface analysis of WSe2 crystals: spatial and electronic variability. *ACS Applied Materials & Interfaces.* **8** 26400-6

[24] Liu X, Balla I, Bergeron H and Hersam M C (2016) Point defects and grain boundaries in rotationally commensurate MoS2 on epitaxial graphene. *The Journal of Physical Chemistry C.* **120** 20798-805

[25] Caulfield J C and Fisher A J (1997) Electronic structure and scanning tunnelling microscope images of missing-atom defects on MoS2 and MoTe2 surfaces. *Journal of Physics: Condensed Matter.* **9** 3671-86

[26] Akdim B, Pachter R and Mou S (2016) Theoretical analysis of the combined effects of sulfur vacancies and analyte adsorption on the electronic properties of single-layer MoS2. *Nanotechnology.* **27**

[27] Zheng H S, Choi Y, Baniasadi F, Hu D K, Jiao L Y, Park K and Tao C G (2019) Visualization of point defects in ultrathin layered 1T-PtSe2. *2D Materials.* **6** 9

[28] Schuler B, Qiu D Y, Refaely-Abramson S, Kastl C, Chen C T, Barja S, Koch R J, Ogletree D F, Aloni S, Schwartzberg A M, Neaton J B, Louie S G and Weber-Bargioni A (2019) Large spin-orbit splitting of deep in-gap defect states of engineered sulfur vacancies in monolayer WS2. *Physical Review Letters.* **123** 7

[29] Barja S, Refaely-Abramson S, Schuler B, Qiu D Y, Pulkin A, Wickenburg S, Ryu H, Ugeda M M, Kastl C, Chen C, Hwang C, Schwartzberg A, Aloni S, Mo S K, Ogletree D F, Crommie M F, Yazyev O V, Louie S G, Neaton J B and Weber-Bargioni A (2019) Identifying substitutional oxygen as a prolific point defect in monolayer transition metal dichalcogenides. *Nature Communications.* **10** 8

[30] Hildebrand B, Didiot C, Novello A M, Monney G, Scarfato A, Ubaldini A, Berger H, Bowler D R, Renner C and Aebi P (2014) Doping nature of native defects in 1T-TiSe2. *Physical Review Letters.* **112** 5

[31] Noh J Y, Kim H and Kim Y S (2014) Stability and electronic structures of native defects in single-layer MoS2. *Physical Review B.* **89** 12

[32] Yankowitz M, McKenzie D and LeRoy B J (2015) Local spectroscopic characterization of spin and layer polarization in WSe2. *Physical Review Letters.* **115** 5

[33] Liu H J, Chen J L, Yu H Y, Yang F, Jiao L, Liu G B, Ho W K, Gao C L, Jia J F, Yao W and Xie M H (2015) Observation of intervalley quantum interference in epitaxial monolayer tungsten diselenide. *Nature Communications.* **6** 6

[34] Yang D X, Fan X L, Zhang F X, Hu Y and Luo Z F (2019) Electronic and magnetic properties of defected monolayer WSe2 with vacancies. *Nanoscale Research Letters.* **14** 9

[35] Cao D, Shu H B, Wu T Q, Jiang Z T, Jiao Z W, Cai M Q and Hu W Y (2016) First-principles study of the origin of magnetism induced by intrinsic defects in monolayer MoS2. *Applied Surface Science.* **361** 199-205

[36] Zhang C D, Chen Y X, Johnson A, Li M Y, Li L J, Mende P C, Feenstra R M and Shih C K (2015) Probing critical point energies of transition metal dichalcogenides: surprising indirect gap of single layer WSe2. *Nano Letters.* **15** 6494-500

Chapter 6

1H-WSe_2/Au(111) heterostructure

This chapter focuses on a 1H-WSe_2/Au(111) heterostructure which displayed a complex electronic structure. Initial observations from STM of the moiré superlattice indicate an incommensurate system, and the similarities and differences of the STS measurements with the expected 1H-WSe_2 are noted. ARPES measurements are then presented to further confirm this perturbed electronic structure. The effect of substrates has been previously seen in similar systems [1, 2], however the simple hybridisation explanation does not appear to hold here. Therefore, a comprehensive study involving QPI patterns to probe the electronic structure of the heterostructure, combined with ARPES and theory is used to identify the root of the complex system.

6.1. Moiré super-lattice

At the heterostructure interface, one of the forms of interaction is due to the moiré potential, which arises from the mismatch in lattice parameters between 1H-WSe_2 and Au of 0.329 nm and 0.288 nm respectively. The STM image shown in figure 6-1(a) shows a clean area of the surface with the moiré super-lattice clearly visible over the atomic lattice structure of the 1H-WSe_2. The super-lattice manifests as a repeating triangular pattern covering about 3 1H-WSe_2 atomic sides. Figure 6-1(b) shows a FT-STS of the inset image, showing the 6 lattice points of the 1H-WSe_2 and Au marked by G_{WSe_2} and G_{Au}. The points due to the moiré super-lattice are marked by the white circles and are arranged into two groups. The first form a hexagonal pattern surrounding the centre. They each consist of two points, arranged with one closer to Γ than the other, and correspond to the *primary 1st order moiré vectors*. The second group of points is observed around these primary points and close around Γ, and they produce a secondary moiré. This secondary moiré produces a lower frequency hexagonal pattern of bright spots in the STM images, with a spacing of 23 Å. Both real space contributions to the pattern are seen when the moiré super-lattice is isolated in the FFT, as done in figure 6-1(c).

All the features from the lattice points and moiré points are overlaid on the FT-STS in figure 6-1(d). The 1H-WSe_2 and Au reciprocal lattice points are represented by the white and red dots respectively, and it can be clearly seen that the orientation of the 1H-WSe_2 monolayer is rotated by about 25°±1° from the Au substrate. The red hexagon marks the first BZ showing that the primary moiré points are located around the K points. Figure 6-1(e) shows

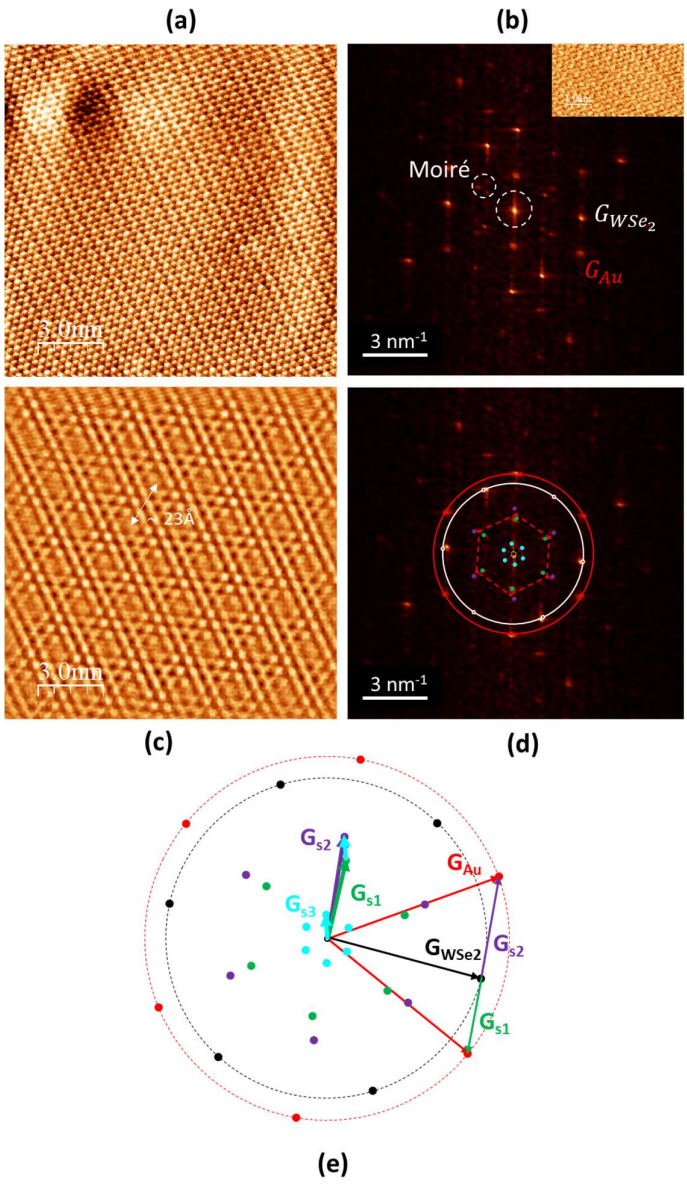

Figure 6-1. (a) STM image of an area of the 1H-WSe_2 monolayer surface, which is clear of defects and showing the moiré pattern. (b) The FFT of the inset z-image showing the 6 lattice points of the 1H-WSe_2 and Au marked as G_{WSe_2} and G_{Au} respectively, and the points corresponding to the moiré super-lattice. The two points highlighted by the outer white circle are the primary moiré vectors, and the points surrounding the centre highlighted by the larger circle are due to the secondary vectors. (c) Image showing the isolated moiré pattern from the FFT. The secondary moiré pattern is the larger hexagonal pattern of points spaced by 23 Å. (d) FFT with an overlay showing the position of the lattice vectors and moiré points. The BZ is marked by the red hexagon. (e) Decomposition of the FFT. The two lattice vectors are shown with black for 1H-WSe_2 and red for Au(111) and arranged 25 degrees to each other. The vectors between these G points are represented by the green G_{s1} and purple G_{s2} vectors, which are then plotted from the centre to give the primary moiré points. The aqua vector between G_{s1} and G_{s2} is the secondary moiré vector G_{s3}, and again plotted from the centre to give the secondary moiré points.

a diagram describing the vectors involved in the construction of the moiré super-lattice. The vectors G_{S1} and G_{S2} between adjacent lattice points of the 1H-WSe_2 and Au correspond to the vectors from the centre out to the moiré points observed in the FFT, proving that is their origin. The secondary moiré pattern comes from the vector between these two primary moiré points as denoted G_{S3}. The same moiré pattern and orientation is observed from every area scanned on the monolayer, which is as expected due to the two single crystals used. This also suggests there is either no local reconstruction or a large-scale reconstruction of the Au or 1H-WSe_2 at the interface.

A simulation of the resulting geometries at the interface was done to simulate the FFT with different twist angles between layers. The STM currents was approximated as,

$$I(z,\vec{R}) = C\int_0^{eV} \rho_s(E,\vec{R})e^{-2\gamma(E)z(\vec{R})}dE\,, \tag{6-1}$$

where $\rho_S(E,\vec{R})$ is the surface LDOS. Assuming the LDOS and the wavefunction decay rate are approximately constant in energy gives,

$$I(z,\vec{R}) \propto \rho_s(\vec{R})e^{-2\gamma z(\vec{R})}\,, \tag{6-2}$$

where $\rho_s(\vec{R}) = \rho_{WSe2}(\vec{R}) + 0.1\times\rho_{Au}(\vec{R})$. The separate LDOS for 1H-WSe_2 and Au(111) are shown in figure 6-2(a) and (b) respectively for a 27.5° twist angle. At constant current, $\rho_s(\vec{R})e^{-2\gamma z(\vec{R})} = \rho_s(\vec{R}_0)e^{-2\gamma z(\vec{R}_0)}$ so the tip height variation is,

$$dz(\vec{R}) = z(\vec{R}) - z(\vec{R}_0) \propto \ln\left(\frac{\rho_s(\vec{R})}{\rho_s(\vec{R}_0)}\right), \tag{6-3}$$

A Fourier transform of eq. 6-3 was performed for twist angles 25°, 27.5°, and 30° and the results are shown in figure 6-2(c). The lattice constants of 1H-WSe_2, the LDOS of which is shown in figure 6-2(b), are represented by the bright spots in the FFT. For the 27.5° and 30° rotation the 6 points can be seen arranged in a hexagon, while the 25° rotation shows 4 clearly with the other 2 points reduced in intensity. The moiré super-lattice for the 25° and 27.5° twist angles are constructed from the arrays of points around the K points, and the 6 points close around the Γ point. The 30° case is an ideal situation where the super-lattice is commensurate with the symmetry points of the 1H-WSe_2, so the primary moiré vectors are equal and therefore only a single point is observed around the K point and at the Γ point. As can be seen, the FFT with a twist angle of 25° matches very well with the experiment FFT shown in figure 6-1(d) agreeing with the proposed twist angle of about 25°. The evolution of the moiré pattern's size and shape with a small rotational variation shows the importance of the twist angle on the resulting heterostructure's electronic structure, as even a small variation can change the periodicity of the moiré super-lattice.

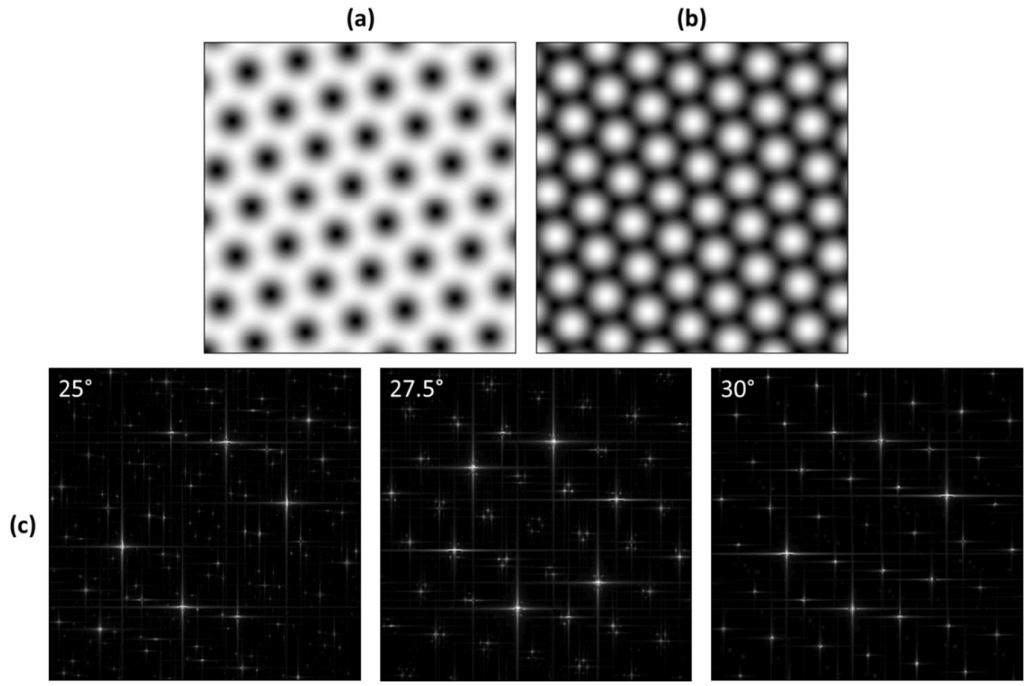

Figure 6-2. Calculated LDOS functions of (a) honeycomb 1H-WSe_2 orientated at 47.5° and (b) hexagonal Au orientated at 20° with a clockwise rotation. The area is 2x2 nm^2. (c) FFTs of the tip height variation based on the LDOS function for different twist angles. The 6 bright points correspond to the 1H-WSe_2 lattice points. The moiré pattern is represented by the points around the K points, and the 6 point directly surrounding Γ, or the single point in the 30° case.

6.2. Spectroscopy: Electronic band-structure

Point spectroscopy from the different 1H-WSe_2 flakes was taken to help identify them and determine the critical points of the electronic structure. The measurements confirmed them as 1H-WSe_2 due to the presence of the bandgap (*quasi-particle gap*) and a difference from measurements on the Au substrate. The two curves shown in figure 6-3(a) show the $\mathrm{dI/dV}$ spectroscopy taken from the monolayer and few-layer flake. The monolayer shows a bandgap of about 2 eV; the few-layer flake has slightly shorter gap of 1.6 eV. The influence of interlayer interactions can be seen between these two flakes, when compared to the bulk bandgap value of 1.2 eV from figure 6-3(b). This agrees with the literature, which highlights the strong thickness dependence of the electronic structure due to interlayer coupling [3-5]. Another difference is the Fermi level position relative to the band edges between the bulk crystal and the layers on Au(111) is shifted to the left, indicating that the heterostructure flakes are more *p-doped*.

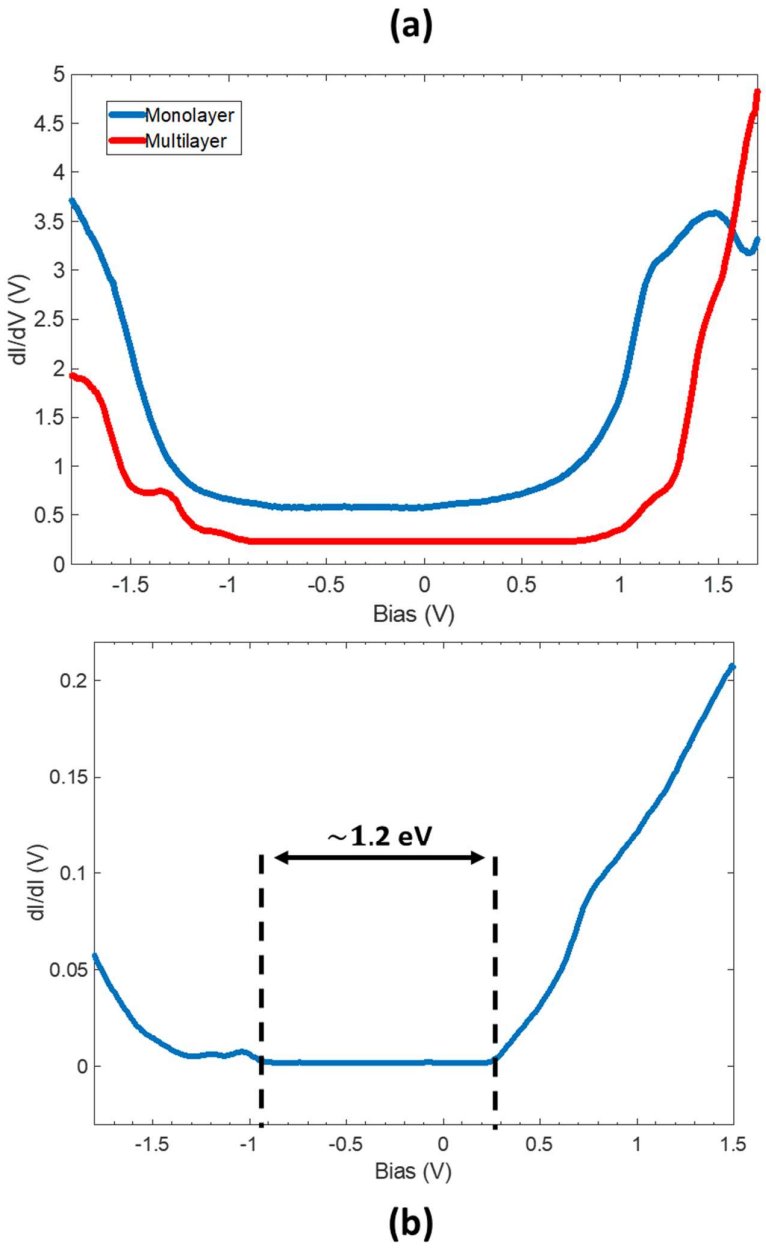

Figure 6-3. (a) dI/dV spectroscopy of the monolayer area (blue) and the multilayer area (red). The curves are slightly offset for clarity. (b) dI/dV spectroscopy of the bulk WSe_2 crystal.

Identifying the critical point states

From these curves it is difficult to clearly identify the edges of the conduction and valence band, and the other critical points. Therefore variable-z spectroscopy $(\partial I/\partial V)_I$ was performed to account for the change in signal at different bias and allow for the detection of these quickly decaying states, as described in section 3.2.3. In figures 6-4 and 6-5,

measurements from the monolayer and multilayer flakes of the valence band and conduction band edges are shown respectively, which display the location of these critical points much clearer. The valence band spectroscopy for the monolayer is shown in figure 6-4(b), with a strong peak at -1.58 eV and a weaker peak at -0.88 eV. The $\mathrm{K_V}$ state is the valence band edge for monolayer 1H-WSe_2 and therefore the peak at -0.88 eV, which is the last observable state before the bandgap, can be attributed to it. The fact the peak is still weak even in the $(\partial I/\partial V)_I$, supports this, as the K states with their larger $k_{\parallel}$ will be weaker than other critical points. The much stronger peak at -1.58 eV, suggests a state with a *smaller* $k_{\parallel}$; its deeper position in the valence band shows it is the state at the Γ point. Further proof of the identity of these states comes from the energy separation between them, $\Delta_{\Gamma-\mathrm{K}} = \sim 0.7$ eV which is supported by a previous study using this method [6]. The slight differences can be explained by the use of a Au(111) substrate rather than HOPG. Between these peaks is the state at the $\mathrm{K_2}$ point, which is the lower energy level band of the spin-split K valley.

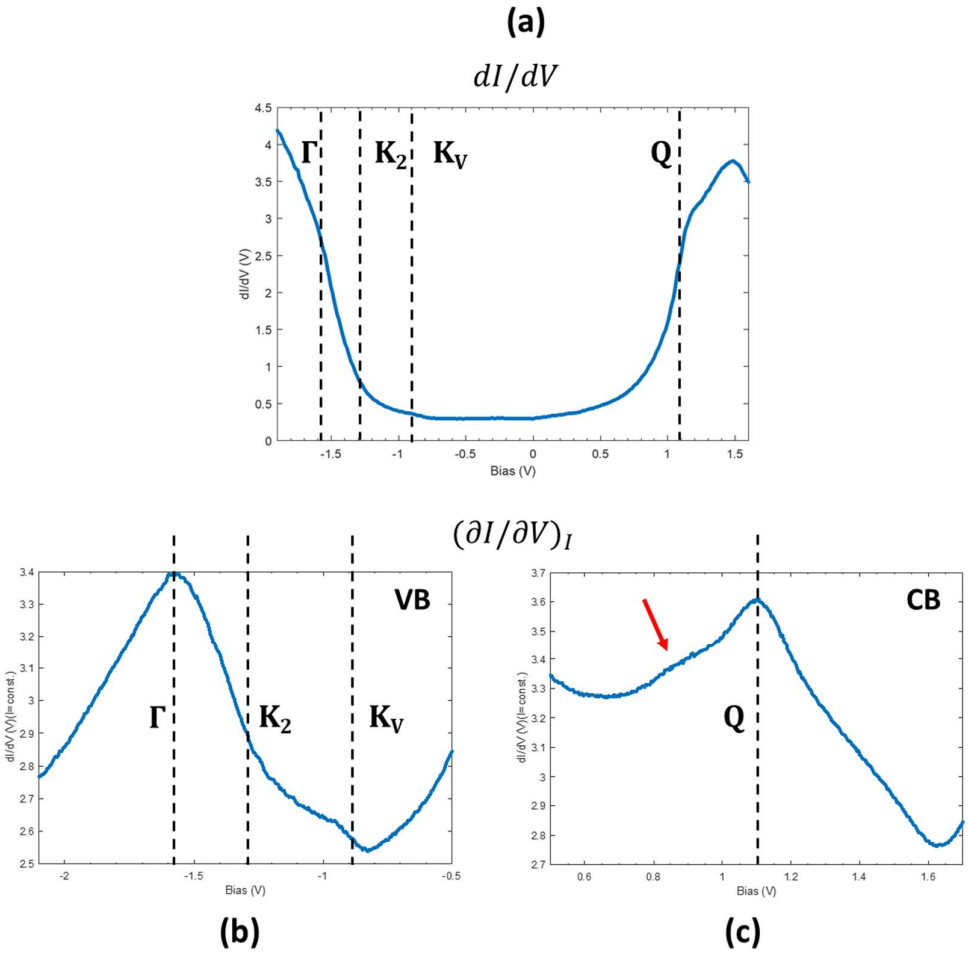

Figure 6-4. (a) dI/dV spectroscopy on the 1H-WSe_2 monolayer with the proposed critical points marked. Variable-z spectroscopy of the valence band (b) and the conduction band (c), showing the features of the critical points much clearer than the dI/dV.

This is located at -1.3 eV, which gives an energy separation between these two K states of 0.42 eV, in agreement with experimental [6] and theoretical [7] results of splitting due to spin-orbit coupling.

For the multilayer flake, the $(\partial I/\partial V)_I$ of the valence band edge is very different to the monolayer as expected. From figure 6-5(b) the spectroscopy now shows 3 clearly separated peaks with the highest at -0.78 eV, indicating a slight *shortening of the bandgap* from this side. Since the expected valence band edge is now at Γ, this peak can be assigned to the state at this point. The intensity of this peak and the peak next to it, and the difference with the smaller peak at -1.35 eV suggests the neighbouring peak is of a *similar nature* and a Γ state as well. What is unusual is the proximity of these states, as simulations typically show the separation is larger and the top K state is between them. A possible explanation for this shift could arise from the additional interaction with the substrate, as the Γ states consist of out-of-plane W-d_{z^2} and Se-p_z orbitals and so are more likely to be affected by perturbations in the z-direction. The smaller peak here could be the top of the second K state, although it is difficult to determine without supporting evidence.

The conduction band $(\partial I/\partial V)_I$ for the monolayer flake is shown in figure 6-4(c), displaying a main peak at 1.1 eV, and a very weak peak at 0.85 eV indicated by the red arrow. Due to the nature of the 1H-WSe_2 band-structure, the K and Q valleys of the conduction band are *almost degenerate* in energy and therefore their peaks in spectroscopy will overlap, making determination of the two states difficult. Some calculations describe 1H-WSe_2 as a direct band-gap semiconductor, where the direct gap lies between the K points of the valence and conduction bands. From this, it could be said that the strong peak at 1.1 eV can be assigned to the Q point and the weak peak to the K_C point, which would mean a shorter bandgap of about 1.75 eV for the monolayer. However, even in these cases the conduction band edge is shown to be almost degenerate in energy between the K and Q critical points, whereas here there is a relatively large gap of 0.25 eV, suggesting that this assignment is not correct. Furthermore, some calculations predict that it is the Q point instead at the conduction band edge closely followed by the K point. This would mean that the peak at 1.1 eV overlaps with the K peak, and the lack of any obvious second peak can be explained by the larger $k_{\parallel}$ of the K state compared to the Q state; meaning a much weaker STM signal. This arrangement is supported by experimental observations using the same technique with additional $(\partial Z/\partial V)_I$ and decay constant κ measurements [6], and PL measurements of the direct and indirect optical gaps [8]. Comparison with the $(\partial I/\partial V)_I$ from the multilayer conduction band in figure 6-5(c) also helps to identify the Q state, as it is now the conduction band edge and attributed to the lowest peak at 0.8 eV. Like the monolayer this is the largest peak. The shift of the Q band reveals another smaller peak at 1 eV, which is likely due to the K state. The p-orbitals making up the Q band consist of the Se-p_x, -p_y, and -p_z orbitals whilst the K band only has Se-p_x, and -p_y. Since the interlayer coupling is mediated by the Se atoms, the out-

of-plane Se-p_z explain why the Q point shifts more than the K point. This suggests that the Q and K peaks overlap when thinned down to the monolayer.

This leaves the weak peak in the monolayer conduction band marked by the red arrow *unaccounted* for. While certain defects can induce defect states at the edges of the conduction and valence bands, the measurements here were taken from areas free of defects so this can be ruled out. This peak is not the only anomality from the measurements; looking within the bandgap of the monolayer spectroscopy in figure 6-4(a), there are bumps throughout and it begins to curve upwards before the determined bandgap edges. Comparing this to the bandgap of the few-layer flake in figure 6-5(a), which shows a completely flat region indicating the expected absence of states, suggests the presence of other bandgap states in the monolayer. As this sample has been placed on a metallic substrate, it is expected that the conduction within the bandgap is raised due to the presence

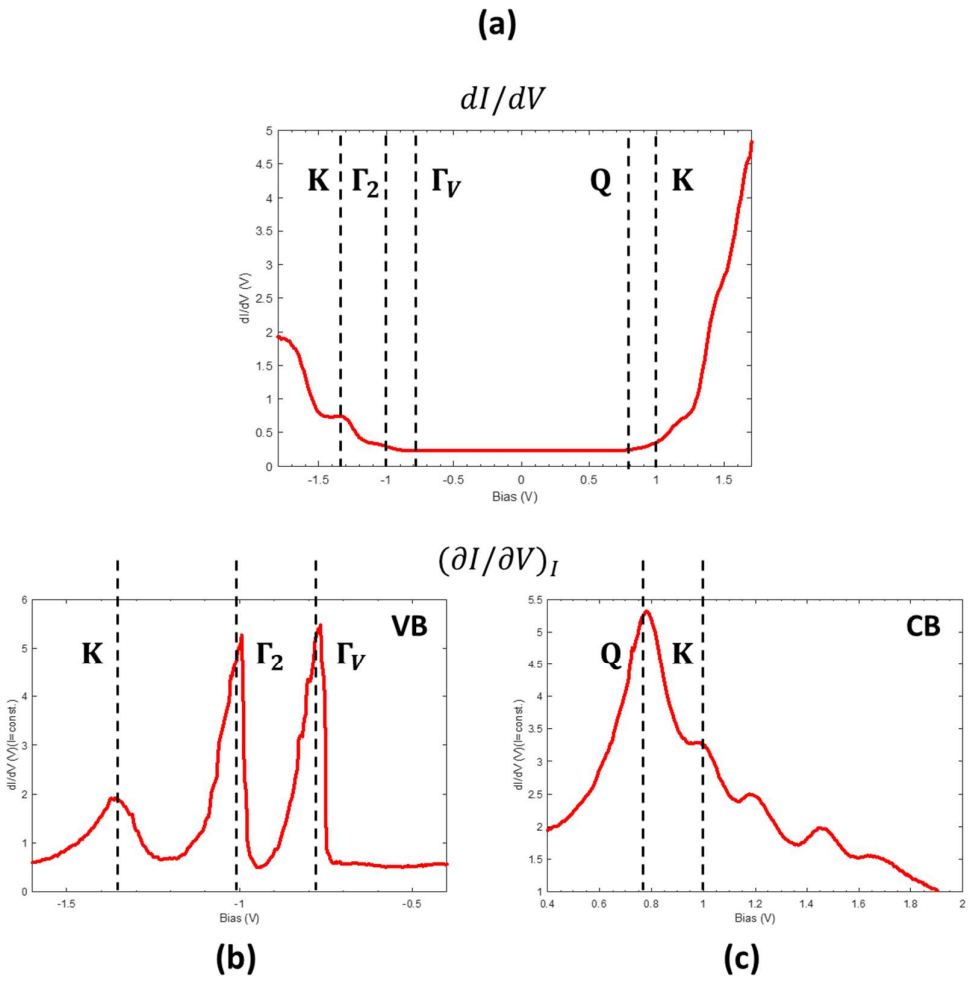

Figure 6-5. (a) dI/dV spectroscopy from the multilayer WSe_2 flake with the proposed critical points marked. Variable-z spectroscopy of the valence band (b) and the conduction band (c).

of the Au(111) states to allow for tunnelling to be possible. These states though are from the continuum of metal states, which should result in a near flat DOS as seen in the $\mathrm{dI/dV}$ measurements from Au(111) presented earlier in chapter 4, except for the localised surface state at around -0.46 eV. These new features therefore *cannot* simply arise from the presence of Au(111) states and must be from the interlayer interaction between the two layers. This could be due to hybridisation of the bands if the orbitals have sufficient out-of-plane momentum to overlap, such as around the Γ point. Another possibility is that the new states arise from the effect of the moiré super-lattice. The new periodicity could induce band-folding, resulting in a mixing of bands around the bandgap edges as well as the shifting of states to new positions. If the potential is strong enough, minigaps could also appear where the states mix. However, STS measurements alone are not enough to determine this.

6.3. ARPES: Optical band-structure

ARPES measurements were taken to help clarify the electronic structure in the valence band of the heterostructure. Measurements were taken from regions on both a thicker flake and the monolayer investigated with STM, as the thicker flake was expected to be "de-coupled" from the interface interaction and provide a base for comparison. The thicker flake used was much larger than the multilayer flake measured with STS in the previous section to avoid any signal overlap from the Au substrate. Figure 6-6 shows isoenergic contour maps taken using the NanoESCA of the thick flake, in an energy range of -2 eV to the band gap edge at -0.8 eV. These maps represent the reciprocal space at a given energy and the states can be directly visualised. The evolution of the 1H-WSe_2 valence band states can be seen, with the K and Γ states providing the greatest contribution. The states at K have a triangular shape and shrink in towards the K point as the energy increases until they reach a single point at the band edge. The spin-splitting of the bands is also seen, which is clearest in the -1.7 eV contour. The Γ band too shrinks with increasing energy from a hexagonal shape to circular and becomes much less prevalent towards the band edge. It is interesting that the signal from around Γ does not fully vanish in the -0.8 eV contour, as for a bulk crystal the Γ states should lie lower than the K states.

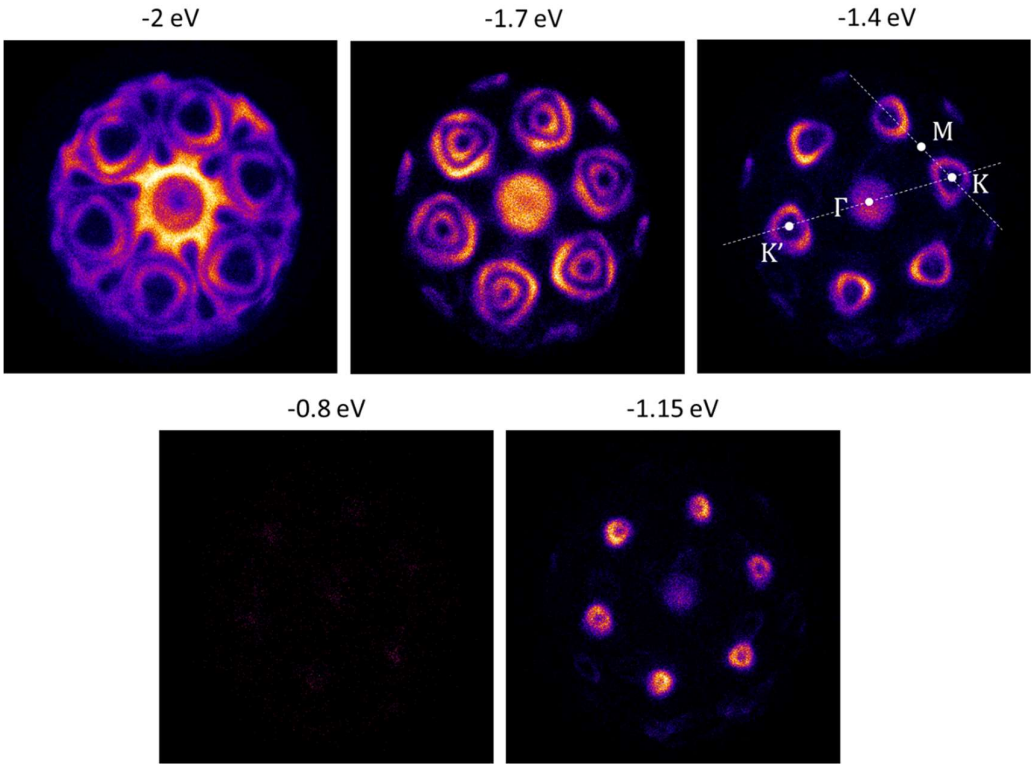

Figure 6-6. NanoESCA. Isoenergetic cuts from a thick WSe_2 flake on Au(111) showing a progression from -2 eV to the valence band edge at -0.8 eV. The critical points and cuts are marked for the energy of -1.4 eV.

Comparing isoenergetic cuts from the Au substrate and the 1H-WSe_2/Au(111) allowed for the rotation angle between layers to be determined as well. Integrated images from all of the isoenergetic cuts in the energy ranges -0.4 eV to the Fermi level for the Au(111) substrate, and -0.93 to -0.85 eV for 1H-WSe_2/Au(111) are shown in figure 6-7(a) and (b) respectively. The greater intensity from these integrated images means the critical points can be more easily seen. In figure 6-7(a) the Au Fermi surface consisting of the sp-bands is shown by the hexagonal shaped band just inside the overlaid white hexagon, with the critical points M^* and K^* of Au labelled. The 6 points of the Au sp-bands correspond to the M^* critical points. For the 1H-WSe_2/Au(111) in figure 6-7(b), the energy range is integrated just below the top of the valence band, so the 6 bright points correspond to the K points of 1H-WSe_2. The dotted lines in both (a) and (b) are vectors between two opposite points of M^* or K^*, and the solid line in (b) is between two K points. If the two lines for M^* and K lined up in (b) it would mean that the lattices were rotated by exactly 30° degrees, whereas here there is a few degrees difference between them. This was found to be 3-4° meaning that the rotation between layers is about 26° which is within agreement with the twist angle determined by the moiré pattern in FT-STS and simulations.

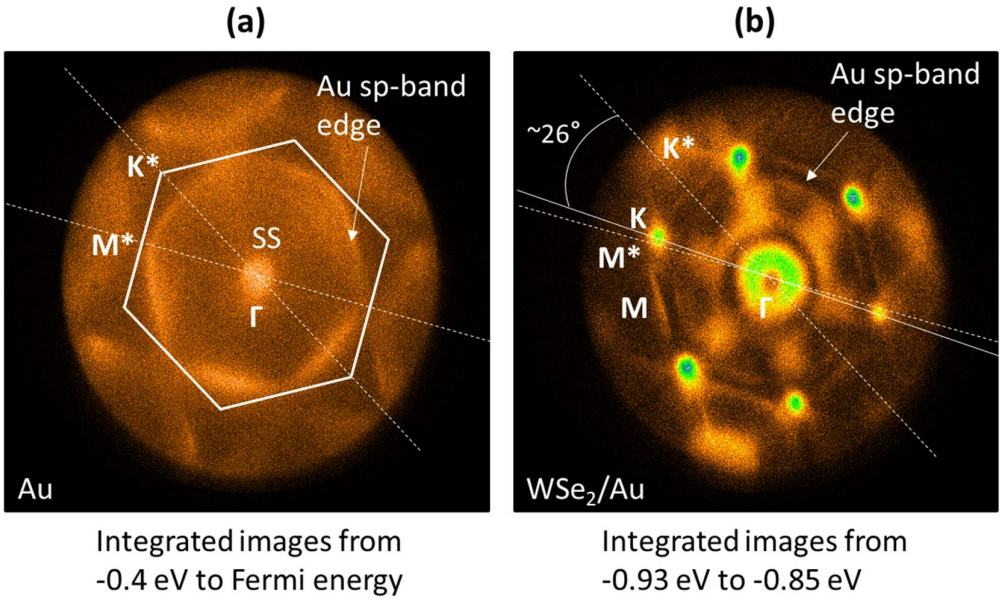

Figure 6-7. NanoESCA. (a) Integrated image of isoenergetic cuts from -0.4 eV to the Fermi energy taken from the Au(111) substrate. The Au(111) Fermi surface is shown as the hexagonal shaped band and the central spot at Γ marks the surface state. The white hexagon shows the critical points. (b) Integrated images between -0.93 eV and -0.85 eV taken from the monolayer 1H-WSe_2/Au(111). The bottom of the 6 valleys at K can be seen and comparison between these points and the M^* points of Au(111) gives a rotation angle of 26° between layers. The appearance of double lines for the Au Fermi surface is due to back folding of the bulk state edge at the interface through a surface Umklapp process.

A feature of the isoenergetic cuts that stand out are the bands which remain above the valence band edge as seen in figure 6-8 (a). The edge of the valence band is located at -0.8 eV and this energy contour shows bands located around the Q points marked by the red arrow. Normally there are no bands located at this point in the upper valence band so close to the bandgap, but here they are present and continue to exist in the energy contours above the valence band edge as seen in the contours for -0.45 eV and -0.05 eV. The intensity of the band increases as it gets closer to the Fermi energy which can be seen more clearly in the energy vs $k_{\parallel}$ cut shown in figure 6-8(b) which highlights this band with a red ellipse. This cut also shows that the band has virtually no dispersion with energy, which is very unusual for the usually localised gap states.

The NanoESCA measurements takes signal from the whole flake, whilst the Nano-ARPES is a more local measurement with a spot size of a few nm. Figure 6-9(a) shows two isoenergic cuts in the bandgap, which were taken using Nano-ARPES and have very similar features to those in figure 6-8. The contrast is inverted, and a dark spot can be seen at the Q point which has greater intensity at the Fermi level. The Au(111) Fermi surface can also be seen, as well as the ring around the Γ point. Measurements taken from multiple places on the flake

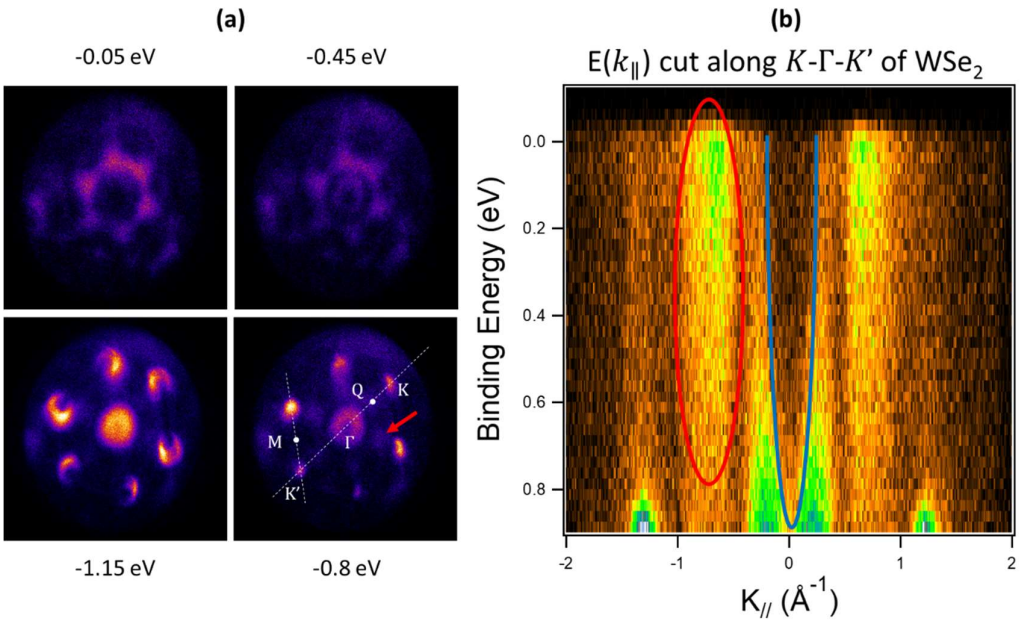

Figure 6-8. NanoESCA. (a) Isoenergetic cuts showing the progression from below the valence band edge at -1.15 eV to deep inside the bandgap at -0.05 eV. The valence band edge is at -0.8 eV and the critical points are marked in white in this image. 6 points at the Q point can be seen which can be observed below the valence band edge and into the bandgap, with increased intensity towards the Fermi level. The central ring around Γ is due to the edge of the Au(111) bulk states. (b) Energy cut along K-Γ-K' showing just the top of the valleys at K, and the Au(111) sp-bulk band edge marked by the blue curve. The features seen at Q in (a) are marked with the red ellipse.

showed no variation between them either. The fact that these features are present in both large scale and very local measurements indicates the uniformity in the coupling between the 1H-WSe_2 and Au(111) across the flake.

The Au(111) has a localised *surface state* which can be seen in the measurements taken from the substrate where there is no overlayer of 1H-WSe_2, as in figure 6-9(b). This is the bright parabolic band starting from -0.46 eV and rising upwards centred around Γ, and is consistent with the STS measurements of the substrate. However, in figure 6-9(c) showing an energy cut from the 1H-WSe_2/Au(111) this band can no longer be seen. A simple answer is that it cannot been detected through the 1H-WSe_2 overlayer but in figure 6-7(b) the Au(111) sp-bulk band edge can be seen, and figure 6-9(b) shows these are less intense compared to the surface state. This instead suggests the band has been shifted upwards which leads to an increase in the spectral weight of the edge of the Au(111) sp-bulk band continuum, and explains why they are seen a lot clearer and at smaller $k_{\parallel}$ than before (marked by the blue line in figure 6-8(b)). When the 1H-WSe_2 layer is put on top, the NanoESCA now shows a replica of this band as highlighted by the white lines in figure 6-9(c). This feature has been observed before in a system with an ordered adlayer placed on top of Au. The surface emission in ARPES is backfolded by a surface Umklapp process. The presence of this process

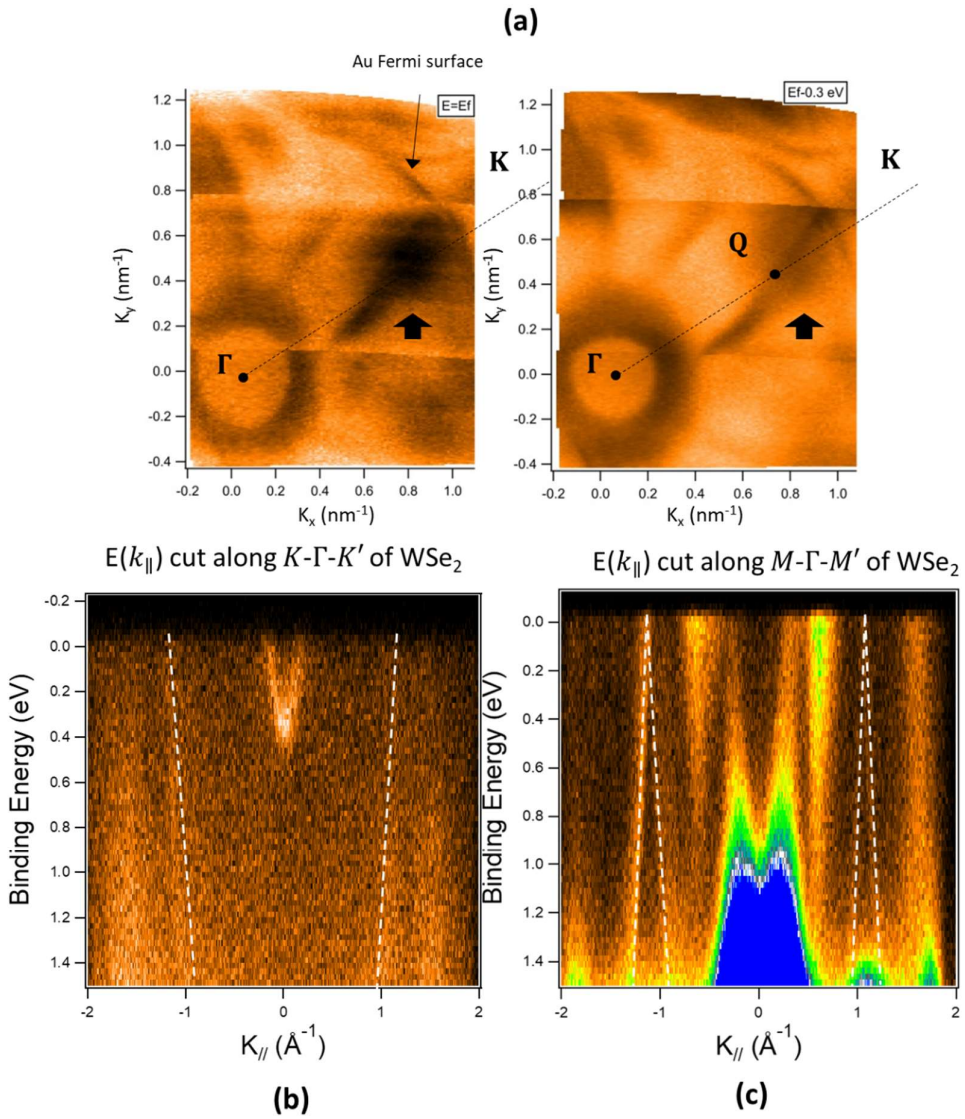

Figure 6-9. Nano-ARPES. (a) Inverse log-scale isoenergetic cuts at the Fermi energy and -0.3 eV. The state around the Q points can be seen and has increased intensity at the Fermi energy consistent with the NanaESCA. NanoESCA. (b) Energy cut from the Au(111) substrate but along the K-Γ-K' direction of the 1H-WSe_2. The bright band centred on Γ, with its minimum at -0.46 eV is the surface state of Au(111). The less intense bands either side around ±1 eV are the edges of the continuum of bulk states marked by the white dotted lines. (c) Energy cut from the 1H-WSe_2/Au(111) substrate but along the M-Γ-M' direction of the 1H-WSe_2. The bulk Au band edge now shows a second replica feature marked by the white dotted line.

and the absence of the surface state suggests a hybridisation between the two layers in the heterostructure [9].

Figure 6-10(a) shows a cut along the K-M-K′ direction revealing the spin-split bands of the K valleys, with the valence band edge state starting at around -0.82 eV and the second K state

beginning at -1.28. This gives a spin-split energy separation of 0.46 which is consistent with the value observed from the STS measurements in figure 6-4(b). Another feature of the K bands along this cut direction is that each valley appears to be composed of two separate parabolas, as marked by the coloured lines in the figure. This is evidence of the presence of band replicas around the K points, which occur when the bands are folded. These replicas are expected to only show along certain cuts of energy contour. Their position is determined by the vectors of the moiré super-lattice which causes the band folding. A schematic diagram illustrating this is shown in figure 6-10(b), with the replica positions marked around the K and Γ points by black crosses and circles. The positions of the replicas around K mean they are easily missed in most cuts straight through the Γ point, and easier to catch in cuts between two K valleys.

In figure 6-8(b) the top of the bands at Γ can be seen, which are unusually close to the top of the bands at K. An energy cut from the Nano-ARPES over a larger energy range is shown in figure 6-11(a), which shows a *large concentration* of states around Γ. In suspended 1H-WSe_2 there is only the one Γ band that is located here which is centred on Γ and has negative dispersion with energy. From the Au only the band edge of the sp-bulk states can be observed as marked in figure 6-8(b). Neither of these can explain the large density of states and therefore it can only be caused by interaction between the two layers. Slightly away from the Γ point by about 0.25 nm^{-1}, a vertical dark line is observed indicating a dip in the

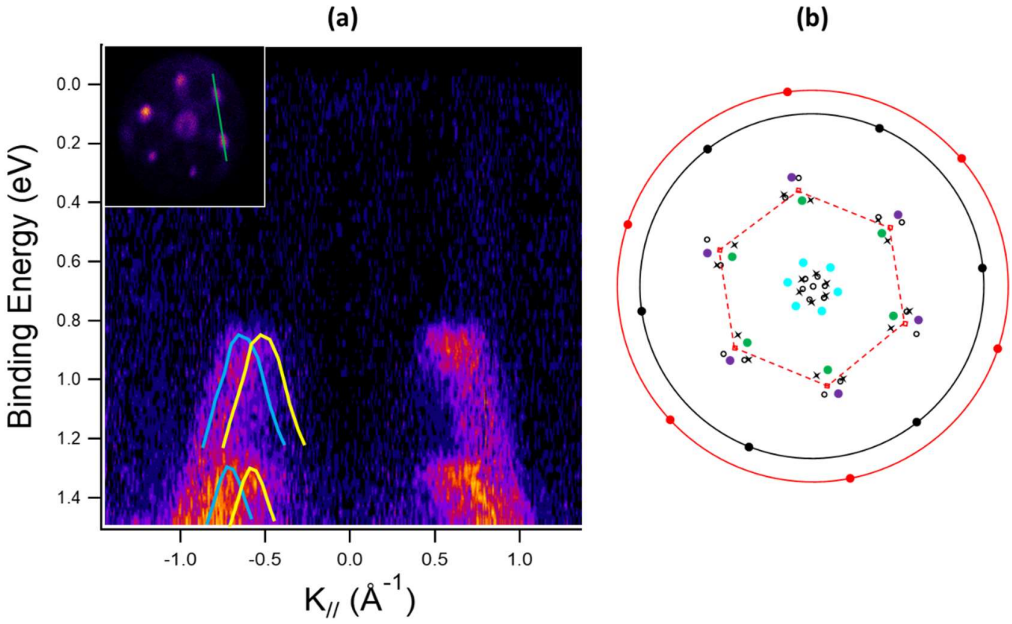

Figure 6-10. NanoESCA (a) Energy cut along K-K' as shown in the inset. The K valleys consist of the original band and a replica as indicated by the blue and yellow curves. (b) Schematic diagram showing the positions of expected replicas marked by black crosses and circles. The black and red dots represent the 1H-WSe_2 and Au lattice points respectively. The primary moiré points are marked by the green and purple dots and the secondary points by the light blue dots.

intensity of states. Looking at the isoenergetic cuts in 6-11(b), which are inverted in intensity, this depression surrounds the Γ point in the shape of a *David's star*; it also does not appear to disperse with energy. A possible explanation for this feature could be due to bands

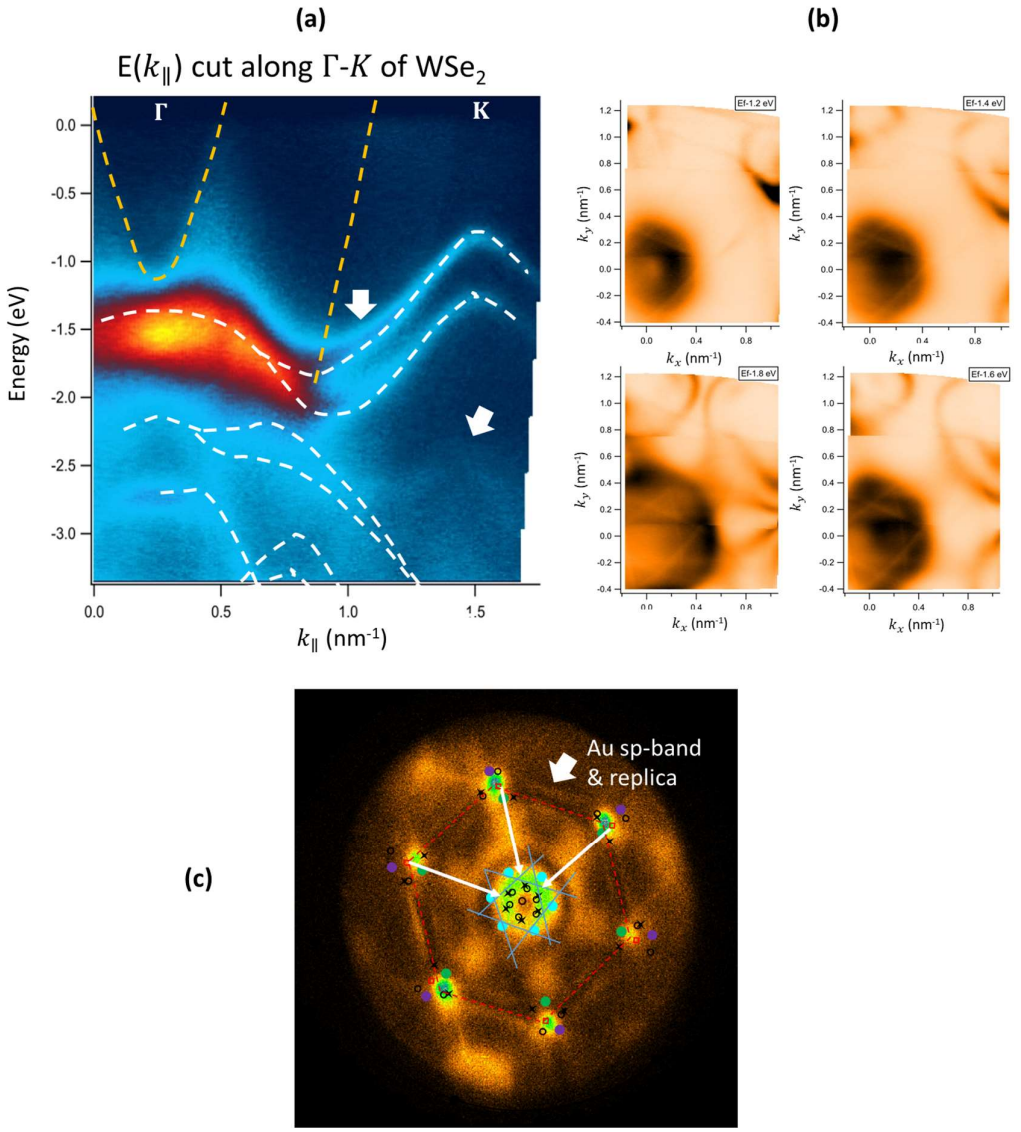

Figure 6-11. Nano-ARPES. (a) Energy cut from the monolayer 1H-WSe_2/Au(111) along the Γ-K direction. The red/orange intensity marks the large concentration of states around the Γ point, with the dark vertical depletion through it seen at -0.5 nm^{-1}. The upper arrow marked the usual doubling of states towards the K point, and the lower arrow marks the new states not previously observed from either layer separately. (b) Isoenergetic cuts at energies from -1.2 to -1.8 eV, showing the David' star pattern of the intensity drops around Γ. The position of the star does not disperse with energy. NanoESCA (c) David's star feature (blue lines) overlaid onto an isoenergetic cut showing the moiré features and replicas. The red dotted line is the BZ. The Au sp-band edge states can be clearly seen and folding back towards the centre from these using moiré vectors results in the David's star. 3 examples are shown by the white arrows.

crossing, which would occur *if they had been folded*. Figure 6-11(c) shows an isoenergetic cut at -0.9 eV from NanoESCA with all the moiré features and replica locations marked. The blue lines in the centre forming the David's star are taken from the pattern in 6-11(b) and superimposed onto this isoenergetic cut with relative positions to K points and BZ obtained from the Nano-ARPES data. By taking the moiré vectors and folding them back from the Au sp-bulk band edge towards the centre, they end up on the David's star pattern. This is evidence that the bands at the edge of the Au continuum have been *zone-folded* by the moiré super-lattice. This explains the presence of the many states around Γ due to them all being folded back onto it from all directions.

Another unusual feature observed in figure 6-11(a) is the appearance of multiple bands moving towards the K point marked by the top arrow. The spin-split bands can be clearly seen at the K point, yet from each of these bands there appears to be another band splitting off. This is clearly not due to the spin degeneracy and is unlikely to be another degree of freedom. A much clearer explanation could come from the above-mentioned band-folding, which would result in the folding of the original Γ-K band back on itself. This would also contribute to the bands around Γ, especially those at higher energy than normally expected; and is discussed in much greater detail in section 6.5. The presence of states other than those around Γ which are not seen in the intrinsic materials are observed too. Deeper in energy underneath the K point starting around -2.4 eV and -3 eV are two *new* parabolic states marked by the lower arrow in figure 6-11(a). ARPES of 1H-WSe_2 has not previously observed

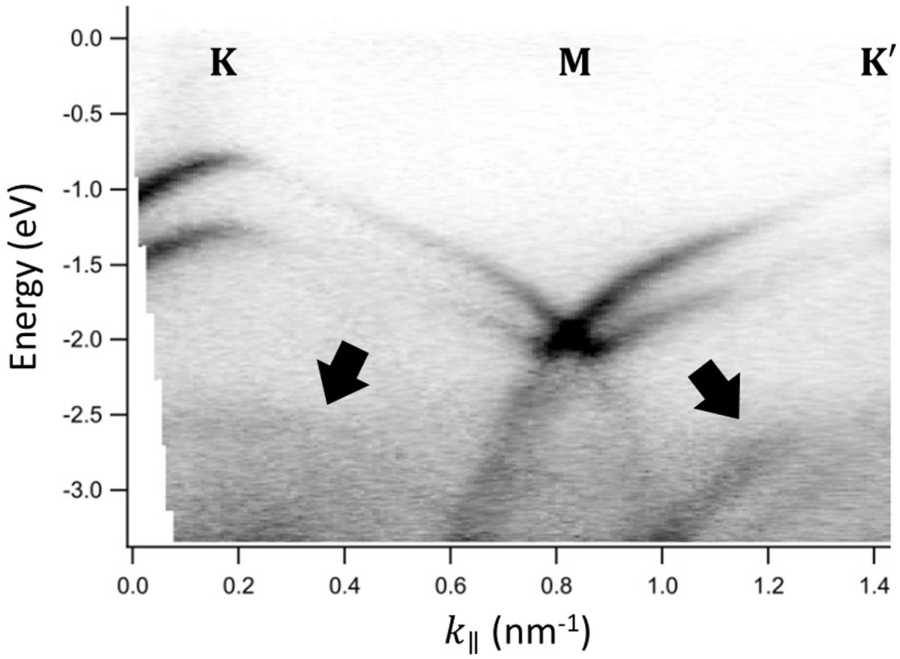

Figure 6-12. Nano-ARPES. Energy cut along the K-K' direction, showing two K valleys and the M point. The bands marked by green arrows are the new states.

any states at this position [10, 11], and the Au(111) bulk states consist of a continuum so they are not intrinsic to either layer. New states can also be seen in the energy cut between two K valleys, as marked by the arrows in figure 6-12.

6.4 Using atomic scale defects as probes of the electronic structure of the WSe_2/Au(111) heterostructure

6.4.1 Heterostructure characterisation via STM and $\mathrm{dI/dV}$ mapping

To complement and clarify the ARPES results it was also necessary to probe the heterostructure system created - which in the remainder of the chapter will be referred to as R25° 1H-WSe_2/Au(111) - at the local level. FT-STS, an STM-derived technique, was introduced as a technique that can probe the electronic structure from both valence and conduction bands (as opposed to traditional ARPES which probes only states below the Fermi energy) *via* scattering from defects located on the surface of the system. Electronic band dispersion relationships could be determined in this way in simpler systems, and some examples of FT-STS usage were already given in Chapters 3 and 5.

The R25° 1H-WSe_2/Au(111) is an incommensurate system, for which we expect an intricate band-structure, therefore performing an FT-STS study on it would appear to be very challenging. There was a two-fold interest when performing it: (i) to see to what extent FT-STS can still capture information about the electronic bands of the 2D overlayer, and (ii) to assess whether using different types of defects as local probes it can selectively access different types of electronic bands, such as those arising from different components of the heterostructure.

Consequently, we performed a comprehensive mapping of LDOS as a function of energy spanning from the bottom of the valence band of WSe_2, through the band-gap, and into the conduction band of WSe_2. Nano-ARPES, NanoESCA and STS put the VBE for the R25° 1H-WSe_2/Au(111) system at about - 0.85 eV, while the CBE was determined from STS to be around 1 - 1.1 eV, while NanoESCA revealed some intra-gap non-dispersive features that cross the Fermi energy, making the system metallic. Figures 6-13 to 6-16 show a selection of characteristic z and $\mathrm{dI/dV}$ images at different bias voltages within this energy range, from which several important points can be made.

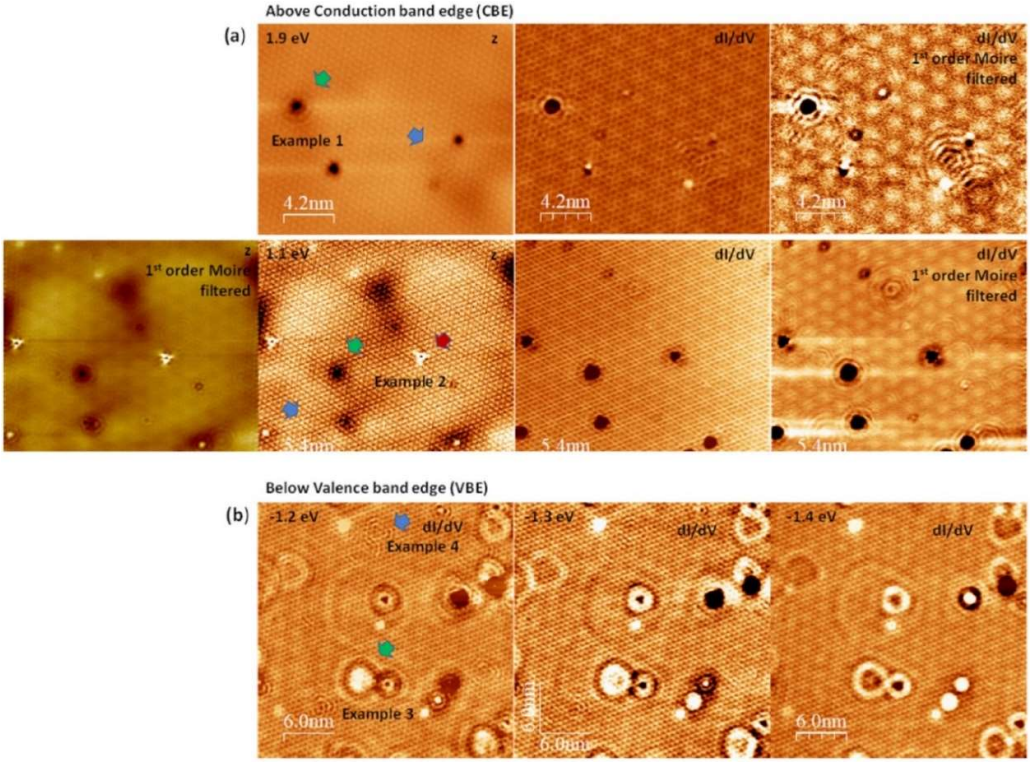

Figure 6-13. (a) Collection of defects of different type. The z and dI/dV images show surface (red arrows), interfacial (green arrows), and subsurface (blue arrows) defects. The defects labelled "example" are discussed in the text.

There are different categories of defects that interact with this system in very different ways, yielding QPI scattering patterns that have distinctive spectral components in the reciprocal space.

Figures 6-13(a) and (b) show examples of these different types: (i) defects within the 1H-WSe_2 monolayer (shown with red arrow in (a) and labelled Example 2); (ii) defects that are most likely interfacial, i.e. located between the WSe_2 overlayer and the Au substrate (shown with green arrows in (a) and (b), some of them being labelled Examples 1 and 3, respectively); and, finally, (iii) *subsurface* defects, which most likely lie within the Au substrate itself (shown with blue arrows in (a) and (b)).

The *surface* defects, that involve in one way or another the layers of WSe_2, show atomic scale detail in both z and $\mathrm{dI/dV}$ images (see Figure 6-13(a), bottom panel) and yield both inter- and intra-valley scattering from energy bands with strong W- or Se- character, and their QPI disperse with energy. The behaviour of the defect labelled "Example 2" in figure 6-13(a) is discussed in detail in figure 6-28.

Interfacial defects tend not to be localized on single atomic sites but can interact strongly with bands that belong uniquely to WSe_2, indicating that they might have bound to the bottom layers of WSe_2. The defect labelled "Example 1" is analysed in section 6-5, in

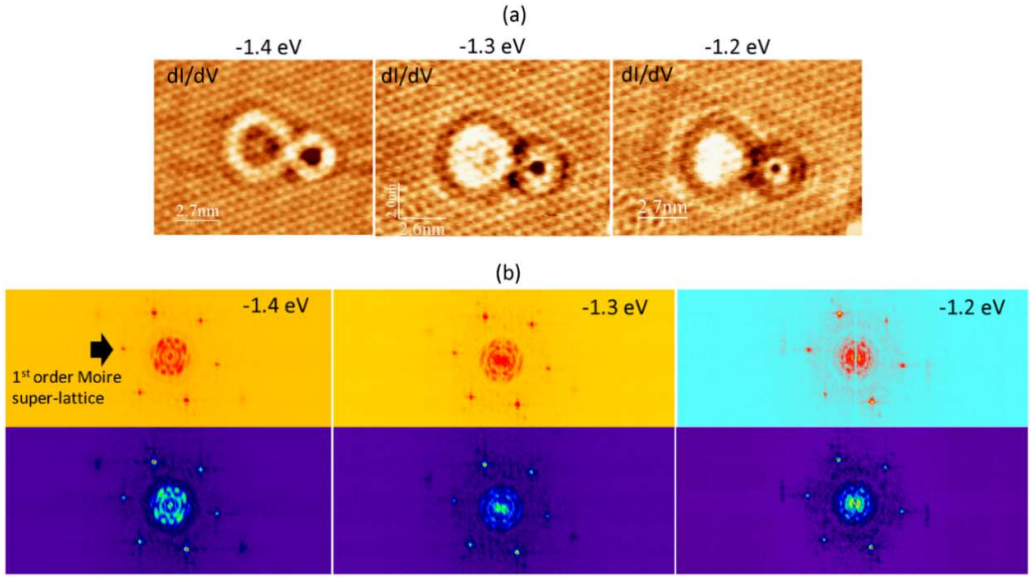

Figure 6-14. (a) dI/dV images and (b) FT-STS showing the complex behaviour of QPI patterns from an interfacial defect; the effect is strong and happens over a short energy range, indicating the folding of bands at the Γ point.

figure 6-30 and provides insight about the behaviour of W- and Se-derived energy bands at high energy above the conduction band edge. Below the valence band edge, such defects were able to probe the intricate band-structure around the valence band edge where folding of energy bands due to the super-lattice are expected to be more visible. Indeed, the defect labelled "Example 3" in figure 6-13(b), in the -1.4 to -1.2 eV range (i.e. just below the valence band edge) yielded QPI patterns with strong contribution around Γ; which changed strongly and in a complex way with energy as shown in figure 6-14. This behaviour indicates that folding of energy bands did indeed occur in the R25° 1H-WSe_2/Au(111) and in a way consistent with figure 6-16(a). These types of effects are discussed in great detail in section 6-5.

The *subsurface* defects are virtually invisible in the z images, becoming visible only in the dI/dV images (see various panels in figure 6-13(a)). Their QPI patterns involve large $\vec{k}$ vectors, with CEC contours reaching towards the edge of the Brillouin zone of 1H-WSe_2, and which virtually do not disperse with energy (see figures 6-15(a) and (b)). This takes place across the whole intra-gap energy range, which is very unusual. As is discussed in section 6.5 (figure 6-22 and 6-23), the only type of states that give contributions in the band-gap of the 1H-WSe_2/Au(111) system are states resulting from hybridisation of W- or Se- states with the continuum of bulk Au states. These are the only states able to provide a tunnelling channel between deep subsurface defects and the STM tip (which probes the top surface of the heterostructure). Such states can be responsible for the creation of the "rosette" continuum observed in NanoESCA (figures 6-11(c) and 6-16(b)), which, unusually, does not exhibit obvious energy dispersion.

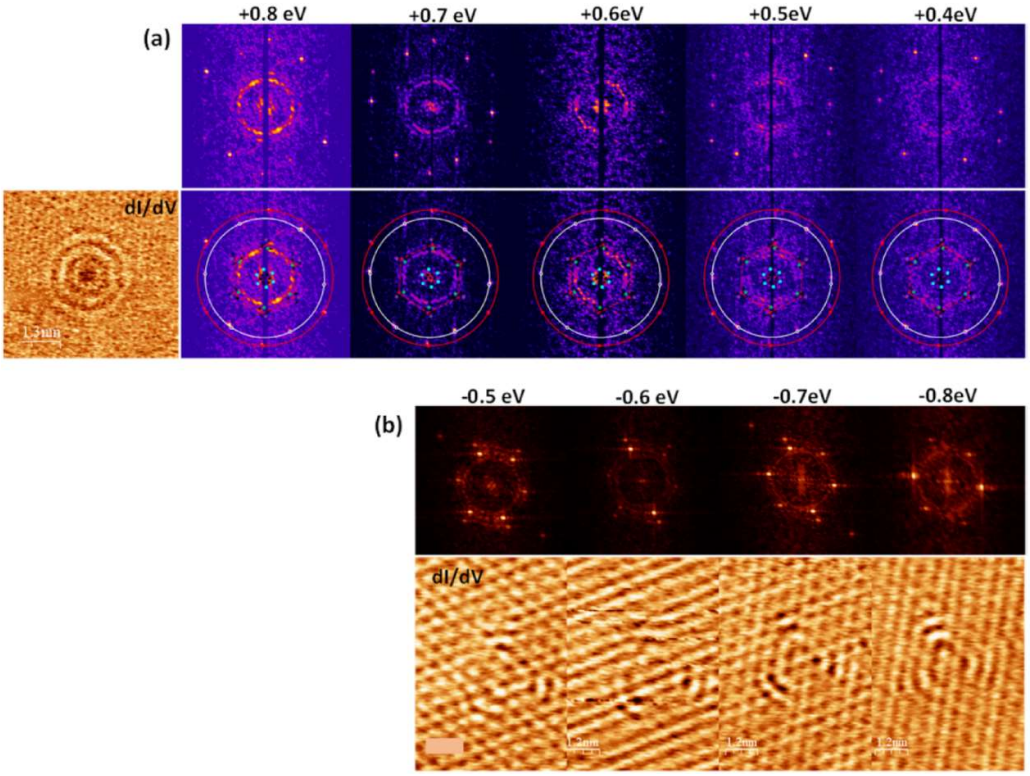

Figure 6-15. (a) and (b) dI/dV images and corresponding QPI patterns from subsurface defect showing virtually no dispersion in energy of the energy contour around the BZ.

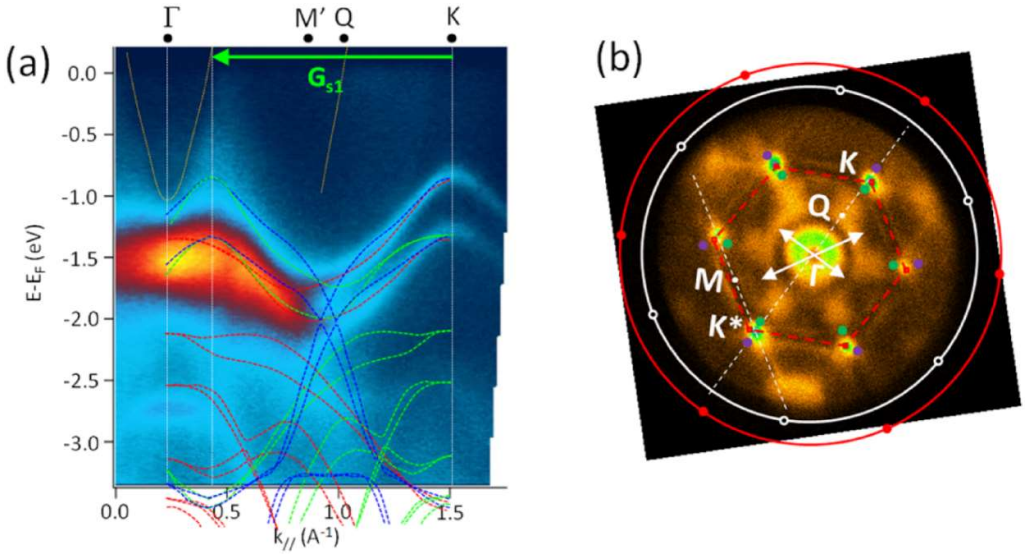

Figure 6-16. (a) Nano-ARPES energy cut with the overlaid (1x1) unfolded 1H-WSe_2 bands (red) and Umklapp folding of the (1x1) bands (green, blue). (b) NanoESCA isoenergetic cut highlighting the scattering vectors associated with the non-dispersive states.

6.5 Discussion: R25° 1H-WSe_2/Au(111) is an Umklapp, hybridised system

6.5.1 Important features revealed by ARPES and comparisons with electronic structure theory

The analysis of the moiré super-lattice presented in figure 6-1 showed that the Au(111) substrate is rotated clockwise by 25°±1° relative to the overlaid 1H-WSe_2 monolayer. Both the Au(111) surface and 1H-WSe_2 have hexagonal symmetry, with lattice constants of 2.88 Å and 3.28 Å, respectively [12], which leads to a lattice mismatch of about 1.2%. Figure 6-17 shows two orientations of 1H-WSe_2 relative to an Au(111) underlayer: (a) for a relative rotation matching our experimental case, and (b) for a 30° relative rotation. Both cases in figure 6-17 are incommensurate, with (a) leading to a relatively large approximate unit cell, while (b) can be locally described by the (√3 × √3) R30° unit cell of 1H-WSe_2. Appendix 1 identifies other potential unit cells for our experimental R25° 1H-WSe_2/Au(111) system that are closer approximations of a commensurate system than the unit cell shown in figure 6-17(a) by being larger, but are also computationally very expensive.

Because the small difference between 25° and 30° rotation angles leads to *locally very similar atomic environments* (as opposed to other selected angles which result in segregation of regions of very *different stacking* between 1H-WSe_2 and Au(111) across the surface); and because even to be able to theoretically describe the 30° rotation case, the lattice of either Au or WSe_2 needs to deform to achieve commensuration and hence periodicity, in the

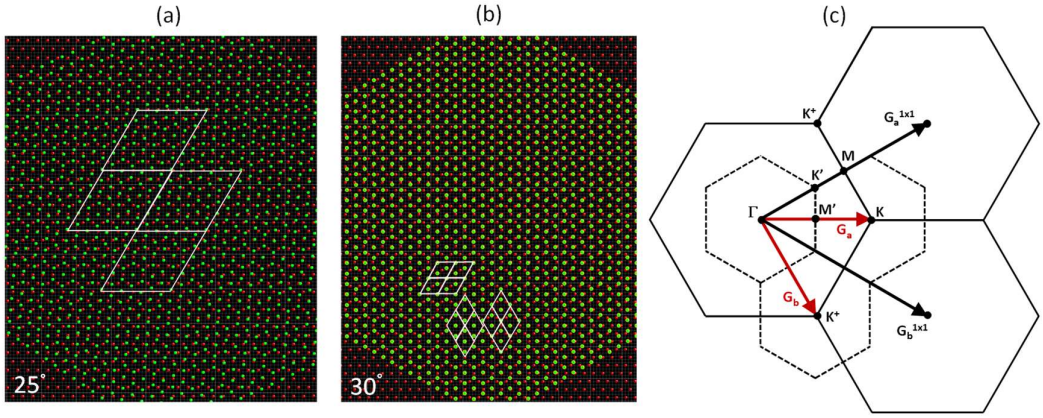

Figure 6-17. Ball-and-stick representation of a 1H-WSe_2/Au(111) heterostructure: for 25° (a), and 30° (b) relative layer rotation respectively. For simplicity, only Se (green) atoms are shown for 1H-WSe_2, with Au atoms in red. Several associated unit cells are shown across the layers. (c) Brillouin zone (BZ) for the original, unfolded 1x1 1H-WSe_2 (continuous lines), and reduced BZ corresponding to the (√3 × √3) R30° 1H-WSe_2 system (dashed lines). Unit cell vectors in the reciprocal space are also shown in black and red, respectively (see also main text).

following we consider the commensurate (√3 × √3) R30° 1H-WSe_2/Au(111) system, where the Au lattice is the one that has been adjusted. As will be demonstrated, this adjusted, approximate system is capable of revealing many important features of our experimental system; while departures from it will be highlighted where appropriate.

Figure 6-17(c) compares the original BZ of (1x1) 1H-WSe_2 (i.e. the "un-folded" monolayer) with the reduced BZ of the (√3 × √3) R30° system, which is a perfectly "folded" system, where the original K points are folded onto Γ, and the M' points of the super-lattice system are midway between Γ and K.

Two theoretical descriptions of the (√3 × √3) R30° 1H-WSe_2 were then used, as provided by Dr Simon Crampin. A tight-binding (TB) method (using parameterisation resulting from density function theory (DFT) calculations) for the *isolated* WSe_2 monolayer was used to

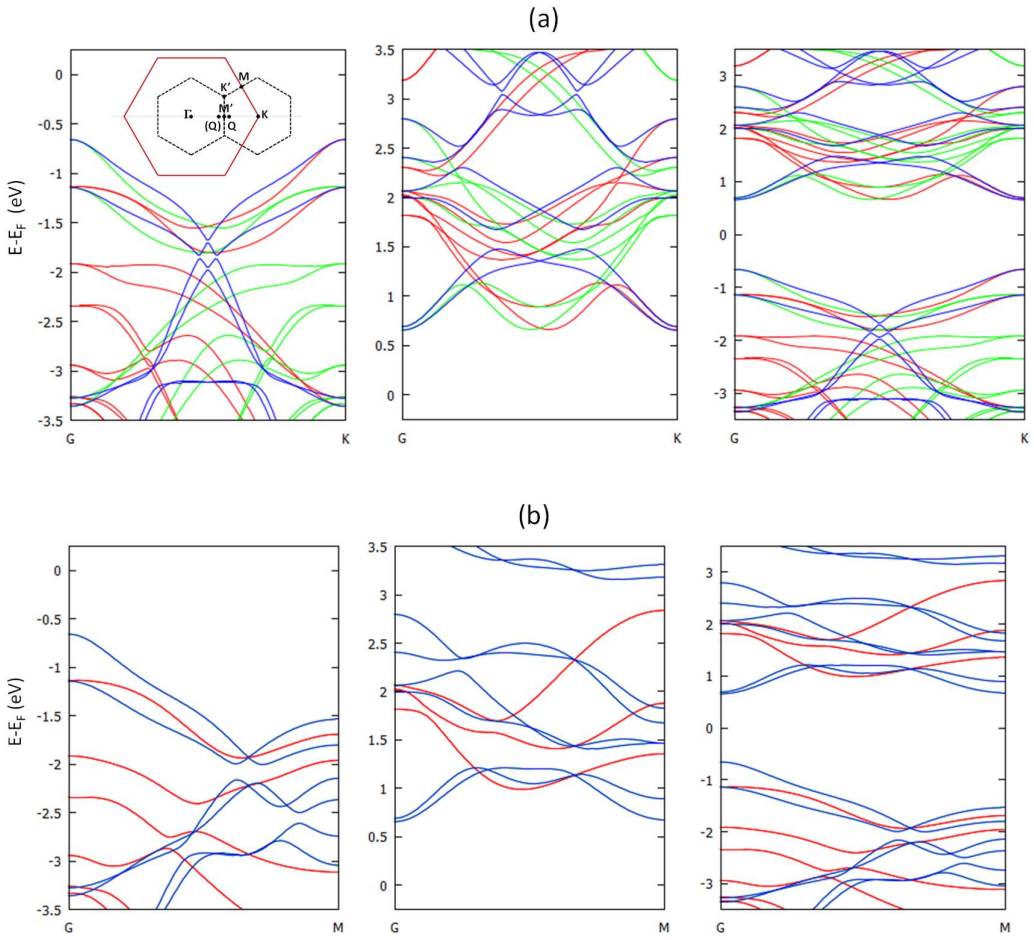

Figure 6-18. DFT calculations with spin-orbit coupling of energy bands of the isolated (√3 × √3) R30° 1H-WSe_2 system, shown along the main symmetry directions of the un-folded (1x1) 1H-WSe_2 system, Γ-K (a) and Γ-M (b), respectively. Green and blue refer to bands resulting from the folding of the original bands of (1x1) 1H-WSe_2, shown in red, by the two reciprocal unit cell vectors of the (√3 × √3) R30°system, as described in main text.

reveal effects on the electronic bands of 1H-WSe_2 resulting purely from zone folding; this was compared with an entirely DFT-based calculation, using the plane wave pseudopotential code CASTEP [13] and spin-orbit coupling, and excellent agreement was obtained between the two. A DFT calculation for the (√3 × √3) R30° 1H-WSe_2/Au(111) system, using a supercell of 3 (√3 × √3) R30° 1H-WSe_2 unit cells with 11 layers of 4 Au atoms per layer as the substrate, was also performed in order to reveal how the WSe_2 monolayer and Au substrate interact and perturb each other. DFT simulations for the isolated (1x1) 1H-WSe_2 were also performed for various comparisons. For this, the (1x1) 1H-WSe_2 structure was relaxed using a 15x15x1 k point sampling and 675 eV basis set. The resulting lattice parameter was 3.3018 Å, and the W-Se distance in the normal direction was 1.682 Å.

Figure 6-18 shows a DFT calculation of the isolated (√3 × √3) R30° 1H-WSe_2 monolayer revealing the effect of "folding" by the super-lattice on the (1x1) 1H-WSe_2. Spin-orbit coupling was included, with the giant spin-split effects being reproduced as expected. The resulting electronic structure was found to be indistinguishable from applying translation operations with the super-lattice reciprocal unit cell vectors $\vec{G}_a$ and $\vec{G}_b$ (marked with red on Figure 6-17(c)) to the bands of the isolated (1x1) 1H-WSe_2. This means that any moiré reciprocal super-lattice vector, i.e. a linear combination of $\vec{G}_a$ and $\vec{G}_b$, produces bands that superpose perfectly onto those obtained just by the folding with the principal, shortest reciprocal vectors of the super-lattice.

Colour coding visualises the effect of the folding by $\vec{G}_a$ and $\vec{G}_b$: in addition to the original, unfolded bands of (1x1) 1H-WSe_2 shown in red, there are "mirror" bands around M' (which lie on the original Γ-K direction, see figure 6-17(c) and inset of figure 6-18(a), left), shown in green, resulting from the folding with $\vec{G}_a$:

$$E^{green}_{\sqrt{3}\times\sqrt{3}}(\vec{k}) = E_{1\times1}(\vec{k} - \vec{G}_a), \tag{6-4}$$

and bands resulting from the folding with $\vec{G}_b$, shown in blue:

$$E^{blue}_{\sqrt{3}\times\sqrt{3}}(\vec{k}) = E_{1\times1}(\vec{k} - \vec{G}_b), \tag{6-5}$$

where $\vec{G}_a = (\vec{G}_a^{1\times1} + \vec{G}_b^{1\times1})/3$ and $\vec{G}_b = (\vec{G}_a^{1\times1} - 2\vec{G}_b^{1\times1})/3$, with vectors in the reciprocal space as defined in figure 6-17(c).

In particular, as shown by figure 6-18(a), left, this process folds the bands from K of the original (1x1) system onto Γ; and doubles the number of bands at the valence band edge (VBE) around the M' point of the reduced BZ, producing an effect similar to what has been observed in the Nano-ARPES data (see figure 6-11(a)). Mid-way along Γ-K, i.e. around the M' point (see inset of figure 6-18(a), left), there is a strong concentration of bands across the entire valence band (VB), which is also observed in Nano-ARPES.

Along the original Γ-M direction, the folding by $\vec{G}_a$ and $\vec{G}_b$ produces degenerate bands, shown in blue, in addition to the original (1x1) bands shown in red:

$$E^{blue}_{\sqrt{3}\times\sqrt{3}}(\vec{k}) = E_{1\times1}(\vec{k} - \vec{G}_a) = E_{1\times1}(\vec{k} - \vec{G}_b) \quad (6\text{-}6)$$

Along this direction too there is again strong resemblance between the bands of our experimental R25° system (see figure 6-12) and those obtained in figure 6-18(b), left, for the (√3 × √3) R30° system.

With this observation, we can now advance the hypothesis that our experimental R25° 1H-WSe_2/Au(111) can be described as an *Umklapp*-ed system, where the behaviour is dominated by the shortest vectors of the moiré super-lattice, such as $\vec{G}_{s1}$, which are slightly different in length than $\vec{G}_a$ and $\vec{G}_b$ (see vector definitions in figures 6-1 and 6-17(c)). This leads to an "imperfect" folding, in that the original bands from K are now folded onto $\vec{k}$ points slightly offset from Γ, as shown in figure 6-19. Were the system better described as a periodic system with a large unit cell, as shown in figure 6-17(a), the signature of a very small BZ should have been visible in both ARPES and STM/FT-STS. As we will see further below, the STM-derived data, such as quasi-particle interference (QPI) from scattering on defects, does not support the hypothesis of a super-lattice system with a large unit cell (i.e. with small BZ), but is rather consistent with a *weakly interacting*, *Umklapp* system that roughly reflects the symmetry of the "reduced" (√3 × √3) R30°system.

The next point to assess was how and to what extent the 1H-WSe_2 monolayer and the Au(111) substrate perturb each other. For this, electronic structure calculations were performed using the CASTEP ab-initio plane wave pseudopotential DFT code [13]. The exchange-correlation effects were treated within the generalised gradient approximation using the Perdew, Burke and Ernzerhof (PBE) parameterisation Ultrasoft pseudopotentials generated "on-the-fly" [14], with a 475 eV cut-off for relaxing structures (force threshold of 0.05 eV/Å) and 300 eV cut-off for calculating band-structures were used. Figures 6-20 and 6-21 below show the energy bands of the (√3 × √3) R30° 1H-WSe_2/Au(111) with the Au modelled as an 11 layer thin film and WSe_2 placed on one face only. Here the directions on which the bands are shown correspond to the high symmetry directions of the reduced BZ (which relate to the original, un-folded (1x1) BZ as shown in figure 6-17(c)). Because of a highly increased computational cost, spin effects were not included in these calculations but are not expected to affect the resulting trends in any substantial way.

Figure 6-20 compares the isolated (√3 × √3) R30° 1H-WSe_2 monolayer with the (√3 × √3) R30° 1H-WSe_2/Au(111) system, with the relative W, Se (top or interface layer), or Au contents of each of the electronic bands highlighted in different panels by blue dots of size proportional to the respective weighting; hence one can understand the atomic origin of each of the

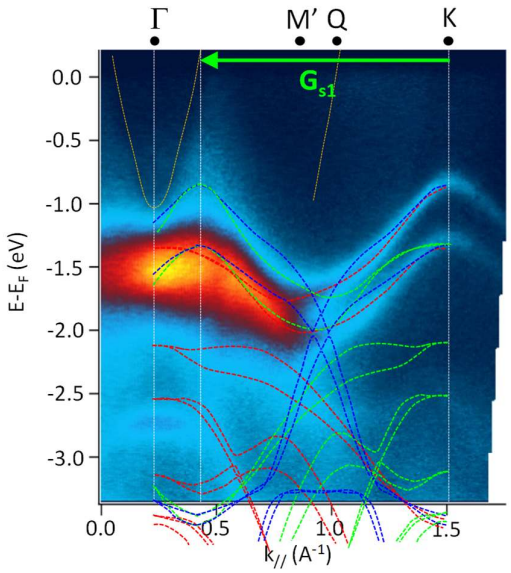

Figure 6-19. Qualitative explanation of the occurrence of additional bands in the measured R25° 1H-WSe_2/Au(111) system via Umklapp of the original (1x1) 1H-WSe_2 by $\vec{G}_{s1}$, the shortest 1st order vector of the moiré superstructure. The same colour coding as described in the main text has been observed. Folding along the Γ-K direction is shown.

electronic bands. The (√3 × √3) R30° band-structure of 1H-WSe_2 is largely preserved in the energy regions above the conduction and valence band edges. The main effect caused by the proximity of the Au substrate is that it induces WSe_2-Au hybridisation in the original band gap region of 1H-WSe_2, rendering the super-lattice system *metallic*, thus supporting the NanoESCA data from figures 6-8(b) and 6-9(c); a detailed description of which WSe_2 states are predominantly involved in hybridisation is given in figure 6-21 below. Relatively minor effects of mini-gap opening also occur within the original CB and VB of (√3 × √3) R30°.

Note that when comparing experimental measurements and the energies of electronic states calculated using density functional theory (DFT) it is necessary to bear in mind that the DFT Kohn-Sham eigenvalues (or differences between them) are not formally related to quasi-particle excitation energies, although there are similarities between the Schrodinger-like equation describing the latter and the Kohn-Sham equations. Indeed empirically, the two sets of energies are often remarkably similar, which has enabled the widespread use of DFT Kohn-Sham eigenvalues to interpret experimental spectroscopies. The differences typically increase moving away from the Fermi energy. In the case of semiconductors, DFT normally underestimates the band gap (compare figures 6-20 and 6-3), which to a first approximation can be accounted for by the "scissor-operator", a rigid shift of the conduction band upward relative to the valence band [15]. Hence, when comparing the DFT simulations with the experimental ARPES and STM/FT-STS/QPI data in the following instead of referring to absolute energy levels we will refer to energies relative to CB and VB edges (where these

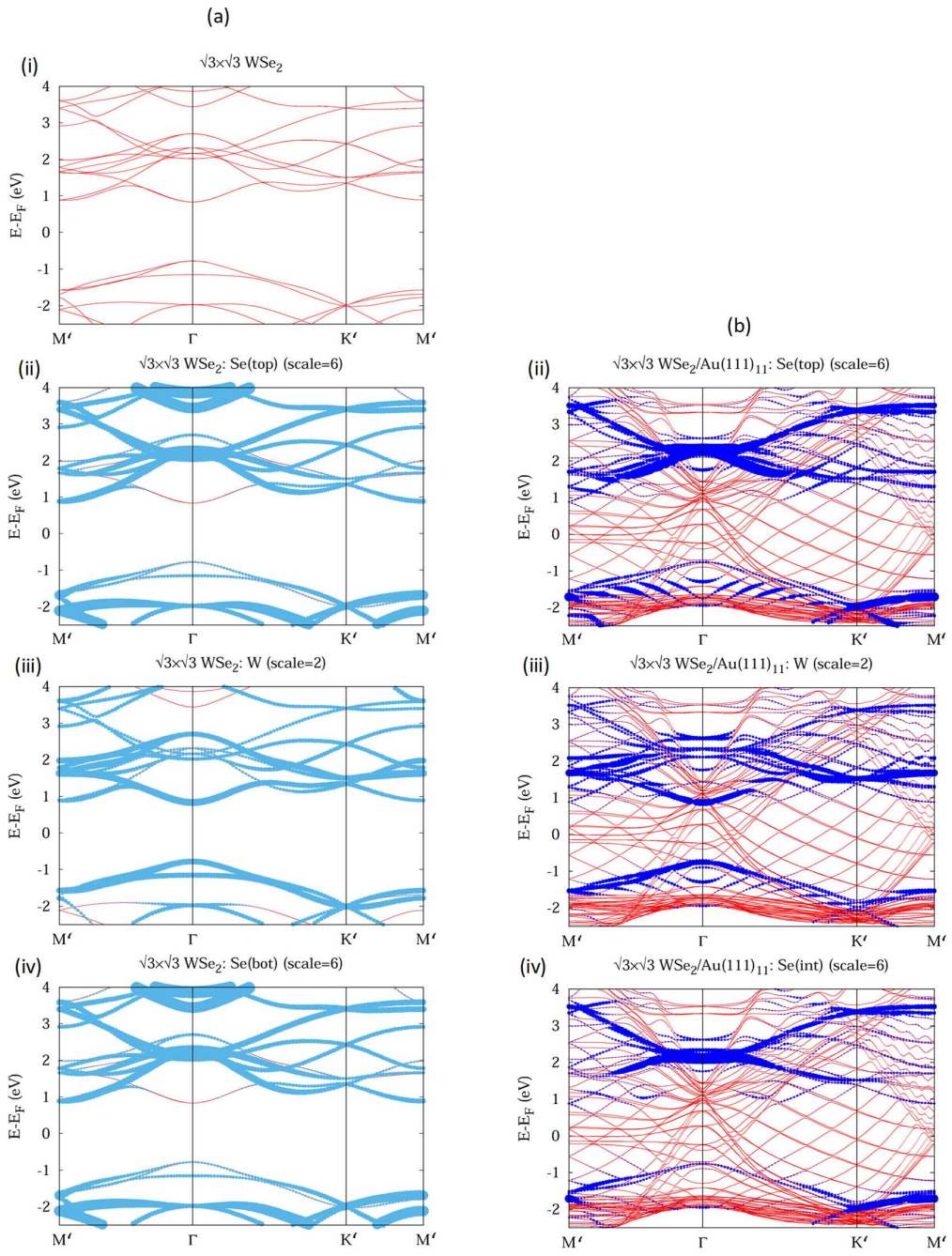

Figure 6-20. Comparison between (a) the energy bands of the isolated (√3 × √3) R30° 1H-WSe_2 system, and (b) those of the (√3 × √3) R30° 1H-WSe_2/Au(111) system. DFT calculations without spin-coupling. Representation along the main symmetry directions of the folded (√3 × √3) R30° 1H-WSe_2 system. Blue coloured disks of varying radius reflect the projected density of the associated state onto the orbitals of the W, Se or Au located in different planes of the 1H-WSe_2/Au(111) heterostructure, monolayer or the 11-layer Au substrate. The position of the Shockley SS of the interfacial Au layer modified by the 1H-WSe_2 overlayer has been located above the CBE of the (√3 × √3) R30° WSe_2 system.

edges refer to the WSe_2 -derived bands despite the system having acquired a metallic character).

Figure 6-21 shows the effect of WSe_2 on the band-structure of Au(111), with the contributions of interface, middle and bottom of the 11 Au layers to the electronic structure of the whole system highlighted in separate panels (i to iii). The most striking observation is that the Shockley surface state (SS) of Au(111), which is present on the interface Au layer, is

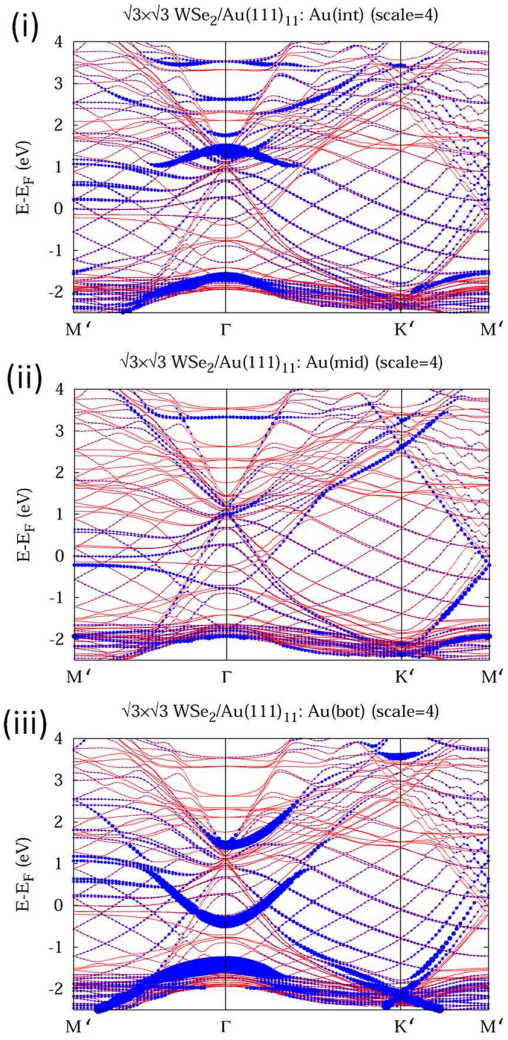

Figure 6-21. Energy bands of the (√3 × √3) R30° 1H-WSe_2/Au(111) system with 11 layers of Au, with focus on the Au-derived bands shown in blue. These calculations are twinned with those from figure 6-20; an increased amplitude of Au-derived states is symbolised by blue disks of increased radius, for the interfacial Au layer, a middle one, and the very bottom one. The position of the Au(111) Shockley SS is affected by the 1H-WSe_2 overlayer and has been located above the CBE of the (√3 × √3) R30° WSe_2 system. The finite number of Au layers is reflected by the discrete number of Au-derived bands instead of a continuum of states.

now pushed from below the Fermi energy to high up in the CB of WSe_2, from around the 1 to 1.3 eV energy range as shown in figure 6-21, panel (i), and disperses "negatively" (i.e. the *k* radius of the isoenergetic contour of the state decreases with increasing energy). The bottom Au layer displays the Shockley SS around -0.5 eV as expected as this layer is too far away from the WSe_2 overlayer to be significantly affected; together with the d-orbital derived deep states. Appendix 2 shows a set of simulations of the (√3 × √3) R30° 1H-WSe_2/Au(111) system where the separation between WSe_2 and the Au(111) substrate is artificially increased in steps of 0.5 Å: even a minor increase from the equilibrium separation distance by just 0.5 Å significantly lowers the energy of the Shockley SS on the interface layer, and changes its dispersion with energy from "negative" to "positive"; while a separation distance increased by 2 Å recovers the expected below-Fermi energy position and negative dispersion of the Shockley SS. Note that these calculations where only 11 layers of Au were considered display discrete Au energy levels across the band-structure instead of the expected bulk band-derived continuum. The effect of such a continuum will be briefly addressed in the discussion of figure 6-22.

Hybrid states can be distinguished from the "native" W or Se states by comparing the bands of the isolated (√3 × √3) R30° 1H-WSe_2 system (figure 6-22(a)) with those of the (√3 × √3) R30° 1H-WSe_2/Au(111) (figures 6-22(b)-(c)). Hence, hybridisation between Au-derived and WSe_2-derived states result in orbital weight on the WSe_2 monolayer of electronic states *within* the energy range of the WSe_2 band gap. The relative amplitude decreases with increasing energy separation from the WSe_2 conduction and valence band edges and varies across the Brillouin zone. Hence, going down in energy from the CBE, hybrid states with pronounced W character are found (i) mid-way along Γ-K and extending towards Q of the original, unfolded (1x1) WSe_2 BZ, and (ii) in the half part of the Γ-K' segment (aligned with the Γ-M direction in the (1x1) BZ), and all along the K'-M' directions; closing a contour in the $\vec{k}$ space. On the VB side, W content in hybrid states is found predominantly mid-way in both Γ-M' and Γ-K' directions. Going down in energy from CBE hybrid states with Se character are found notably around M' in the (√3 × √3) R30° BZ, i.e. mid-way along Γ-K and extending towards Q of the (1x1) WSe_2 BZ; (ii) close to K' on the Γ-K' (Γ-M) line; and (iii) to a lesser extent in pockets close to M' on the K'-M' lines. On the VB side, Se content is concentrated in a region mid-way along the Γ-K' segment, and covering the first half of the Γ-M' segment (on the Γ-K direction of the (1x1) WSe_2 BZ). These $\vec{k}$ regions where substantial amplitude of either W and Se-derived states exists are plotted across the BZ of the (1x1) WSe_2 system, resulting in a very qualitative picture of what occurs close to the CB and VB edges - as shown in figure 6-23, centre and right panels. Despite the qualitative nature of this description one can note the striking resemblance of this amplitude map for the VB side with the isoenergetic cuts in the intra-gap region of WSe_2 recorded in NanoESCA; hence, the "rosette" with intensity spots around the Q points of the (1x1) WSe_2 BZ observed in NanoESCA can be tentatively assigned as originating from WSe_2/Au hybridisation.

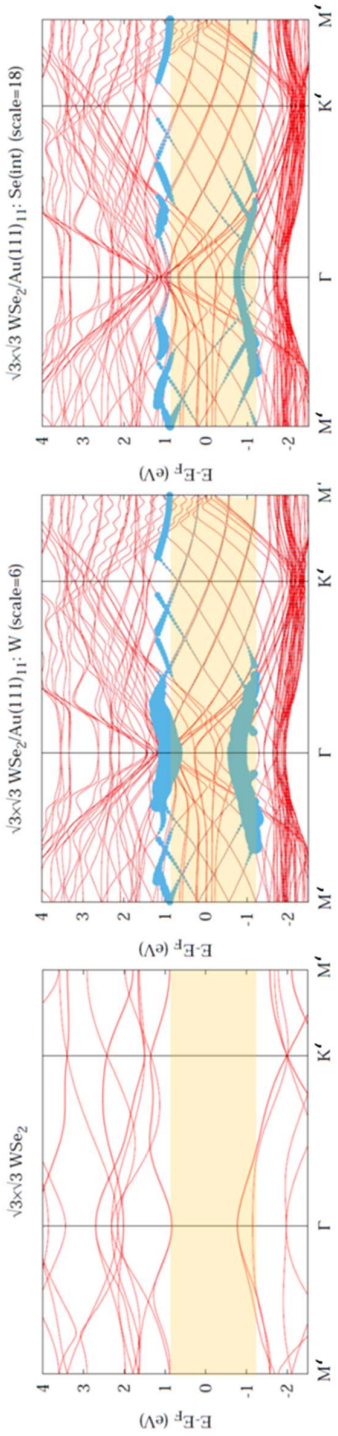

Figure 6-22. Analysis of presence of intra-gap hybrid states in the (√3 × √3) R30° 1H-WSe_2/Au(111) system: origin and distribution across the $\vec{k}$ space. The intra-gap region is highlighted by a yellow rectangle. Superimposed upon the energy bands in the energy range –1.2 to +1.2 eV are disks whose radius reflects the projected density of the associated state onto the orbitals of the atoms within the different planes of the WSe_2 monolayer, such as W (middle panel) and interface Se (right panel) layers. The panel titles also state an additional scale factor applied to each layer. There are no such hybrid states in the isolated (√3 × √3) R30° 1H-WSe_2 system in this energy range (left panel).

Note that in the current DFT calculations where an 11 Au layer thin film is used, the Au energy states form a set of discrete energy bands, whereas a fully-extended Au substrate would have a continuum of states. The projected weights of the discrete bands displayed in figure 6-22 are indicative of the degree to which hybridisation of the continuum of states of an extended Au crystal with the states of the monolayer WSe_2 will produce WSe_2 character in similar intra-band-gap regions of E-$\vec{k}$ space. That the states within the "rosette" form in fact a continuum, and are not discrete quasi-particle states, might explain their noted negligible energy dispersion, as visualized in figures 6-8(b) and 6-9(c).

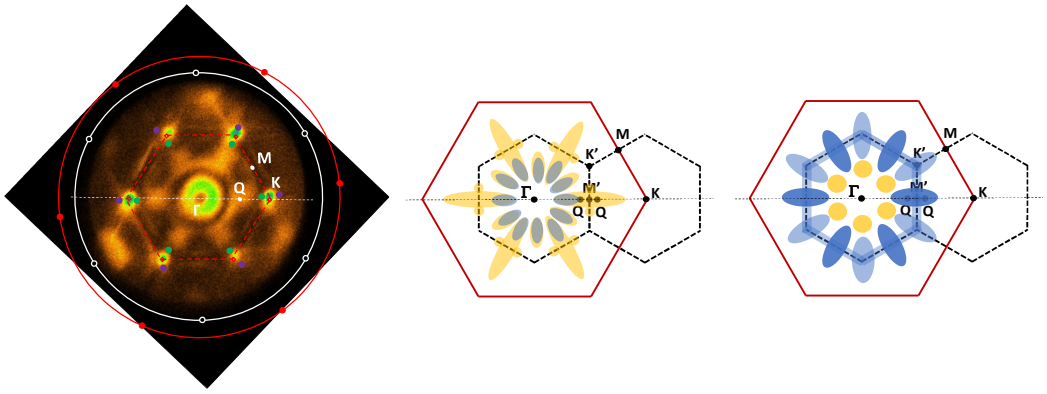

Figure 6-23. Qualitative mapping across the original (1x1) WSe_2 BZ of regions with substantial orbital weights of W (in blue) and interfacial Se-derived (in yellow) states, for the (√3 × √3) R30° 1H-WSe_2/Au(111) system, and as resulting from the DFT simulations in figure 6-22; for top of the VB (middle panel), and bottom of CB (right panel). Left panel: an experimental isoenergetic contour for the experimental R25° 1H-WSe_2/Au(111) system from NanoESCA and for energies close to the VBE.

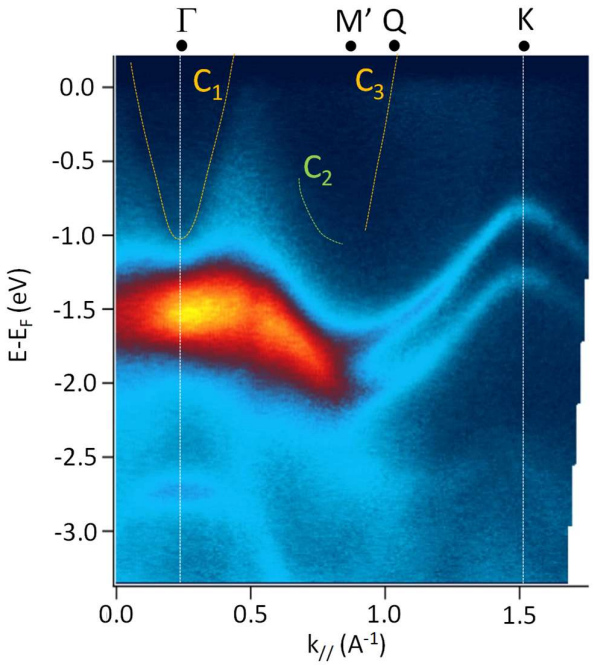

Figure 6-24. Nano-ARPES. C_2 and C_3 contours point to the rough location of WSe_2/Au(111) hybrid states, from the VBE up to the Fermi energy. Example is given along the Γ-K *direction.*

Based on the analysis from figures 6-22 and 6-23, figure 6-24 identifies on the Nano-ARPES data that above the VBE, hybrid states with mixed W and Se character can be found at the left of contour C_2; as well as at the right of contour C_3, around the Q points of the (1x1) WSe_2 system, where the character is predominantly Se-derived.

6.5.2 Important features of electronic structure and quasi-particle scattering as revealed by FT-STS.

The nature of the experimental R25° 1H-WSe_2/Au(111) system and how best to describe it can be further probed by utilising QPI from scattering on defects in FT-STS. In general, the approach is to correlate the complementary FT-STS information with the knowledge of the system revealed by ARPES and theory, to fully characterize this real-life, complex system. Figure 6-24 compiles an FFT portfolio from sets of isoenergetic $\mathrm{d}I/\mathrm{d}V$ images covering the -1.4 to +1.9 eV range, or alternatively, from the VB to the CB of 1H-WSe_2. These images were 32 x 32 nm^2 in size, leading to a point resolution in $\vec{k}$ space of $2\pi/L \approx 0.19$ nm^{-1} (where L is the side of the image). As the system appears to be metallic by virtue of hybrid WSe_2/Au(111) states that span the whole energy gap and cross the Fermi energy, band-bending effects as usually encountered in semiconductor systems are not an issue.

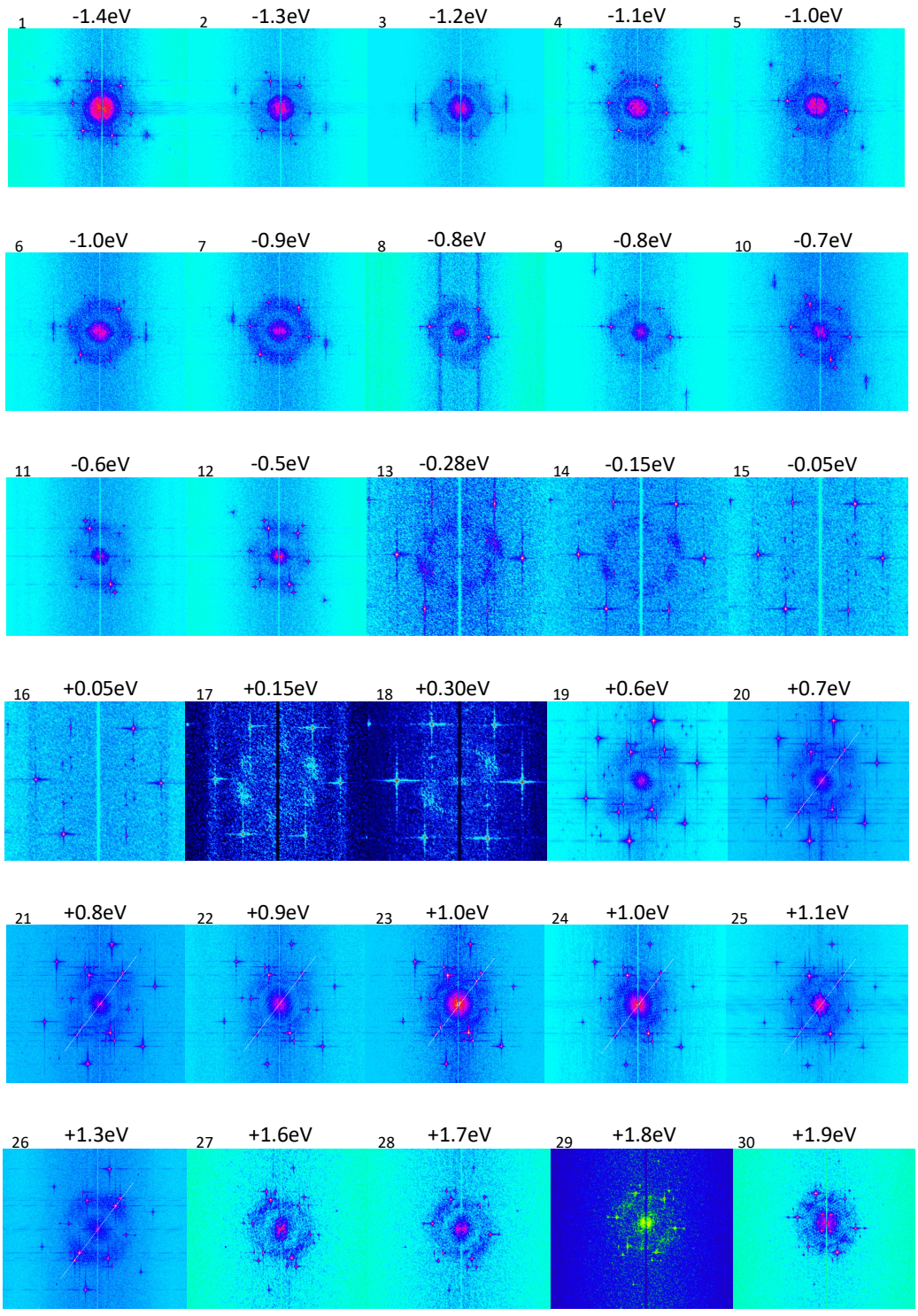

Figure 6-24. Characterization of the R25° 1H-WSe_2/Au(111) system via FFTs of isoenergetic dI/dV maps over a wide energy range. A series of 30 FFTs (indexed at the top left corner) evolve continuously from -1.4 to +1.9 eV while the system spans from the VB through the intra-gap region and into the CB, grouping into several energy ranges where distinct characteristics are exhibited. Invariant features, explained in figure 6-25, are related to the invariant moiré superstructure or atomic lattices, and are used for both reference and calibration purposes.

As shown in section 6.4, there are several types of defects that give quite different signatures in FT-STS, and are distinguished by their depth/location within the multi-layered, complex 1H-WSe_2/Au(111) system. For this reason, FFTs of isoenergetic $\mathrm{dI/dV}$ maps can suffer from larger variability than a simple reference system, such as the 2D electron gas formed at the surface of Au(111). Nevertheless, by analysing multiple sets of data over the same energy range, or which overlap at least at some energy values, there is confidence that a generic picture emerges as shown in figure 6-24. Figure 6-25 together with figure 6-1 from section 6.1 show some invariant (energy independent) features in $\vec{k}$ space of the FFT image – such as the position of WSe_2 or Au lattice points, the points corresponding to the shortest, 1st order reciprocal vectors of the moiré superstructure, $\vec{G}_{s1}$ and $\vec{G}_{s2}$, or the corners of the BZ of the unfolded (1x1) 1H-WSe_2 system – relative to which the various scattering processes we uncover can be referred to. This is similar to the analysis of the QPI processes from defects on the surface of bulk crystals of WSe_2 described in Chapter 5.

In figure 6-24, the FFT slides between -1.4 eV to -0.8 eV reveal strong contributions from *disk-like* $\vec{k}$ spectral regions centred around Γ, whose lateral spread decreases by moving towards the Fermi energy, located here at 0 eV. The VBE has been identified from both Nano-ARPES/NanoESCA (section 6.3 and figure 6-19) and STS (section 6.2) as being located around -0.8 eV. Below this VBE, a strong concentration of states is expected around Γ, resulting from the Umklapp, "imperfect" folding of states from the original K points of the (1x1) 1H-WSe_2 system (see figure 6-19); hence, the agreement with the FT-STS observations. The -0.8 to + 0.8 eV energy range falls within the intra-gap region, where hybridised WSe_2/Au(111) states are expected to lie (see discussion in section 6.5.1), and for which the dominant spectral features lie within *ring-like* contours of *large* $\vec{k}$ radius/lateral extent, tending towards the Γ-K distance. As discussed in the following section, such behaviour appears to be consistent with the presence of hybridised states belonging to a continuum. Very close to the Fermi energy, such as in the -0.3 to +0.3 eV range, the spectral features group into "pockets" located around the K points of the (1x1) 1H-WSe_2 system, indicating the dominance of inter-valley scattering processes (as introduced in Chapter 3). Moreover, the intensity of these features is very weak, which appears to be consistent with the decrease in W- and Se-content for energy states that depart from the VB or CB edges, as illustrated in figure 6-22. This also suggests that, indeed, scattering processes that take place within the intra-gap energy window must be mediated by the WSe_2/Au hybrid states, and are not controlled by states with solely Au content. Above about +0.8 eV and up to about +1.3 eV, a non-monotonic variation in the contribution of low $\vec{k}$ states to Γ-centred "disks" is observed; this can be the result of the interplay between W-related states located at the CBE and the "pushed-up" Shockley SS of Au which disperse differently with energy (see below). Finally, at higher

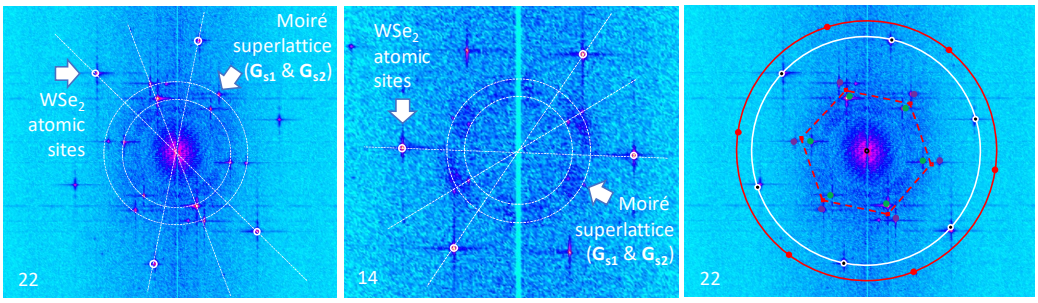

Figure 6-25. Invariant features of FFTs of isoenergetic dI/dV maps of the R25° 1H-WSe_2/Au(111) system. Examples given (left and middle panels) - using FFT nos. 14 and 22 from the series in figure 6-24 - reveal different scanning directions during dI/dV image acquisition, resulting in the rotation of the reference features. The panel at right also shows, overlaid, the BZ of the (1x1) 1H-WSe_2 system (red, dashed contour).

energies, tending towards 1.9 eV (the largest energy probed in this work) more complex FFT patterns with reminiscence of hexagonal symmetry emerge (see for example FTT no. 30), which will be linked in subsequent sections to the specifics of a "folded" electronic band-structure.

In the following sub-sections, further evidence is given in support of the scenarios proposed above.

Evidence of folding of energy bands by the moiré super-lattice

Above the conduction band edge (CBE): from +0.8 to + 1.3 eV

Figure 6-26 presents the main contributors in this energy range to the DFT-calculated energy bands of (√3 × √3) R30° 1H-WSe_2/Au(111) side-by-side: on the one hand, there is the negatively-dispersing, "pushed-up" Shockley SS arising from the interfacial Au layer, highlighted in green in the left panel; and on the other hand, at lower energy there is the original K state of (1x1) 1H-WSe_2 folded onto Gamma by the (√3 × √3) R30° super-lattice and dispersing positively with energy, also highlighted in green in the right panel.

Figure 6-27 shows $\vec{k}$ -line profiles extracted from the appropriate FFT "slides" (nos. 20 to 26) from figure 6-24 on the directions indicated by the white, thin lines that connect diagonally opposite moiré super-lattice points and pass through Γ. The width of the central disk-like feature increases from almost nothing at +1.3 eV to about two thirds of the width of (1x1) 1H-WSe_2 BZ at +1 eV, hence, suggesting intra-valley scattering involving a flat band (i.e. with

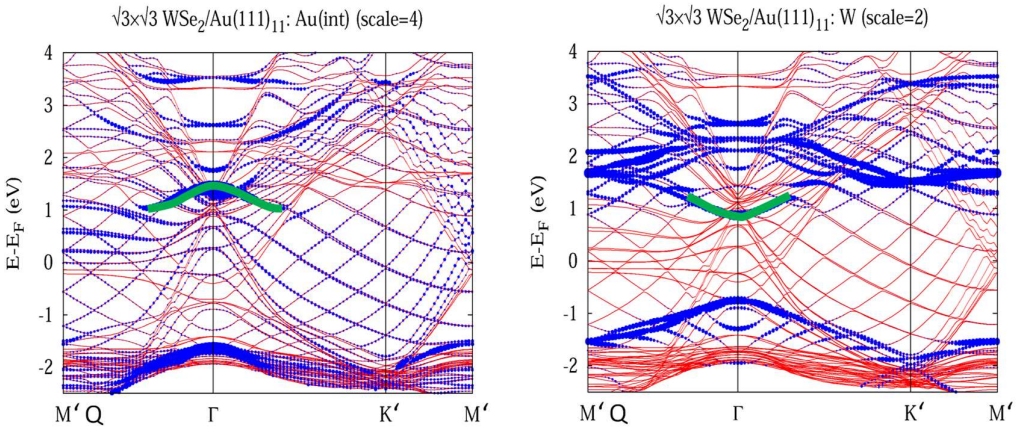

Figure 6-26. Dominant states present around Γ at intermediate energies above the CBE. Location of the Shockley SS associated with the interfacial Au layer, green in left panel; and that of a W-derived state resulting from folding onto Γ of states originally located at K in the (1x1) 1H-WSe_2 system.

very large dispersion). This behaviour agrees with the characteristics of the flattened Shockley SS of the interfacial Au layer shown in figure 6-26. As energy decreases to +0.8 eV, the width of the disk starts decreasing again indicating intra-valley scattering involving a state centred on Γ that disperses positively. This observation has implications as in the unfolded (1x1) 1H-WSe_2 system there is no such state at energies around the CBE, therefore this is a clear signature that energy band folding occurred in the WSe_2 system by the moiré super-lattice.

Complementing this data that arises from the analysis of full images (where not all scattering centres scatter in the same frequency range, as discussed at the beginning of the section), the behaviour of an appropriately selected, individual defect was also analysed over the same energy range. Figure 6-28 shows a defect that most certainly lies within the WSe_2 monolayer (i.e. it does not lie at the interface between WSe_2 and the Au substrate, nor is this a defect in the Au substrate). Future targeted simulations would be able to confirm its exact atomic configuration, but this is not required to reach the conclusions below. The top row of figure 6-28 shows the QPI patterns for this defect at energies in the range of interest. Besides

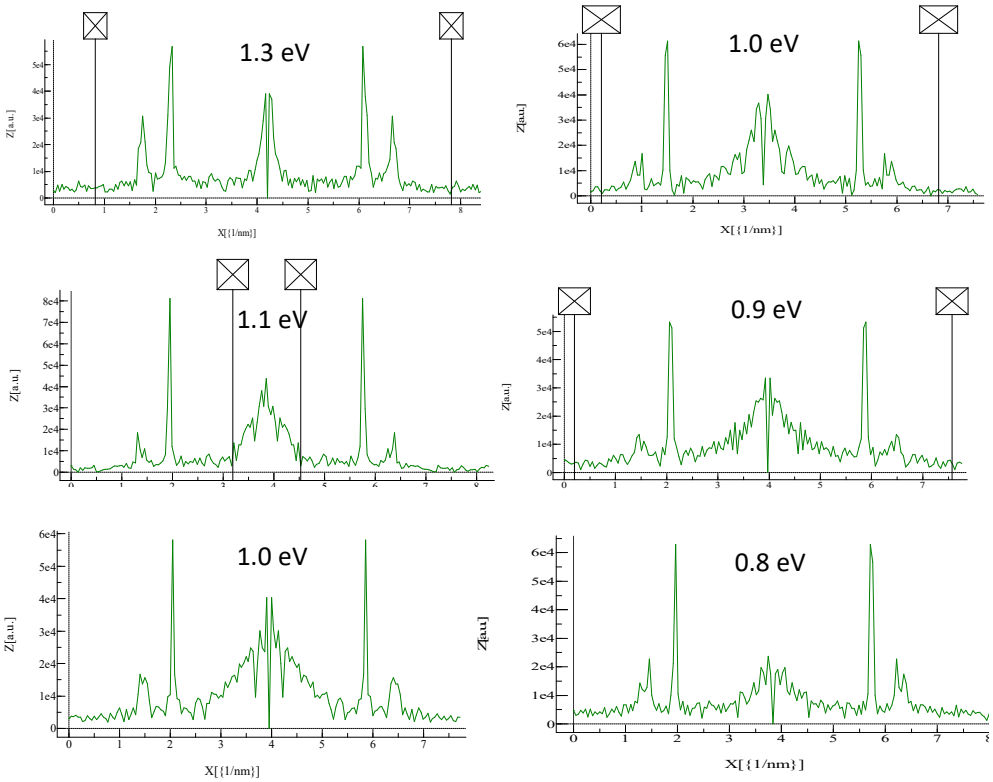

Figure 6-27. $\vec{k}$ -line profiles extracted from FFT "slides" nos. 26 to 21. The broad, disk-like feature around Γ *disperses with energy, while the sharp pair of peaks surrounding it do not disperse with energy as it corresponds to the moiré super-lattice.*

the 6-fold symmetry appearance of the pattern at 1.3 eV, reminiscent of scattering from small defects in unfolded 1H- or 2H- WSe_2 (see Chapter 5), the development of a ring-like contour around Γ is followed instead. This ring contour grows from very small to large when the energy decreases from 1.3 to 1 eV, and then decreases again when the energy decreases to +0.9 eV. This is the same trend as shown in figure 6-27 above, consistent with the probing of the two bands highlighted in figure 6-26.

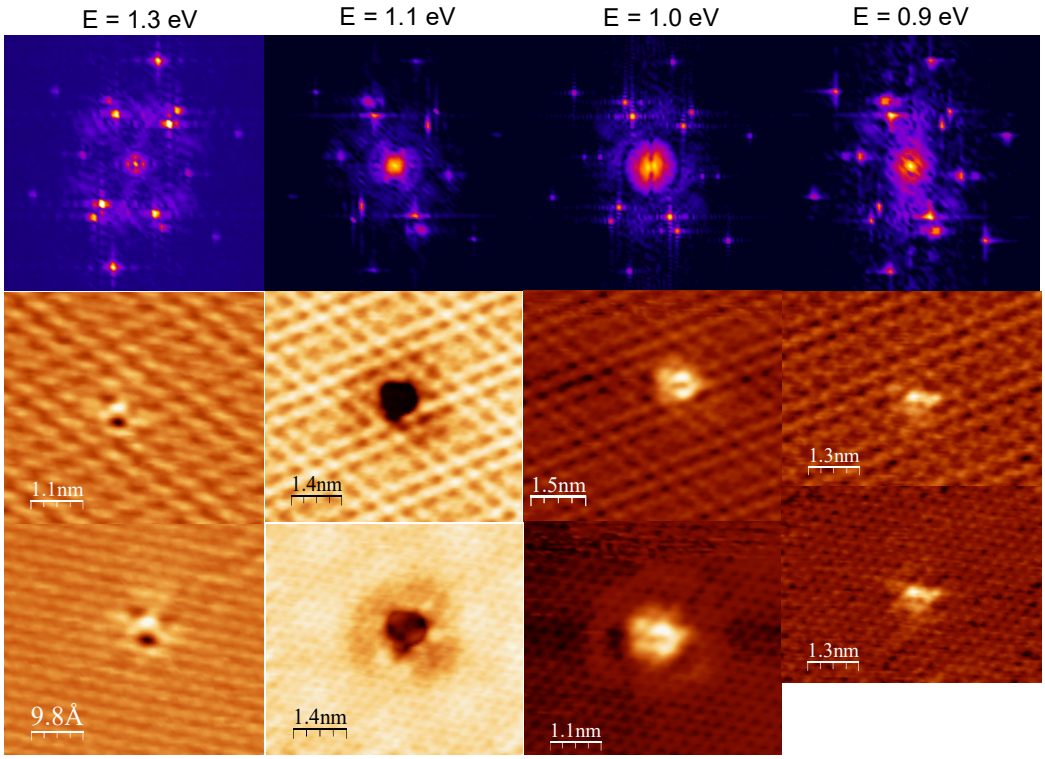

Figure 6-28. FT-STS derived QPI patterns from defect within the WSe_2 layer for energies between +1.3 and 0.9 eV. Top row: series of QPI patterns. FFTs show the QPI specific to the defect, together with the atomic lattice of WSe_2 and the moiré super-lattice. Middle row: dI/dV images of the defect. Bottom row: dI/dV images of the defect from which the contribution of the moiré super-lattice was filtered out.

High energy bands: from +1.6 to +1.9 eV

This energy range is of special interest. The reason for this is revealed by combining information from figure 6-26, left panel, which shows the energy bands with dominant Au character that correspond to the interfacial Au layer; and figure 6-29 which compares the isolated (√3 × √3) R30° 1H-WSe_2 system with its (√3 × √3) R30° 1H-WSe_2/Au(111) counterpart, focusing on the W- and top Se-derived energy bands. Within the energy band marked in yellow, which exceeds the energy range of our measurements, there are virtually no dominant Au-derived bands, except the one at very low $\vec{k}$ marked with a green star. This means that in this energy range there is an opportunity to probe bands that belong almost exclusively to WSe_2, with both W and top Se-character, which occur in $\vec{k}$ regions in the vicinity of M' (i.e. close to the Q point of the original (1x1) BZ) and K' points of the reduced BZ of the (√3 × √3) R30° super-lattice. These energy bands are also significantly like those of the isolated (√3 × √3) R30° 1H-WSe_2 system shown by the left panel of Figure 6-29.

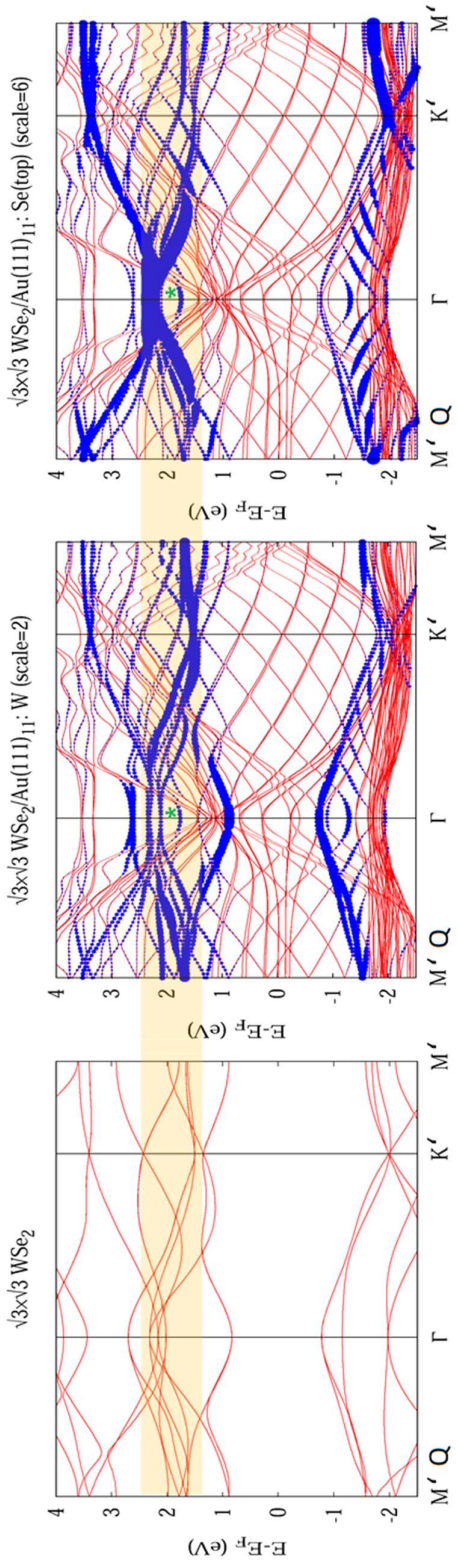

Figure 6-29. States at high energy in both isolated (√3 × √3) *R30° 1H-WSe_2 and* (√3 × √3) *R30° 1H-WSe_2/Au(111). In the latter case, states originate almost exclusively from WSe_2; only the state marked with a green star, at low* $\vec{k}$*, has significant Au orbital weighting.*

Consequently, FT-STS measurements in this energy range can reveal the folding of the WSe_2 bands by the moiré super-lattice in a region where this occurs without ambiguity.

Figure 6-30 shows the QPI pattern resulting from scattering on an individual defect at E = +1.9 eV. This defect has already been introduced by in section 6.4; it is not a point defect, has an apparent lateral size of about 1 nm, and is visible in both z (STM) and $\mathrm{d}I/\mathrm{d}V$ images. Its QPI pattern reveals several contours of approximate hexagonal symmetry, that are

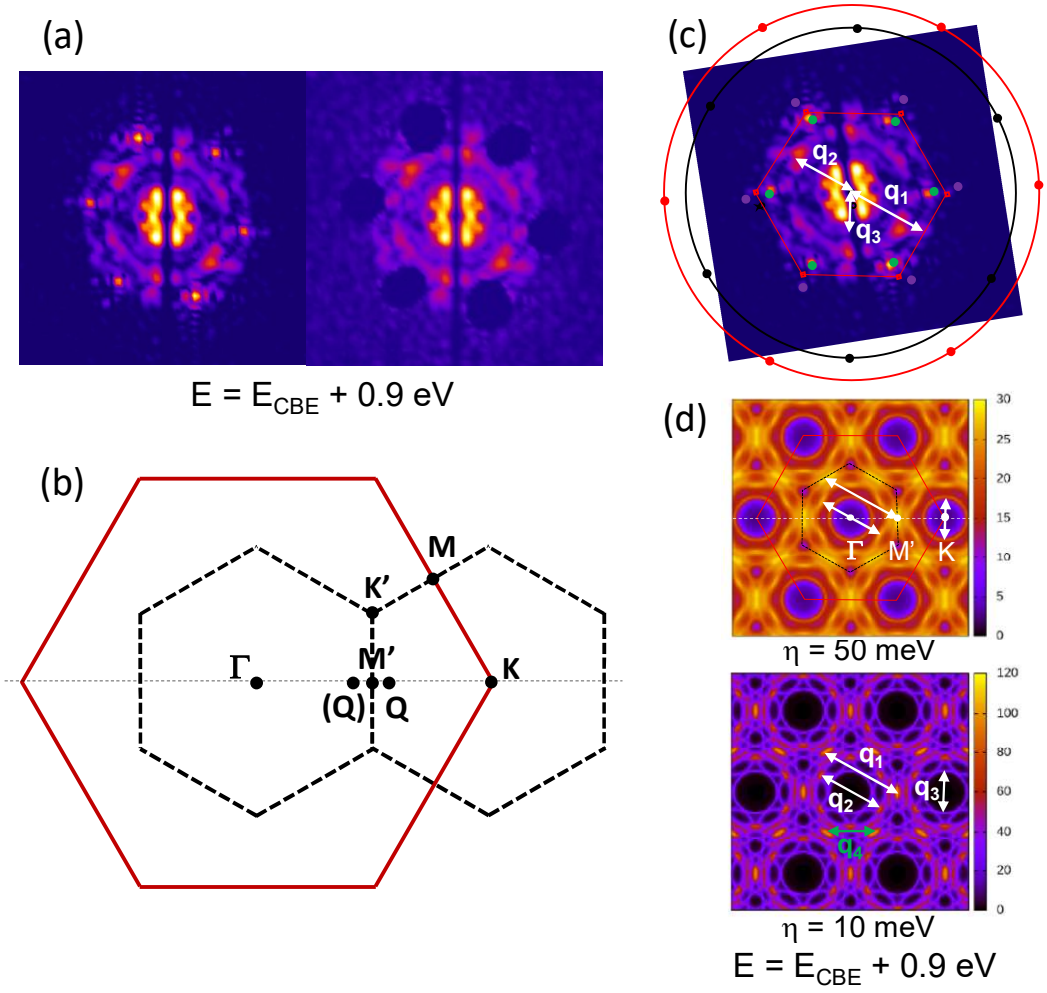

Figure 6-30. FT-STS derived QPI pattern from individual defect at high energy (E = 1.9 eV) (a), with the moiré super-lattice points shown (left) and after filtering them out (right). (b) Reduced (√3 × √3) R30° *(in black), and unfolded (1x1) (in red) BZs, with relevant high symmetry points. (c) Exchanged* $\vec{q}$ *vectors determined from the various experimental contours making the QPI. (d) Mapping the exchanged* $\vec{q}$ *vectors onto relevant regions of the band-derived isoenergetic contours of the folded* (√3 × √3) *R30° 1H-*WSe_2 *system. Two energy-broadened cases were considered (η= 10 and 50 meV). Reduced and unfolded BZs are superimposed for clarity.*

centred around Γ and cover a relatively broad spectral range in the $\vec{k}$ space. The QPI pattern is complex, with some of the contours revealing regions of high intensity along the Γ-M direction of the (1x1) BZ. The contours with smaller $\vec{k}$ have a clear hexagonal shape, while some degree of anisotropy and warping is observed in the larger $\vec{k}$ contours. Figure 6-30(c) shows the dominant $\vec{q}$ scattering vectors from this defect obtained from its QPI pattern. Figure 6-30(d) shows energy-band derived isoenergetic contours corresponding to (√3 × √3) R30° 1H-WSe_2 using the DFT calculations with spin-orbit coupling shown in Figure 6-18. Two cases were considered, with less (η = 10 meV) or more (η= 50 meV) broadening, where the larger broadening corresponds more closely to the experimental conditions, as bias modulation of about 50 meV was applied to the STM tip during the FT-STS experiment when acquiring $\mathrm{dI/dV}$ images. By comparing (c) with (d) one can see how the experimentally-derived exchanged $\vec{q}$ vectors map onto both the reduced BZ of the (√3 × √3) R30° system, and the original (1x1) one. The two BZs are shown superimposed (with black and red lines, respectively) onto the isoenergetic contours in (d). In (d), the experimental $\vec{q}$ vectors either map transitions well between regions of enhanced density of states (such as $\vec{q}_1$) or correspond to back-scattering between closed isoenergetic contours (such as $\vec{q}_2$ and $\vec{q}_3$).

In contrast, the experimental $\vec{q}$ vectors determined in figure 6-30(c) do not map well onto the band isoenergetic contours of the unfolded (1x1) 1H-WSe_2 system, as shown in Figure 6-31. There are no possible transitions that approximate $\vec{q}_1$ and $\vec{q}_2$ well, and the only relevant

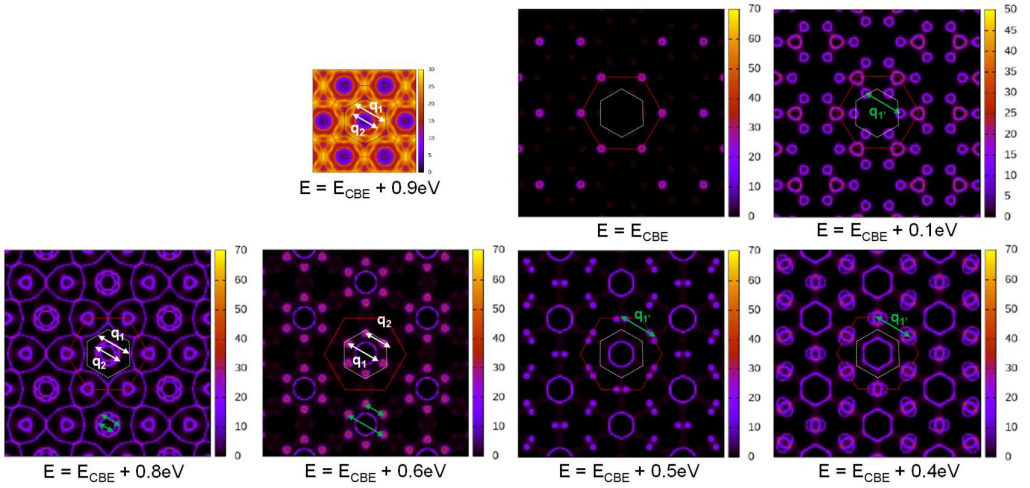

Figure 6-31. Mapping the experimental exchanged $\vec{q}$ vectors determined in figure 6-30(c) onto band-derived isoenergetic contours of the unfolded (1x1) 1H-WSe_2 system, for various energies. None of the possible transitions allowed by this system, shown in green, appear to match the size and orientation of the exchanged $\vec{q}$ vectors. An isoenergetic contour corresponding to the folded (√3 × √3) *R30° 1H-WSe_2 system was also shown (top row, left) to show the contrast in the unit cell sizes of the two systems. The same $\vec{k}$ scale was used for both folded (reduced) and unfolded systems.*

$\vec{q}$ in figure 6-31 is $\vec{q}_1'$ (shown in green and corresponding to spin-conserving intervalley scattering), but this is too large in magnitude. In addition, the overall shape and orientation of the isoenergetic contours of the (1x1) system does not closely match the experimental QPI pattern from 6-30 (a).

Finally, the same defect investigated in figure 6-30 was also probed at lower energies, and the resulting series of QPI patterns is shown in figure 6-32(b). The QPI patterns evolve into more complex shapes at lower energies, that enlarge the spectral $\vec{k}$ range involved. $\vec{q}_1$

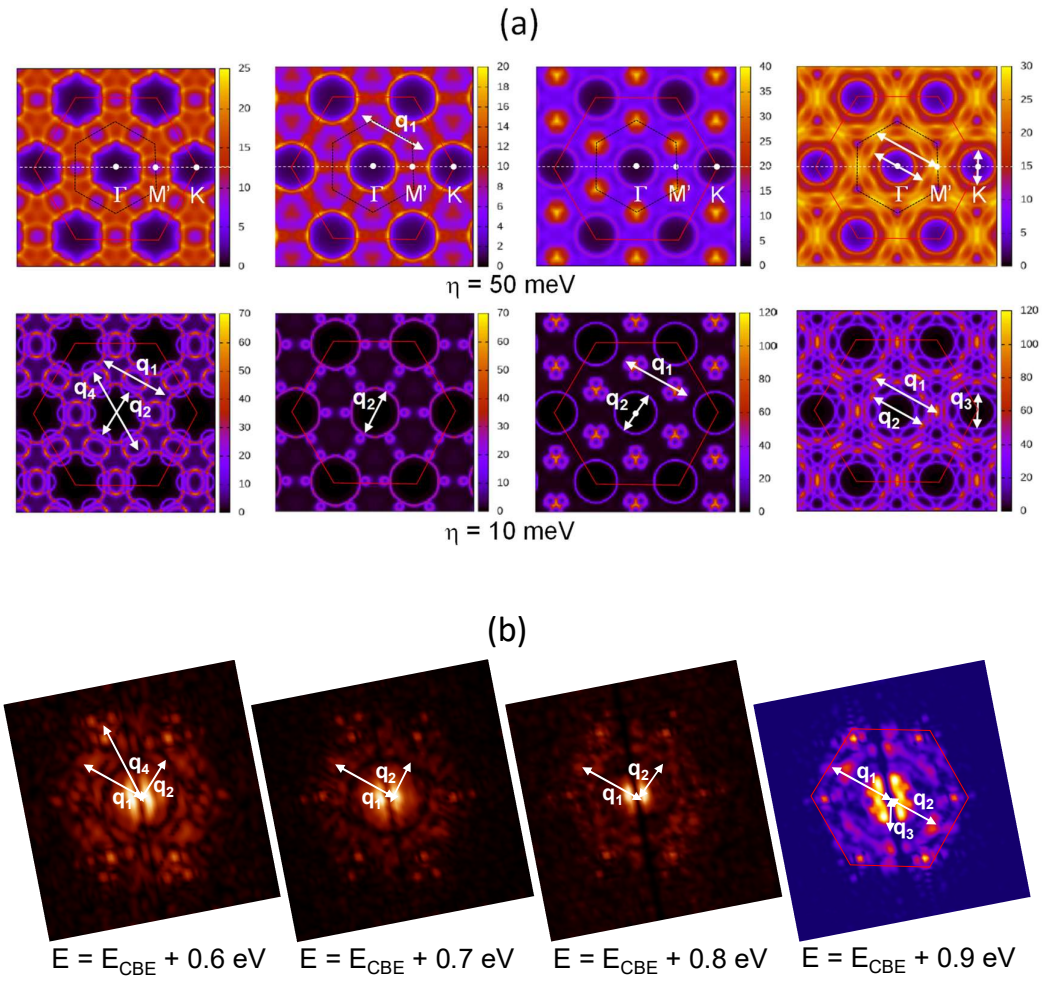

Figure 6-32. FT-STS series of QPI patterns from the same defect probed over an energy range. (b) experimental results. (a) DFT-based, band-derived isoenergetic contours for the (√3 × √3) *R30° 1H-WSe_2 system at different energies mapping the experiment. Two energy-broadened cases were considered (η = 10 and 50 meV).*

remains a dominant exchanged scattering vector, while $\vec{q}_2$, $\vec{q}_3$ and $\vec{q}_4$ closely map various possible transitions within the isoenergetic contours of the folded (√3 × √3) R30° 1H-WSe_2 at the respective energies (see figure 6-32(a)).

6.6. Conclusions

An in-depth analysis of a 1H-WSe_2/Au(111) heterostructure has been carried out to identify the observed complex electronic structure from STS and ARPES measurements. There are two main results; the first is that the incommensurate R25° 1H-WSe_2/Au(111) can be considered a weakly interacting Umklapp system, where the bands of the (1x1) WSe_2 are folded back by the R25° 1H-WSe_2/Au(111) primary reciprocal unit cell vectors; the second, is that the Au and WSe_2 bands hybridise in the intragap region to form continuum states, that retain their WSe_2 nature; as indicated by QPI maps showing that the hybridised states are non-dispersive and weaken the further from the WSe_2 band edges they get. These states result in the metallic nature of the heterostructure, supported by the NanoESCA measurements. Further QPI observations have determined the location of the “pushed-up” Shockley surface state of Au(111), which is supported by the theory; as well as direct evidence of the band-folding via probing at an energy with no dominant Au bands; allowing just the scattering from WSe_2 states, with the scattering vectors matching well with the calculated (√3 × √3) R30° 1H-WSe_2 CECs, and not at all with the (1x1) bands.

References

[1] Dendzik M, Bruix A, Michiardi M, Ngankeu A S, Bianchi M, Miwa J A, Hammer B, Hofmann P and Sanders C E (2017) Substrate-induced semiconductor-to-metal transition in monolayer WS2. *Physical Review B.* **96** 6

[2] Dendzik M, Michiardi M, Sanders C, Bianchi M, Miwa J A, Gronborg S S, Lauritsen J V, Bruix A, Hammer B and Hofmann P (2015) Growth and electronic structure of epitaxial single-layer WS2 on Au(111). *Physical Review B.* **92** 7

[3] Bradley A J, Ugeda M M, da Jornada F H, Qiu D Y, Ruan W, Zhang Y, Wickenburg S, Riss A, Lu J, Mo S K, Hussain Z, Shen Z X, Louie S G and Crommie M F (2015) Probing the role of interlayer coupling and coulomb interactions on electronic structure in few-layer MoSe2 nanostructures. *Nano Letters.* **15** 2594-9

[4] Yun W S, Han S W, Hong S C, Kim I G and Lee J D (2012) Thickness and strain effects on electronic structures of transition metal dichalcogenides: 2H-M X-2 semiconductors (M = Mo, W; X = S, Se, Te). *Physical Review B.* **85** 5

[5] Zhao W J, Ghorannevis Z, Chu L Q, Toh M L, Kloc C, Tan P H and Eda G (2013) Evolution of electronic structure in atomically thin sheets of WS2 and WSe2. *ACS Nano.* **7** 791-7

[6] Zhang C D, Chen Y X, Johnson A, Li M Y, Li L J, Mende P C, Feenstra R M and Shih C K (2015) Probing critical point energies of transition metal dichalcogenides: surprising indirect gap of single layer WSe2. *Nano Letters.* **15** 6494-500

[7] Xiao D, Liu G B, Feng W X, Xu X D and Yao W (2012) Coupled spin and valley physics in monolayers of MoS2 and other group-VI dichalcogenides. *Physical Review Letters.* **108** 5

[8] Hsu W T, Lu L S, Wang D, Huang J K, Li M Y, Chang T R, Chou Y C, Juang Z Y, Jeng H T, Li L J and Chang W H (2017) Evidence of indirect gap in monolayer WSe2. *Nature Communications.* **8** 7

[9] Basagni A, Vasseur G, Pignedoli C A, Vilas-Varela M, Pena D, Nicolas L, Vitali L, Lobo-Checa J, de Oteyza D G, Sedona F, Casarin M, Ortega J E and Sambi M (2016) Tunable band alignment with unperturbed carrier mobility of on-surface synthesized organic semiconducting wires. *ACS Nano* **10** 2644-51

[10] Mo S K, Hwang C, Zhang Y, Fanciulli M, Muff S, Dil J H, Shen Z X and Hussain Z (2016) Spin-resolved photoemission study of epitaxially grown Ws2 and WSe2 thin films. *Journal of Physics: Condensed Matter.* **28** 7

[11] Tanabe I, Komesu T, Le D, Rawal T B, Schwier E F, Zheng M T, Kojima Y, Iwasawa H, Shimada K, Rahman T S and Dowben P A (2016) The symmetry-resolved electronic structure of 2H-WSe2(0001). *Journal of Physics: Condensed Matter.* **28** 10

[12] Wang Y Y, Yang R X, Quhe R, Zhong H X, Cong L X, Ye M, Ni Z Y, Song Z G, Yang J B, Shi J J, Li J and Lu J (2016) Does p-type Ohmic contact exist in WSe2-metal interfaces? *Nanoscale.* **8** 1179-91

[13] Clark S J, Segall M D, Pickard C J, Hasnip P J, Probert M J, Refson K and Payne M C (2005) First principles methods using CASTEP. *Zeitschrift Fur Kristallographie.* **220** 567-70

[14] Perdew J P, Burke K and Ernzerhof M (1996) Generalized gradient approximation made simple. *Physical Review Letters.* **77** 3865-8

[15] Godby R W (1992) Exchange and correlation in solids. *Topics in Applied Physics.* **69** 51-88

Chapter 7

Phase transitions and doping of TMDs

The ability of TMDs to adopt multiple different phases each with their own electronic properties is of great interest in material science. The three phases that WSe_2 can adopt are ideally suited for different roles. The 2H semiconducting phase has shown good performance as FET devices [1] and promising behaviour as a waveguide to control the valley degree of freedom [2]. The metallic 1T has been used as an electrode material in supercapacitor devices [3], and the distorted 1T' phase exhibits the quantum spin Hall effect (QSHE) [4]. Clearly control over the phase and the ability to mix them would enable the opportunity for many novel heterostructure.

There are many ways to cause a phase transition, but one of particular interest here is the substrate mediated transition. Since the previous chapter dealt with a heterostructure with a modified electronic structure, the possibility of this route to achieve this comes to mind. First the mechanisms by which these transitions happen is investigated. The properties of the heterostructure are contrasted with those of different phases to determine if it has undergone a transition. However, the observations show clearly it has not. The question remains then why this is the case when very similar systems have done.

The second part investigates another method to tune the electronic properties of surfaces through using dopants. Pd atoms were evaporated onto the surface of a WSe_2 crystal and STM used to examine the effect on the electronic structure. From this we can see that the Pd atoms cause a local influence on the LDOS and induce states into the bandgap edges, resulting in a small reduction. The overall picture of the crystal is that is it p-doped by the coverage of Pd nanoclusters. The sample was then annealed, and a large-scale reconstruction of the surface was observed. One such region exhibited structural properties of the 1T' phase, indicating a phase transition through intercalation or alloying with the Pd dopants.

7.1. Conditions and mechanism for phase transition

The most stable phase of WSe_2 is the 2H phase which is the most commonly examined and used. However, the other phases can be prepared like in the case of MBE grown 1T' WSe_2 where the low temperature growth was the key factor [5], or the intercalation of Li ions into MoS_2 during exfoliation resulting in the metastable 1T phase [6, 7]. These other phases are

of interest for different reasons as their properties differ from the 2H phase as discussed in chapter 2.

Another route to phase transition is that which is substrate induced. This is of particular interest here as the WSe_2/Au(111) heterostructure discussed in the previous chapter is a potential candidate for this situation. The phase transition of both MoS_2 on Cu, Ag, Au and graphene, and WSe_2 on Au has been investigated, with all displaying a 2H to 1T' change [8, 9]. In these experiments' CVD grown MoS_2 and WSe_2 were chemically transferred onto their respective substrates and annealed at temperatures between 200°C and 550°C. The annealing is described as the key mechanism for the phase transition on the substrates, with the highest yield of 85.7% 1T' phase on MoS_2/Cu for 300°C, and 58.8% on WSe_2/Au(111) upon annealing at 250°C. This annealing is said to enhance the interfacial hybridisation between layers resulting in an increase in the interfacial binding energy and charge transfer from the substrate. This charge transfer is visualised in the calculations of figure 7-1(a), showing an increased charge accumulation for substrates with stronger hybridisation and therefore a higher proportion of phase transition. The effect of annealing for the MoS_2/Cu case is shown to further enhance this charge transfer. This charge transfer leads to a weakening of the metal-chalcogen bond strength which further facilitates the phase transition process through a decreased phase transition barrier [8].

The proposed mechanism for phase transition is shown by figure 7-1(b), illustrating the 2H phase as 00 and the 1T' phase as 06 with the intermediate stages in between. The 1T' phase

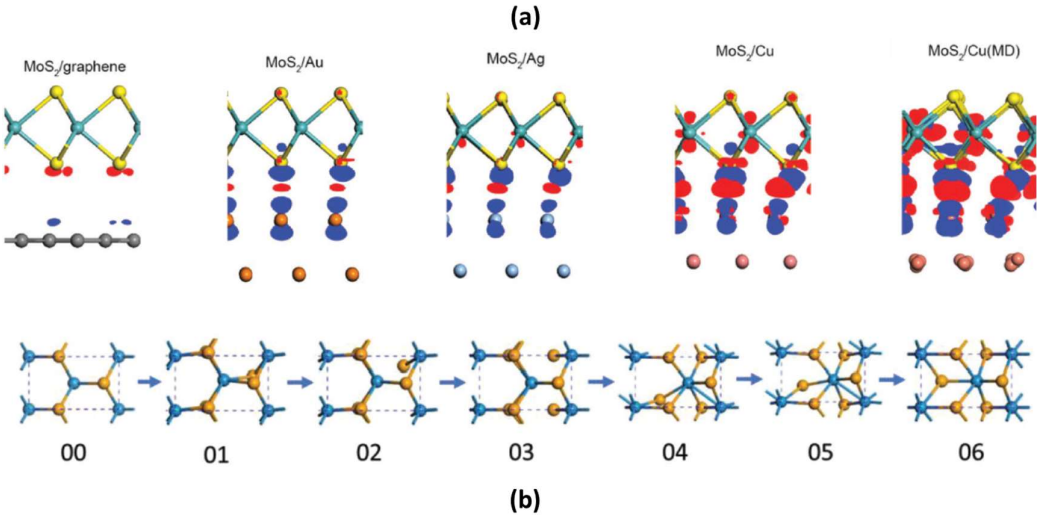

Figure 7-1. (a) Charge density difference plots for 1H-MoS_2 on different substrates. The red marks the charge accumulation regions and the blue the charge depletion. The graphene is 1/10 the isosurface values of the others due to the low hybridisation between layers. The final plot on the right indicates the difference annealing makes, showing an increase in the charge transfer from the substrate to the MoS_2. (b) Top down view of the proposed mechanism from the 2H phase (00) to the 1T' phase (06). [8]

was found to have a lower equilibrium energy than the 1T phase hence why it is not part of the route. This transition involves the edge chalcogen atoms shifting to the centre, the centre chalcogen atoms sliding to the edge along the zig-zag direction, and the metal atom moving slightly along the armchair direction.

In a similar case to this, a 2H-1T phase transition was observed instead in a MoS_2 decorated with Au nanoparticles (NP) [10]. Here an incident laser was used to excite plasmons in the Au NP which then generate hot electrons which were transferred to the underlying MoS_2, as displayed in the schematic shown in figure 7-2(a). The mechanism proposed for this is shown in figure 7-2(b), which in a similar way to the 1T' transition, sees the destabilisation of the 2H

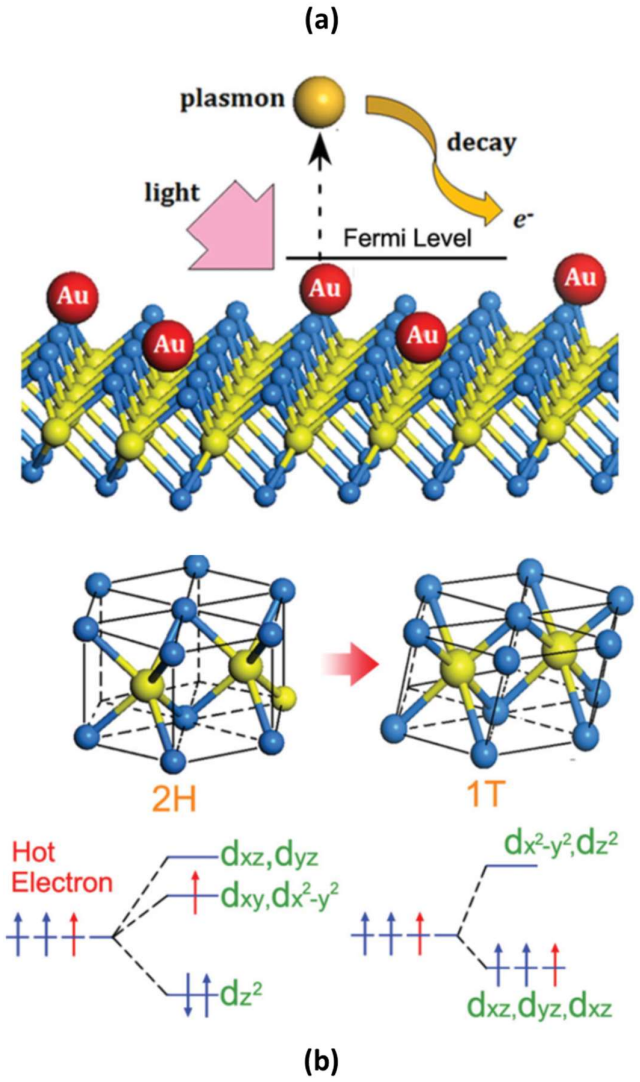

Figure 7-2. (a) Diagram of the process to induce phase transition in a MoS_2 surface decorated with Au nanoparticles. (b) Mechanism of phase transition, detailing the addition of the hot electrons (red arrows) into the Mo orbitals which destabilises the 2H phase, and results in the transition to the 1T phase. [10]

lattice through charge transfer. The population of the metal 4d-orbitals leads to the phase transition, resulting in the incomplete occupation of three orbitals which gives the metallic nature to the 1T phase. This also decreases the lattice stability. A point to note is that both in this case and the above-mentioned transition to 1T', the same Raman peaks were referred to as characteristic peaks for both phases. While there are other studies of 1T' with the same Raman peaks [11], other studies have observed the 1T phase using different techniques such as STM [7], and STEM [12] showing that this metastable phase can also be formed.

The 1T phase is metastable and expected to decay back to the 2H phase within 5 days in ambient conditions [7] or from annealing [12, 13], but can be stabilised through charge transfer from butyl groups [3]. This means that sufficient charge transfer from a substrate or overlayer could enable a stabilised phase transition to 1T. Further support for this comes

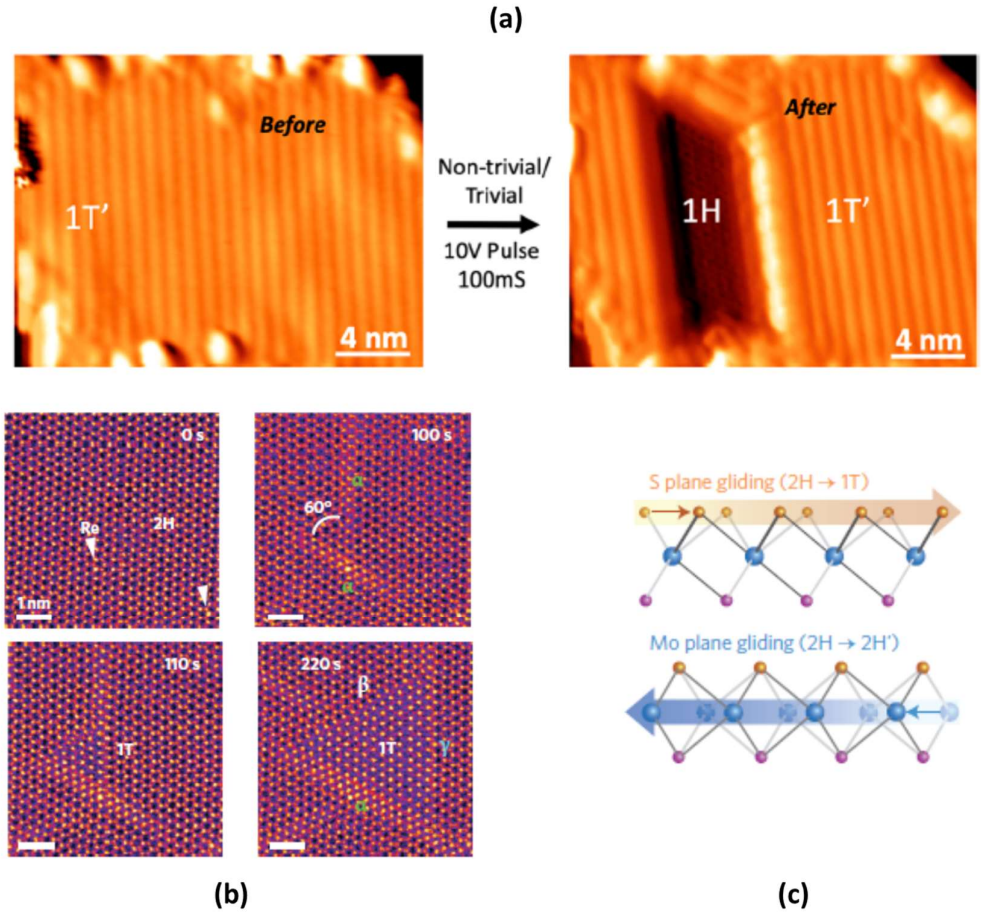

Figure 7-3. (a) STM images before and after a tip applied voltage pulse of 10V. The pulse induces a local area phase transition from the 1T' phase to the 2H phase. (b) STEM images of the MoS_2 surface at 600°C showing the progression of the phase transition from the 2H to the 1T phase. The precursor α phase can be seen to form Mo zigzag chains before it transitions into the 1T phase, forming different types of domain boundaries with the 2H phase. (c) Schematics showing two ways the planes can slide to result in 2H to 1T, or 2H to 2H' phase transitions. [14, 15]

from a technique to grow WS_2 on Ag assisted by pulsed laser deposition, which enabled a phase transition from 2H to 1T and allowed it to be stabilised by electron donation from the Ag substrate after growth [13].

Another interesting method of inducing phase transition was performed by pulsing the surface of WSe_2 with an STM tip [14]. The WSe_2 layer was grown using MBE to create mixed phases of 2H and 1T' as well as single phase domains. By pulsing with a voltage ≥ 6V different orientations of the 1T' chains could be created, resulting in the formation of 1T'/1T' domain boundaries. However, by pulsing with a voltage ≥ 10V a local area transformation to the 2H phase could be induced, as seen in figure 7-3 (a). In a similar manner, the phase transition from 2H to 1T was induced and controlled using a STEM at 60 kV and high temperatures of 400-700°C [15]. Figure 7-3(b) shows the evolution of the phase transition with time, showing the precursor α phase and the two domain boundaries β and γ that can form. The precursor α phase was found to be stable under electron irradiation and high temperature and is essential for the phase transition. Figure 7-3(c) shows a schematic showing how the top S plane glides during the 2H-1T transition, as well as another type of phase transition from 2H-2H' where the Mo plane glides in this case. It was found that phase transition did not occur except under electron beam irradiation, suggesting that the accumulation of negative charge can trigger the phase transition.

7.2. Absence of phase transition in 1H-WSe_2/Au(111) heterostructure

The previous chapter considers the electronic effects at the interface of the heterostructure but assumes a 2H phase of the WSe_2. As seen from literature, these heterostructures have been observed to undergo phase transition especially when annealed, and here the possibility that this has occurred for this sample will be discussed.

Some STS measurements taken from the sample before it was annealed at high temperature show a different I/V curve from what is expected, with a smaller bandgap and more metallic character. An example is displayed as the blue curve in figure 7-4 with the more typically observed curve of the 2H phase shown in red for comparison, and the presence of both types could indicate the existence of different phases across the sample. After annealing, spectroscopy of this type was no longer observed indicating the heterostructure is much more uniform than it was prior to annealing. This could simply be due to the annealing process improving the interface between the layers by removing any impurities between them and reducing the interfacial distance, but it could also indicate a phase transition back to the 2H phase from any metastable 1T regions. Regardless, after annealing only

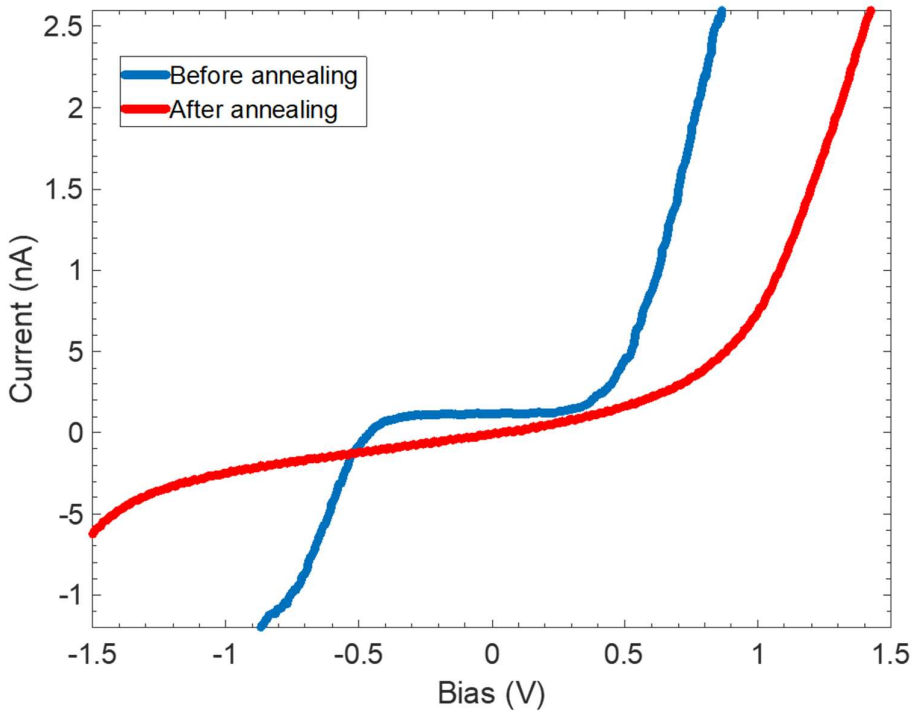

Figure 7-4. Spectroscopy I/V curves from the WSe_2/Au(111) sample, showing an example of a region with a shorter bandgap (blue) that was only observed prior to annealing. After annealing only spectroscopy similar to the red curve was observed.

spectroscopy like the red curve was observed. The reason the I/V curve appears sloped is an artefact of the STM system, and not due to the Au contribution.

Our heterostructure was annealed at a temperature of 500°C which from the discussed literature would suggest while not optimal, it could still contain a significant percentage of the 1T' phase. The methods used to identify 1T' in most of the above cases did not include STM which would give an obvious structural change due to the distorted structure. From all of the areas scanned on our sample, the distorted rows of the 1T' phase was not observed meaning that this phase transition did not occur here, or it was in such a low percentage it would not affect the sample as a whole. It is less clear with the 1T phase transition as ideally it would appear very similar to the 2H structure under STM as discussed in section 2-2. If it has undergone a distortion and developed a super-lattice it would be observable, appearing as in figure 2-6(b) in chapter 2, but this does not seem to be the case here either with the super-lattice observed explained by the moiré pattern. From the topographic image there is no reason to suggest the 1T phase, and this is supported by the STS which all display a bandgap indicating a semiconducting rather than metallic character. The ARPES measurements however show states crossing the Fermi level which suggest a metallic nature.

The metallic states suggest a transition to the 1T phase however this phase also has a very different band-structure from the 2H phase, as seen in the simulated band-structures of 2H and 1T shown in figure 7-5(a) and (b) respectively. Comparing these with the ARPES results in figure 7-5(c), the bands fit better to the 2H case indicating that the base structure of the WSe_2 is still in the 2H phase. This can be clearly seen around the M point where the bands for the 1T phase are much higher and form a peak far into what is the bandgap in the 2H phase. The peak usually at the K point is shifted along the Γ-K direction and again is further up in energy than the 2H bands. Comparing with the band-structure of the 1T' phase also reveals significant differences, notably in the absence of the signature inverted band

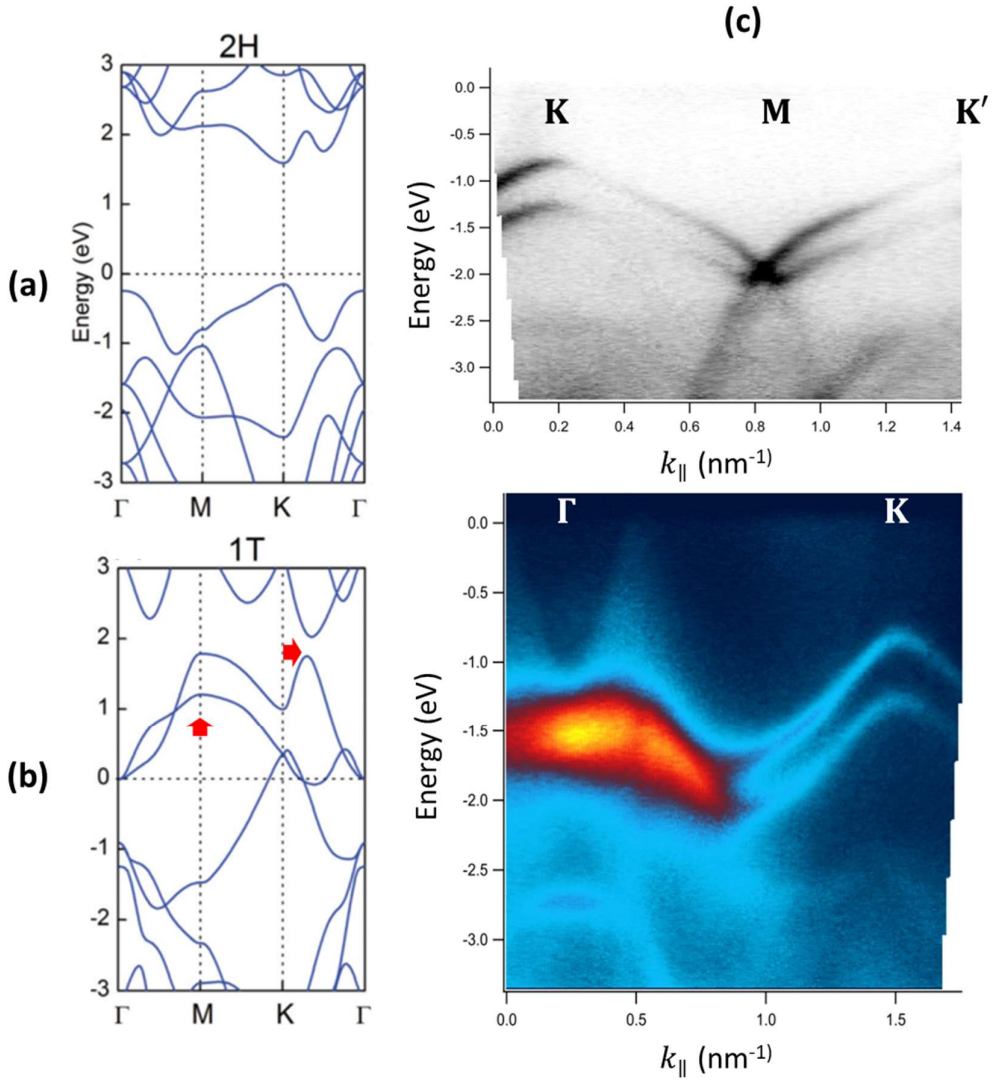

Figure 7-5. Simulated 2H (a) and 1T (b) band-structures. The red arrows indicate positions which are very different from the ARPES measurements. [16] (c) ARPES energy cuts along the K-M-K' and Γ-K directions.

structure of the 1T' bands which is shown in figure 2-12(b) in chapter 2. Therefore, the WSe_2 in this heterostructure remains in the 2H phase and does not undergo a phase transition.

The STM measurements revealed no domain boundaries in the WSe_2 suggesting it was single domain, which is to be expected as it was exfoliated from a single crystal source. This also suggests that there has been no change to the local structure due to the Au interaction or annealing process, meaning it is unlikely a phase transition has occurred elsewhere on the sample. The uniformity of the sample is supported by the ARPES measurements, with both the very local measurements from the Nano-ARPES and the sample-wide NanoESCA measurements displaying the same features. Measurements from different points of the sample with the Nano-ARPES also showed no difference.

Reasons why a phase transition is not observed are likely down to the preparation method and the high stability of the interface. The only chance for impurities or any sort of external influence to affect the sample was in the short time after exfoliating the WSe_2 and placing it on the Au(111) crystal, and putting in into the load lock. From then on, all annealing and STM measurements were carried out in UHV. All the other methods resulting in a phase transition used another method of growth or application of the layers, so the exfoliation of a single crystal impairs any phase transition. The twist angle between the layers could also play a part, as during growth of layers they typically favour an orientation which may make the phase transition route more favourable. In this case the angle was not tuned to any such direction and simply stacked as it was with a twist angle of about 25°. For the ARPES measurements the sample was briefly exposed to air during transfer, but the results from ARPES confirm it to be very uniform demonstrating a high stability.

7.3. Electronic doping via Pd atomic decoration

A WSe_2 crystal was decorated with Pd atoms on the surface to investigate the effect on the lattice and electronic structure a dopant would have. The purpose of this experiment was to prepare for doping with magnetic dopants such as V or Mn, as a route towards long-range ferromagnetic order in TMDs.

STM images showed that the Pd atoms formed either as single or few-atom clusters or coalesced to form larger nano-crystals. The clusters can be seen in the images shown in figure 7-6(a) which shows two single Pd atoms and figure 7-6(b) which displays a cluster of 4 Pd atoms marked by the white dotted circles. They appear as bright protrusions on the surface, extending roughly over 3 Se atomic sites. Calculations performed of Pd atoms adsorbed on a MoS_2 surface have shown that the Pd atoms favour the site on top of the metal atom as

displayed in figure 7-6(c), and covalently bonds with the neighbouring Se atoms [17]. This results in a charge accumulation around the adatom as displayed in the charge density difference maps in figure 7-7(a), explaining the surrounding contrast and larger apparent size of the Pd atoms in figure 7-6(b). The atomic structure surrounding the adatom site is also expected to be slightly distorted due to the bonding with the Pd adatom. In figure 7-6(a) intrinsic defects from the surface can be seen and whilst it might be thought that the adatoms too are intrinsic, the study of the WSe_2 crystal defects in chapter 5 observed nothing of this kind. They appeared only after deposition and since they would be situated on the surface, the bright contrast agrees with what one would expect unless it was a strong acceptor dopant that could balance the topographic affect, which does not appear to be the case for Pd based on its appearance. Whether Pd is an acceptor or donor however is not always clear, as in one case it has been shown to act as a donor with the Pd atom valence

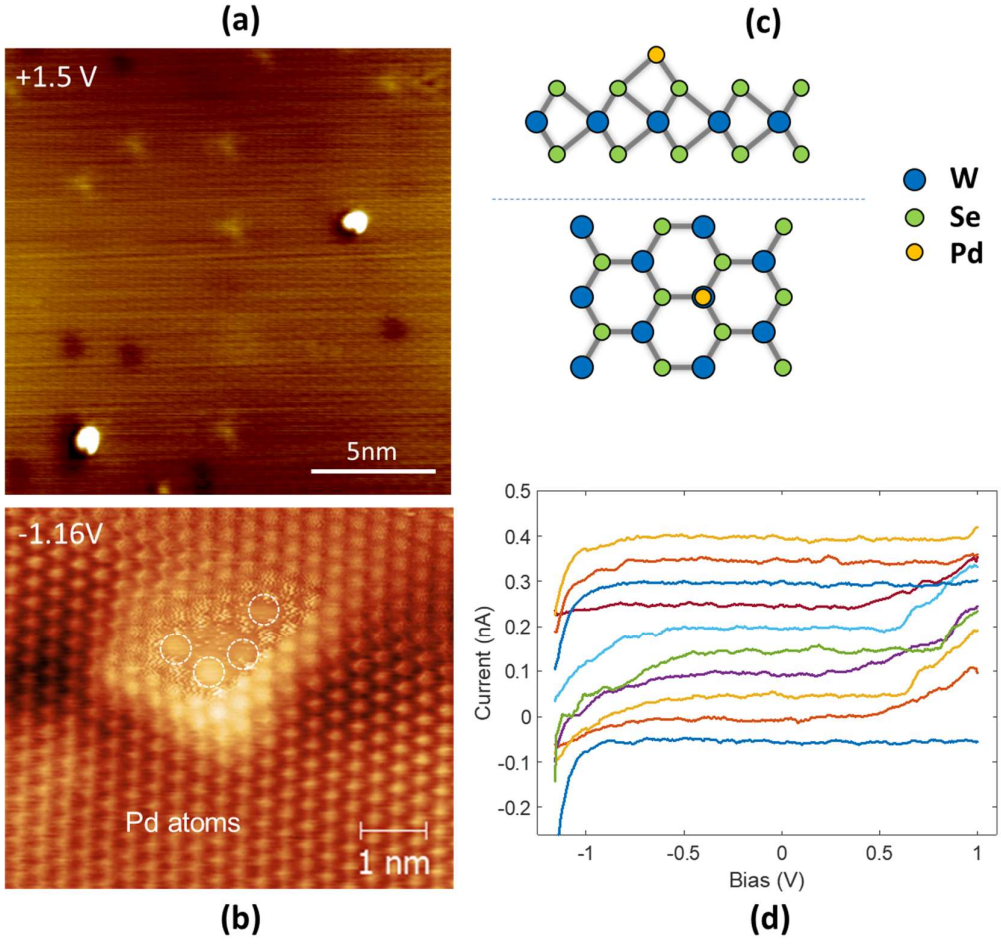

Figure 7-6. (a) STM image at +1.5V, 0.8 nA showing two Pd atoms decorating the surface, and multiple types of intrinsic defects. The odd shape of the Pd atoms is due to the shape of the tip, where it is not entirely spherical. (b) STM image at -1.16V, 0.2nA showing a cluster of 4 Pd atoms marked by the white arrows. (d) Point spectroscopy measurements taken across the cluster in (b) showing presence of additional states around the valence and conduction band edges.

configuration of $4d^{10}5s^{0}$ donating 0.25e to the MoS_2 surface layer [17], but in others it has been calculated to be an acceptor with a charge transfer of -0.12e [18]. The difference between these cases seems to depend on its position, with the first case adsorbing it to the surface, whereas the second it substitutes a Se atom, implying that it acts as a donor for this sample. Their presence on the surface can also be seen from the tendency of the tip to move them across the surface as it scanned over them.

The cluster in figure 7-6(b) has a bright region directly surrounding the Pd atoms indicating that they have a local effect on the LDOS of the neighbouring atoms. This was confirmed by taking point spectroscopy across the cluster, with the resulting I/V curves shown in figure 7-6(d). At the site of the Pd atoms and directly adjacent to it the band gap is shortened, with contributions of states at both the valence and conduction band edges. Simulations have predicted dopants to have similar effects on the electronic structure with reduction of the bandgap reported due to Se doped MoS_2 which could be tuned with concentration [19], and transition metal Cr doping [20]. Other dopants have induced a change to metallic or semi-metallic character [20, 21]. In most of these cases however the dopant substitutes either a metal or chalcogen atom, rather than decorating the surface. The Pd atom does not show fully metallic nature, showing it does not induce a change of character, but does show the reduction in the bandgap predicted by [17, 18]. This is due to the presence of states located in the gap region, however in contrast to this result calculations have suggested these states

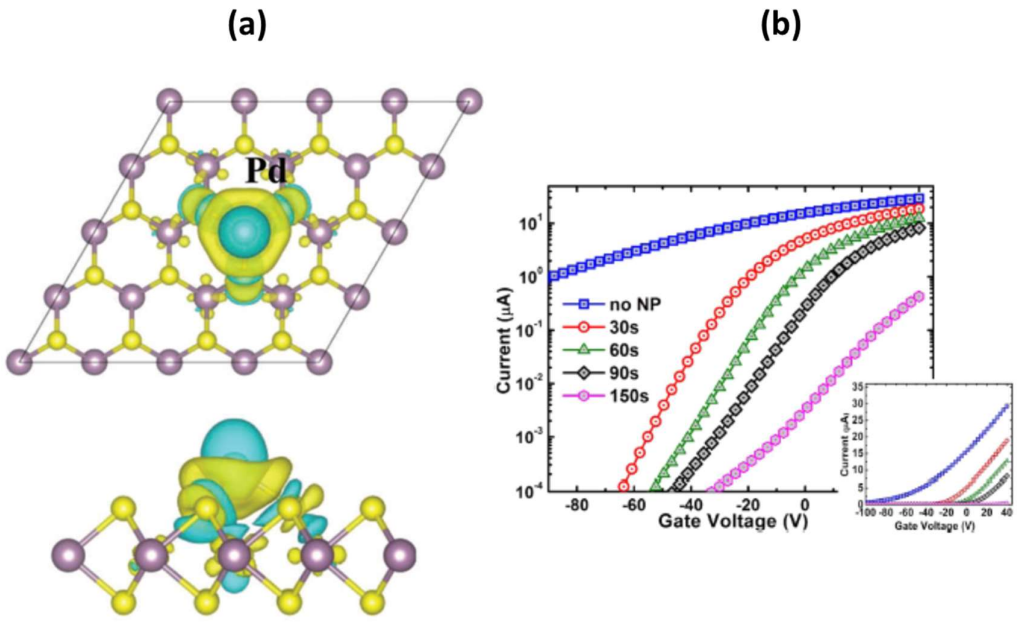

Figure 7-7. Calculated charge density difference plots of a Pd adatom adsorbed above the metal atom site on MoS_2. (b) Drain current as a function of gate voltage curves for a MoS_2 FET, showing different levels of Pt doping and the effect on the transfer characteristics this has. The curves on a linear scale are shown in the inset. [17, 22]

should not be close the VB or CB edges, rather acting as trap or recombination centres for the carriers in the mid gap region.

Scanning over a larger area shows that nano-crystals have formed across the surface, as shown in figures 7-8(a) and (b). These were typically triangular crystals 5-10 nm in size and appeared to have two different orientations marked by the white dotted lines in figure 7-8(b). Spectroscopy measurements revealed a similar but stronger effect on the WSe_2 bandgap, indicating that these were formed of Pd atoms. The triangular nature of the crystals suggests that there was a nucleation site from which the crystal grew out from, and their formation must have occurred during the deposition phase as these images were acquired prior to any annealing. This is in agreement with previous experiments of Pd deposited on MoS_2 by evaporation, from which STM images show very similar triangular shaped clusters orientated in 2 directions [23], and calculations that predict Pd adatoms prefer to form nanotemplates on the surface [17]. X-ray diffraction discovered that the clusters lie in a Pd(111) plane, and is not rotated relative to the top layer Se lattice, rather they grow epitaxially on the surface. This supports the previous calculations that the Pd atoms lie on top of the metal atom site. Some of the crystals appear with a brighter contrast compared to others suggesting that they may have a 3D structure and not be monolayers, which was also the conclusion of a similar study of Pd on MoS_2 where the clusters structure had a 3D pyramidal shape as they grew larger [24].

To examine the effect of the Pd on the electronic structure of WSe_2, $\mathrm{dI/dV}$ curves were taken from a clear area of the WSe_2 surface and compared with $\mathrm{dI/dV}$ measurements of the crystal taken before depositing Pd on it. The comparison of these curves is shown in figure 7-8(c), showing that the Pd doped crystal (orange curve) has a rigid shift of the bands from the pristine crystal (blue curve). The Fermi level has been shifted away from the conduction band edge moving the centre of the bandgap closer to the Fermi level, indicating this is p-type doping. This was observed to be a global affect across the sample where these nano-crystals are located. This result contrasts with those suggesting that the Pd atoms adsorbed on the surface act as donors, as the nature of the doping shows they're acceptors. It is possible that some of the Pd atoms have substituted with Se atoms or filled previous Se vacancies during the deposition process or from diffusion afterwards, which could explain the shortening of the bandgap from both VB and CB edges. However, from the images, the vast majority seems to appear on the surface meaning that this must be the cause of the doping. The results are similar to previous experiments as decoration of Pd nanoparticles on a MoS_2 FET has let to p-type doping [22], and Au adatoms have previously been shown to p-dope WSe_2 [25] and MoS_2 [26] supporting the ability of adatoms to dope a sample. The effect of increasing the coverage of NP on the surface has also been seen in the case of Pt decoration of a MoS_2 FET, with increased threshold voltages needed to switch on the back-gated FET with larger doses. Therefore, higher levels of Pd decoration are expected to increase the p-doping of the WSe_2 sample, further shifting the bands.

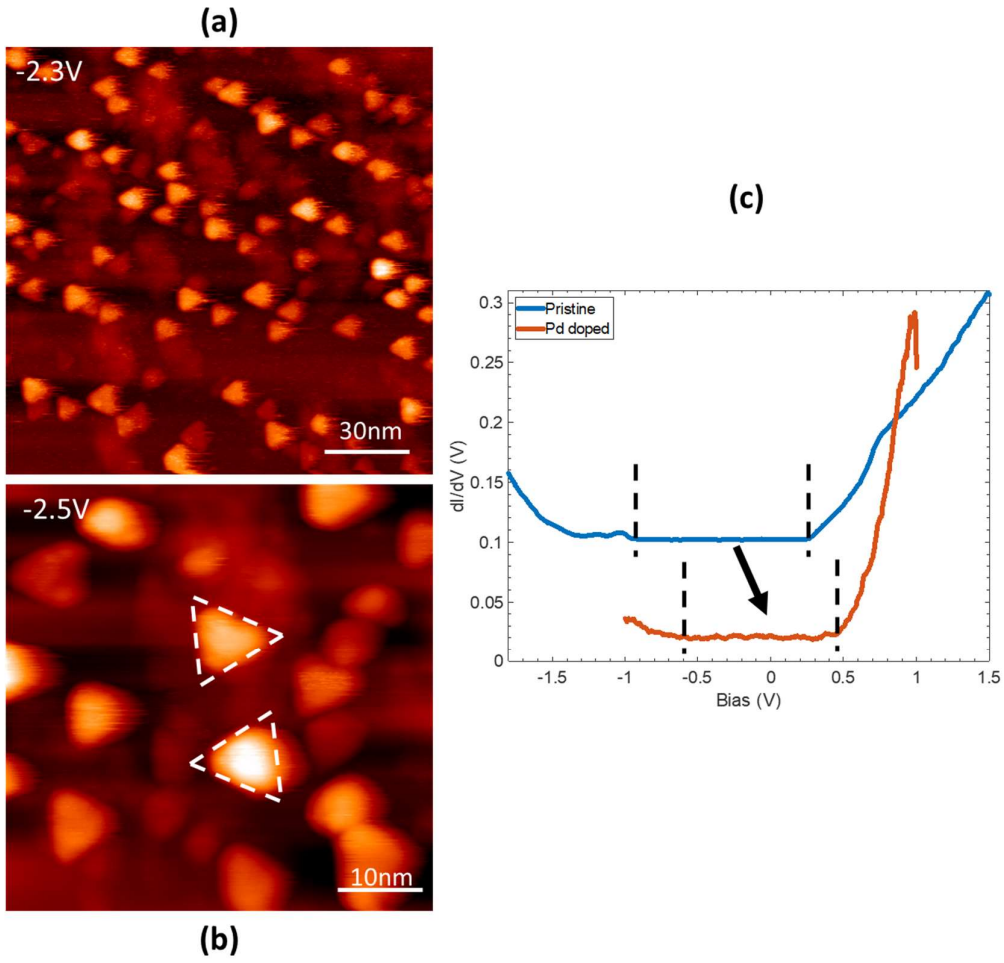

Figure 7-8. (a) STM image at -2.3 V, 0.12 nA over a larger area displaying the triangular Pd nano-crystals covering most of the surface. (b) Closer STM image at -2.5 V, 0.13 nA focusing on two nano-crystals with opposite orientations marked by the white triangles. (c) STS curves displaying the rigid p-type shift of the bands due to doping from the Pd nano-crystals on the WSe_2 surface. Both measurements were taken from areas clear of defects or Pd dopants.

7.4. Phase transition via Pd intercalation/alloying

The sample was annealed twice after the initial STM investigation of the clusters and nano-crystals, with no change after the first annealing at 600°C and the features observed as above. The second annealing was done at 900°C and a significant modification of the surface was observed, most notably by the absence of the small nano-crystals and the formation of much larger domains with polyhedral shape as seen in figure 7-9(a). The surface topography now has a much larger variation in height, with regions appearing to overlap or stack on one

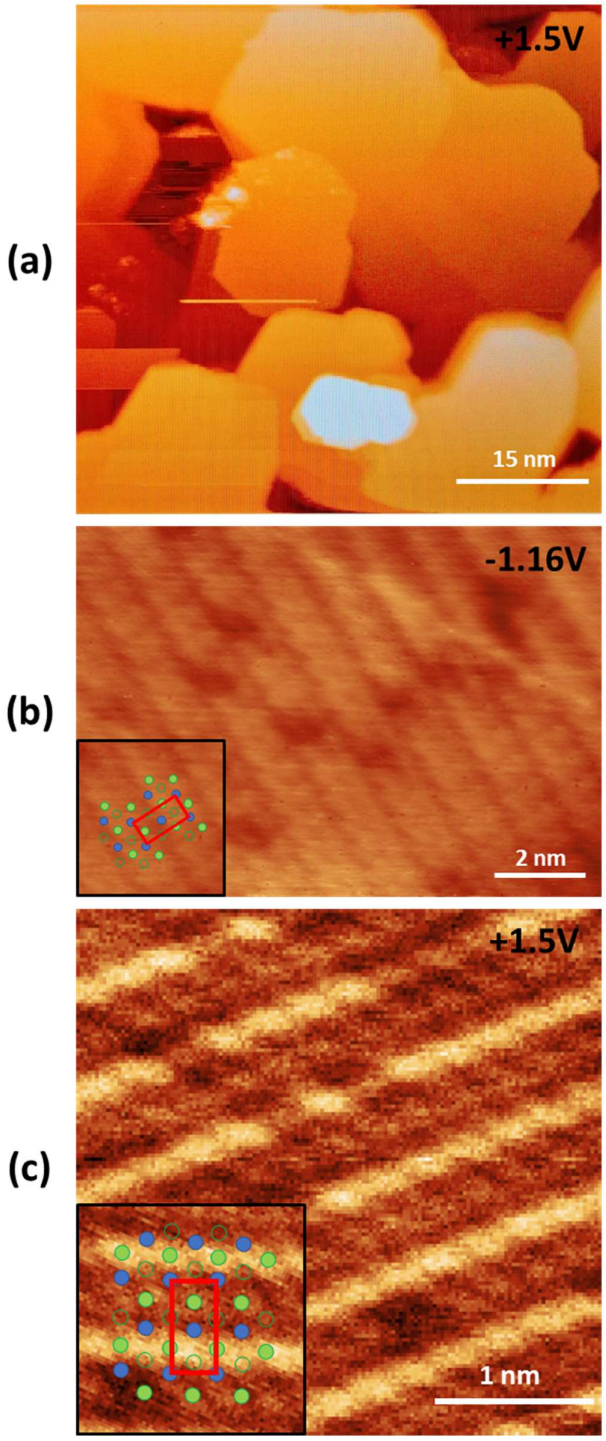

Figure 7-9. (a) STM image at +1.5 V, 0.28 nA of a 60 nm^2 area showing large polyhedral regions across the surface that overlap. Aside from one area the surface appears very clean. (b) STM image at -1.16 V, 1.72 nA zoomed in on a domain with rows. (c) STM image at +1.5 V, 0.28 nA showing an increased contrast on alternating rows, which shows the position of the W zigzag chain. The insets show regions with the atomic positions of the 1T' phase overlaid, with the same scale as the base images. The filled green, filled blue, and hollow green dots represent the top Se, W, and bottom Se atoms respectively. The unit cell is displayed by the red rectangle.

another and some areas having large steps or pits. Given the amount of Pd deposited on the surface was not sufficient to form a monolayer, the structural change must also involve the surface WSe_2 layers. The weak interlayer van der Waals bonding between layers means that this is possibility, with the impurity Pd atoms and the high annealing temperature providing the means to do so. Upon closer inspection of these domains revealed that some now had a modified surface structure as seen in figure 7-9(b), consisting of stripes along one direction. These stripes appear as a pair of two rows, each staggered from the other, and with one appearing brighter than the other. This is more clearly seen under different imaging conditions as in figure 7-9(c), which has a larger contrast between the non-equivalent rows. Along the brighter rows the spacing between bright points is 0.30-0.36 nm, which is consistent with the atomic spacing of Se-Se atoms, and between bright rows the spacing is about 0.6 nm. This is consistent with the 1T' phase discussed in section 2-2 and shown in figure 2-8 and is in agreement with other STM studies of this phase [5, 14, 27]. The atomic structure of the 1T' phase is overlaid in the insets of figures 7-9(b) and (c), showing the positions of the top layer Se atoms (filled green dot), the W atoms (filled blue dot), and the Se atoms in the lower layer (hollow green dot). The unit cell of the 1T' phase is marked by the red rectangles over the structure and is perpendicular to the row direction. This matches very well with the pattern, where the brighter rows are along the direction of the metal zigzag chain, due to the raised Se atoms above them.

This type of pattern was not observed for all domains with other patterns appearing as displayed in figure 7-10(a). Region 1 shows a similar row pattern but has no atomic resolution compared to region 3 which does. Region 3 lies on top of region 1 so there is a step between

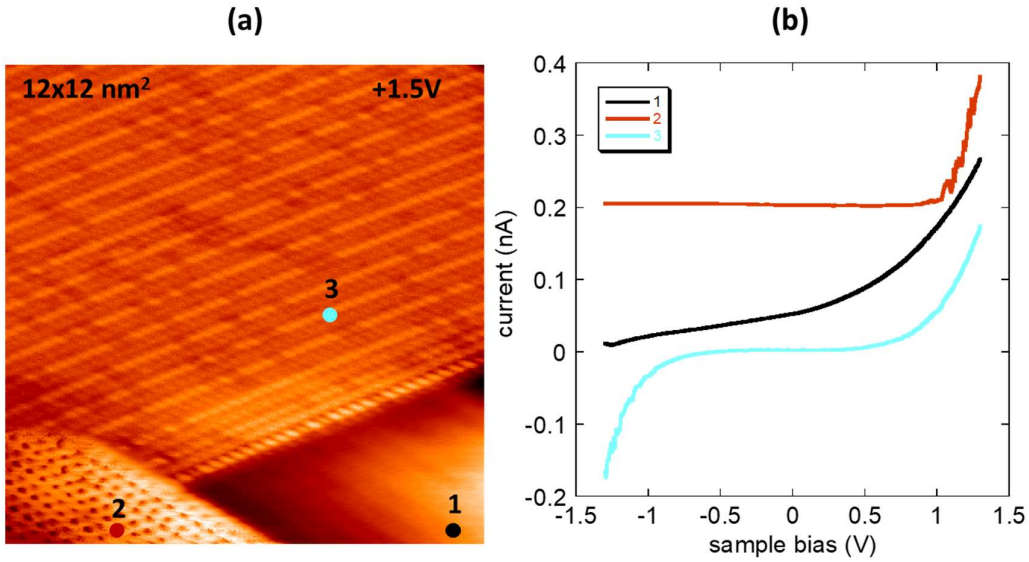

Figure 7-10. (a) STM image at +1.5 V, 0.28 nA showing three regions with differing structure. Here a clear overlap of layers can be seen with region 2 on the top and region 1 at the bottom with region 3 in-between. (b) Point spectroscopy I/V curves taken from the three regions marked 1-3 in (a).

them but there is sufficient area for the tip to be able to scan correctly, therefore there is a clear difference between these regions. Another observation from region 3 is the high number of defects, which appear very localised suggesting they lie in the surface layer. Region 2 also displays a different pattern, which is more akin to the hexagonal pattern of 2H-WSe_2. Spectroscopy from the three regions show that each region has a different electronic structure, as shown by the resulting curves in figure 7-10(b). Region 1 interestingly shows a slightly more metallic character in contrast to the expected 2H-WSe_2, suggesting there is a large presence of Pd atoms in this region. Region 3 displays a more typical 2H-WSe_2 electronic band-structure although with a shorter bandgap. This is unusual as the 1T' phase has a much-reduced bandgap compared to the 2H phase and contrasts with the observed structure of the region. A possibility is that the bulk 2H phase underneath is contributing to the spectroscopy and this phase is only on the surface layer. Another potential explanation could come from the high number of defects, which are known to affect the electronic structure of materials, although this would be an extreme case as they would usually increase the number of states in the bandgap rather than shift it towards insulating.

Considering the nature of the 1T'-WSe_2 phase as a QSH insulator, a further suggestion could be that the mix of different regions here has affected the conductive states resulting in a slightly larger bandgap. The possibility to tune the nature of the 1T' phase has been discussed before in the context of an applied electric field [28], where the conductive helical edge states were destroyed. In a similar vein to that of chapter 6, placing this layer on a substrate could induce changes to its electronic structure. This explanation may be supported by the spectroscopy from region 2, which displays a significant Schottky barrier, which is expected at the junction between a metal and semiconductor. This implies that this region includes an overlap between a metallic layer and the bulk semiconducting WSe_2 and demonstrates that a range of different domains and quasi-heterostructure exist.

A potential explanation for the formation of these varied regions could be due to intercalation of the Pd in between layers or inside of a single layer of WSe_2. Intercalation is commonly used to induce phase transition in these layered materials too which could explain the observation of regions with the 1T' structure. How it came to be intercalated is unclear, as annealing at high temperature is expected to cause the Pd atoms to desorb from the surface, starting from about 420°C [29]. However, the spectroscopy reveals clearly that some of it remains. The formation of the fractured surface with lots of steps could have been mediated by the Pd atoms on the surface during the annealing process, which then allowed intercalation of some of the Pd atoms at the step edges.

Another possible explanation is that the Pd and WSe_2 formed an alloy. A wide variety of different TMDs and their alloys have been reported but they are usually formed in the growth process through combination of different precursors [30]. However, one study showed that WSe_2 placed on Pt could be transformed through annealing in vacuum at 600-700°C, and

formed a W-Pt-Se alloy [31]. The annealing temperature is below the thermal decomposition of WSe_2 in vacuum of 930°C, which implies that the chemical reaction is Pt induced. This shows the potential for the Pd and WSe_2 to have alloyed in our case and undergone a structural transformation. It has also been seen that in an alloy of W-Nb-Se that the substitution of the Nb atoms can induce lattice distortions due to the difference in bond length with the Se compared to the W, resulting in a structural change [32]. In the same alloy, the change in the atomic bonding resulted in a reduction of the bandgap [33]. Both of these suggest that the alloy could have structural distortion and a reduction of the bandgap similar to what we see, and due to both WSe_2 and $NbSe_2$ exhibiting the 2H phase shows the potential for a greater difference with a mismatch of phases. Looking at $PdSe_2$ it has a preferred phase of 1T, and it is also a semiconductor with a bandgap [30]. An alloy between these two could therefore lead to a large distortion in structure, especially as in WSe_2 the 1T phase is unstable and will relax to the 1T' phase. An increase in the bandgap would also not be unforeseen as the WSe_2 would no longer be in its pure 1T' phase.

7.5. Conclusions

The WSe_2/Au(111) heterostructure has been compared to the properties of the other phases and found it does not exhibit the features of a phase transition despite observations of this in similar systems and conditions. The electronic structure and structure match well with the 1H phase, with all the critical points of the phase clearly observable. It is also seen to be highly uniform and stable under short periods in ambient conditions.

Doping the WSe_2 crystal with Pd dopants showed their ability to adsorb to the surface through covalent bonding demonstrated by a local modulation of the LDOS. This resulted in a shortening of the bandgap through the addition of induced states at the edges in the locality of the dopants. Furthermore, the adatoms were seen to coalesce into larger triangular nanoclusters, which orientated themselves in one of two directions. The orientation and epitaxial growth of the clusters, as well at the single dopant position shows they prefer the metal atom site. The decoration of the surface was seen to induce a rigid shift of the bands in spectroscopy measurements indicating a p-type doping by the Pd atoms.

Annealing the crystal at 900°C resulted in a reconstruction of the surface layers, leading to regions with different electronic properties. One region which was commonly observed showed a 1T' structure suggesting a phase transition either through intercalation or the formation of an alloy between WSe_2 and Pd. A slight discrepancy was observed with the electronic structure, indicating more work is required to understand this transformation.

References

[1] Fang H, Chuang S, Chang T C, Takei K, Takahashi T and Javey A (2012) High-performance single layered WSe2 p-FETs with chemically doped contacts. *Nano Letters.* **12** 3788-92

[2] Tang Y H, Mak K F and Shan J (2019) Long valley lifetime of dark excitons in single-layer WSe2. *Nature Communications.* **10** 7

[3] Acerce M, Voiry D and Chhowalla M (2015) Metallic 1T phase MoS2 nanosheets as supercapacitor electrode materials. *Nature Nanotechnology.* **10** 313-8

[4] Ugeda M M, Pulkin A, Tang S J, Ryu H, Wu Q S, Zhang Y, Wong D, Pedramrazi Z, Martin-Recio A, Chen Y, Wang F, Shen Z X, Mo S K, Yazyev O V and Crommie M F (2018) Observation of topologically protected states at crystalline phase boundaries in single-layer WSe2. *Nature Communications.* **9** 7

[5] Chen P, Pai W W, Chan Y H, Sun W L, Xu C Z, Lin D S, Chou M Y, Fedorov A V and Chiang T C (2018) Large quantum-spin-Hall gap in single-layer 1T' WSe2. *Nature Communications.* **9** 7

[6] Eda G, Yamaguchi H, Voiry D, Fujita T, Chen M W and Chhowalla M (2011) Photoluminescence from chemically exfoliated MoS2. *Nano Letters.* **11** 5111-6

[7] Wypych F, Weber T and Prins R (1998) Scanning tunneling microscopic investigation of 1T-MoS2. *Chemistry of Materials.* **10** 723-7

[8] Yin X M, Tang C S, Wu D, Kong W L, Li C J, Wang Q X, Cao L, Yang M, Chang Y H, Qi D Y, Ouyang F, Pennycook S J, Feng Y P, Breese M B H, Wang S J, Zhang W J, Rusydi A and Wee A T S (2019) Unraveling high-yield phase-transition dynamics in transition metal dichalcogenides on metallic substrates. *Advanced Science.* **6** 14

[9] Yin X M, Wang Q X, Cao L, Tang C S, Luo X, Zheng Y J, Wong L M, Wang S J, Quek S Y, Zhang W J, Rusydi A and Wee A T S (2017) Tunable inverted gap in monolayer quasi-metallic MoS2 induced by strong charge-lattice coupling. *Nature Communications.* **8** 9

[10] Kang Y M, Najmaei S, Liu Z, Bao Y J, Wang Y M, Zhu X, Halas N J, Nordlander P, Ajayan P M, Lou J and Fang Z Y (2014) Plasmonic hot electron induced structural phase transition in a MoS2 monolayer. *Advanced Materials.* **26** 6467-71

[11] Nayak A P, Pandey T, Voiry D, Liu J, Moran S T, Sharma A, Tan C, Chen C H, Li L J, Chhowalla M, Lin J F, Singh A K and Akinwande D (2015) Pressure-dependent optical and vibrational properties of mono layer molybdenum disulfide. *Nano Letters.* **15** 346-53

[12] Eda G, Fujita T, Yamaguchi H, Voiry D, Chen M W and Chhowalla M (2012) Coherent atomic and electronic heterostructures of single-layer MoS2. *ACS Nano.* **6** 7311-7

[13] Loh T A J, Chua D H C and Wee A T S (2015) One-step synthesis of few-layer WS2 by pulsed laser deposition. *Scientific Reports.* **5** 9

[14] Pedramrazi Z, Herbig C, Pulkin A, Tang S J, Phillips M, Wong D, Ryu H, Pizzochero M, Chen Y, Wang F, Mele E J, Shen Z X, Mo S K, Yazyev O V and Crommie M F (2019) Manipulating topological domain boundaries in the single-layer quantum spin hall insulator 1T'-WSe2. *Nano Letters.* **19** 5634-9

[15] Lin Y C, Dumcencon D O, Huang Y S and Suenaga K (2014) Atomic mechanism of the semiconducting-to-metallic phase transition in single-layered MoS2. *Nature Nanotechnology.* **9** 391-6

[16] Ma F X, Gao G P, Jiao Y L, Gu Y T, Bilic A, Zhang H J, Chen Z F and Du A J (2016) Predicting a new phase (T'') of two-dimensional transition metal di-chalcogenides and strain-controlled topological phase transition. *Nanoscale.* **8** 4969-75

[17] Wu P, Yin N Q, Li P, Cheng W J and Huang M (2017) The adsorption and diffusion behavior of noble metal adatoms (Pd, Pt, Cu, Ag and Au) on a MoS2 monolayer: a first-principles study. *Physical Chemistry Chemical Physics.* **19** 20713-22

[18] Ma D W, Ju W W, Li T X, Zhang X W, He C Z, Ma B Y, Tang Y A, Lu Z S and Yang Z X (2016) Modulating electronic, magnetic and chemical properties of MoS2 monolayer sheets by substitutional doping with transition metals. *Applied Surface Science.* **364** 181-9

[19] Gong Y J, Liu Z, Lupini A R, Shi G, Lin J H, Najmaei S, Lin Z, Elias A L, Berkdemir A, You G, Terrones H, Terrones M, Vajtai R, Pantelides S T, Pennycook S J, Lou J, Zhou W and Ajayan P M (2014) Band gap engineering and layer-by-layer mapping of selenium-doped molybdenum disulfide. *Nano Letters.* **14** 442-9

[20] Liu S, Huang S L, Li H P, Zhang Q, Li C S, Liu X J, Meng J and Tian Y (2017) Tunable electronic behavior in 3d transition metal doped 2H-WSe2. *Physica E: Low-Dimensional Systems & Nanostructures.* **87** 295-300

[21] Li H P, Liu S, Huang S L, Zhang Q, Li C S, Liu X J, Meng J and Tian Y (2016) Metallic impurities induced electronic transport in WSe2: First-principle calculations. *Chemical Physics Letters.* **658** 83-7

[22] Sarkar D, Xie X J, Kang J H, Zhang H J, Liu W, Navarrete J, Moskovits M and Banerjee K (2015) Functionalization of transition metal dichalcogenides with metallic nanoparticles: implications for doping and gas-sensing. *Nano Letters.* **15** 2852-62

[23] Perrot E, Humbert A, Piednoir A, Chapon C and Henry C R (2000) STM and TEM studies of a model catalyst: Pd/MoS2(0001). *Surface Science.* **445** 407-19

[24] Piednoir A, Perrot E, Granjeaud S, Humbert A, Chapon C and Henry C R (1997) Atomic resolution on small three-dimensional metal clusters by STM. *Surface Science.* **391** 19-26

[25] Chen C H, Wu C L, Pu J, Chiu M H, Kumar P, Takenobu T and Li L J (2014) Hole mobility enhancement and p-doping in monolayer WSe2 by gold decoration. *2D Materials* **1** 11

[26] Shi Y M, Huang J K, Jin L M, Hsu Y T, Yu S F, Li L J and Yang H Y (2013) Selective decoration of Au nanoparticles on monolayer MoS2 single crystals. *Scientific Reports.* **3** 7

[27] Chen W, Xie X D, Zong J Y, Chen T, Lin D J, Yu F, Jin S E, Zhou L J, Zou J Y, Sun J, Xi X X and Zhang Y (2019) Growth and thermo-driven crystalline phase transition of metastable monolayer 1T'-WSe2 thin films. *Scientific Reports.* **9** 6

[28] Qian X F, Liu J W, Fu L and Li J (2014) Quantum spin Hall effect in two-dimensional transition metal dichalcogenides. *Science.* **346** 1344-7

[29] Kamaratos M and Papageorgopoulos C A (1987) Adsorption studies of Pd on MoS2. *Applied Surface Science.* **29** 279-86

[30] Zhou J D, Lin J H, Huang X W, Zhou Y, Chen Y, Xia J, Wang H, Xie Y, Yu H M, Lei J C, Wu D, Liu F C, Fu Q D, Zeng Q S, Hsu C H, Yang C L, Lu L, Yu T, Shen Z X, Lin H, Yakobson B I, Liu Q, Suenaga K, Liu G T and Liu Z (2018) A library of atomically thin metal chalcogenides. *Nature.* **556** 355

[31] Kim H, Park H, Lee G and Kim J (2019) Intimate Ohmic contact to two-dimensional WSe2 via thermal alloying. *Nanotechnology.* **30** 6

[32] Kim Y, Kim A R, Yang J H, Chang K E, Kwon J D, Choi S Y, Park J, Lee K E, Kim D H, Choi S M, Lee K H, Lee B H, Hahm M G and Cho B (2016) Alloyed 2D metal-semiconductor heterojunctions: origin of interface states reduction and schottky barrier lowering. *Nano Letters.* **16** 5928-33

[33] Seo J, Hwang K J, Baik S I, Lee S, Cho B, Jo E, Choi M, Hahm M G and Kim Y J (2018) Three-dimensional atomistic tomography of W-based alloyed two-dimensional transition metal dichalcogenides. *ACS Applied Materials & Interfaces.* **10** 30640-8

Conclusions and future work

Conclusions

In this thesis, three different sections were covered. The first experimental results dealt with the observation of intrinsic defects in a WSe_2 crystal; across the surface a wide range of different types were seen. Scanning tunnelling microscopy (STM) has proved itself as an excellent probe of surfaces and therefore this technique was applied to examine them, through the structural appearance of the defect site, and the modifications to the electronic structure they can induce. Some defects exhibited a bias dependence appearance, which is highly likely to be due to the contribution of the defect states to the local density of states (LDOS), depleting them at an energy of -0.8 eV to present a featureless topography. Defect states are also detected at just within the valence band edge for an extended defect, indicating the doping effect they can have on the LDOS. Two types of defect were identified from their structure and assigned to the top layer Se monovacancy, which had the appearance of a very local depression on a Se atomic site as expected, and the Se or O interstitial defect centred on a metal site. The Se monovacancy also exhibited a dark star pattern at different energies, in these cases showing its charge depletion of neighbouring sites.

The main result from this section stemmed from the defects ability to act as a scattering centre of the quasi-particles; with their quantum interference giving rise to patterns in the LDOS. The $\mathrm{d}I/\mathrm{d}V$ maps probe the LDOS; hence, the quasi-particle interference patterns (QPI) can be directly probed. This allowed for the determination of the scattering picture from the defect indicating whether spin-flip scattering channels between valleys of opposite spin are permitted. A common metal centred point defect showed only to exhibit spin-conserving processes in its QPI pattern, indicating the non-magnetic nature of the defect. A larger defect complex however showed strong QPI features between the Γ and K points; characteristic of the spin-flip process. The structural appearance of this defect is also consistent with a $\mathrm{V_{WSe6}}$ defect, which is expected to carry a magnetic moment of $6\mu_B$; thus, confirming the spin-flip channel is allowed. This result reveals a promising method to determine spatially resolved magnetic defects, which can be employed to examine the coupling behaviour between multiple magnetic moments on the surfaces of materials.

This technique was further used to probe indirectly the electronic structure of a 1H-WSe_2/Au(111) heterostructure; initially revealing the strong moiré super-lattice features from the surface due to the mismatch of the lattices. The super-lattice has two separate primary vectors, due to the unusual twist angle of 25°±1°. STS and ARPES measurements indicated a deviation from the expected electronic structure of the heterostructure; as this was not simply a superposition of the 1H-WSe_2 and Au(111) bands. DFT calculations revealed that folding the bands of the (1×1) WSe_2 system by the super-lattice reciprocal vectors of the

(√3 × √3) R30° 1H-WSe_2/Au(111), showed good agreement with the angle-resolved photoemission spectroscopy (ARPES) results; and was indistinguishable from simply applying translation operations with the super-lattice reciprocal unit cell vectors. Hence, the experimental R25° 1H-WSe_2/Au(111) can be described as a weakly interacting Umklapp system.

An analysis of the QPI patterns showed that the intragap state observed in ARPES resulted in the observation of non-dispersing features, which get weaker towards the centre and stronger towards the edges. Further DFT calculations indicate that these states are a hybridised continuum of states between the WSe_2 and Au(111), explaining the observation of the non-dispersive bands in ARPES. The weakening of their intensity as well as the observation of pockets close to the Fermi level indicates they retain a WSe_2 nature. Higher up in energy a positively dispersing disk changes nature to negatively dispersing at 1 eV showing an interplay between the "pushed-up" Shockley surface state of Au; another indication of the interaction between the two layers and demonstrating the ability of STM to measure the QPI pattern and determine small details of the electronic structure. A clear signature of the band-folding is seen at even higher energies; in a region empty of Au(111) dominant bands, where the QPI patterns from WSe_2 bands can be independently measured. Scattering vectors only match possible scattering processes on isoenergetic contours of the (√3 × √3) R30° 1H-WSe_2 bands and do not fit well with the un-folded (1×1) system. This comprehensive study involving many parts demonstrates the complex nature of this system; providing the tools to understand the interfacial interaction between layers. This is a very important factor to consider when designing novel heterostructures as it may perturb the desired properties.

The final section addresses the possibility that the heterostructure has undergone a phase transition to explain the perturbed electronic structure. However, the evidence is in contrary to this and indicates that the WSe_2 maintains the 1H phase. Further experiments with the decoration of Pd adatoms onto the surface of a WSe_2 crystal show that high temperature annealing at 900°C leads to a phase transition to the 1T' phase. STM images reveal the characteristic distorted structure; however, the spectroscopy reveals a slight difference in the electronic structure suggesting that this is not a pure 1T'-WSe_2 domain. Intercalation of Pd atoms or the formation of an alloy are proposed as the reasons for the phase transition. This demonstrates a potentially new mechanism to induce phase transition in TMD materials, in which the level of phase transition could be potentially tuned by the concentration of dopants.

Finally, there are a few more general points to be made:

- Typically, QPI combined with FT-STS is used in far simpler systems as it has greater success dealing with single bands. However, as demonstrated here we have been

able to obtain meaningful information despite the complexity of this heterostructure system; by careful cross analysis with ARPES and theory. To our knowledge this is the only such extensive analysis across such a wide range of energies in a complex system.

- As seen, the use of defects of different types and locations in the sample is viable, and shows it is possible to access information about a variety of states in the heterostructure
- The interaction of a monolayer and metal substrate will not produce a good system for decoration with atomic species; the resulting system is too complicated for this. For such studies, it requires at least 2 layers.
- Nevertheless, we have created an interesting system, which is governed by the strength of interaction between layers. This system did not result in a small BZ due to folding; instead it is an Umklapp system, which hints that some bands can still be exploited for spin or valley applications

Future work

The findings presented in this thesis could be developed upon further by:

- Performing combined STM/NC-AFM measurements on defects to get a more accurate description of the difference between their topography and local charge accumulation/depletion. Additional targeted spectroscopy measurements would allow for the determination of the defect state, for comparison with the STM images at that energy.
- Fabrication of new 1H-WSe_2/Au(111) heterostructures to determine the effect of the twist angle, and separately the annealing conditions, on the coupling interaction between the interface layers.
- Further Pd decoration to determine the mechanism by which the phase transition occurs and whether the transition can be tuned by the concentration of dopants.
- This study produced a fertile ground for developing the appropriate theoretical framework required to describe properties like the Umklapp system, the non-dispersive bands, the formation of the continuum and how it interacts with quasiparticles.

Appendix 1

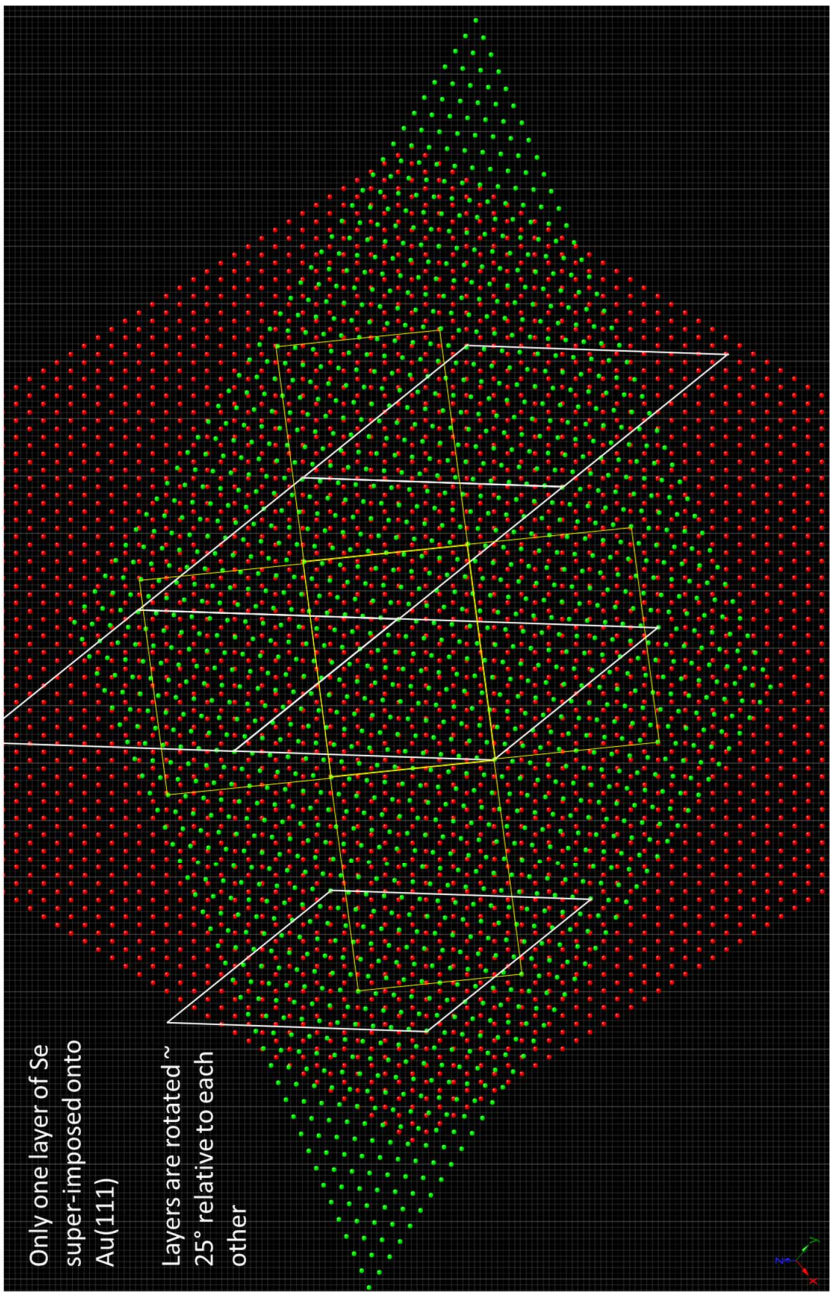

Figure 1-App1. Other potential units cells for the R25° 1H-WSe_2/Au(111) which are closer approximations of a commensurate system than the (√3 × √3) R30°; but are very computationally expensive.

Appendix 2

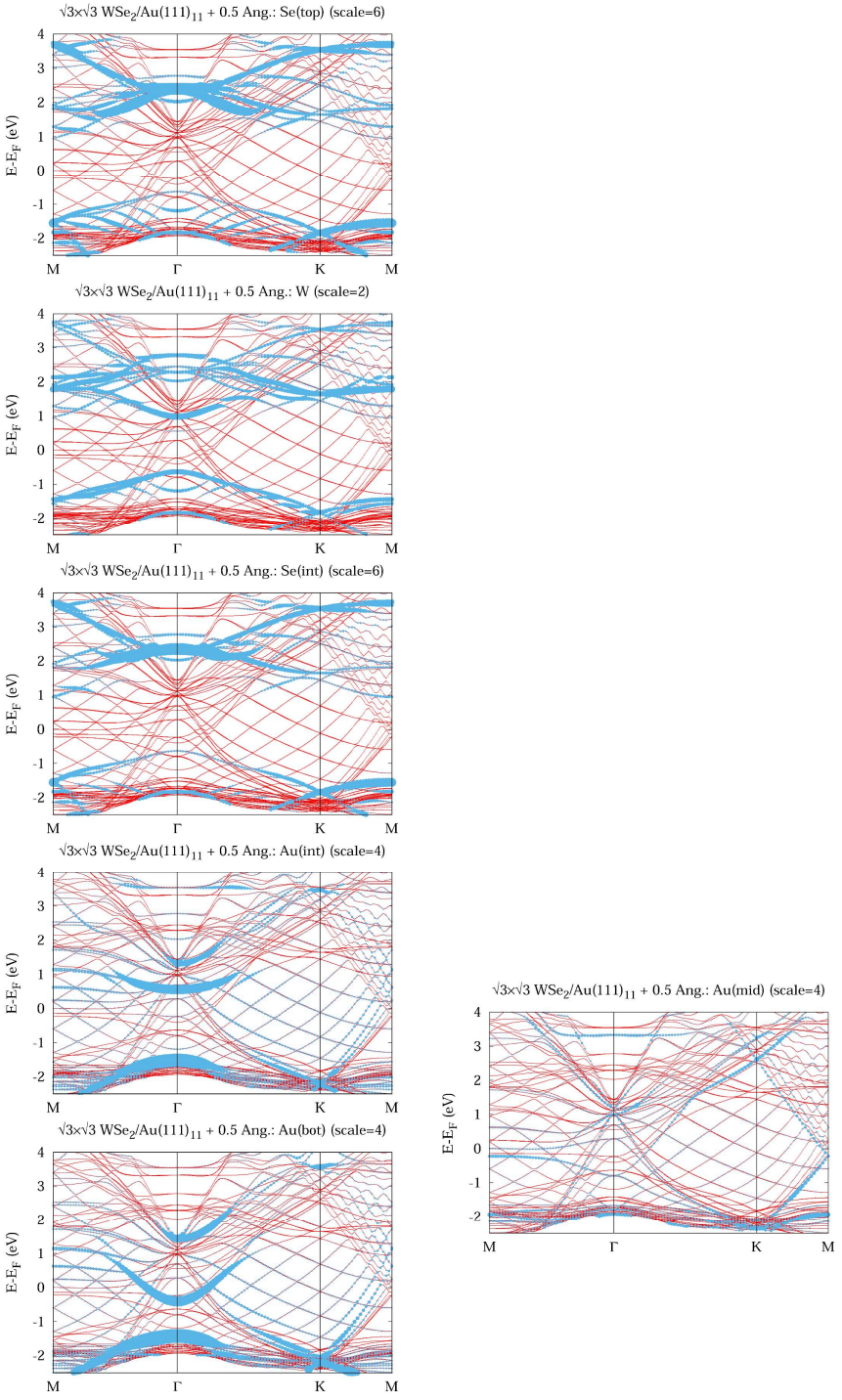

Figure 1-App2. DFT simulations for the (√3 × √3) R30° 1H-WSe_2/Au(111) system with a +0.5 Å shift from the equilibrium position.

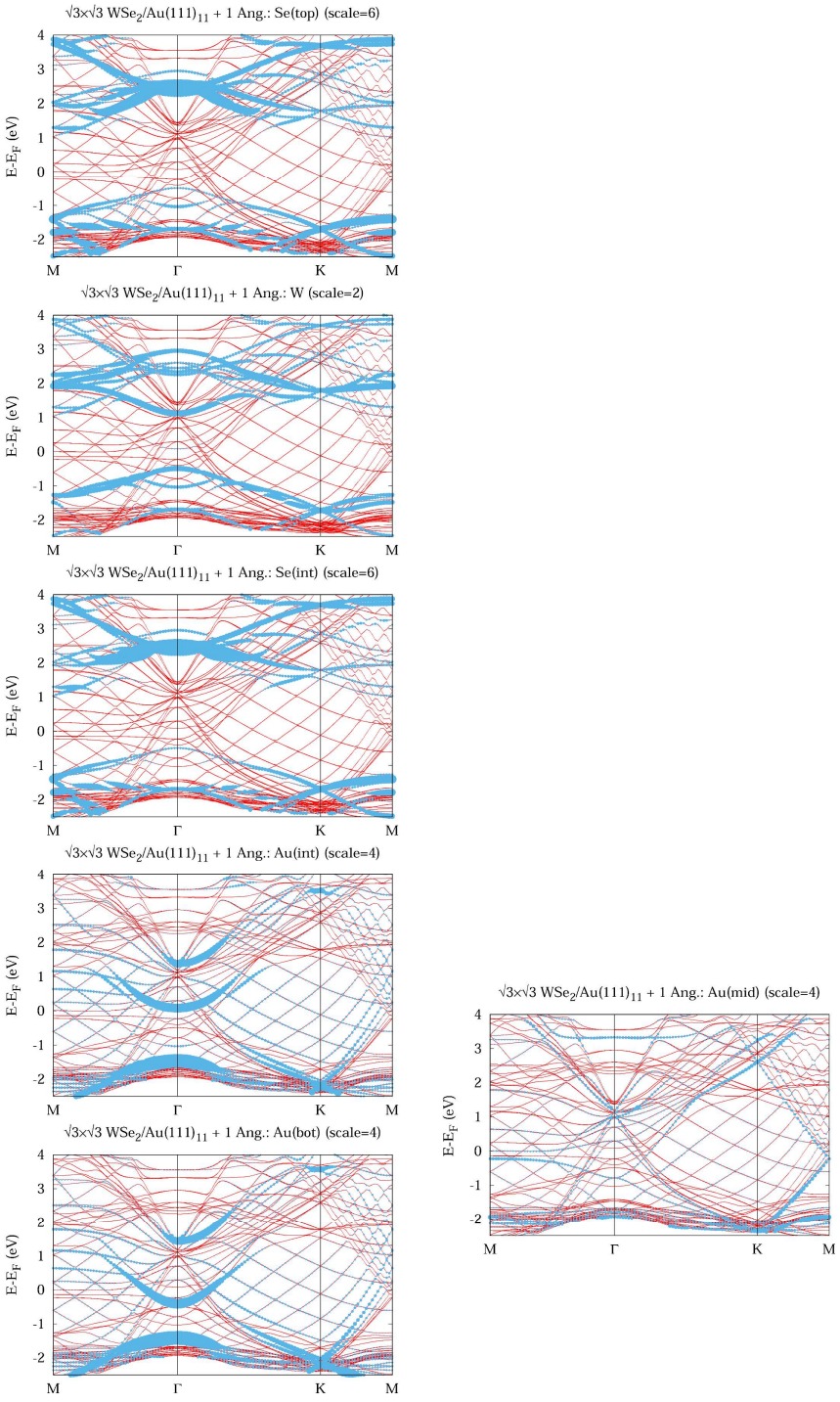

Figure 2-App2. DFT simulations for the (√3 × √3) R30° 1H-WSe_2/Au(111) system with a +1.0 Å shift from the equilibrium position.

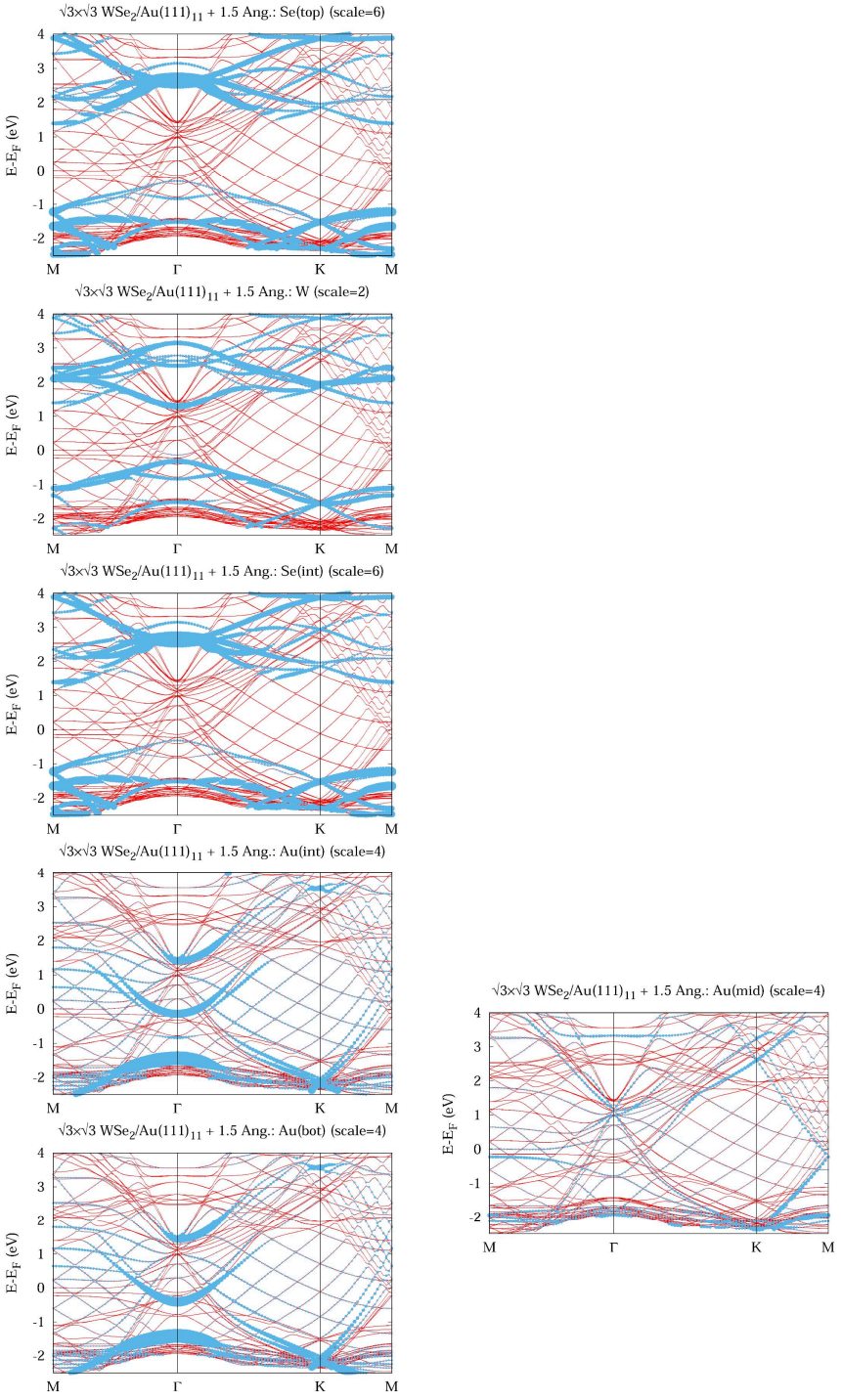

Figure 3-App2. DFT simulations for the (√3 × √3) R30° 1H-WSe_2/Au(111) system with a +1.5 Å shift from the equilibrium position.

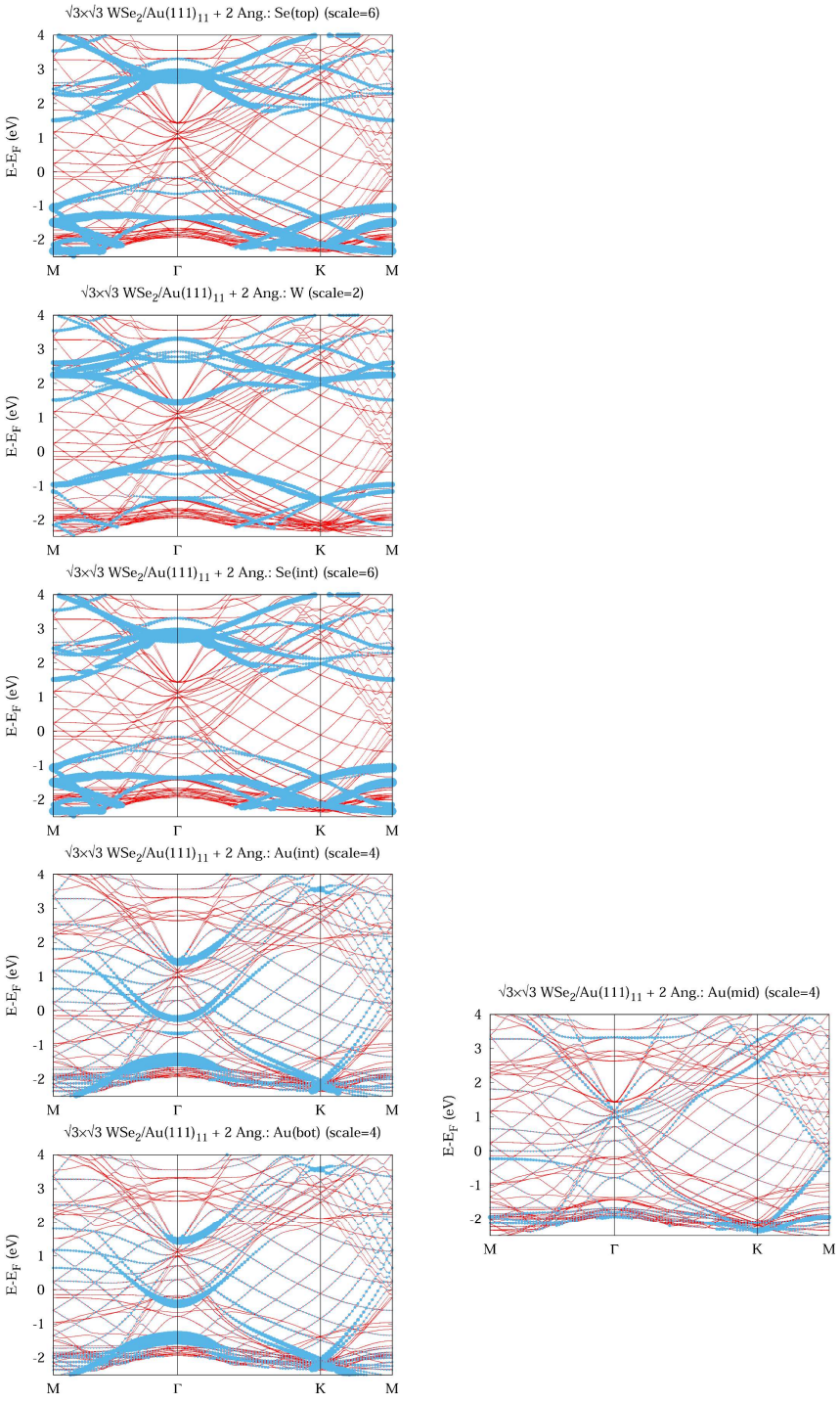

Figure 4-App2. DFT simulations for the (√3 × √3) R30° 1H-WSe_2/Au(111) system with a +2.0 Å shift from the equilibrium position.